Retrofitting of Reinforced Concrete Beams with CARDIFRC in Hot Climate

By

Mohamed Ashour Ewaze
Master in Civil Engineering. (Trinity College)

Thesis submitted to Cardiff University
In candidature for degree of
Doctor of Philosophy

June, 2010

School of Engineering
Cardiff University
Wales

UMI Number: U517417

UMI
Dissertation Publishing

ProQuest

In The Name of the Allah

The Beneficent, the merciful

Acknowledgement

First of all, I would like to express my thanks to my supervisor Professor B. L. Karihaloo for his support, guidance, patience and encouragement during the investigations and the preparation of this thesis and also the friendly relationship that he followed.

Many thanks for the technical staff, especially for Mr. Carl Wadsworth, Des Sandford., Len Czekaj, Brian Hooper, Ian King and Harry Lane for their valuable help during my experimental work.

I would also like to thank my colleagues Dr. Christopher Joseph, Mr. Abdulhamid Alwaer and the Libyan Postgraduate students in school of engineering at Cardiff University for their valuable help and advices during the time of my study.

Special thanks to my mother, brothers and sisters for thier support and encouragement and deepest thanks also to my wife and my lovely children Noran, Safwan and Hala for their understanding and support throughout the period of my study.

Finally, I would like to give my appreciation to my country Libya especially to Engineer Alssadi Algadafi for giving me this chance to get the degree and support me financially during the duration of my study.

Hypothesis

A new retrofitting technique using CARDIFRC®, a material compatible with concrete, has recently been developed at Cardiff University. It overcomes some of the problems associated with the current techniques based on externally bonded steel plates and FRP (fibre-reinforced polymer), which are due to the mismatch of their tensile strength and stiffness with that of concrete structure being retrofitted.

The study investigates the effect of hot climate on the performance of reinforced concrete control and retrofitted beams. The concrete beams were exposed to a maximum temperature of 90°C from the room temperature of about 25° C. The number of thermal cycles varied from 0 to 180 cycles. After the requisite number of thermal cycles, the beams were tested at room temperature in four-point bending.

The tests indicate that the retrofitted beams are stronger, stiffer and more importantly failed in flexure. No visual deterioration or bond degradation was observed after thermal cycling of the retrofitted beams (the bond between the repair material and the concrete substrate remained intact) attesting to the good thermal compatibility between the concrete and CARDIFRC®. Therefore, this type of retrofit material can be successfully used in hot climates.

This study also evaluates the performance of normal and high strength concretes repaired with CARDIFRC® using the wedge splitting test (WST). The main factors that could affect the bond between the repair material and concrete such as the surface roughness and thermal cycling are also investigated. It is shown that surface roughness plays a significant role in the overall bonding system, and no visual deterioration is observed after thermal cycling.

An analytical model based on the concepts of fracture mechanics was used for predicting the ultimate moment capacity of the retrofitted beams. The model predicts very well the ultimate moment capacity of the retrofitted beams.

LIST OF CONTENTS

Chapter 4 High Performance Fibre Reinforced Cementitious Composites HPFRCC-An overview

Chapter 5 Performance of NSC Bonded to CARDIFRC® after Thermal Cycling

Chapter 6 Performance of HSC Bonded to CARDIFRC® after Thermal Cycling

Chapter 7 Retrofitting of Reinforced Concrete Beams with CARDIFRC after thermal cycling

Chapter 8 Analysis of the Reinforced Concrete Beams Retrofitted with CARDIFRC®

Chapter 9 Conclusions

List of References
Appendices

xii

xiii

1.1 Introduction

Concrete [1 or 24], used as a main construction material in the world owing to its
reliability and durability, ideally concrete has been conducted to evaluate both the
mechanical and fracture properties at room temperature, for example, the strength,
toughness, stiffness and fracture energy. Several references cover the applications and
the details of concrete properties, e.g. Neville (1996), Mindress, 1996; Shah et al.,
(1995) and Van Mier (1997).

The most parts of arid climate, the conditions are very low humidity and high
ambient temperatures, combined with intense solar radiation. In winter as the
radiation may reach temperature, they can lead to every microclimate, the
summer daytime temperatures are high and ground surface reach 70°C, while
night may be high temperatures. In addition, however, the surface temperature
of exposed concrete surface temperatures reach 60°C to 80°C when the ambient
temperature in the daytime at the temperatures drop to 10°C at the night time
(Davies and ...).

Many investigations have done the influence on structural properties at elevated
temperatures (e.g., 1996 (a) properties of concrete ... [1], Bertagner and Nasser,
1992; Schrijver et al., ... Harmathy, 1996 (a)... et al., 1996). However,
the studies ... concrete behaviour at pressure ... limited temperature, 1996;
Bazant, Kaplan at high temperature. Few investigations has been done to investigate
the concrete property for hours of climate conditions, and when exposed to daily
and annual temperature conditions temperatures.

Regarding the studies for the to the wetting cycles ... mentioned above accounting
for temperature effects, only the moisture transport ... has always has been considered.
However, these temperature transport ... conditions, any practical applications, it has
been demonstrated that the time of concrete behaviour analysis can be determined based
on the content of modelling, it can mode developed by Terai et al. (2001) and the
concrete properties may be and temperatures ... (2003).

1.1 Introduction

Concrete is widely used as a main construction material in the world owing to its reliability and durability. Much research has been conducted to evaluate both the mechanical and fracture properties at room temperature, for example the strength, toughness, stiffness and fracture energy. Several textbooks cover the applications and the details of the concrete properties (e.g. Neville, 1995; Karihaloo, 1995; Shah et al., 1995 and Van Mier, 1997).

The most profound characteristics of hot dry regions are very low humidity and high summer temperature in the daytime. Also direct solar radiation is intense as the radiation reflected from the high coloured and bare land. In many arid regions, the summer day air temperature can reach 50°C and the ground surface about 70°C, while night may be cool and even cold (Baruch, 1998). Moreover, the surface temperature of exposed concrete may reach somewhere between 80°C to 90°C when the ambient temperature is 40°C during the daytime, while it can fall to 10°C at the night time (Soroka and Jaigerman, 1984).

Much research has been done to investigate the material properties at elevated temperatures (above 100°C) (e.g. Bertero and Polivka, 1973; Berwanger and Sarkar, 1973; Schneider, 1976; Castillo and Durrani, 1990 and Saad et al., 1996). However, the studies that discuss the fracture behaviour are generally limited (e.g. Bažant, 1988; Baker, 1996 and Zhang et al., 2000). Recently attention has been paid to investigate the concrete properties in hot dry climatic environments and when exposed to daily and annual temperature fluctuations (thermal cycling).

Regarding the studies related to the fracture properties mentioned above accounting for temperature effects, only the size-dependent fracture energy has been considered. However, size-independent fracture energy is required in practical applications. It has been demonstrated that the size-independent fracture energy can be determined based on the concept of boundary effect model proposed by Duan et al (2001) and its additional verifications by Abdalla and Karihaloo (2003).

1.1.1 Retrofitted concrete

Intensive studies have been conducted during the last decades to investigate the characteristics of concrete in different conditions to evaluate its behaviour (mechanical and fracture properties). Some of the research focused on the development of concrete mixes with improved properties, for instance high performance fibre reinforced concrete mixes. However, several problems have been observed and recorded in the concrete members, for example poor performance or abnormal conditions leading to initiation and propagation of cracks, causing deterioration of the structure and therefore a need for repair.

The temperature is one of important factors that affect the concrete strength and its stress-strain relationship (Cheng et al., 2004). The hot climate is an example for temperature variation where it can reach more than 45°C in the day-time and fall to 10°C lower than the ambient temperature at the night-time (Soroka and Jaigerman; 1984). The common repair and strengthening technique for RC beams is to bond steel plates to the tension side and/or both vertical sides. The use of this technique introduces many problems such as corrosion of steel plates, difficulty in handling heavy steel plates, etc. (Ziraba et al., 1994).

Recently, attention has been paid to the repair of concrete members based on the use of fibre reinforced plastic (FRP) plates, which are characterized by high strength / weight ratio and improved durability over their steel counterparts (Meier et al., 1992; Meier, 1997). However, using this retrofitting material can lead to undesirable brittle failure due to a large mismatch in the tensile strength and stiffness with that of concrete (Farhat, 2004). Another problem that has been observed is the effect of long exposure to temperature variation (Sen et al., 2000; Zhen and Chung, 2000). Exposures can result in the weakening of the interface between FRP composites and concrete, causing a change in the failure mechanism or a change in performance (Karbhari, 1998).

The effective bonding of repair material to the old concrete is one of the main parameters that must be pointed out; this involves concerns about surface preparation as well as the quality of adhesion and the compatibility of the bonding material with the parent concrete (Farhat, 2004). In hot climatic conditions where fluctuations of

temperature on concrete surfaces may reach 80°C on a typical summer day, de-bonding of the repair material from the old concrete at the repair joint can take place. A durable repair material needs to resist the climatic influences that are caused by large changes in temperature or humidity.

A new retrofitting material has been developed at Cardiff University called the CARDIFRC®. It is characterized by high tensile / flexural strength and high energy absorption capacity that make it particularly suitable for repair of concrete structures (Alaee and Karihaloo, 2003). The findings of Karihaloo et al. (2002) showed that the retrofitting of RC members using CARDIFRC® plates on the tension face improves the flexural load carrying capacity and also decreases the crack width and the deflection.

1.2- Objectives

Some studies have been conducted at Cardiff University using CARDIFRC® for the rehabilitation and strengthening of damaged RC flexural members (Karihaloo et al., 2000; Karihaloo et al., 2002; Alaee et al., 2001). This study is an extension of those studies. The main objectives of the study are:

1. To evaluate the effect of hot climate on the mechanical and fracture properties of normal and high strength concretes.
2. To evaluate the role of the interface when normal and high strength concretes are retrofitted, focusing on the effect of thermal cycles and surface preparation on the repair system.
3. To investigate the performance of RC beams retrofitted with CARDIFRC® and subjected to large temperature fluctuation between 25°C and 90°C. Each thermal cycle consists of a temperature rise time of 20 min during which the temperature is raised from 25°C to 90°C, a dwell period of 8 hours at 90°C, then a cooling period of 15 hours and 40 min in which the temperature is reduced from 90°C to 25°C.

1.3 Outline of Thesis

Starting with the introductory chapter, the thesis is divided to nine chapters. The layout of these chapters is explained in the following:

Chapter 1 gives a general introduction to the topic and introduces also the objectives and the outline of the thesis.

Chapter 2 gives an overview of various retrofitting systems that are used with the concrete members for example, steel plates, fibre reinforced plastics (FRP), and High Performance Fibre Reinforced Cementitious Composites (HPFRCC), for instance Engineered Cementitious Composites (ECC) and CARDIFRC®. Details of each system are presented.

Chapter 3 introduces the principal concepts of fracture mechanics (FM). Firstly, the linear elastic fracture mechanics (LEFM) for brittle materials is discussed, and it is found not to be suitable for concrete. Therefore, the concepts of non-linear fracture mechanics theories for concrete are explained. Secondly, the discussion includes the fracture behaviour of the retrofitted systems. Lastly, an application of fracture mechanics to reinforced concrete structures is demonstrated on longitudinally reinforced beams.

Chapter 4 reviews in brief the behaviour of normal and high strength concretes (NSC, HSC), and also of the high performance and fibre reinforced concretes (HPC, FRC). High Performance Fibre Reinforced Cementitious Composites are reviewed and discussed thoroughly including their fracture properties, with particular reference to CARDIFRC®.

Chapter 5 and **Chapter 6** describe experimental investigations into the mechanical and fracture properties of NSC, HSC and CARDIFRC® mixes under thermal cycling, and evaluate the performance of NSC and HSC specimens retrofitted with CARDIFRC®, using the wedge splitting (WS) test. The evaluation also considers the effect of the surface roughness and the thermal cycles on the repairing system.

In **Chapter 7,** two types of retrofitted reinforced concrete beams (with and without shear reinforcement) have been investigated after subjecting them to different thermal cycles. The test results show that the retrofitted beams are stronger and stiff than the control beams and fail in flexure rather than shear. It is shown that there is no deterioration after the beams are exposed to temperature variations.

Chapter 8 A computer programme has been used to predict the maximum moment resistance using an analytical model based on fracture mechanics. The model follows the initiation and growth of the flexural crack which leads to the beam failure. The prediction of such model is in excellent agreement with the experimental test results.

Chapter 9 is devoted to general conclusions.

Retrofitting
of Concrete Structures

2.1 Introduction

The recovery of concrete structures has been mean strengthening or rehabilitation have been exposed to many different conditions such as fire damage, corrosion, climate effects, faulty design. These conditions allow cracks to propagate and create large deflections in the concrete structure. The repair of deteriorated concrete beams is must important to improve their safety and serviceability and also to increase their strength or [...]

Generally, the recovery of structures can be placed in four categories (Isabel, 2004) and these are:

- Repair is the [...] the damaged structures to their original performance level

- Strengthening applies to enhancing the structural performance over the original design level

- Retrofitting is defined as the addition of something component after failure structure [...]

- Rehabilitation [...] the [...] the subject of repairing and [...]

Concrete construction be found mostly environment methods, for instance change in service loads, change in temperature and deterioration of the, therefore repairing of deteriorated concrete structures is becoming more important rather than rebuilding or demolishing. The technique of enhancing structural capacity using steel plates or fibre reinforced plastic (FRP) plates bonded to the tension side are known techniques and widely used. However, many new repair materials were developed in the last decades, for instance, High Performance Fibre Reinforced Cementitious Composites (HPFRCCs), which are found to be more reliable and effective materials than conventional because they are compatible with concrete (Li, 1992, Li, et al., 1996, Lin and Li, 1997, Rokugo et al., 2009, Boshoff et al., 2011).

2.2 Externally bonded steel plates

The technique of strengthening existing reinforced concrete structures using external steel plate bonding by a structural adhesive is a well-known system. This system has

2.1 Introduction

The majority of concrete structures that need repair, strengthening or rehabilitation have been exposed to many different conditions such as fire damage, corrosion, climatic effects, faulty design. These conditions allow cracks to propagate and create large deflections in the concrete structure. The repair of deteriorated concrete beams is most important to assure their safety and serviceability and also to increase their strength and stiffness.

Generally, the repairing and strengthening can be placed in four categories (Farhat. 2004) and defined as follows:

- Repair: to bring the deteriorated structures back to their original performance level.

- Strengthening: this term applies to enhancing the structural performance over and above the original level.

- Retrofitting: It is defined as the addition of structural components after initial construction.

- Rehabilitation: It is a generic term indicating any aspect of repairing and strengthening.

Concrete structures can be found unsafe for different reasons, for instance change in service loading, poor performance and inadequate design, therefore repairing of deteriorated concrete structures is becoming more important rather than rebuilding or demolishing. The retrofitting of concrete structures using steel plates or fibre reinforced plastic FRP plates bonded to the tension side are known techniques and widely used. However, some new repair materials were developed in the last decade, for instance High Performance Fibre Reinforced Cementitious Composites (HPFRCCs), which are found to be more reliable and effective materials for retrofitting because they are compatible with concrete (e.g. CARDIFRC®) (Li et al., 1995; Lim and Li, 1997; Karihaloo et al., 2000; Karihaloo et al., 2001).

2.2 Externally bonded steel plates

The technique of strengthening existing reinforced concrete structures using external steel plate bonding by a structural adhesive is a well known system. This system has

been used worldwide for over 30 years and, since 1975, in the UK (Barnes and Geoffrey, 2004). The advantages of this technique can be summarized as:

- Low cost.
- Ease of maintenance.
- Minimum effect on headroom.
- Increase in both serviceability and ultimate load capacity.
- The ability to strengthen part of the structure whilst still in use.

The disadvantages of this method are: corrosion of steel plates, installation of heavy plates, transportation and handling of steel plates and limitation in supplying plates of required lengths.

2.2.1 Flexural Strengthening

Several researchers have investigated the flexural strengthening of existing concrete members using steel plates bonded to their tension face (e.g. Jones et al., 1980, 1988, Swamy et al., 1987). The investigations reflected essential improvement in structure serviceability and ultimate strength. Jones et al. (1980) reported the test results of eighteen reinforced beams strengthened with steel plates bonded to the tension face of the beams. Two different types of adhesive material and two types of steel plate with different yield strengths were used. The effects of adhesive material thickness, plate lapping, multiple plates and pre-cracking prior to bonding were investigated. They concluded that epoxy bonded steel plates enlarge the range of elastic behaviour, reduce tensile stresses, increase flexural strength and stiffness, and improve ductility at flexural failure. Moreover, another study by Macdonald and Calder (1982) has investigated bonding steel plates externally to rectangular beams. The results showed significant improvement in the ultimate strength of the strengthened beams.

Flexural strengthening of rectangular reinforced concrete (RC) beams using continuous horizontal steel plates has been carried out after pre-loading (Arslan et al., 2006). These retrofitted RC beams have been then tested under the same conditions as during pre-loading. They found that the retrofitted system is highly effective in improving the flexural behaviour of previously damaged slender RC beams.

7

2.2.1.1 Flexural Failure Modes

Early attention had been paid to the use of steel plates on the tension face of RC beams. However, since then many studies have been carried out to classify the flexural failure after the RC beams have been loaded. Ziraba et al. (1994) classified the flexural failure into three common types (Figure 2.1) as follows:

- Flexural failure.
- Plate peel off.
- Interface separation.

These modes occur due to various reasons, for example weak adhesion and improper gluing can lead to interface separation which can be avoided by proper quality control. Also if the allowable strength values for interface are exceeded, the plate may separate, resulting in premature failure. If the bonding adhesive is weak, this type of failure may be characterised by plate de-bonding proceeding away from the support so that the effective plate length is reduced and the peak peeling stresses progressively increase to a value where a shear critical crack develops, leading to sudden failure (Figure 2.1a). If the adhesive material is strong enough to prevent plate de-bonding, cracking emanates from the location of plate curtailment. The existence of peak peeling and shear stress at the plate curtailment zone, in addition to the bonding stress, results in a biaxial tensile stress state, forcing the crack to move in an essentially horizontal direction just below the level of internal reinforcement where the section is weakest. Failure ensues when the moving horizontal crack joins an existing shear flexural crack, culminating in a steep vertical ascent towards the point of loading (Figure 2.1b).
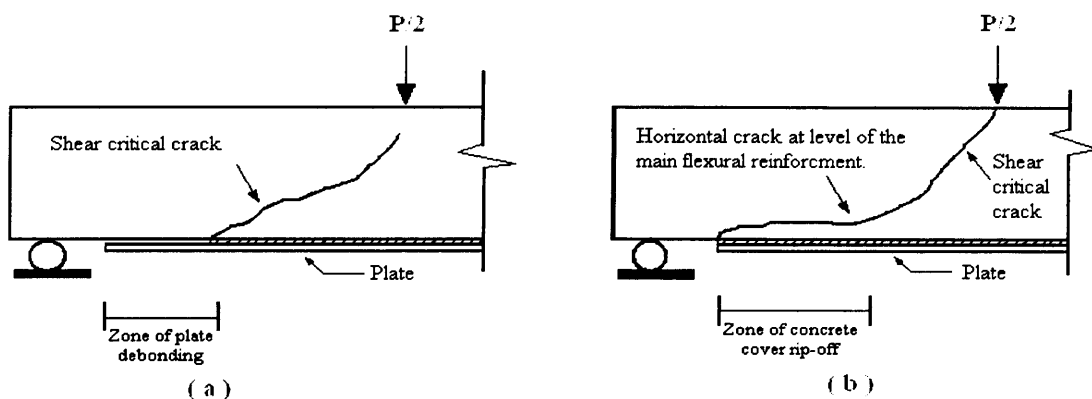
Figure 2.1 Failure of beams retrofitted with steel plates: (a) by plate de-bonding and (b) by ripping off of the concrete cover (after Ziraba et al. 1994)

2.2.2 Shear Strengthening

Shear failure is one of the most serious problems that can occur in concrete structures due to the fact that it gives no advance warning. Various studies have been conducted using steel plates bonded to the vertical side of RC beams which can increase their load capacity in shear. Different configurations have been used to prevent shear failure. Sharif et al., (1995) investigated the shear behaviour of reinforced concrete beams strengthened by using a group of steel plate configurations such as U- and flat steel, vertical strips, bonding over the shear span (Figure 2.2) in order to eliminate shear failure and to develop ductile failure. They observed that the beams retrofitted with jacket plate (Figure 2.2a) gave the highest resistance increase and improvement in ductility. The other retrofitting schemes produced an improvement in the shear resistance but the beams failed suddenly by tearing and splitting of the concrete cover.

Another experimental work has been reported by Barnes and Geoffrey (2004) to investigate the behaviour of reinforced concrete beams strengthened in shear by externally bonded continuous steel plates and hence to provide engineers with appropriate design guidance. The shear strengthening and testing to failure of 15 rectangular section reinforced concrete beams was conducted. To account for the different potential types of shear failure (diagonal tension, shear compression and deep beam failure) three shear span to depth ratios were used. A further 15 experiments were then conducted using T-section beams. In most cases the addition of externally bonded shear plate reinforcement provided enhancement in shear capacity comparable with that provided by conventional internal shear links designed to BS8110.

Adhikary and Mutsuyoshi (2005) carried out an experiment for enhancing the shear capacity of RC beams using different configurations. Two groups of beams were designed; the first group of beams were designed in such a way that the strengthened beams failed in ductile flexural mode thereby avoiding the brittle shear failure. The second group of beams were designed to fail in shear mode to assess the actual increase in shear strength by the devised strengthening configurations. Two beams were kept as control beams, whereas the other beams were strengthened. The results of the experiment confirmed that the externally epoxy bonded steel plates, vertical strips and externally anchored stirrups can improve the ultimate shear strength of

reinforced concrete beams and change the failure mode from brittle shear to flexural one. From the experiments the continuous steel plate method was found to be convenient and more effective in enhancing the shear capacity than the vertical strips. This method also provides additional stiffness against bending and contributes to flexural strengthening (Figure 2.3).
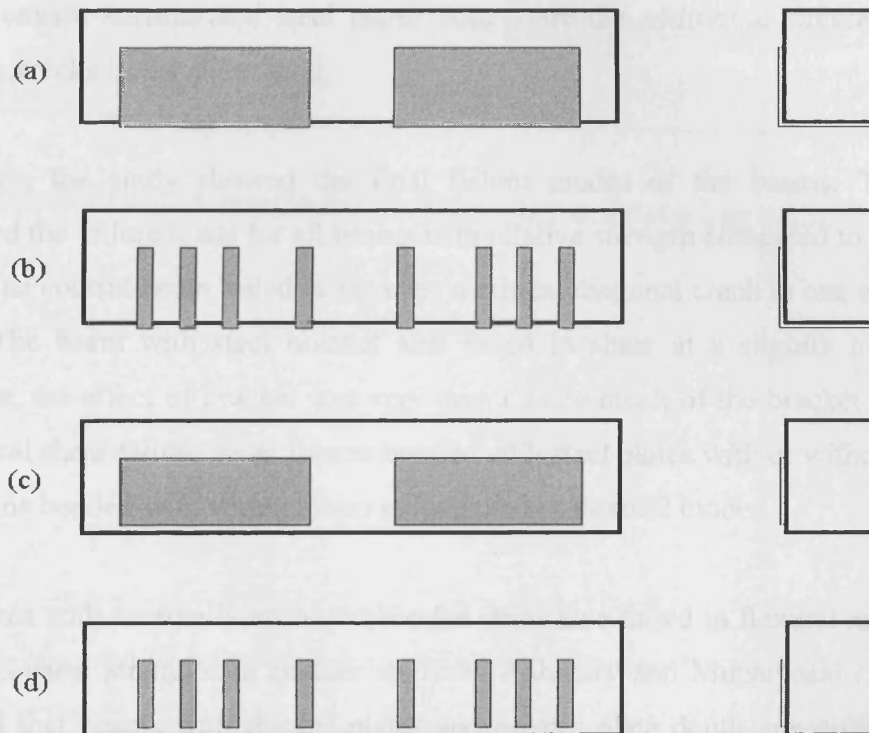
Figure 2.2 Different shear-strengthening schemes (a) Full encasement of shear zone by jacket plate, (b)U- strips on the shear zone, (c) Flat plates on the sides of the beams, (d) Flat strips in the shear zone (after Sharif et al. 1995)
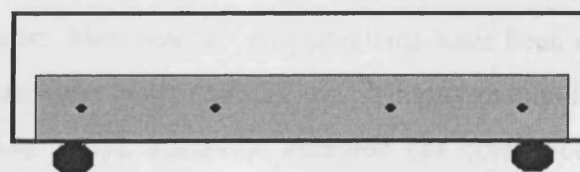
Figure 2.3 RC beam strengthened with continuous horizontal steel plate

2.2.2.1 Shear failure modes

An experimental work on the failure modes carried out by Adhikary and Mutsuyoshi (2005) reported that beams without shear reinforcement (control beams) failed as soon as the first critical shear cracks formed. In the case of steel plate bonded beams, the steel plates alone take up the additional stresses once concrete cracks. Steel plates provide very effective bridging across the cracks, leading to a relatively higher contribution to the shear strength. In the case of beams with internal shear reinforcement, stirrups and steel plates both share the additional stresses once the concrete cracks in the shear span.

Moreover, the study showed the final failure modes of the beams. The results estimated the failure loads for all beams with relative strength compared to the control beam. The control beam failed in shear by a critical diagonal crack in one of the shear spans. The beam with steel bracket also failed in shear at a slightly higher load. However, the effect of bracket was very minor since much of the bracket was out of the critical shear failure zone. Beams bonded with steel plates with or without anchors and beams bonded with vertical steel strips failed in flexural mode.

The beams with externally anchored bonded strips also failed in flexural mode due to enhanced shear strength. In another study by Adhikary and Mutsuyoshi (2005) they recorded that beams with thicker plates and greater plate depth are stiffer than the beams with thinner plates and smaller plate depth and showed the typical shear failure of the RC beam (Figure 2.4). It is thus clear that the best possible way to enhance the shear strength is to use deeper plates rather than thicker plates.

The repairing and strengthening of concrete structures using steel plates bonded to the both beam sides and the bottom have been tested by different researchers, and found to be a good technique. However, several problems have been encountered with this technique such as corrosion of steel plates and difficulty in handling heavy steel plates (Alaee and Karihaloo, 2003). Recently, attention has been focused on the use non-metallic composite materials as an alternative to steel plates to prevent the problems just mentioned.

Figure 2.4 Typical failure of RC beam with web-bonded continuous steel plates.

2.3 Fibre Reinforced Plastics (FRP)

The use of fibre reinforced plastics (FRP) offers many advantages for tackling several civil engineering problems in places where other materials fail to provide satisfactory service life. Thin FRP laminates are durable, have high strength and stiffness to weight ratio and are chemically inert, cost effective and offer significant potential because of their light weight (Nanni 1995, Buyukozturk and Hearing 1998).

Many experimental works have been carried out to evaluate the behaviour of FRP as a retrofitting and strengthening material. Bonfiglioli and Pascale (2004) presented an experimental modal analysis to assess the decrease in stiffness due to damage, as well as the stiffness recovery due to strengthening. The results obtained indicate that an experimental modal analysis can give useful information on the severity of damage and the effectiveness of strengthening by FRP.

Numerical analysis using the ABAQUS finite element program (Hsuan et al., 2004) has shown that the use of fibre-reinforced plastics can significantly increase the stiffness as well as the ultimate strength of reinforced concrete beams. In addition, with the same fibre-reinforced plastic layers, the ultimate strengths of beams strengthened by fibre-reinforced plastics at the bottom of the beams are much higher than those strengthened by fibre-reinforced plastics on both sides of the beams. Moreover, an investigation established that FRP is capable of substantially increasing the load capacity, ductility and energy absorbing capacity, and is effective in the strengthening and repair of damaged RC beams (Lee and Haussmann, 2004). The

strengthening of RC T-section beams using FRP with carbon or glass fibres is an effective method to increase their ultimate carrying capacity and also to enhance the ductility of the strengthened beams (Abdelhady et al., 2006).

The application of FRP for external strengthening of concrete structures has been studied by many researchers; however, many of the studies have also introduced new repairing and strengthening systems using FRP materials that improve the properties of FRP. Although these materials have high strengths, they are very brittle (Nabil et al., 2004), and the loading of these materials in tension exhibits a linear stress–strain relation up to failure without exhibiting a yield plateau or any indication of impending failure. The various FRP systems used for repairing and strengthening are:

- Strengthening with Glass Fibre Reinforced Polymer (GFRP).
- Strengthening with Carbon Fibre Reinforced Polymer (CFRP).
- Strengthening with Hybrid Fibre Reinforced Polymer (HFRP).
- Repairing and Strengthening with Sprayed Fibre Reinforced Polymer composites (SFRP).
- Repairing using E-glass Fibre Reinforced Ultraviolet (UV) curing vinyl ester.
- Strengthening with Ductile Fibre Reinforced Cementitious Composite (DFRCC).
- Strengthening using near surface mounted (NSM) and externally bonded reinforcement (EBR) techniques

The implementation of these techniques with FRP in the strengthening of existing reinforced concrete structures has been demonstrated. The use of the SFRP system enables an increase in the load capacity, ductility and energy absorption; it is also intended to assess the feasibility of using SFRP as a repairing and strengthening material of deteriorating RC beams (Lee and Hausmann, 2004). The scheme that employed hybrid FRP laminates, which consist of a combination of either carbon and glass fibres, or glass and aramid fibres is the best system to strengthen concrete beams by attaching CFRP laminates on the sides of the beam 20 mm above the bottom surface and anchored GFRP laminates at its bottom surface (Abdelhady et al., 2006).

The advantages of these systems of strengthening of RC beams are an increase in ductility, stiffness, durability, and flexural and shear loading capacities.

2.3.1 Flexural Strengthening

The use of externally bonded FRP composite materials for flexural strengthening of reinforced concrete structures in tension has received considerable attention. Strengthening in the tension face parallel to the principal stress direction is possible to increase the ultimate strength and stiffness of the repaired member and have been discussed in many studies (Teng et al., 2002; Rahimi and Hutchinson 2001; Meier and Kaiser 1991). Significant progress has been made based on experiments, theoretical analysis and numerical simulation to demonstrate that the bonding of FRP strips to the tension soffit of reinforced concrete beams can improve much the ultimate flexural strength and stiffness, although some reduction in ductility of the beam is caused (Gao et al., 2007).

The effects of interface bond properties in terms of stiffness, strength, fracture energy, and bond curve shape have been investigated; it is concluded that bond fracture energy is the main parameter influencing the structural strength and ductility (Hedong and Zhishen, 2006). Moreover, a study to establish the effectiveness of FRP composite sheets in upgrading the reinforced concrete beams showed that FRP sheets increase the flexural strength and ductility of RC beams to a great extent (Tarek, 2006).

2.3.1.1 Flexural Failure Modes

Strengthening of reinforced concrete structural components may lead to different failure modes. These modes depend on the strengthening system parameters and the performance of the beam. The most common failure modes have been classified by Gao et al. (2007) (see Figure 2.5) and these are as follows:

- **Compression failure before yielding of steel:** The concrete crushes in compression before yielding of reinforcing steel and fracture of FRP strips.
- **Rupture of FRP strips:** The FRP strips rupture at the point of ultimate strain following the yielding of reinforcing steel rebar in tension.

- **Shear failure:** the shear cracks extend from the vicinity of the support to the loading point when the shear capacity of the beam is exceeded.
- **Delamination of FRP strips:** The delamination of FRP strip occurs rather catastrophically in an unstable manner with a thin layer of concrete residue attached to the delaminated FRP sheets.
- **Compression failure after yielding of steel:** The reinforcing steel yields due to tensile flexure and is followed by crushing of the concrete in the compression zone before the tensile rupture of the FRP strips.
- **Concrete cover separation:** The failure is initiated due to stress effects at the end of FRP plate.

These are the main flexure failures modes which may be expected, the two desirable modes are compression failure following yielding of steel reinforcement and the rupture of FRP strips following yielding of steel reinforcement. Concrete sections with small amounts of reinforcement result in failure due to FRP tensile rupture, while large amounts of reinforcement lead to crushing in the compression zone of concrete section (Bakis et al., 2002). Rupture without yielding of steel reinforcement is sometimes regarded as a kind of flexural failure mode; it is unlikely to occur unless the steel in tension is located very near the centre of the beam (Gao et al. 2007).

Furthermore, shear failure occurs when there is low shear reinforcement in the RC beam; it may also be caused by applying flexural strengthening only, which cannot improve the shear strength of the beam. It has been found however, that restoring or upgrading the beam shear strength using side FRP strips can result in increased shear strength and stiffness by substantially reducing shear cracking (Chaallal et al., 1998).

Concrete cover separation is a very common failure mode; in this mode a crack initiates in one of the FRP plate ends and then grows to the level of the tension steel reinforcement. Under increased loading, the crack propagates horizontally towards the mid-span along the steel rebar (Gao et al. 2007). The failure mode caused by delamination of FRP strips is due to sudden failure in the bond between the concrete and FRP strip and results in the catastrophic propagation of a crack along the FRP concrete interface. There are many reasons for this failure, for instance: (a) strength

and thickness of adhesive (b) flexural and flexural/shear cracks that have developed in the concrete (c) flexural rigidity of the cracked plated section (d) ratio of the width of the bonded plate to its thickness (Triantafillou and Plevris, 1992; Ziraba et al., 1994).
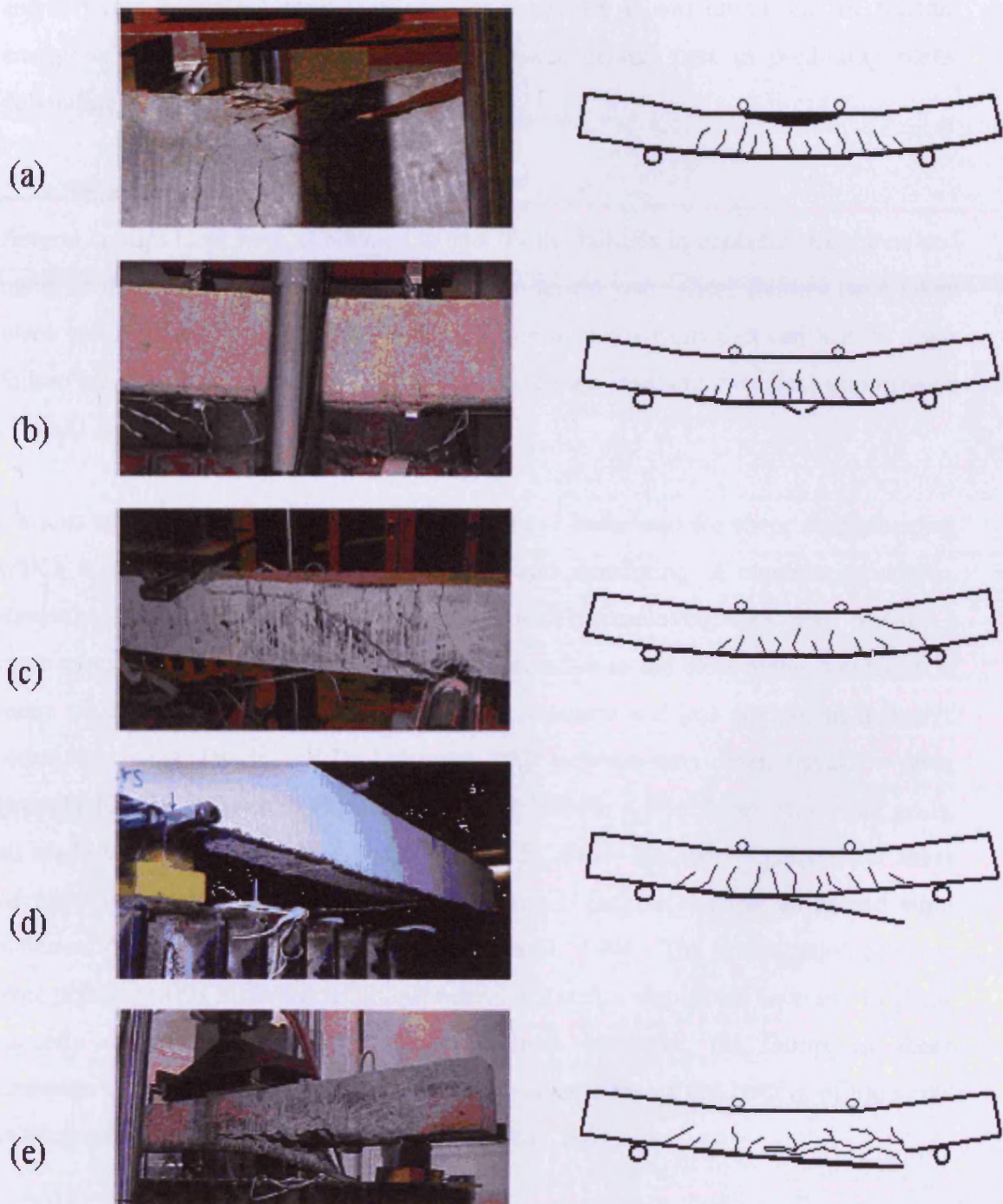
Figure 2.5 Failure modes of FRP strengthened RC beams: (a) compression failure; (b) rupture of FRP strips; (c) shear failure; (d) delamination of FRP strips and (e) concrete cover separation.

A numerical model was proposed by Carlos et al. (2005) to predict the failure of RC beams strengthened in flexure with fibre-reinforced polymeric (FRP) laminates. The model results were validated against experimental data obtained from 19 beams strengthened with different types of FRP. These beams failed by concrete crushing, cover failure and plate debonding. The effect of the concrete constitutive behaviour and different modelling considerations was evaluated. It was found that the fracture energy of the concrete–repair interface plays a central part in predicting plate-debonding failures.

2.3.2 Shear Strengthening

Several studies have been conducted to specify the failures in concrete structures, and many of these focus on flexural failure. In the recent years shear failures have taken place and resulted in catastrophic failure. Some of the reasons that can lead to shear failure are low shear reinforcement, increased service load and the effect of corrosion (Farhat, 2004).

Various retrofitting materials and techniques have been used for shear strengthening, which are based on a great need for repair and retrofitting of concrete structures. Recently, FRP plates and sheets have been widely employed; they may provide a more economical and technically superior alternative to the steel plates technique in many situations and can result in less labour-intensive and less equipment intensive retrofitting work (Hadi, 2003). Different FRP systems have been used for shear strengthening of RC beams (Figure 2.6), these include a fibre wrap, strips and grids, all made up of carbon fibre (Islam et al., 2005). Other methods employed for shear strengthening of RC beam sections are bonding U jackets, vertical strips and wing plates as shown in Figure 2.7 (Al-Sulaimani et al., 1994). The investigation of shear strengthening with different techniques demonstrated a significant increase in shear capacity especially with the U jacket method. However, the failure of shear strengthened beams occurs after the maximum shear stress at the bottom of the strips or wings reaches the interface shear stress (Farhat, 2004).

A laboratory work was conducted by Sundarraja and Rajamohan (2007) to clarify the role of glass fibre reinforced polymer inclined strips epoxy bonded to the beam web for shear strengthening of reinforced concrete beams. Included in the study are

effectiveness in terms of width and spacing of inclined GFRP strips, spacing of internal steel stirrups, and longitudinal steel rebar section on shear capacity of the RC beam (Figure 2.8). The results showed that the initial cracks are formed at higher loads than their respective control beams. This shows that the use of GFRP strips is more effective in the case of strengthening of structures in shear. The ultimate strength of beams can be also increased by the use of GFRP inclined strips, and the load carrying capacity of the retrofitted beams was found to be greater than that of the control beams, thus the externally bonded FRPs were able to help in taking more load.
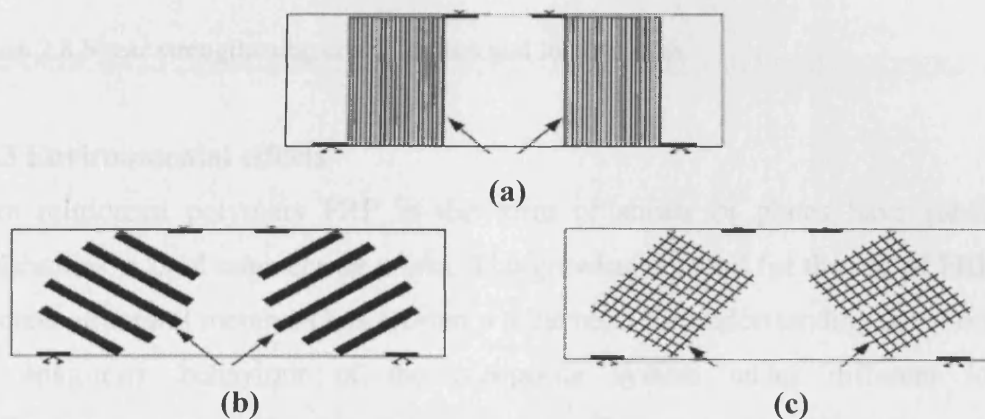
Figure 2.6 Different CFRP systems: (a) FRP wraps (b) FRP strips (c) Grids
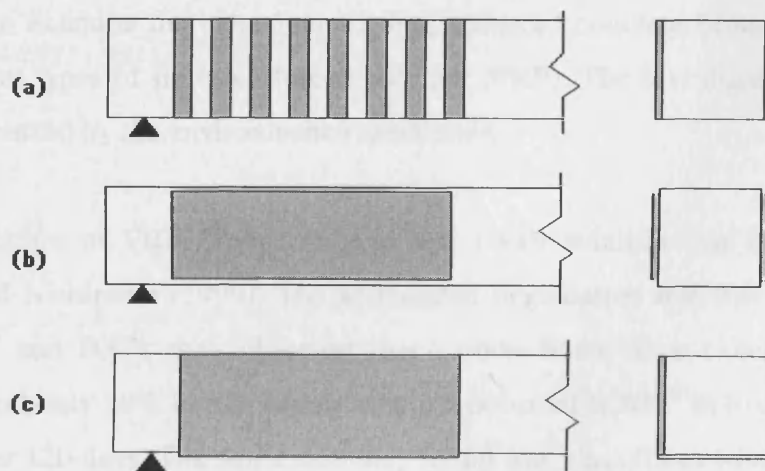
Figure 2.7 Other shear strengthening methods: (a) Vertical stripes (b) Shear wings, and (c) Bonded U jackets

18
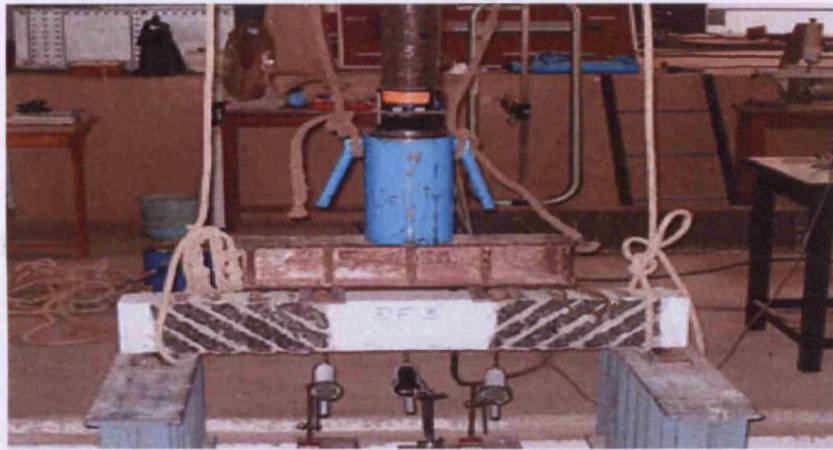
Figure 2.8 Shear strengthening configuration and load process

2.3.3 Environmental effects

Fibre reinforced polymers FRP in the form of sheets or plates have substantial applications in civil engineering works. The growing demand for the use of FRP with concrete structural members has created a great need for understanding the short-term and long-term behaviour of the composite system under different loading configurations and environmental conditions. The environmental actions on the retrofitted RC concrete structures such as freeze-thaw, wet-dry and temperature cycles or aqueous solutions can affect their mechanical and physical properties and lead to a reduction in both the strength and durability. Several investigations have been conducted to examine the behaviour of the reinforced concrete beams strengthened with different types of fibre reinforced polymer (FRP). The investigations examined the effects caused by the environmental conditions.

The degradation of FRP fabrics in acid and alkali solution was investigated by Uomoto and Nishimura (1999). The accelerated degradation test was carried out at $20C^0$, $40C^0$ and $80C^0$; they observed that carbon fibres have excellent chemical resistance and only 20% loss in tensile strength occurred at $80C^0$ in hydrochloric acid solution after 120 days. The worst case they found was glass fibres when immersed in any of the solutions at a temperature of $80C^0$. The glass fibres showed, for example, 96% strength reduction in sodium hydroxide alkaline solution within just 9 hours. The bond strength evaluation between concrete and glass, or carbon fabric before and after aging them under acidic and alkaline solutions, and to temperature and humidity

changes has been investigated by Ganga and Barger (2001) under conditioning durations varying between 1 and 9 months. They observed that the average variation in the bond strength of the specimens (glass and carbon fibres) under accelerated aging were within 10% of un-aged specimens. They also observed that 20% sustained stress had no noticeable effect on bond strength of both carbon and glass fabrics with concrete. Sen et al. (2000) observed slight bond degradation in the interfacial phase of CFRP/Epoxy/ Concrete. In another experimental work conducted by the same authors in 1999 a visible bond crack was observed when CFRP was exposed to hot and cold cycles.

Almusallam et al. (2001) have examined the performance of concrete cylinders wrapped with GFRP composite sheets subjected to different environment exposure conditions. The results showed that exposure to high temperature, outside environment and wet/dry conditions had little effect on the compressive strength of specimens wrapped with GFRP sheets, especially when compared with the values obtained for samples kept at room temperature. The effect of alkaline solution environment was significant, especially for samples kept at elevated temperature, in which a high degradation occurred in the fibre composites themselves.

Myers et al. (2001) conducted an experimental program to investigate the durability of bond between concrete and various FRP sheets (carbon, glass, aramid). The results showed that the combined environmental exposure has an adverse effect on the bond performance of FRP sheets to concrete. Members strengthened with three different FRP sheets indicated a reduction in flexural stiffness of the member through the degradation of bond of FRP sheet with concrete. It was also concluded that specimens conditioned under higher sustained loads (40% of ultimate load) degraded more in bond when compared to unloaded specimens.

Leung et al. (2001) investigated the flexural capacity of strengthened concrete beams exposed to different environmental conditions. In this investigation, it was proved that strengthening with CFRP provides greater enhancement than strengthening with steel plates. Exposure to water for long periods caused a change in the load carrying capacity as well as the mid-span deflection.

Grace and Grace (2001) studied the durability of the reinforced concrete beams externally strengthened with CFRP plates and fabrics under adverse environmental conditions such as 100% humidity, salt-water, alkali solution, freeze–thaw thermal expansion, and dry-heat. They observed that the long-term exposure to humidity was the most-detrimental factor affecting the bond strength between CFRP plates/fabrics and RC beams.

Another study has been carried out by Almusallam (2006) to test the durability of reinforced concrete beams strengthened with glass fibre reinforced polymer (GFRP) laminates. The results of experiments performed on GFRP strengthened beams established the sound durability of GFRP sheets in varied environmental conditions. It was observed that GFRP sheets attached to the beams and exposed to different curing conditions for a period of 6–24 months showed no degradation in imparting the strength and stiffness to strengthened beams.

The effect of UV rays was also studied on the durability of GFRP sheets by exposing UV painted and unpainted strengthened specimens to solar radiations for 6–24 months. Again, no degradation in the performance of GFRP sheets was observed due to exposure to solar radiations (containing UV rays). However, the degradation effect of solar radiation cannot be neglected if the GFRP sheets are exposed to such radiations for a long time (e.g. number of years).

The exposure to a variety of environmental conditions can change failure modes of the FRP composites and result in the weakening of the interface between FRP composites and concrete causing a change in the failure mechanism and sometimes a change in performance (Karbhari, 1998).

2.3.3.1 The effect of fire exposure

The exposure of concrete members to fire can be lead to yielding of the steel reinforcement and a subsequent reduction of load bearing capacity; it represents one of the most severe risks to buildings and structures, the main aspects of fire behaviour that must be considered include:

- Fire resistance.
- Smoke evolution and toxicity.
- Heat generation characteristics.
- Flame spread.

The performance of the composites at elevated temperatures depends solely on their constituents: the fibres, the matrix, the proportion of fibre to matrix, and the relative stiffness of each. Limited range of relevant studies has been previously carried out, to evaluate the mechanical properties of the RC structures. Carbon fibres alone are capable of resisting temperatures well in access of 1000^0 C without serious strength loss (ACI, 2001). The epoxy matrix, however, is the critical component governing fire behaviour of the overall composite (Williams et al., 2003). When the FRP composite is exposed to fire it is liable to be effected by burning because of the flammability of the matrix.

Gamage et al. (2006) investigated the behaviour of CFRP–concrete composites under fire using a 3D model. The results showed that the epoxy adhesive being used in the construction industry is very sensitive to temperature variations, and the epoxy temperature should not exceed 70^0C in order to maintain the integrity between the CFRP and concrete at high temperature. The CFRP concrete composites reach the failure point within 5.5-6.0 min under exposure to the standard fire.

2.3.3.2 The effect of freeze and freeze-thaw

In cold environments, freezing and thawing can be harmful for a porous brittle material such as concrete when it is subjected to lower temperatures. According to the previous studies, it is reported that the high strength concrete subjected to freezing and thawing cycles may deteriorate rapidly and cause damage in concrete resistance leading to failure.

The damage process is accelerated and the extent of damage increased under the simultaneous action of load and freeze-thaw cycles (Sun et al., 1999). Nollet et al. (1999) investigated the short-term flexural performance of beams strengthened by CFRP strip under room temperature ($+25^0C$) and freezing temperature (-25^0C). It was

observed that due to freezing, both the load and deflection increased. A 35% increase in flexural capacity was noted under freezing temperature.

Furthermore, Karbhari et al. (2000) cycled carbon/epoxy confined concrete cylinders between 22.5^0C and -20^0C 201 times without prior moisture exposure and noted there was insignificant change in levels of ultimate strength, although a decrease in hoop strain levels was seen. It was noted, however, that "dry" freeze-thaw cycling did result in substantial matrix micro-cracking that in the presence of moisture could result in significantly accelerated degradation in overall response under ambient conditions rather than under conditions of exposure. The biaxial compressive strength of plain concrete also decreased as the freeze–thaw cycles were repeated (Shang and Song, 2006).

2.4 High Performance Fibre Reinforced Cementitious Composites (HPFRCCs)

Recently, intensive studies have been carried out to produce alternative repair and strengthening materials to avoid the problems that are caused by bonded steel and FRP plates to concrete members. Generally, the repairing material should be durable and have a good bond with substrate under service conditions. High performance fibre reinforced cementitous composites materials have been evaluated, and found to be excellent materials for retrofitting (Hammil 1999; Karihaloo et al., 2001).

Naaman and Reinhardt (2004) suggested that the use of a performance-based design classification of FRC composites can be expressed to four levels of performance, namely: Crack control; Deflection hardening; Strain hardening; High energy absorption. This classification has the advantage of following current applications; indeed low fibre content is used in numerous applications in slabs on grade for crack control; deflection hardening composites with a moderate volume content of fibres are used in beams in combination with conventional reinforcement such as in seismic resistant structures; strain hardening composites are used in stand-alone thin sheets applications and require a relatively higher volume fraction of fibres; and very high fibre contents are used in blast and impact resistant structures which require high energy absorption capacity

2.4.1 Engineered cementitious composites (ECC)

A micro-structurally tailored Engineered Cementitious Composite (ECC) serving as the repair material was found to be most effective in trapping interface cracks which typify failure modes in repaired systems, such as spalling or delamination (Lim and Li, 1997). It was also observed that, for the same geometry and loading conditions, the ECC repair system is stronger, more ductile, more energy absorbing, and shows better crack width control in comparison with controlled systems with concrete or a typical fibre reinforced concrete repair material.

An experiment was carried out by Li and Kamada (2000) to investigate the effect of surface preparation on the kink-crack trapping mechanism of engineered cementitious composite (ECC)/concrete repair systems using different substrates. Generally, surface preparation of the substrate concrete is considered essential to achieve a durable repair. In this experiment, the smooth surface system showed more desirable behaviour in the crack pattern and the crack widths than the rough surface system. This demonstrates that the smooth surface system is preferable to the rough surface system, from the view point of obtaining a durable repaired structure.

The engineered cementitious composite was consolidated using different materials such as reinforcement by polyethylene (PE) fibres (Li et al., 1998). Thereby, the ultimate material strength and ductility of the self consolidating PE-ECC were lower than the normal (cast and vibrate) PE-ECC containing higher fibre volume fractions. Recently, ECC material reinforced with hydrophilic poly (vinyl alcohol) (PVA) fibres has been developed, using extensive micromechanical design and experiments to obtain appropriate PVA fibre bridging response (Li and Kanda, 1998; Wu, 2000). The ultimate tensile strain in PVA-ECC was achieved with 2% vol. of PVA fibres. In addition, PVA-ECC is favoured for practical applications, since it is more cost-effective than PE-ECC.

Li et al. (2003) conducted work to develop high performance self-consolidating PVA-ECC with ductility comparable to normal PVA-ECC by applying the same approach as used in the development of the self consolidating PE-ECC. It resulted in a ductility of self-consolidating PVA-FRC being lower than that of the self-consolidating PE-ECC made with the same matrix. The excellent properties of the PVA-FRC mix, due

largely to uniform fibre dispersion, suggest that the use of the PVA fibre as the reinforcement of the ECC material can afford the use of higher fibre content than the PE-ECC without sacrificing the self-consolidating performance.

Moreover, an experimental work was carried out by Mustafa and Li (2007) to investigate the durability of ECC material with regard to cracking and healing under combined mechanical loading and environmental loading conditions. ECC coupon specimens were firstly pre-loaded under uni-axial tension to different strain levels, and then exposed to an alkaline environment up to 3 months at 38°C and reloaded up to failure. The results indicated strong evidence of self-healing of the micro-cracked ECC material, which can still carry considerable tensile stress and strain and restore nearly the original stiffness. The phenomenon of self-healing effectively closes the micro-cracks even after one month exposure period.

2.4.2 Retrofitting with CARDIFRC®

CARDIFRC is a new material that has been developed in Cardiff University. It is a high performance fibre reinforced cementitious composite material characterised by high tensile and flexural strength and also a high energy absorption capacity. The special characteristics of CARDIFRC® make it particularly suitable for repair, remedial, and upgrading activities (i.e., retrofitting) of existing concrete structures. Farhat (2004) expressed the main advantages of CARDIFRC® as a retrofitting material as follows:

- Improving the serviceability of RC concrete structure.
- Ensuring gradual failure without delamination.
- Ensuring compatibility with the material of the structure being retrofitted.
- Can be used as a repairing material without fibre (e.g. for filling cracks, replacement of spalled concrete)

Strengthening RC beams with CARDIFRC® can be done firstly by adhesive bonding of pre-cast strips to RC beams. This system requires that the retrofit material adheres precisely and safely to concrete members. Secondly by using the direct cast system of wet CARDIFRC® on to the structure. This technique requires a special formwork and

25

thus limits the application in practice. The applications of CARDIFRC® as a retrofitting material are shown in Figure (2.9). The different techniques used thin pre-cast strips adhesively bonded to the tension face and/or both RC beam sides for flexural and shear strengthening.
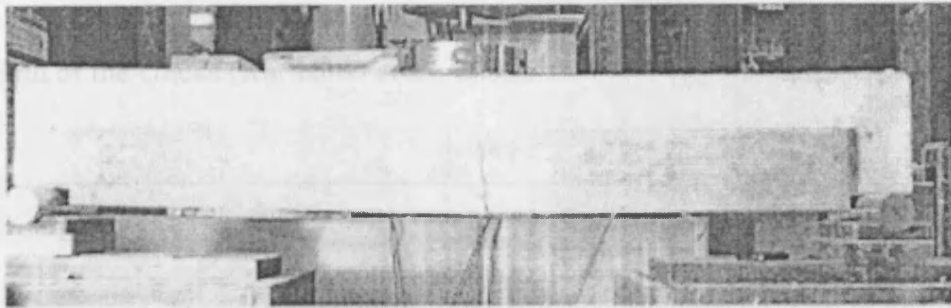
(a)

(b)

Figure 2.9 Flexural cracking in beam retrofitted with: (a) three thick strips and (b) four trapezoidal strips on sides and continuous strip on tension face

2.4.2.1 Flexural Strengthening

Flexural strengthening of deteriorating RC beams using CARDIFRC® strips can be achieved by bonding CARDIFRC® strips to the tension face of RC beams. Several experiments have been conducted by Karihaloo et al. (2003) using damaged RC beams retrofitted with CARDIFRC® strips. The test beams consisted of two types: beams without shear reinforcement and beams with adequate shear reinforcement. The retrofitted beams were loaded to failure and compared with the control beams; all beams failed at loads at least equal to the average failure load of the control beams with flexural, shear or a combination of flexural and shear failures modes.

2.4.2.2 Flexural and Shear Strengthening

Flexural and shear strengthening of the damaged RC beams can be achieved using CARDIFRC® strips in tensile face and each side of beams in different configurations (Figure 2.10). In comparison with beams retrofitted in tension only, the different types of flexural and shear strengthening configurations produced significant improvements in load carrying capacity and serviceability in terms of reduction in the number and the width of the cracks (Karihaloo et al., 2003).
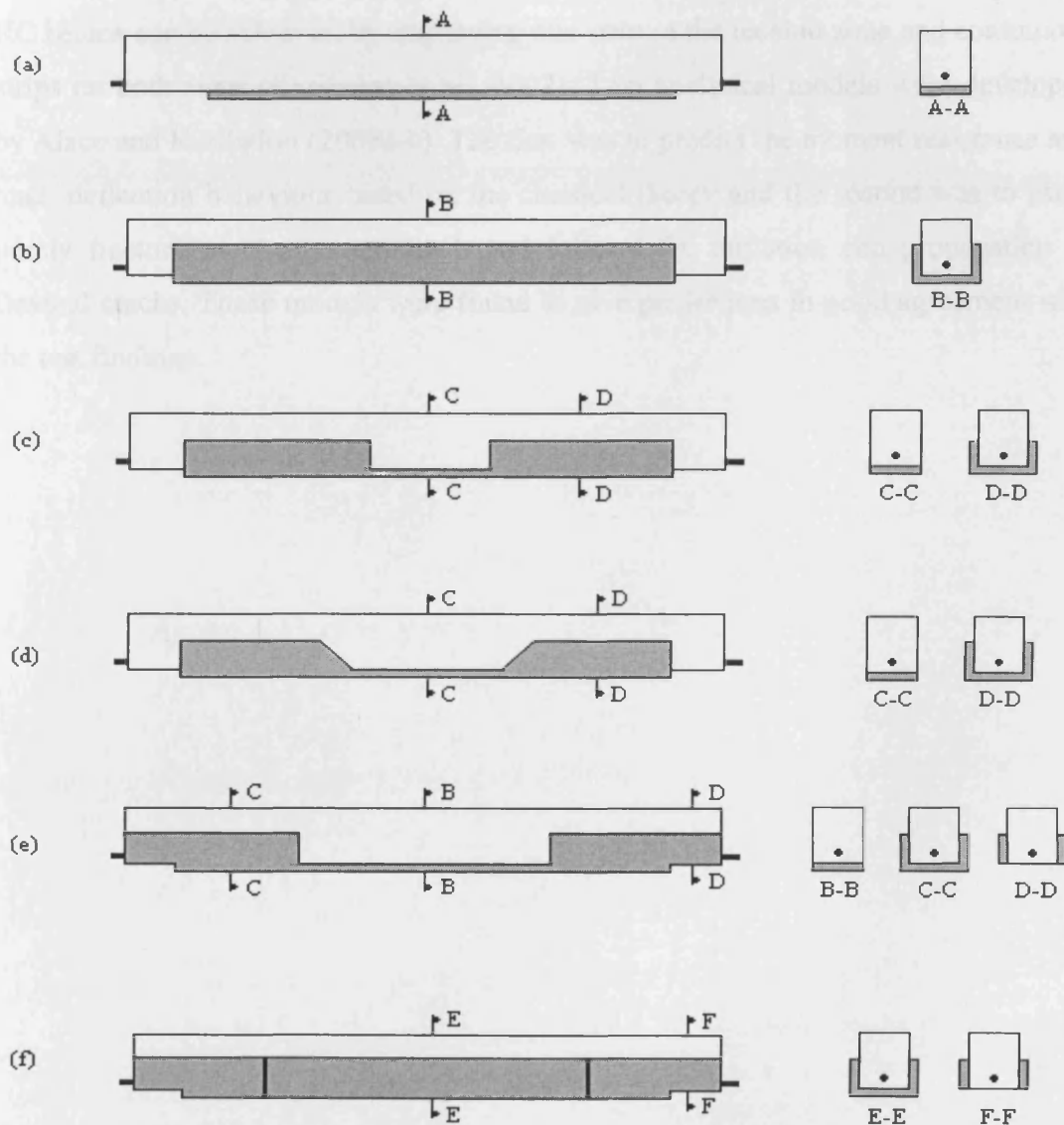
Figure 2.10 Configurations of retrofitting RC beams with CARDIFRC® : (a) beam retrofitted with one strip on tension side; (b) beam retrofitted with one strip underneath and two side strips; (c) beam retrofitted with one strip underneath and four rectangular side strips; (d) beam retrofitted with one strip underneath and four trapezoidal side strips; (e) one strip bonded on tension face and four short strips on vertical sides covering supports and ends of tension strip; and (f) one strip bonded on tension face and four short and two continuous strips on vertical sides, fully covering supports and tension strip sides

Failure was characterised by the formation and opening of a single flexural crack around the mid-span of the beam (Figure 2.10). Alaee (2002) investigated RC beams with sufficient shear reinforcement retrofitted by one strip on the tension face and two short strips on both sides to avoid shear cracks. It was found to be very effective in improving flexural and shear behaviour but does not improve the load carrying capacity of the RC beams

The high load carrying capacity and stiffness without any shear distress in retrofitted RC beams can be achieved by employing one strip in the tension zone and continuous strips on both sides (Karihaloo et al., 2002). Two analytical models were developed by Alaee and Karihaloo (2003a-b). The first was to predict the moment resistance and load- deflection behaviour based on the classical theory and the second was to use a purely fracture mechanics approach and follows the initiation and propagation of flexural cracks. These models were found to give predictions in good agreement with the test findings.

3.1 Introduction

For engineering materials can be classified into brittle, where suddenly drops to zero using a brittle material fractures, ductile, where a stress constant or increases when a quasi-brittle solids, and quasi-brittle stress gradually decreases after the peak stress.

There are materials such as stone, glass varieties, but ceramic, air voids, water filled pores, etc. in concrete. By the effect of the external loading these flaws develop, microcracks such as microfracture in concrete until fractures are formed which causes failure. When the stress concentrate, these microcracks are arranged along the loading direction, and a fracture zone through them to an actual fracture. Therefore microcracks provides an energy based failure theory that can be predicted. The energy release rate to explain the consequences of crack initiation and propagation in solids (Griffith, 1921).

The concepts that the initial introduction of fracture mechanics (Parker, 2004) to provide a framework for formulation of fracture mechanics will be useful in the different characteristics of concrete. Fracture mechanics that found in (Kesh, 1953, Brook, 1974, Jenck, Swain and Wuishu 1973, Ingraham, David Shames et al 1995 and also Mindess, 1983). It deals with an estimate based on linear elastic fracture mechanics of concrete fracture mechanics of approaches for concrete. The fundamentals of non-linear fracture mechanics for concrete are introduced. The concepts based upon fracture mechanics for concrete. The fracture behavior of the reporting structural applications of fracture mechanics in reinforced concrete structures is demonstrated on a longitudinally reinforced cracked beam.

3.2 Linear Elastic Fracture Mechanics

3.2.1 Griffith Theory of Brittle Fracture

GRIFFITH (1920) explained that real stress discrepancy research the theoretically predicted and actual strength values of how brittle materials leads to the presence of small cracks and micro crack-like defects in these materials. The theory is based on the assumption that the brittle materials in the concrete contain at very high tensile stress concentrations, cracks are induced around the crack tips when the load is applied (Anthony and Petersen 1980). Consider a large plate of unit thickness containing a

3.1 Introduction

The engineering materials can be classified into; brittle: stress suddenly drops to zero when a brittle material fractures, ductile: stress remains constant or increases when a ductile material yields, and quasi-brittle: stress gradually decreases after the peak stress.

There are many inherent flaws in a concrete structure, for example; air voids, water filled pores and shrinkage cracks. By the affect of the external loading these flaws develop, merge with existing or newly-formed microcracks until fractures are formed which cause the collapse of the concrete structure. To date these structures are designed without regard to the propagation of large cracking zone through them or an energy failure criterion. Fracture mechanics provides an energy based failure theory that can be useful for designing cement-based structures against the consequences of crack initiation and propagation (Karihaloo, 1995)

This chapter follows the outline in the third chapter of Farhat's thesis (Farhat, 2004). It provides a summary of fracture mechanics theories that will be useful in the subsequent chapters. An intensive literature on this topic can be found in Knott, 1973; Broek, 1978 and 1989; Ewalds and Wanhill, 1985; Karihaloo, 1995; Shah et al., 1995 and Van Mier, 1997. We begin with an introduction into the linear elastic fracture mechanics (LEFM) for brittle materials; it shows that the LEFM is not suitable for concrete. Therefore, the concepts of non-linear fracture mechanics for concrete are introduced. The topics discussed also touch upon the fracture behaviour of the repairing system and an application of fracture mechanics to reinforced concrete structures is demonstrated on a longitudinally reinforced cracked beam.

3-2 Linear Elastic Fracture Mechanics
3.2.1 Griffith Theory of Brittle Fracture

Griffith (1920) explained that the large discrepancy between the theoretically predicted and real tensile strengths of hard brittle materials is due to the presence of small cracks and other crack-like defects in these materials. The theory is based on the assumption that the fracture initiates at the cracks as a result of very high tensile stress concentrations, which are induced around the crack tips when the load is applied (Anthony and Newman 1965). Consider a large plate of unit thickness containing a

crack of length $2a$ subjected to a uniform far-field tensile stress (Figure 3.1a). From Inglis's (1913) solution for a slit-like cut the vertical displacement of the upper face of the cut is:

$$v(x) = \frac{2\sigma}{E}\sqrt{a^2 - x^2}, \qquad 0 \le |x| \le a \tag{3.1}$$

where E is Young's modulus.

With reference to Figure 3.1, it is clearly seen that the elastic plate with the slit-like cut of length $2a$ can be considered as the superposition of an elastic plate without a cut under external stress σ and the same plate without external σ but with equal and opposite stresses (i.e.- σ) applied gradually to the faces of the intended cut. Hence the stress σ on each of the two faces is displaced by the amount $v(x)$ of equation (3.1), so that the work done is given by:

$$W = 2\left[-\frac{\sigma}{2} \int_{-a}^{a} v(x)dx \right] = -\frac{\pi a^2 \sigma^2}{E} \tag{3.2}$$

The negative sign in equation (3.2) indicates the stress and displacement are of the opposite sign, and the factor ½ in the square brackets appears because the stress gradually increases from 0 to σ.
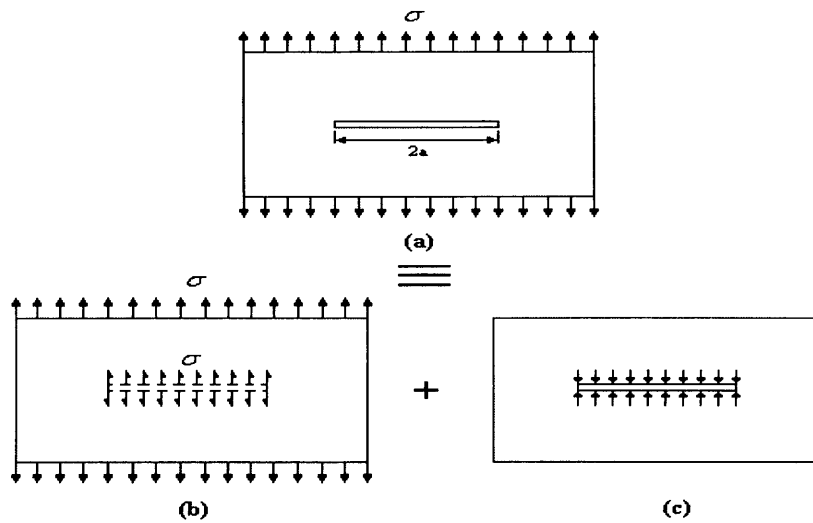
Figure 3.1 The principle of superposition (a) the plate is under external tension (b) uncracked plate under σ (c) plate without external σ but with equal opposite stress applied to the crack to create a stress-free crack (After Karihaloo, 1995)

30

If the loaded boundaries of the panel are free to move, then the elastic strain energy U of the body increases during the crack process, and the change in W is equal to the change in the potential energy Π of the system for an incremental crack growth.

$$dW = -d\Gamma \tag{3.3}$$

where

$$\Gamma = 4a\gamma \tag{3.4}$$

Γ is the surface energy consumed in the creation of the crack, and γ is the surface energy density, that is the energy required to create a unit crack surface.

The principle of minimum potential energy is applied for a stable crack, and it may be rewritten as:

$$\frac{\partial}{\partial a}(W + \Gamma) = 0 \tag{3.5}$$

Substituting (3.2) and (3.4) into (3.5) gives

$$\sigma^2 = \frac{2E\gamma}{\pi a} \tag{3.6}$$

For a given material (i.e. given E and γ) it follows that

$$\sigma\sqrt{\pi a} = \sqrt{2E\gamma} = const. \tag{3.7}$$

According to the Griffith fracture criterion or the global energy criterion a brittle material will fracture when the stress σ reaches the value σ_c that satisfies equation (3.7). It shows that the strength of a brittle material σ_c is dependent on physical parameters such as the Young modulus, the surface energy density, and the length of the crack.

3.2.2 Irwin Theory of Brittle Fracture

Griffith's work was significant; however it did not include materials other than brittle ones in its consideration. Irwin (1957) began to see how the theory would apply to ductile materials. He determined that there was also a certain energy from plastic deformation that had to be added to the surface energy of Griffith in order for the theory to work for ductile materials as well, creating what is known as the strain energy release rate. If the energy used in the plastic deformation is included in equation (3.7), it becomes,

$$\sigma = \sqrt{\frac{2E(\gamma + \gamma_P)}{\pi a}} \qquad (3.8)$$

where γ_p is the energy used in the plastic deformation associated with the crack extension.

Generally, there are three possible modes of deformation at a crack tip (Figure 3.2):

- Mode I - opening or tensile mode, where the crack surfaces move directly apart (Figure 3.2a).

- Mode II - sliding or in-plane shear mode, where the crack surfaces slide over one another in direction perpendicular to the leading edge of the crack (Figure3.2b).

- Mode III - tearing or antiplane shear mode, where the crack surfaces move relative to one another and parallel to the leading edge of the crack (Figure 3.2c).

(a) Opening Mode I　　　　(b) Sliding Mode II　　　　(c) Tearing Mode III
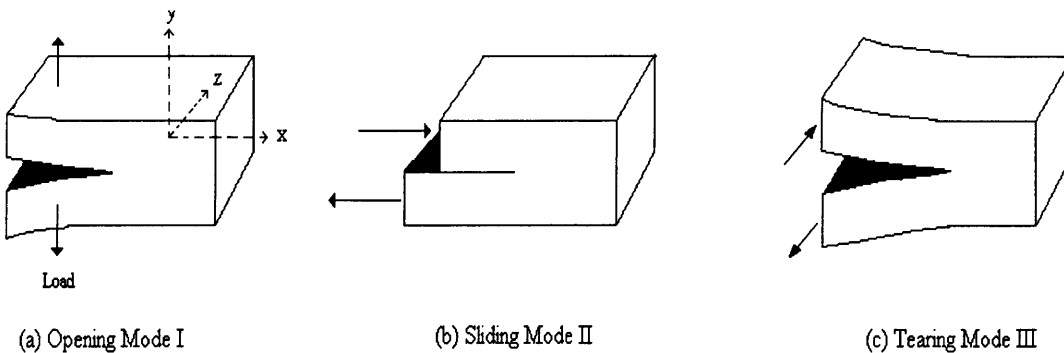
Figure 3.2 Modes of crack propagation

The most severe mode from the point of view of fracture is mode I, as the propagation of crack in real material under pure Mode II and III conditions needs a great amount of energy, due to friction between the crack faces.

Now, consider a two dimensional (plane) body of infinite extent subjected to a uniform stress remote from the crack, which induces an opening mode of stress at the crack tips (Figure 3.3). The stress and displacement components of a point in the vicinity of the crack tip can be written as:

$$\sigma_{ij} = \frac{K_I}{\sqrt{2\pi r}} f_{ij}(\theta) + \ldots \qquad i,j \in \{x,y\} \qquad\qquad (3.9)$$

$$u_i = \frac{K_I(1+v)}{E} \sqrt{\frac{2r}{\pi}} g_i(\theta) + \ldots \qquad i \in \{x,y\} \qquad\qquad (3.10)$$

where r and θ are the polar co-ordinates of the point with respect to the crack tip. E and v are the Young modulus and the Poisson ratio of the material, respectively.
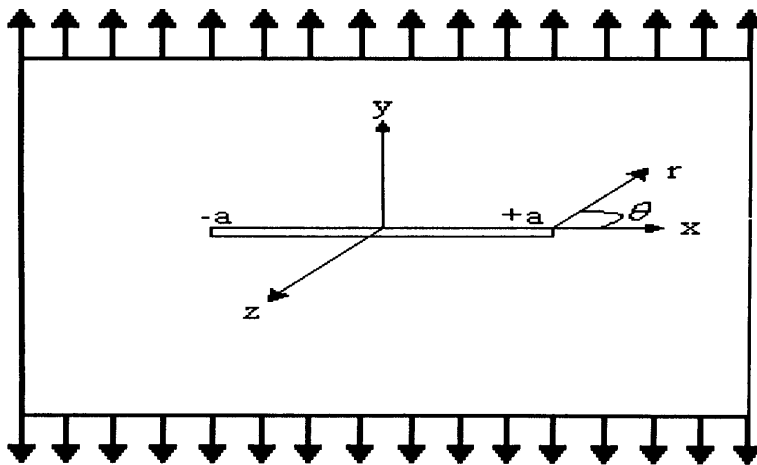
Figure 3.3 An infinite elastic body with a sharp crack of length 2a under mode I

The parameter K_I (I denotes Mode I) called the stress intensity factor depends on the geometry of the body and manner in which the loading is applied. For the geometry shown in Figure 3.3, K_I is given by

$$K_I = \sigma \sqrt{\pi a} \qquad\qquad (3.11)$$

Generally, K_I is finite and positive. There can be situations when K_I vanishes, but it can never be negative. The shapes of the crack tip zones and the stress distributions ahead of the tips are shown in Figure 3.4 for $K_I > 0$, $K_I < 0$ and $K_I = 0$. When $K_I = 0$ (Figure 3.4c), the crack faces close smoothly and the stresses ahead of the crack tip are finite. It should be mentioned that the constant term or terms which depend on r and thus vanish as $r \to 0$, have been omitted from equations (3.9) and (3.10).
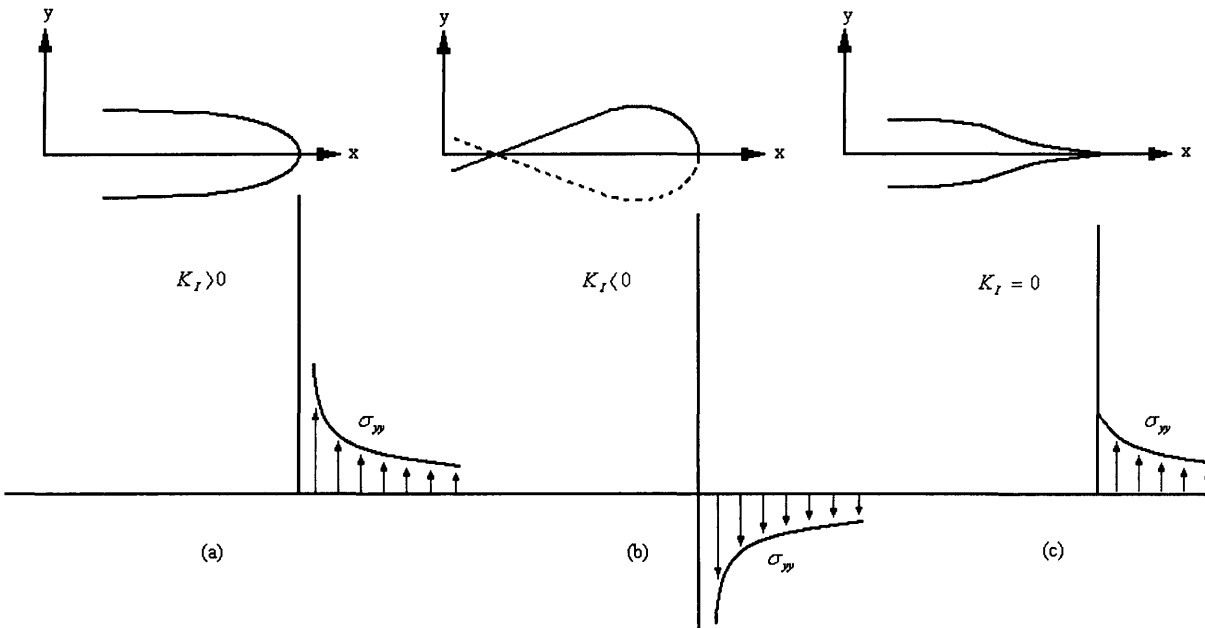
Figure 3.4 Shapes of traction-free crack tip zones and distribution of normal stress, σ_{yy} in front of the crack tip for $K_I > 0$, $K_I < 0$ and $K_I = 0$ (from Karihaloo, 1995).

According to the Irwin fracture criterion, a sharp crack in a brittle material will propagate when the stress intensity factor K_I reaches a critical value, denoted K_{Ic}. This critical value is a material constant and is called the fracture toughness of the

material. The distinction between K_{Ic} and K_I is important, and is similar to the distinction between strength and stress. In other words, K_{Ic} is related to the stress intensity factor K_I for opening mode crack in the same way that a material's tensile strength is related to the stress in a tensile specimen (Brown and Srawley, 1996). For the geometry and mode I loading of Figure 3.3, Irwin's criterion gives:

$$\sigma_c \sqrt{\pi a} = K_{Ic} \tag{3.12}$$

According to this relation, when the external stress reaches the value σ_c the crack will propagate. Comparing equation (3.12) with (3.7) indicates that the Irwin local stress criterion at the crack tip where the fracture process is taking place is exactly identical to the Griffith global energy criterion. The constant in the right hand side of equation (3.7) can be identified with K_{Ic}, i.e.

$$\sqrt{2E\gamma} = K_{Ic} \tag{3.13}$$

Or

$$K_{Ic}^2 = EG_c \tag{3.14}$$

where, G_c is the critical Griffith surface energy density or the critical energy release rate, with $G_c = 2\gamma$.

Today, Irwin's fracture theory is more widely used than Griffith's because it much easier to determine directly the fracture toughness K_{Ic} than it is to determine the surface energy density γ (Karihaloo, 1995).

The fracture toughness of material can be determined from a pre-cracked specimen. The most commonly used specimen shape for the determination of K_{Ic} is a notched beam loaded in three-point bending. The specimen is loaded gradually until the sharp notch begins to propagate. The corresponding maximum load is noted to calculate the

bending moment at mid-span (M_{max}). The critical stress intensity factor K_{Ic} is then calculated using the formula (Karihaloo, 1995).

$$K_{Ic} = \frac{6YM_{max}\sqrt{a}}{BW^2} \qquad (3.15)$$

where Y is a function of a/W (i.e. the ratio of the depth of notch to the height of the specimen), B and W are the width and the height of the beam, respectively.

3.2.2.1 Irwin Theory and Local Energy Considerations

Consider a crack of length 2a in an infinite body of unit thickness under mode I loading (Figure 3.3) and calculate the change in its potential energy when the crack grows by an infinitesimal amount Δa at each end. Using the superposition approach, we need only to eliminate the stress σ_{yy} due to the remote mode I loading at the location of the crack by applying equal stress of opposite sign and calculate the work done by this stress when the crack face open up. As mentioned earlier, this work done equals the change in the potential energy of the body, $\Delta \Pi$

$$\Delta \Pi = -2 \int_0^{\Delta a} \sigma_{yy} u_y \, dx \qquad (3.16)$$

The negative sign in front of the integral indicates that the displacement and corresponding stress have opposite signs, and the factor 2 allows for the symmetric growth of the two crack tips. The stress and displacement components (i.e. σ_{yy} and u_y) are chosen from equation (3.9) and (3.10), respectively for $\theta = 0$ (i.e. in the direction of crack advance). After integrating equation (3.16), we obtain

$$\Delta \Pi = -\frac{2K_I^2}{E} \Delta a \qquad (3.17)$$

36

On the other hand, the energy required to extend the crack by an amount Δa is $\Delta \Gamma = 4\gamma \Delta a$. Noting that $-\Delta \Pi = \Delta \Gamma$, the relation between γ and stress intensity factor in the loading mode I can be written as

$$\frac{2K_I^2}{E} = 4\gamma \qquad (3.18)$$

At the critical instant of crack propagation, this relation would take the form $K_{Ic}^2 = 2E\gamma = EG_c$, which is identical to equation (3.14). Therefore, the important relationship between Griffith and Irwin criteria of fracture from energy consideration alone is re-obtained.

Now, from equation (3.17) the rate of change in the potential energy for growing a crack tip in a brittle material under mode I loading can be derived as

$$-\frac{d\Pi}{da} \equiv G = \frac{K_I^2}{E} \qquad (3.19)$$

where G is the energy release rate.

3.2.3 Barenblatt's Cohesive Crack Model

The main features of LEFM described above are:

(i)   The description of brittle fracture involves only one additional material parameter, besides the usual two constants E and f_t. This parameter may be related to the energy of the body (material toughness) G_{Ic} or to the stress field near the crack tip present in the fracture toughness K_{Ic}.

(ii) The stresses and strains in the vicinity of a crack tip are very large (at the tip itself they tend to infinity).

(iii) During the fracture process the entire body remains elastic; the energy is only dissipated at the crack tip.

Griffith (1920) had observed the inconsistency between the linear elastic fracture model and the real physical situation prevailing at the crack tip. He therefore, proposed that the crack face should be allowed to close smoothly (Figure 3.4c) under the influence of large cohesive forces.
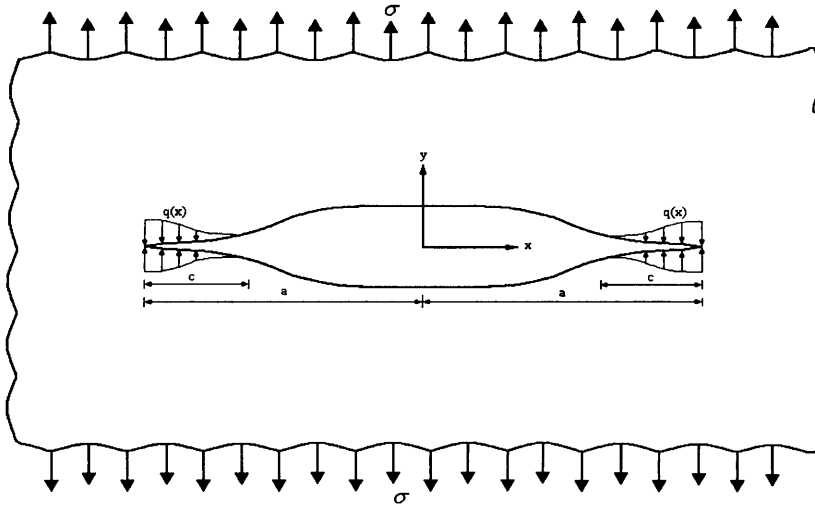
Figure 3.5 Barenblatt's cohesive crack model in mode I. Note $c \ll a$

Barenblatt (1959) gave the first fracture mechanics analysis based on the concept of a crack-tip cohesive zone in which he assumed that there were large cohesive forces $q(x)$ (see Figure 3.5) acting over a small zone of length c ($c \ll a$) near the crack tip and that the crack forces close smoothly. The distribution of cohesive forces is generally unknown and due to the presence of other defects it is difficult to ascertain.

Dugdale (1960) and Bilby et al. (1963) used a similar cohesive zone model to describe the behaviour of the elastic-plastic materials but they considered the cohesive stress to be constant and invariant with the crack opening. In fact, a plastic zone will form at each crack tip and extend as far as is necessary to satisfy the yield condition ($\sigma_{yy} \leq \sigma_y$). Therefore, the closing stress over the plastic zone will be constant and equal to the yield stress of the material (σ_y).

3.3 Is LEFM Applicable to Concrete?

Attempts were made to apply LEFM to concrete, which was thought to be a brittle material, but these proved unsuccessful. Intense research in this field revealed that all the cement-based materials that were traditionally regarded to be brittle exhibit in reality a different response. Figure 3.6a shows the load-deformation response of these materials in tension/flexure. It can be seen that a substantial non-linearity exists before the maximum stress is reached (AB) and there is a region of tension softening after the attainment of the maximum load (BC). These are primarily a result of randomly formed micro-cracks. The tail region of tension softening (CD) is caused by the aggregate interlock and other frictional effects.

The pre-peak non-linearity has only a minor influence on the fracture behaviour of concrete. The major influence in fact comes from the tension softening response because it reduces the flux of energy which can be released in to the crack tip and thus leads to an increase in the fracture surface area. Hence, the application of LEFM to concrete structures is limited, due to the existence of the tension softening response. In other words, the fracture behaviour of concrete is influenced by the formation of an extensive fracture process zone ahead of the pre-existing notch/crack, as illustrated in Figure 3.6b.
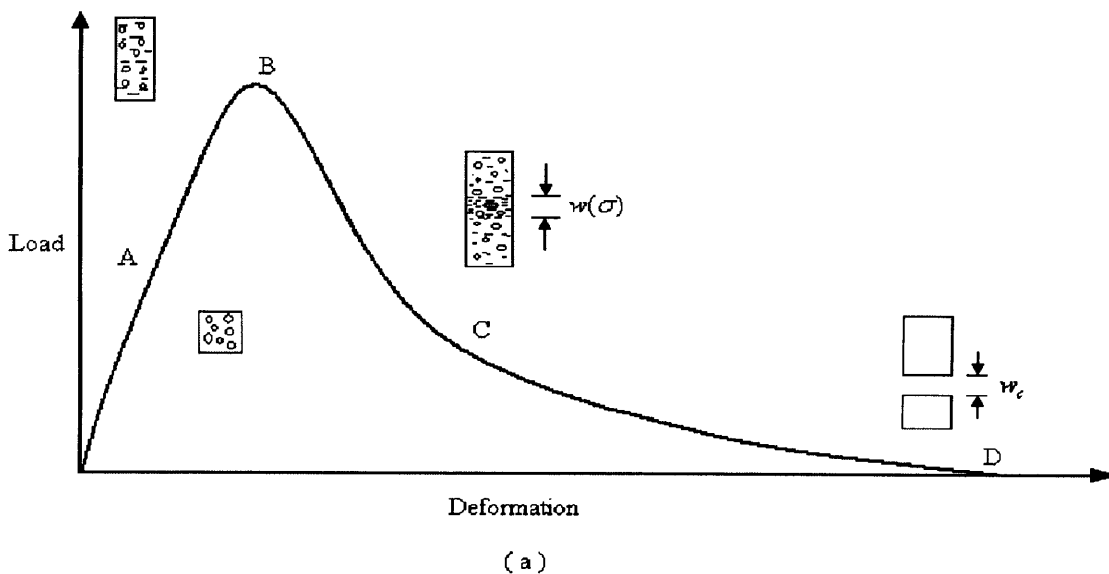
Figure 3.6a Typical load-deformation response of a quasi-brittle material in tension / flexure.

(b)
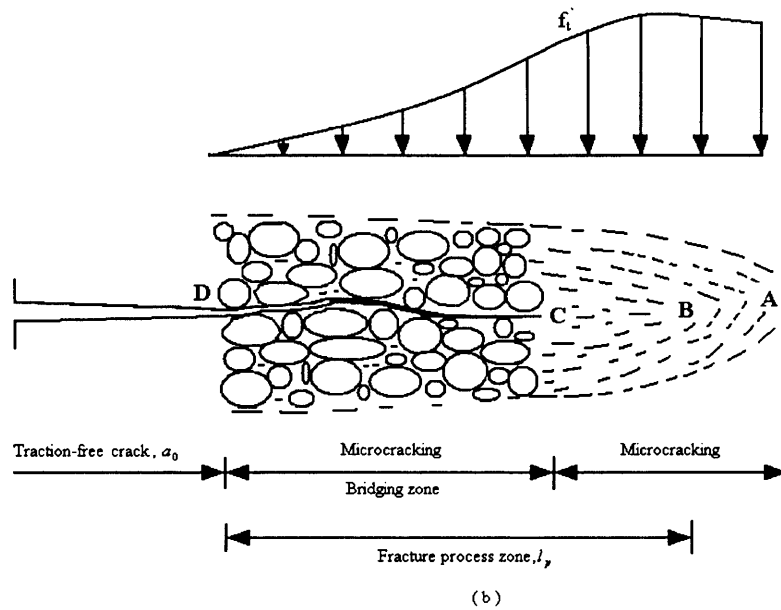
Figure 3.6b The fracture process zone ahead of the real traction-free (After Karihaloo, 1995)

3.4 Nonlinear Fracture Theory of Concrete (NLFM)

In the previous section it was argued that the LEFM is not applicable to concrete due to the existence of the inelastic toughening mechanisms (i.e. fracture process zone) that appear around a crack when it propagates. Therefore, a fracture theory capable to describe the material softening process that takes place in the fracture process zone must be a non-linear fracture theory.

3.4.1 Fictitious Crack Model (FCM)

The first non-linear theory of fracture mechanics for concrete was proposed by Hillerborg et al. (1976). It includes the tension softening fracture process zone through a fictitious crack ahead of the existing crack whose faces are acted upon by a certain closing stress (Figure 3.7). The model, which is known by the name of Fictitious Crack Model (FCM), is applicable to cracks whose faces close smoothly.

The FCM is similar in some points to the Barenblatt and Dugdale models, mentioned above. Like these models, the FCM assumes that the fracture process zone is of negligible thickness and the crack tip faces close smoothly ($K_I = 0$, see Figure 3.4c). However, the closing stresses in the FCM are not constant, as they are in the Dugdale model. They increase from zero at the tip of the pre-existing stress-free crack to the

40

tensile strength of the material, f_t, at the tip of the fictitious crack (Figure 3.7a). In fact, the distribution of the cohesive stresses $\sigma(w)$, along the fracture process zone depends on the opening of the fictitious crack faces, w. The size of the fracture process zone (l_p in Figure 3.7a) in the FCM may also be long compared with that of the pre-existing crack, so the FCM also differs from the Barenblatt model.

In contrast to LEFM which needs a single parameter to describe a brittle material (e.g. K_{Ic} in Irwin's theory), in the FCM it is necessary to have two material parameters.

- The shape of the stress-deformation relation $\sigma(w)$ in the softening zone.
- The area under the tension softening curve which is the specific fracture energy G_F (Figure 3.7c).

$$G_F = \int_0^{w_c} \sigma(w)\,dw \qquad (3.20)$$

where w_c is the critical crack opening at which the closing stress is equal to zero.

There is also another material parameter which can be obtained from the above information, namely the characteristic length of the material

$$l_{ch} = \frac{EG_F}{f_t^2} \qquad (3.21)$$

The characteristic length l_{ch}, is related to the heterogeneity in the material microstructure, giving an indication of its brittleness. It has a value proportional to the length of the fracture process zone. The bigger the characteristic length of the material is, the more ductile will be the material (i.e. less brittle). This is attributed to the fact that a bigger value of characteristic length is an indication of more inelastic toughening mechanisms getting involved around a crack when it propagates, resulting in increased energy absorption. The characteristic length has a value for mortar and concrete in the range of 100 to 200 mm and to 500 mm, respectively (Karihaloo, 1995).
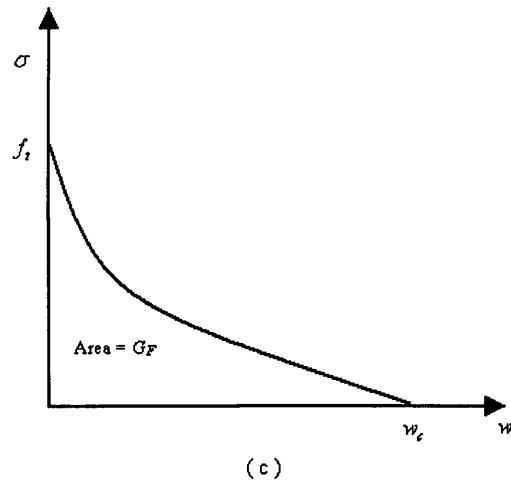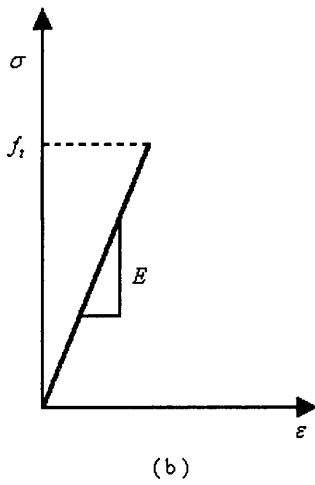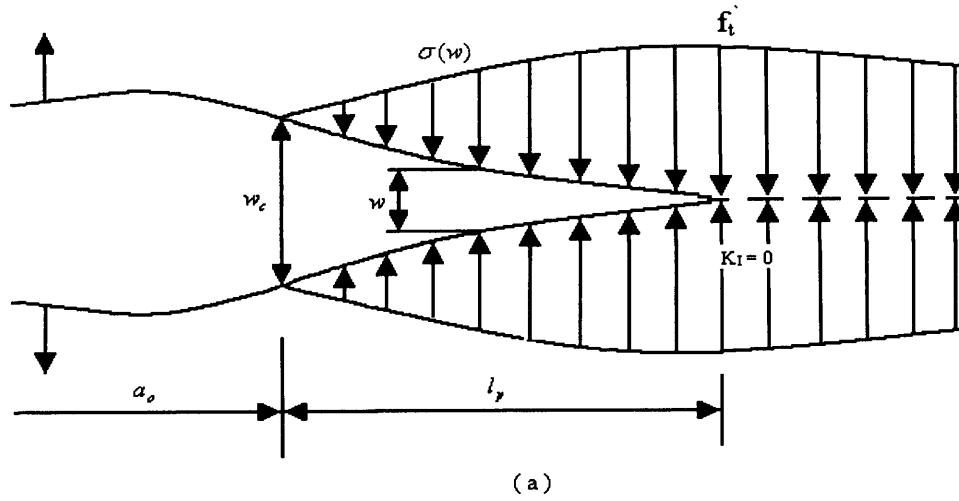
Figure 3.7 (a) A real traction-free crack of length a_0 terminating in a fictitious crack of length l_p whose faces close smoothly near its ($K_I = 0$). (b) The material ahead of the fictitious crack tip is assumed to be linear. (c) But the material within the fracture process zone is softening; the area under softening curve equals fracture energy G_F (after Karihaloo, 1995).

3.4.2 Crack Band Model (CBM)

According to the fictitious crack model, the fracture process zone (FPZ) is assumed to be a line crack with negligible width. Bažant and Oh (1983) developed a similar model called a crack band model (CBM), in which the fracture process zone was modelled by a band of uniformly and continuously distributed (smeared) micro-cracks of width h_b (Figure 3.8a). Stable crack propagation is assumed by progressive micro-cracking within this band, which is described by a stress-strain relationship (Figure 3.8b). The crack opening displacement w is equal to the product of the strain and the width of the crack band, h_b.

Based on the assumption that the energy produced by the applied load is completely balanced by the cohesive pressure $\sigma(w)$ in the fictitious crack approach, the energy consumed due to the crack growth per unit area of the crack band, G_F, is the product of the area under the stress- strain curve in Figure 3.8b, and the width of the crack band, h_b. This lead to

$$G_F = h_b \left[1 + \frac{E}{E_t} \right] \cdot \frac{f_t^2}{2E} \qquad (3.22)$$

where E is the modulus of elasticity, E_t is the strain- softening modulus, and f_t is the tensile strength of the material.

The values of E and E_t are defined as positive. It may be seen that in addition of E the crack band model requires two additional material parameters, namely h_b and E_t. An approximate function $h_b = n_a d_a$ has been proposed to calculate the h_b value, where d_a is the maximum aggregate size in concrete and n_a is a constant, which is equal to 3 for concrete. It should be noted that the main difference between the two mentioned non-linear models (FCM and CBM) is the thickness of the fracture process zone. As the band width h_b in the CBM tends to zero, the two models will merge.
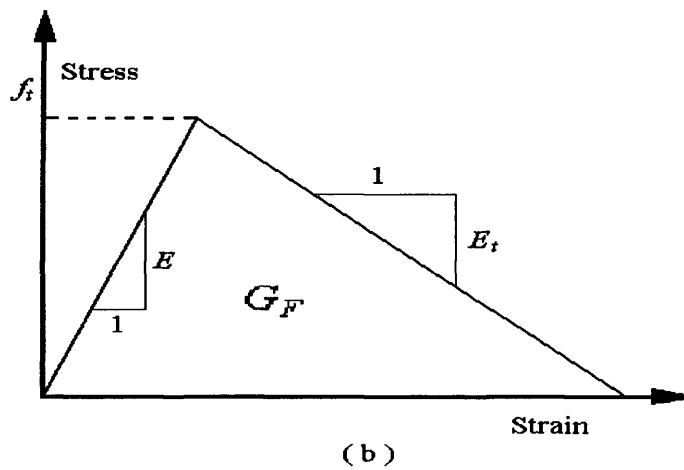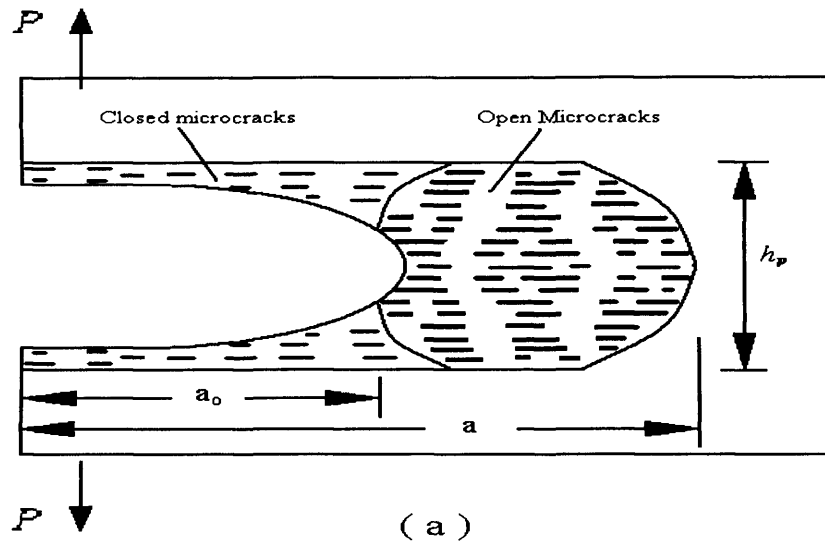
Figure 3.8 Crack band model for fracture of concrete. (a) a micro-crack band fracture and (b) stress strain curve for the micro-crack band (from Shah et al., 1995).

The CBM is generally used when the cracks are diffuse and numerous. That is why it is also called the smeared crack model. The FCM, on the other hand, is used when the cracks are few and isolated. That is why it is also called the discrete crack model.

44

3.5 Determination of Fracture Energy G_F

According to the RILEM recommendation (RILEM, 1985), the specific fracture energy (G_F) is the average energy given by dividing the total work of fracture with the projected fracture area. This parameter can be measured using a pre-cracked (notched) specimen. As for the determination of K_{Ic}, a commonly used specimen shape for the determination of G_F is a notched beam loaded in three-point bending (Figure 3.9). The specimen is loaded generally and the variation of the load (P) is plotted against the mid-span deflection. The specific fracture energy (G_F) is then calculated using the formula

$$G_F = \frac{1}{(W-a)B} \int P \, d\delta$$ (3.23)

where W, B and a are the specimen depth, width and the notch length, respectively. The weight of the specimen can be considered, if necessary (i.e. large specimen). However, most researchers have found that there exist size effects to a certain extent when TPB is used to determine the specific fracture energy of concrete. As a material parameter, fracture energy should be a constant and independent of specimen size. Therefore, some researchers have doubted the validity of G_F obtained using TPB.
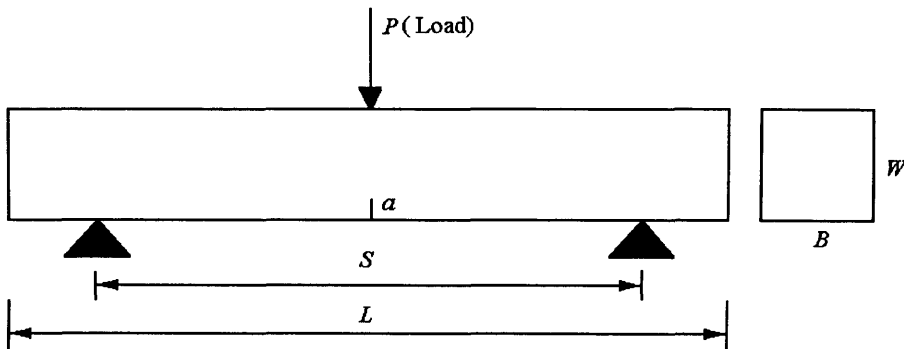
Figure 3.9 Testing configuration and geometry of specimen. P = load, L = specimen length, S = specimen load span, W = beam depth, B = beam thickness and a = initial notched depth.

Because of the testing simplicity, TPB recommended by RILEM Committee FMC-50 is widely used for the determination of fracture energy. However, most experiments are performed on relatively small beams, and therefore the self-weight is large. Hence, the effect of self-weight on fracture properties must be carefully considered in TPB. To overcome this situation, RILEM set up a committee (Rossi et al., 1991) charged with the task of proposing a test method based on compact specimens. The specimen is provided with a groove and starter notch. The fracture parameters are determined by wedging open the starter notch; hence it is called the wedge splitting test (WST). The principle of the WST (Bruhwiler and Wittmann, 1990) is schematically presented in Figure 3.10.

A cubic specimen with an initial rectangular groove carries two-load transmission pieces (Figure 3.10). The loading of the wedge implies a defined horizontal-force F_H application to the specimen, which causes crack propagation. The load is applied gradually and the crack mouth opening displacement (CMOD) is monitored with a clip gauge and used as a feed back signal. The splitting force F_H is calculated from the vertical force F_M on the bearing and wedge angle, taking into account frictional effects.

$$F_H = \frac{F_M \left(1 - \mu \tan \alpha\right)}{2 \tan \alpha \left(1 + \mu \cot \alpha\right)} \approx \frac{F_M}{\left(1 + \mu \cot \alpha\right)\left(2 \tan \alpha\right)} \tag{3.24}$$

where μ is the coefficient of friction. The roller manufacturers quote μ between 0.1 and 0.5 %. For $\alpha = 15°$, the contribution of $\mu \cot \alpha$ in the previous expression is therefore between 0.40 and 1.9 %. Therefore, in the WST, F_H may be expressed by

$$F_H = \frac{F_M}{2 \tan \alpha} \tag{3.25}$$

The area under load-CMOD curve corresponds to the work done to separate the specimens. Dividing this work by the fracture area or ligament area that was intact before the test began yields the measured specific energy G_f. This value characterises

the crack propagation resistance of the test material and can be simply calculated as follows:

$$G_f = \frac{1}{A_{lig}} \int_0^{CMOD_{max}} F_H \, d(CMOD) \qquad (3.26)$$
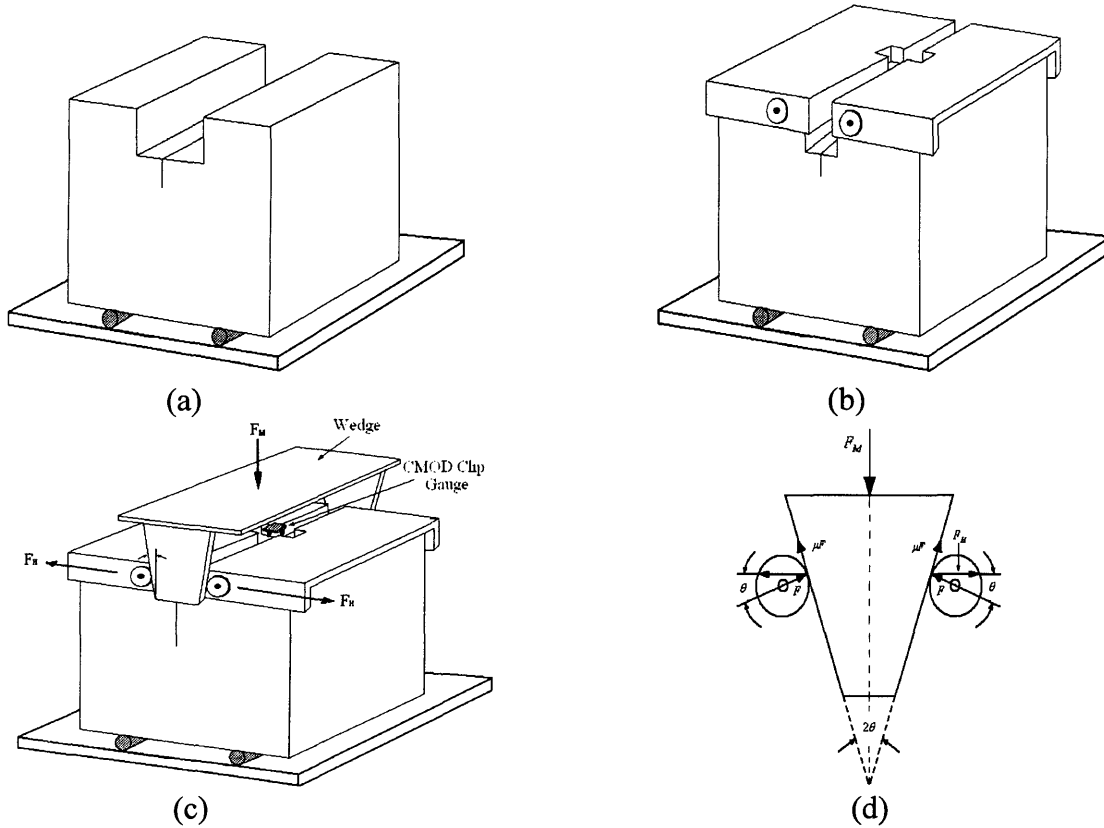
Figure 3.10 Principle of wedge splitting test: (a) a test specimen on a linear support, (b) placing of two load devices with roller bearing, (c) pressing a wedge between bearings, and (d) forces acting on the wedge. (After Rossi et al., 1991)

3.6 Size-Independent Specific Fracture Energy G_F

The specific fracture energy G_F is the most useful material parameter in the fracture analysis of concrete structures (Karihaloo, 1995). The method of experimental determination of the fracture energy, G_F, and even its definition has been a subject of debate among researchers because of its variability with the size and shape of the test specimen (Abdalla and Karihaloo, 2003). Hu and Wittmann (1992) have shown that the specific fracture energy may not be constant along the crack path in a test specimen. Duan et al. (2001) proposed a boundary effect model that assumes that the

fracture energy required for creating a unit crack along the crack path is influenced by the size of the fracture process zone (FPZ) which in turn is influenced by the free boundary of the test specimen. To consider the boundary effect on the propagation of FPZ, they used a bi-linear fracture energy distribution to explain the ligament effect on the fracture energy of concrete. This is needed for an accurate estimate of the load bearing capacity of cracked concrete structures (Abdalla and Karihaloo, 2003).

The fracture process zone (FPZ) around the propagating crack can be considered as consisting of two regions, an inner softening zone (w_{sf}) and an outer micro-fracture zone (w_f) (Karihaloo, 1995; Hu, 1990; Hu and Wittmann, 1992; Duan et al., 2001) (Figure 3.11).
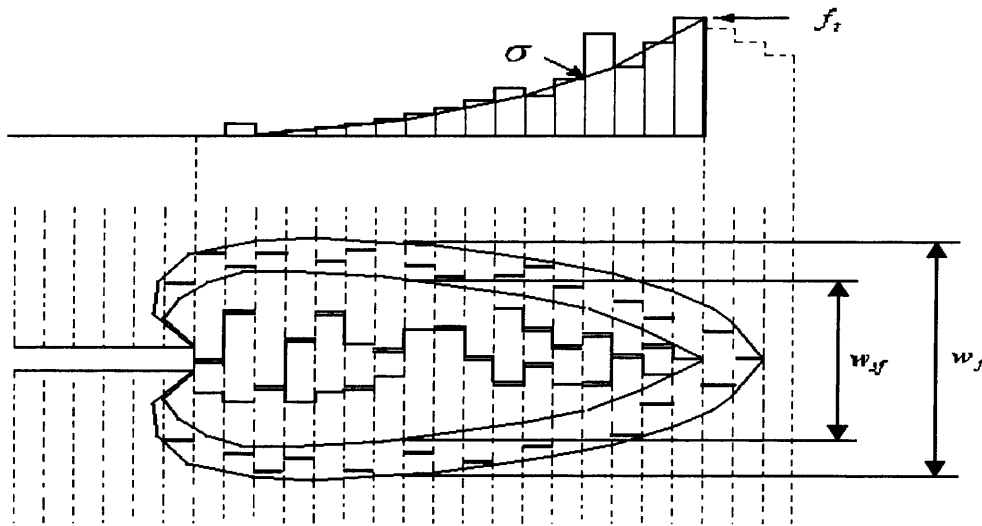
Figure 3.11 The FPZ and discrete bridging stresses. The FPZ is divided into inner softening zone and the outer micro-fracture zone. w_c is related to the width of the inner softening zone w_{sf} (Hu and Wittmann, 1992).

The inner softening zone w_{sf} contains interconnected cracks along the aggregate and mortar interfaces. The main open crack plus a few large crack branches along the interfaces can be formed within the softening zone. The formation and complete separation of the softening zone controls the $\sigma(w)$ relationship. The outer micro-fracture zone contains isolated micro-cracks that are not interconnected. These do not contribute to the concrete softening. The fracture energy consumed in the outer micro-

fracture zone is small, and equations (3.20) and (3.23) should in principle determine the same specific fracture energy (Duan et al., 2001).

However, during crack propagation the inner and outer zone width w_{sf} and w_f may vary according to the crack tip stress field. Obviously the critical crack opening w_c is limited by the inner and the outer zone width. This limit becomes more obvious when a FPZ approaches the free boundary of a specimen. Therefore, a smaller w_c and a smaller fracture energy is found if equation (3.20) is used. These variations in w_{sf}, w_f and w_c lead to the conclusion that the fracture energy G_F defined by equation (3.23) can be dependent on the location of FPZ in relation to the free boundary of the specimen.

To distinguish the fracture energy G_F defined by equation (3.23) from that defined by equation (3.20), Duan et al., (2001) use the symbol g_f for the local fracture energy defined by equation (3.20) (Abdalla and Karihaloo, 2003). Hu (1990) and Hu and Wittmann (1992) have made the following assumption

$$w_{sf}(x) \propto w_f(x)$$

$$w_c(x) \propto w_{sf}(x) \tag{3.27}$$

$$g_f(x) \propto w_c(x)$$

where x denotes a position along a fracture ligament in the FPZ and $g_f(x)$ represents the local fracture energy. The fracture energy defined by equation (3.23) which may be size or ligament dependent is denoted through $G_f(a)$, to differentiate it from the size-independent G_F (Duan et al., 2001).

According to the energy conservation principle, the specific fracture energy $G_f(a)$ defined by equation (3.23) can be determined as follows:

$$G_f = \frac{1}{(W-a)} \int_0^{W-a} g_f(x) dx \tag{3.28}$$

Differentiating equation (3.28) with respect to the crack length gives the local fracture energy $g_f(x)$ at the crack tip.

$$g_f(x) = G_f(a) - (W-a)\frac{dG_f(a)}{da}$$

(3.29)

Equations (3.28) and (3.29) above imply that $G_f(a)$ = constant = G_F, if $g_f(x)$ = constant. If $g_f(x) \neq$ constant, $G_f(a) \neq$ constant, i.e. size or ligament effects are observed. Figure 3.12 shows schematically that if $g_f(x)$ decreases when approaching the boundary of the specimen at later stages of fracture, $G_f(x)$ is indeed dependent on the ligament or initial crack length (Duan et al., 2001).
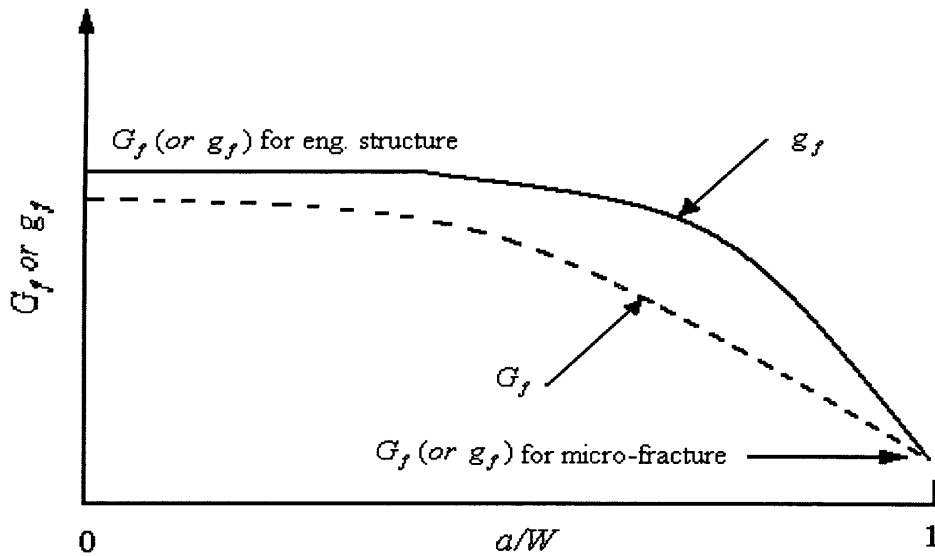
Figure 3.12 g_f decreases monotonically along the ligament, so that G_f has to be dependent on the a/W ratio, as observed in many experiments (Hu and Wittmann (1992).

To simplify the previous local fracture energy analysis Hu (1990) and Hu and Wittmann (1992), $g_f(x)$ is assumed to vary in a bi-linear manner, as shown in Figure 3.13. Figure 3.13a displays a specimen of depth W and an initial crack of size a.

The bi-linear function consists of a horizontal line with the value of G_F and a descending branch that reduces to zero at the back surface of the specimen. The intersection of these two straight lines is defined as the transition ligament size a_l or the crack reference length (Hu and Wittmann, 2000). The transition ligament size a_l is a parameter depending on both the material properties and specimen geometry.
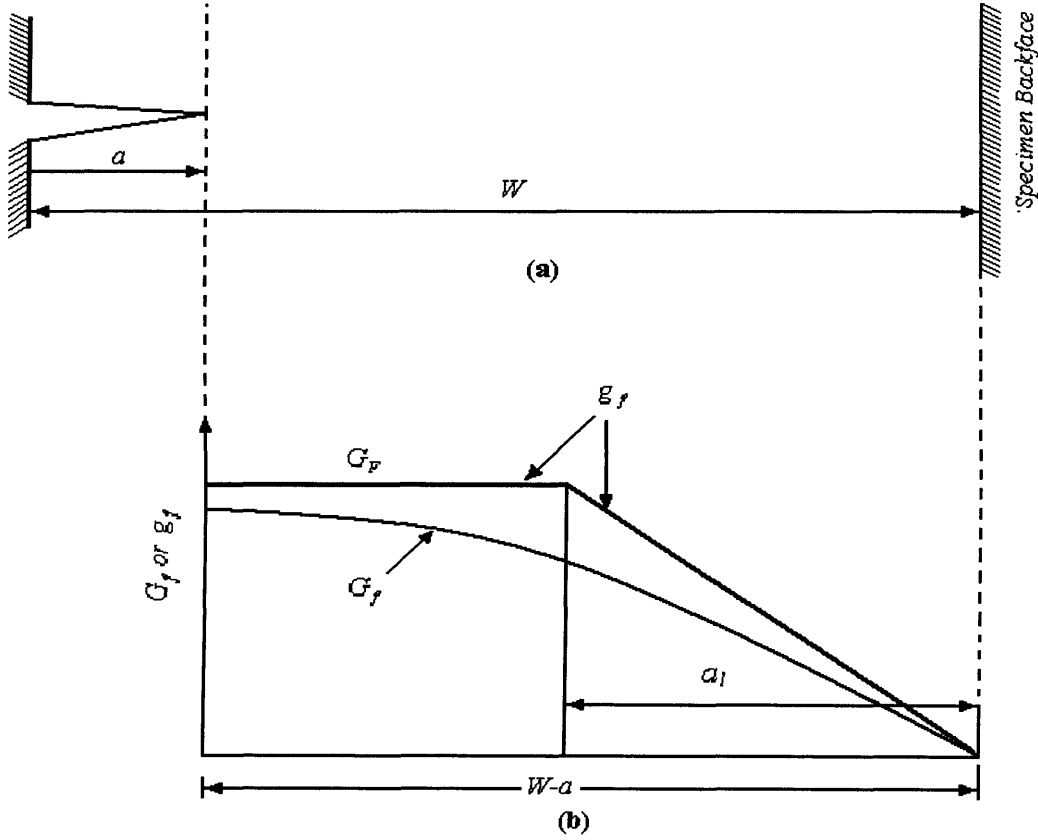
Figure 3.13 (a) A notched test specimen of depth W and notch depth a. (b) showing the distribution of fracture energy (G_f and g_f) along the un-notched ligament, W-a

For specimen with a ligament size (W-a) larger than the transition ligament size a_l, $g_f(x)$ is given by (Hu and Wittmann 2000).

$$g_f(x) = \begin{cases} G_F & x < W - a - a_l \\ G_F \left[1 - \dfrac{x - (W - a - a_l)}{a_l} \right] & x \geq W - a - a_l \end{cases} \qquad (3.30)$$

If (*W-a*) is smaller than the ligament transition length a_l, first function in equation (3.26) disappears. Substituting equation (3.30) into (3.28) and introducing the *a/W* ratio, the size dependent fracture energy G_F is obtained (Duan et al., 2001).

$$G_f\left(a/W,W\right)=\begin{cases} G_F\left[1-\dfrac{a_l/W}{2(1-a/W)}\right] & ; \quad 1-a/W>a_l/W \\[4mm] G_F\cdot 1-\dfrac{(1-a/W)}{2(a_l/W)} & ; \quad 1-a/W\le a_l/W \end{cases} \qquad (3.31)$$

As shown in Figure 3.13, when the initial crack length grows from *a* to *W*, the $G_f\left(\alpha,W\right)$ or $G_f\left(a/W,W\right)$ curve is obtained, showing the ligament effect on the fracture energy. The upper limit of $G_f\left(a/W,W\right)$ is the size-independent fracture energy G_F. It can also be seen from Figure 3.13 that it is not necessary to test a very large concrete specimen, because G_F can be back calculated from the size-independent fracture energy $G_f\left(a/W,W\right)$, as long as (*W-a*) > a_l (Duan et al., 2001).

Abdalla and Karihaloo (2003) further verified the work of Duan et al., (2001) using TPB and wedge splitting (WS) test on normal (NSC) and high strength (HSC) concretes. For the WS test, they tested specimens of different notch to depth ratios 0.2, 0.3, 0.4 and 0.5. From the load-CMOD diagrams the fracture energy $G_f\left(\alpha\right)$ was calculated. These test results were substituted into equation (3.31) in order to determine the size independent specific fracture energy G_F. This experimental work provided further verification of the assumption that $G_f\left(\alpha\right)$ is dependent on both the *a/W* ratio and the specimen size. Furthermore, Karihaloo et al. (2003) simplified the determination of size independent specific fracture energy, G_F by testing a single size specimen with only two notch to depth ratios, provided they are well separated (*a/W* = 0.2 and 0.5 in WS). The selection of the specimen dimensions is dependent on the maximum size of aggregate used in the mix.

3.7 Fracture behaviour of bi-material systems

A bi-material is by definition two materials which are perfectly bonded. For example, a substrate/repair system can be considered a bi-material. Application of any repair

material results in bi-material interface between the repair material and the existing material of the repaired structure. The bonding at the interface is important for safety and durability. Failure of repaired system relates to cracking along the interface or kinking out of the interface. In the interface cracking case, the interface is relatively weaker than the bordering materials, meaning that the interface crack will propagate exclusively along the least resistance path, i.e. the interface. In the crack kinking case, the interface is relatively stronger than at least one of two adjoining materials. Quantitative evaluation of whether an interface crack will advance straight ahead or kink-out of the interface requires the knowledge of interfacial fracture toughness (Li et al., 1995).

3.7.1 Experimental Evaluation

To assess the performance of interfaces, several standardized bond strength tests are currently used. Tensile or shear bond strength is usually accepted as an interface property in practice determined by a variety of test techniques (Emmons 1994). However, tensile or shear bond strength give essentially only a maximum value of the stress. It is very difficult to tell from such technique if de-cohesion or separation is obtained in a brittle or ductile manner. Moreover, there is no information about the amount of energy (fracture energy) needed for the separation of the materials, therefore, the bond strength as such may be useful for ranking of repair materials, but is not expected to have field performance predictive capability due to size and geometric effects. It is important to evaluate the bond properties after the maximum load in order to understand the failure process.

In fracture mechanics, the load-deformation curve contains all information that characterises fracturing of concrete. It is one of the fracture mechanics parameters and is suitable to evaluate the bond failure after the maximum load (Kunieda et al., 2000). To obtain the load deformation curve for a repaired structure, three-point bending and wedge splitting test can be used (Figure 3.14). To date, there are only a few researchers who have used the WS test for evaluating the performance of repaired system, such as Tschegg and Stanzel (1991) (old concrete-new concrete), Tschegg et al., (1995) (Aggregate-cement matrix), (Tschegg (1997) (Bituminous and layer bonds), Irhouma et al., (1998) (Concrete-concrete) and Harmuth (1995) (Concrete-polymer modified cement).

(a)   (b)
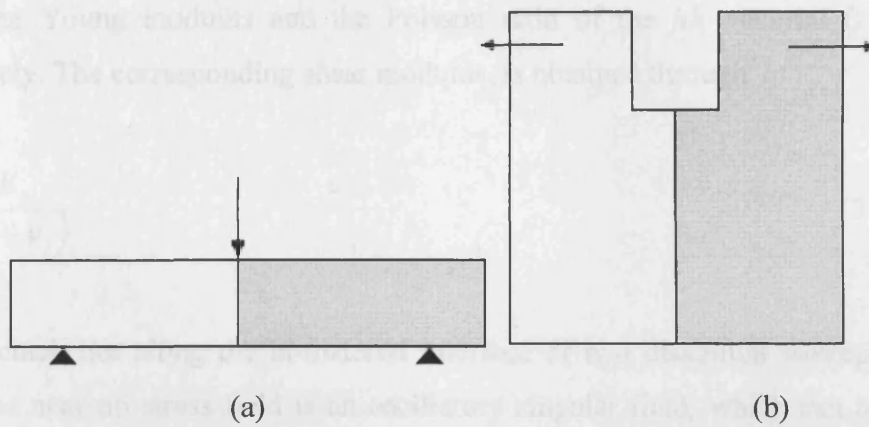
Figure 3.14 Different composite geometry to determine the load-deformation curve for bi-material

3.7.2 Characterisation of Cracks at Bi-material Interfaces

The characterisation of cracks at bi-material interfaces substantially differs from that of homogeneous materials. Unlike homogeneous materials, bi-materials exhibits a coupling of tensile and shear effects. In addition the singular stresses are oscillatory in the vicinity of the interface crack tip. The stress field is characterized by a complex stress intensity factor, K, together with the bi-material constant ε relating to the elastic properties of two materials. An alternative characterization of the near tip stress field involves the energy release rate G, together with the mode mixity χ. The mode mixity is a quantity measuring the ratio between the shear and the normal stresses at the interface in front of the crack tip.
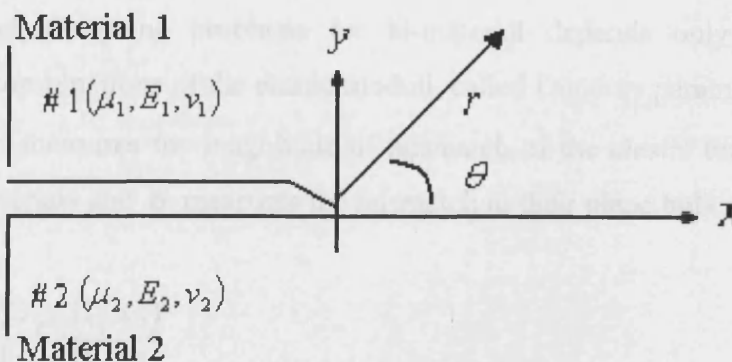
Figure 3.15 Geometry of a bi-material system with an interface crack

54

Assume two isotropic elastic solids joined along the x-axis (Figure 3.15). Let E_j, v_j denote the Young modulus and the Poisson ratio of the *jth* material (j = 1, 2), respectively. The corresponding shear modulus, is obtained through

$$\mu_j = \frac{E_j}{2(1+v_j)} \qquad (3.32)$$

When a crack lies along the bi-material interface of two dissimilar isotropic elastic media, the near-tip stress field is an oscillatory singular field, which can be written (Williams 1959; Rice and Shih, 1965; England, 1965; Shih and Asaro, 1988) as

$$\sigma_{ij} = \text{Re}\left\{\frac{Kr^{i\varepsilon}}{\sqrt{2\pi r}}\right\}\sigma_{ij}^{\approx I}(\theta,\varepsilon) + \text{Im}\left\{\frac{Kr^{i\varepsilon}}{\sqrt{2\pi r}}\right\}\sigma_{ij}^{\approx II}(\theta,\varepsilon) \qquad (3.33)$$

Here r and θ are the polar coordinates; Re and Im denote real and imaginary parts; K is the stress intensity factor; $\sigma ij^{\approx I}$ and $\sigma ij^{\approx II}$ are the dimensionless angular functions of θ and ε (Shih and Asaro, 1988), and the bi-material constant ε is defined by

$$\varepsilon = \frac{1}{2\pi}\ln\left(\frac{k_1/\mu_1 + 1/\mu_2}{k_2/\mu_2 + 1/\mu_1}\right) \qquad (3.34)$$

where k and μ are Lame constants and subscripts 1 and 2 refer to the materials 1 and 2, respectively. The quantity ε vanishes when the two materials are identical. The solution of elastic plane problems for bi-material depends only on two non-dimensional combinations of the elastic moduli, called Dundurs parameters α and β. Physically, α measures the magnitude of mismatch of the elastic tensile moduli of the two bi-materials and β measures the mismatch in their plane bulk moduli

$$\alpha = \frac{\mu_1(k_2+1) - \mu_2(k_1+1)}{\mu_1(k_2+1) + \mu_2(k_1+1)} \qquad (3.35)$$

$$\beta = \frac{\mu_1(k_2 - 1) - \mu_2(k_1 - 1)}{\mu_1(k_2 + 1) + \mu_2(k_1 + 1)}$$ (3.36)

Therefore, the parameter ε can be rewritten as

$$\varepsilon = \frac{1}{2\pi} \ln\left(\frac{1 - \beta}{1 + \beta}\right)$$ (3.37)

The energy release rate G is related to K by

$$G = \frac{(1 - \beta^2)}{E^*}(K_1^2 + K_2^2) = \frac{(1 - \beta^2)}{E^*}|K|^2$$ (3.38)

where $|K|$ is the modulus of K and the effective $E^* = 2E_1' E_2' / (E_1' + E_2')$, in which $E' = E/(1 - v^2)$ for plane strain problems and $E' = E$ for plain stress problems and v is the Poisson ratio. Using the asymptotic field equation (3.33), the tractions at a distance r ahead of the crack-tip along the interface ($\theta = 0$) can expressed according to Hutchinson et al. (1987) as

$$(\sigma_{22} + \sigma_{12})_{\theta=0} = \frac{K r^{i\varepsilon}}{(2\pi)^{1/2}}$$ (3.39)

According to dimensional analysis (Rice, 1998), the modulus of K has the dimension

$$|K| = [stress][length]^{(1/2) - i\varepsilon}$$ (3.40)

Obviously, the dimension of the modulus K is quite different from that of homogeneous materials.

The equations of the above paragraph will be used in Chapter 5.

3.8 Application of Fracture Mechanics to Reinforced Concrete

The application of the theory of fracture mechanics to reinforced concrete elements is relatively new. Nevertheless, the importance of the results obtained is increasingly recognised since this approach has provided new ways of understanding, and often the only possibility of interpreting, the real structural behaviour which shows failure modes depending upon the size of the structure and the amount of reinforcement. Recently, it has been proved experimentally that even the minimum percentage of reinforcement that enables the element to prevent brittle failure, depends on size of the element (Bosco et al., 1990a, b and Bosco and Carpinteri, 1992). This approach was used by Alaee and Karihaloo (2003b) to predict the moment resistance of pre-cracked reinforced concrete beams retrofitted with CARDIFRC$^®$ and the results found to be in agreement with the test results. The calculation of the plastic moment of a cracked beam element will be briefly explained in the next section.

3.8.1 Calculation of the Plastic Moment of a Cracked Beam Element

A cracked section of reinforced concrete beam is shown in Figure 3.16. The section is subjected to a bending moment M and the closing force P applied on the crack surfaces by reinforcement. We can evaluate the angular deformation $\Delta\varphi_{MP}$ produced by the force P, together with the crack opening displacement $\Delta\delta_{PP}$, at the point where the forces P are applied, and, at the same time, the crack opening displacement $\Delta\delta_{PM}$ caused by the bending moment M, together with the angular deformation $\Delta\varphi_{MM}$. By linear superposition, the total crack opening $\Delta\delta$ and the total relative rotation of the crack face $\Delta\varphi$ can be written as

$$\Delta\delta = \Delta\delta_{PM} + \Delta\delta_{PP} = \lambda_{PM}\,M - \lambda_{PP}\,P \qquad (3.41)$$

$$\Delta\varphi = \Delta\varphi_{MM} + \Delta\varphi_{MP} = \lambda_{MM}\,M - \lambda_{MP}\,P \qquad (3.42)$$

where λ_{MM}, λ_{PM}, λ_{MP}, λ_{PP} are the compliances of the member due to the existence of the crack. There factors can be derived from energy principles considering the moment M acting simultaneously with the force P. Denoting by K_{IM} and K_{IP} the stress intensity factors due M and P, respectively, the change in the potential energy,

when the crack is gradually introduced, can be calculated from the integration of (3.19).
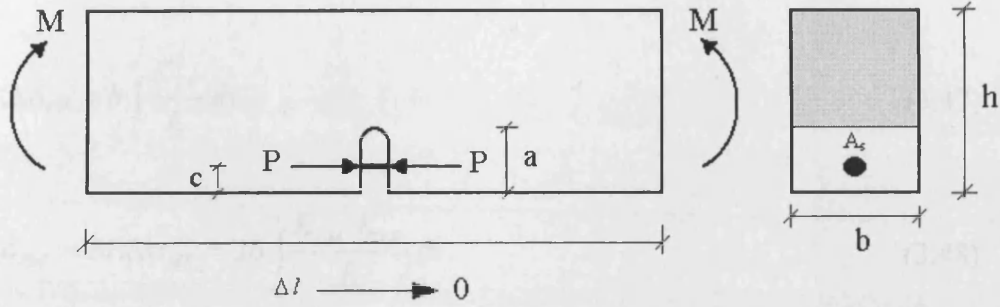
3.16 A small beam segment with a crack showing the bending moment M and steel force P (After Bosco and Carpinteri, 1992)

It should be noted that P does not influence the crack until it has crossed the reinforcing bar

$$\Delta W = \int_0^c \frac{K_{IM}^2}{E} b dx + \int_c^a \frac{\left(K_{IM} + K_{IP}\right)^2}{E} b dx \qquad (3.43)$$

$$\Delta W = b \int_0^a \frac{K_{IM}^2}{E} dx + b \int_c^a \frac{K_{IP}^2}{E} dx + 2b \int_c^a \frac{K_{IM} K_{IP}}{E} dx \qquad (3.44)$$

Note that the first term from the second integral has been combined with the first integral with an appropriate change in limits of integration. Using Clapeyron's Theorem, we also have

$$\Delta W = \frac{1}{2} M.\Delta \varphi_{MM} + \frac{1}{2} P.\Delta \delta_{PP} + \frac{1}{2} \left(P.\Delta \delta_{PM} + M.\Delta \varphi_{MP} \right) \qquad (3.45)$$

Comparing equation (3.45) and (3.44) and recalling Betti's reciprocal theorem $\left(P.\Delta\delta_{PM} = M.\Delta\varphi_{MP}\right)$, we obtain

$$\frac{1}{2}M.\Delta\varphi_{MM} = b\int_0^a \frac{K_{IM}^2}{E}\,dx \qquad (3.46)$$

$$\frac{1}{2}P.\Delta\delta_{PP} = b\int_0^a \frac{K_{IP}^2}{E}\,dx \qquad (3.47)$$

$$P.\Delta\delta_{PM} = M.\Delta\varphi_{MP} = 2b\int_c^a \frac{K_{IM}\,K_{IP}}{E}\,dx \qquad (3.48)$$

The stress intensity factor produced at the crack tip due to moment M can be expressed as (Okamura et al., 1973 and 1975)

$$K_{IM} = \frac{M}{h^{2/3}b}Y_M\left(\xi\right) \qquad (3.49)$$

where ξ is the ratio of the depth of crack to the height of the beam $(a\,/\,h)$. Similarly, the stress intensity factor produced by forces P acting at the level of reinforcement is (Tada et al., 1985)

$$K_{IP} = \frac{P}{h^{1/2}b}Y_P\left(\beta,\xi\right) \qquad (3.50)$$

where $\beta = c\,/\,h$. Substitution of (3.49) and (3.50) into (3.46)-(3.48) gives the compliance coefficients

$$\lambda_{MM} = \frac{2}{h^2 bE}\int_0^\xi Y_M^2\left(x\right)dx \qquad (3.51)$$

$$\lambda_{PP} = \frac{2}{bE}\int_{c/h}^\xi Y_P^2\left(\beta,x\right)dx \qquad (3.52)$$
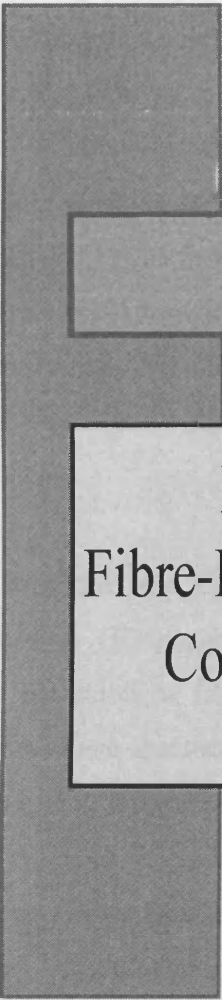
$$\lambda_{PM} = \lambda_{MP} = \frac{2}{hbE} \int_{c/h}^{\xi} Y_M(x).Y_P(\beta,x)dx \qquad (3.53)$$

The compliance functions $Y_M(x)$ and $Y_p(\beta,x)$ will be given in Chapter 8.

Next, if it is assumed that the crack forces do not open (i.e. the net relative displacement $\Delta\delta$ is zero in (3.41)) up to the moment of yielding or slippage of the reinforcement, then the moment at plastic flow or slippage of steel can be computed from (3.41) as

$$M_P = P_P h \frac{\int_{c/h}^{\xi} Y_P^2(\beta,x)dx}{\int_{c/h}^{\xi} Y_M(x).Y_P(\beta,x)dx} \qquad (3.54)$$

where $P_P = A_S f_y$ indicates the yielding force in the reinforcement. As mentioned before, this application will be further discussed and expanded later on in Chapter 8 and the consequences of the assumption that $\Delta\delta = 0$ when P reaches P_p are examined.

Chapter 4

High Performance Fibre-Reinforced Cementitious Composites. HPFRCCs

4.1 Introduction

Concrete has been the most widely used material in the building construction, owing to its versatility and strength. The development of concrete as a structural material has gone through several notable phases. In the early 1940s and around the 1970s concrete reinforcing and prestressing steel was a more cost-effective to steel as reinforcing material. Around 1980s, with the arrival of silica fume and superplasticizers, concrete with compressive strengths of 100 or more were possible, which was the beginning of the high-performance strength concrete. Because of gradual advances, the use of high performance and fibre reinforced concrete (FRC) ... to ... material could be developed, and, in particular, the ultra high performance concrete (UHPC) with ... Strength ... were developed ... ... for civil purposes, ...

Cement matrix ... ... fibres ... and tensile Capacity. In ... ... responses ... properties ... HPFRCC ...

Under the ... ... High Performance Fibre-Reinforced Cementitious Composites (HPFRCC) can be classified into different classes of behaviour ... up to the ... in response to tensile loading, leading to a high failure Strain. Strain-Hardening Cementitious (HPFRCC) are able to ... undergoing a large extension ... to the concrete level ... ... subjected to tensile loading. This has been achieved mostly by some ... ... which include the ... ... the fibres reinforcement ... ... leads to ... ... both ... strength and fracture toughness ...

At the University of Michigan, ... design of ... ... HPFRCC ... moderate fibre high tensile ductility at micro and high energy absorption (Kanda et al ...) ...

4.1 Introduction

Concrete has been the most common material used in the building construction, owing to its reliability and stability. The development of concrete as a structural material has undergone several important phases. In the early 1900s and around 1940s, steel reinforced concrete and pre-stressed concrete took place as alternative to steel as major construction material. Around 1970s, with the arrival of silica fume and superplasticizer as chemical additives and the increase of civil engineering demands, such as long-span bridges and high-rise buildings, high strength concrete became commercialised. In 1980s high performance concrete (HPC) and fibre reinforced concrete (FRC) were proposed and widely studied and began acceptance by the practising community. Nowadays, the ultra high strength concrete (UHSC) with compressive strength more than 140 MPa has successfully been developed in some research institutes.

Cementitious materials are known to be quasi-brittle with low strength and strain capacity in tension (Kaufmann and Hesselbarth, 2007). Therefore, due to these properties, the inclusion of fibres in such materials enhance many of the structural properties, for instance fracture toughness, flexural strength, tensile strength, impact strength, resistance to fatigue and thermal shock (Mansur, et al., 1997).

High Performance Fibre Reinforced Cement Composites (HPRCCs) represent a class of cement composites whose stress-strain response in tension undergoes strain hardening behaviour accompanied by multiple cracking, leading to a high failure strain capacity (Farhat, 2004). Generally, HPRCCs are made by adding a large amount of fibre to the cement based matrix with no effect on the mix workability. This has been made possible by the use of the silica fume and surfactants which reduce the needed water and increase the matrix density. Fibres resist the nucleation of cracks by acting as stress-transfer bridges, and once cracks nucleate, fibres abate their propagation by providing crack tip plasticity and increased fracture toughness (Banthia and Nandakumar, 2000).

A new class of the HPRCCs materials has been recently developed at Cardiff University as a retrofitting material designated CARDIFRC®. It is characterised by high tensile/flexural strength and high energy absorption (Karihaloo et al., 2001). In

this Chapter, the behaviour of CARDIFRC® as a retrofitting material and the other HPFRCCs that have been introduced to the engineering industry so far will be discussed.

4.2 Normal strength concrete (NSC)

Normal strength concrete (NSC) or a plain concrete where the concrete mix consists of four kinds of ingredients, which are cement, water and fine and coarse aggregates has a compressive strength of about 40 MPa. It is usually characterised by low tensile strength and low strain at fracture. Therefore, due to the mentioned characteristics, it is difficult to obtain good mechanical properties unless chemical admixtures are added to the concrete mix.

Several studies have been carried out on the main deficiencies of the NSC (low tensile strength and low strain at fracture) and on the behaviour of concrete materials under loading and also on the mechanisms of microcracking and the new microcrack propagation at the loading stage (Ramakrishnan, 1995; Neville, 1995; Bentur and Mindess, 1986).

Microcracks exist at cement paste–aggregate interfaces within concrete even prior to any load and environmental action. Such microcracks are formed due to drying and thermal shrinkage mismatch of aggregate particles and cement-based matrix which control the strength development. Under externally imposed structural loads and environmental effects, concentration of tensile stresses occurs at the interfaces between aggregates and matrix, causing the growth of microcracks in size and number; propagation of interface microcracks into matrix and eventual joining of microcracks yield large cracks and lead to failure of concrete. The growth of concrete microcracks under damaging load and environmental effects causes deterioration of concrete properties (Soroushian and Elzafraney, 2004).

4.3 High strength concrete

To meet special engineering needs and requirements, concrete properties have been improved. The satisfactory performance of structures in the long term has become essential to the economy. Therefore, these reasons lead to an acceleration of the research on concrete microstructure.

Concrete with compressive strength more than 50 MPa is usually classified as high-strength concrete (HSC).This can be reached by reducing the water/binder ratio and increasing the binder content. Mehta (1999) explains that the low water/cement ratios used in the manufacture of high-strength concrete (HSC) already guarantee that durability requirements, such as low permeability which is one the characteristics that show an internal structure more uniform at the matrix–aggregate interface than normal strength concretes (NSC). HSC mixes are generally characterized by low water/binder ratios, high consumption of cement, and the presence of various chemical and mineral admixtures (Mehta and Aitcin, 1990).

The strength of concrete is influenced by many factors, for instance the amount and type of cement, w/c ratio, aggregate type and grading, and chemical additives. Based on an experimental study, Beshr et al. (2003) reported that the quality of coarse aggregate significantly influenced the compressive strength and split tensile strength of high strength concrete. Furthermore, the length of the tail end portion of the softening curve and the fracture energy increased as the maximum size of coarse aggregate and compressive strength of concrete increased (Appa Rao and Raghu Prasad, 2002). Mazloom et al. (2004) indicated also that as the proportion of silica fume (SF) increased, the workability of concrete decreased but its short-term mechanical properties such as 28-day compressive strength and secant modulus improved. Also the percentage of silica fume replacement did not have a significant influence on total shrinkage; however, the autogenous shrinkage of concrete increased as the amount of silica fume increased.

Nowadays, the use of silica fume is significantly improving the mechanical properties and the durability of HSC. The very high content of amorphous silicon dioxide and very fine spherical particles are the main reasons for its high pozzolanic activity (ACI committee 363 - 1994).

4.4 High performance concrete

In addition to strength, concrete must reach other specific needs, such as workability, durability, and toughness. These characteristics have led to the development of high-performance concrete (HPC). The fracture properties of HPC are different from those of normal and high strength concretes.

Generally, HPC contains the following ingredients: good quality aggregate, ordinary Portland cement (at high content, about 450-550 kg/m^3), silica fume (about 5-15% by volume) and superplasticiser. It has also been suggested that other cementitious material may be added, such as fly ash or ground granulated blastfurnace slag (ggbs) depending on the application (Farhat, 2004). An experimental investigation on fracture properties of high-performance concrete has been conducted by Ricardo and Marta (2006).

To study the effect of the concrete strength on the tensile stress-strain relationship, Raghu Prasad et al. (2005) proposed a new model depending on the load-deflection plots. This model is used to predict the load-deflection plots for the beams with eight different HPC mixes and is compared with the experimental load-deflection plots. The comparisons are found to be good, which indicates that the proposed procedure for obtaining the concrete stress-strain relationship in tension can explain the size effect and brittleness of HPC because of the variation in the w/b ratio and the addition of mineral admixtures such as fly ash or slag.

4.5 Fibre reinforced concrete

In order to improve the concrete properties, fibre reinforced cement (FRC) and concrete materials have been developed progressively since the early work by Romualdi and Batson in the 1960s. With the commercial development of FRC materials and products, an extensive research programme was undertaken to quantify the enhanced properties of FRC materials and more specifically to allow comparisons to be made between various fibres. By the 1990s, a wide range of fibre composites and FRC products were commercially available (Swamy, 1992). The main role of using fibres in the concrete at low volume fractions is to modify the cracking mechanism. Moreover, these fibres generally fall within one of the following four categories (ACI, 1996),

1. Natural (sisal, coconut, bamboo, and jute).
2. Synthetic (acrylic, aramid, carbon, nylon, polyester, polyethylene, and polypropylene).
3. Glass fibre
4. Steel fibre

An experimental investigation has been carried out in the laboratory on steel fibre reinforced concrete (SFRC) as well as on dry-mix of steel fibre reinforced shotcrete (SFRS) at a tunnel site by Yining and Wolfgang (2000). The measurements were performed at about 9 hours and continued up to 81 hours. The investigation demonstrated that the use of fibre reinforcement in concrete/shotcrete can greatly increase the compressive strength, ductility, toughness and energy absorption at early ages.

Moreover, steel fibres are increasingly used as full or partial replacement of conventional web reinforcement in some structural concrete applications, since their inclusion in concrete mix has been shown to enhance shear resistance and ductility (Casanova et al., 1996; Cucchiara et al, 2004). In addition, the deicer-scaling resistance of concrete is reduced by adding steel fibre at the same air content, especially for the air-entrained concrete, even though the flexural strength of concrete is significantly improved by the addition of fibres (Yang and Zhu, 2005).

Burak et al., (2009) investigated the performance of two polymer based micro-fibres (polypropylene and polyvinyl alcohol) in different matrices (high strength and comparatively low strength with fly ash incorporation), and found that the polypropylene (PP) fibres elongate and slip from the matrix easily. Incorporation of fly ash resulted in a frictional bond improvement between matrix and fibre. On the other hand, polyvinyl alcohol fibres (PVA) performed similarly in both matrices because of their relatively rough surface structure. The flexural strength values and toughness improved significantly by incorporation of PVA fibres. However, the stability of this improvement depends on the proper adjustment of matrix and fibre properties.

4.6 High Performance Fibre Reinforced Cementitious Composites (HPFRCCs)

According to Shah et al. (1999), FRCs can be categorized into two classes based on their tensile response: conventional FRC and high performance FRC (HPFRCC) where conventional FRC exhibits an increase in ductility over that of plain concrete, whereas HPFRCCs exhibit a substantial strain-hardening response, leading to a large improvement in both strength and toughness compared with the plain concrete. However, in order to classify the performance of FRC composites and minimize the

increasing number of names and acronyms associated with particular mixtures, designs, or production processes, Naaman and Reinhardt (2004) suggested the use of a performance-based design classification of FRC composites with four levels of performance, namely:

(1) Crack control

(2) Deflection hardening

(3) Strain hardening

(4) High energy absorption

HPFRCCs include materials such as SIFCON (Slurry Infiltrated Fibre Concrete), MDF (Macro Defect Free), ECC (Engineered Cementitious Composites),DSP (Densified Small Particle Systems), CRC (Compact Reinforced Composite), RPC (Reactive Powder Concrete) and CARDIFRC®. These materials are shown to develop outstanding combinations of strength and ductility as well as long-term durability (Reinhardt, 1991; Karihaloo et al., 2001; Li and Kanda, 1998; Lankard, 1985; and Bache, 1981). Moreover, HPFRCCs are characterized by a stress–strain response in tension that exhibits strain-hardening behaviour accompanied by multiple cracking, and relatively large energy absorption capacity (Naaman and Reinhardt, 2004). Many studies have been conducted on HPFRCCs which have clearly shown the advantages from the use of high performance fibre reinforced cementitious composites (HPFRCC) such as UHPFRC, engineered cementitious composites (ECC) and slurry-infiltrated concrete (SIFCON) in structural members under static loading conditions (Bruhwiler at el., 2005; Habel at el., 2007).

4.6.1 Bridging action of the fibre

Considerable attention has been paid to the use of steel-fibre in reinforced concrete during the last three decades. The studies proved that the most fundamental property of a fibre reinforced cementitious composite is the fibre bridging across the matrix crack (Li at el., 1991; Li, 1992; Lim and Li, 1997).

Adding fibres to concrete mixes significantly improve many of the engineering properties of HPFRCCs, especially impact strength and toughness. As fibres are randomly distributed in the concrete matrix, cracks can reach a perpendicular fibre

which can stop crack growth, when propagating through concrete (Gonzalo, 2009). The fibre cracking control capacity depends on mechanical properties of fibre (shape and dimensions). Barluenga and Olivares (2007) found that the inclusion of low volumetric fractions of the two types of AR-glass fibre can control the cracking produced due to very early age shrinkage in both standard concrete and self compacted concrete in two different ways: reducing the total cracked area and the maximum length of the cracks.

The inclusion of fibres delays the dilation of concrete by acting as crack arresters, restricts the development of crack and thus transforming an inherently brittle matrix into a strong composite with better crack resistance and ductility. Moreover, the fibres help to transfer loads at the internal micro-cracks (Ramesh et al., 2003).

According to Balaguru and Shah (1992) when the matrix cracks, the fibre transmits the load across the crack. Since fibres are randomly dispersed throughout the matrix, their orientations relative to the direction of the applied load are an important factor. In a matrix containing randomly distributed fibres, few fibres align in the direction of applied load; instead almost all fibres are oriented at different angles to the load direction (Figure 4.1).
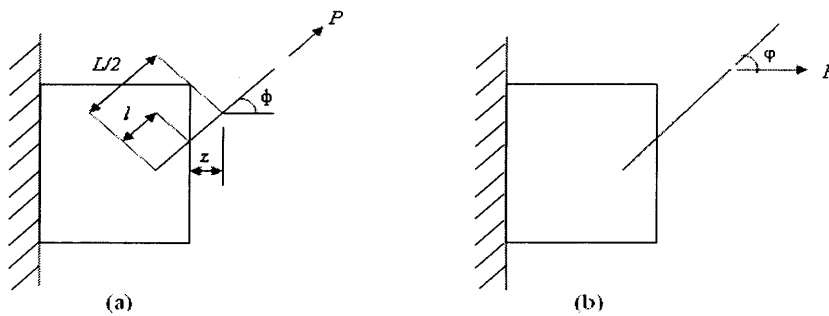
Figure 4.1 (a) A single fibre pull-out without snubbing $(\phi = 0)$ and (b) with snubbing $(\phi \neq 0, \phi = \varphi)$ (After Karihaloo and Wang, 2000)

When a fibre is pulled out from the cementitious matrix, the snubbing friction at the fibre exit point can increase the pull-out resistance, and contribute to the overall composite action. Naaman and Shah (1976) reported that inclined fibres can take a greater load as they bend. The observations confirmed that after matrix cracking, the load and energy required to pullout a steel fibre from the matrix can be higher for fibres inclined to the load direction.

It is assumed that when the crack opening displacement reaches a critical value v_{cr}, some of the fibres bridging the crack will debond from the matrix, resulting in a sudden drop in the bridging force (BC), whereafter these fibres will exert a reduced closure force by frictional pull-out (CD) (see Figure 4.2). This is based on single pull-out tests. From this single fibre relationship, the average closure force on crack faces bridged by many fibres is obtained through an approximation to the fibre distribution function (Figure 4.3). The slope of the elastic part of this averaged pullout diagram gives directly the parameter k in equation (4.2) below.
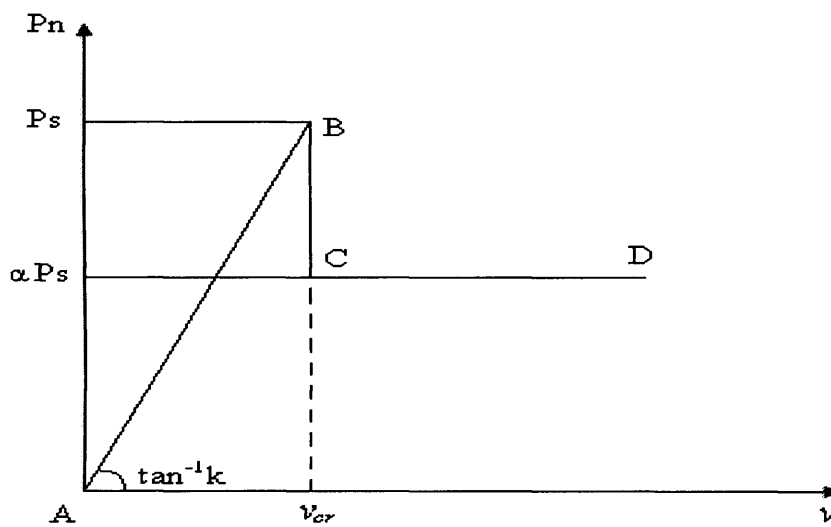
Figure 4.2 A linearized bridging law describing the relation between the bridging force and the crack opening displacement (Karihaloo and Wang, 1997)
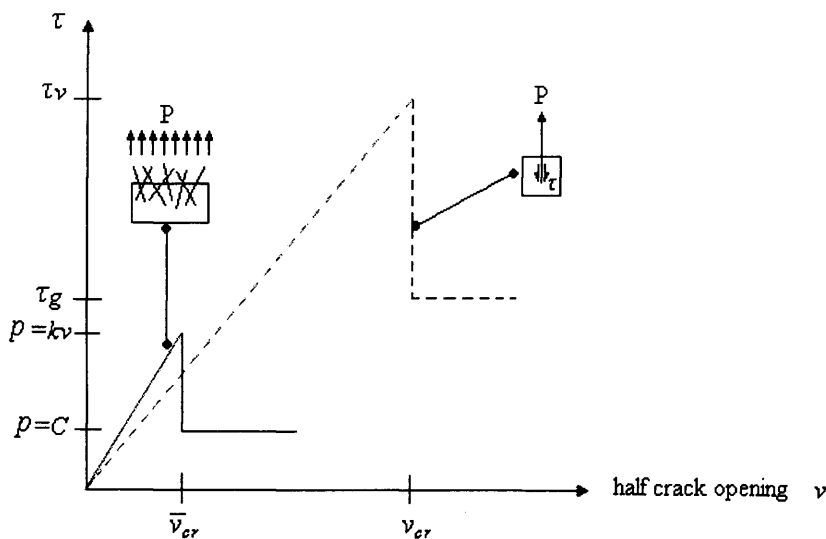
Figure 4.3 Idealized interfacial matrix-fibre shear stress (τ) vs. half crack mouth opening for single fibre (dashed line) and multiple fibre (solid line) pull-out (After Lange-Kornbak, 1997)

When the crack opening exceeds the critical value $\bar{v}_{cr}$, the bridging stress $p(v)=kv$ drops to the constant frictional pull-out value, the parameter C in equation (4.3) below. The bridging stress for multiple fibre bridging is expressed in terms of single fibre properties τ_v, the adhesive bond strength of the fibre and the matrix, and τ_g the frictional pull-out strength of fibre. This is achieved by introducing the ratio

$$\zeta = \frac{\bar{v}_{cr}}{v_{cr}} \tag{4.1}$$

where $\bar{v}_{cr}$ follows from the multiple crack model, since its assumes that slip is initiated immediately after reaching the ultimate tensile load, whereby the corresponding maximum half opening of the crack equals $\bar{v}_{cr}$ (Lange-Kornback and Karihaloo, 1997). The bridging forces are

$$p(v) \approx 2V_f \frac{\tau_v}{\tau_g} E_f \frac{h}{L} v \equiv kv \qquad\qquad v < \bar{v}_{cr} \tag{4.2}$$

$$p(v) \approx \frac{1}{2} V_f \tau_g \frac{L}{d} h \frac{\bar{v}_{cr}}{v_{cr}} \equiv C \qquad\qquad v \geq \bar{v}_{cr} \tag{4.3}$$

where V_f is the volume friction of fibre, L the length of the fibre, d the diameter of the fibre, and h is the snubbing factor (defined by Karihaloo and Wang, 2000) as

$$h = \frac{2}{(4+f^2)} (e^{-f\pi/2} + 1) \tag{4.4}$$

where f is the snubbing friction coefficient.

4.6.2 Constitutive Model

The constitutive model is based on the stress-strain behaviour of short fibre-reinforced cementitious in tension/flexure. Karihaloo and Wang (2000) described two types of FRC (conventional FRC and high-performance FRC) which exhibit the same response

with differences in the constitutive behaviour. Figure 4.4 demonstrates the load deformation response of conventional and high performance FRC to tensile/flexural loading. It can be seen that the total tensile strain and load carrying capacity of HPFRCC are higher than for the conventional FRC, and the amount of stored energy represented by the area under the curve in HPFRCC is much higher than that of conventional FRC.
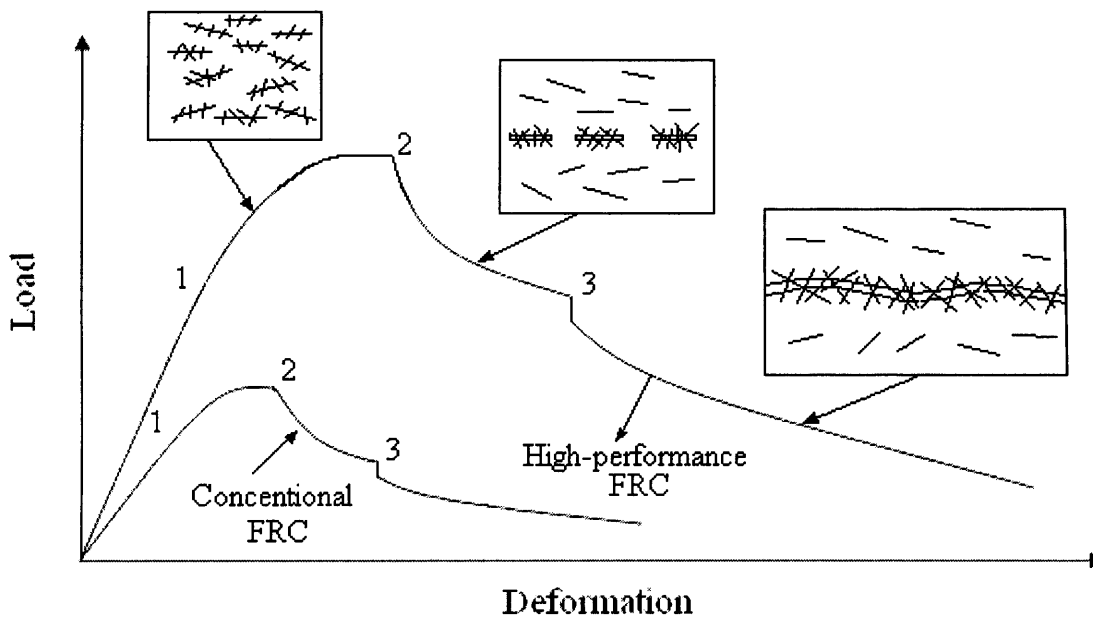
Figure 4.4 Complete pre- and post-peak tensile responses of two short fibre-reinforced cementitious composites (After Karihaloo and Wang, 2000).

The deformation is generally expressed in terms of strain up to the peak load (point 2) and through crack opening displacement thereafter. Both materials exhibit the following response stages (Karihaloo and Wang 2000)

- Stage 1: linear elastic behaviour up to 1

- Stage 2: strain hardening behaviour between 1 and 2.

- Stage 3: tension softening due to localization of damage in the form of unconnected macrocracks 2 and 3.

- Stage 4: continued tension softening due to localization of damage in the form of a through crack until complete rupture.

4.6.3 Types of HPFRCC

4.6.3.1 Macro-Defect-Free Cement (MDF)

The MDF cementitious materials (also called new inorganic materials, NIMs or chemically bonded ceramics, CBCs) are composites combining Portland or high-alumina cement with a water–soluble polymer of high molecular mass (e.g. polyvinyl alcohol, PVA, hydroxypropyl methyl cellulose, HPMC). The latter acts as a rheological aid, reduces the inter-particle friction coefficient and reacts with the hydration products. It prevents flocculation of cement particles, increases the viscosity of the mix at low water to solids ratio, thus permitting the use of intensive-high shear mixing processes without inducing cavitation (Birchall et al., 1981; Shah and Young, 1990).

The MDF pastes have very high tensile strength (150 MPa or more) particularly when mixed with alumina cement. They are prepared under high shear, by mixing inorganic cement with a water-soluble polymer in the presence of limited amounts of water. The final product has very high bend strength, greater than 200 MPa, together with a high modulus of elasticity and relatively high fracture energy (Jennings, 1991). However, the material may display some drawbacks like a high sensitivity to water (Lewis and Kriven 1993). Moreover, the use of fibres in MDF cements is restricted (only long fibres may be used).

To evaluate the influence of poly (vinyl alcohol), cement type, and silica fume, an experimental work was conducted by Santos et al. (1999). The Macro-defect free cements were prepared using the following variables: processing (calendering and hand-mixing), poly (vinyl) alcohol (with different molecular weight and hydrolysis degree), and cement (Portland type I and slag-modified), and additions of silica fume.

The results showed that better processing is achieved by calendering the fresh paste and using poly (vinyl alcohol) with low hydrolysis degree and low molecular weight. Vickers hardness measurements indicate that materials prepared using Portland type I cement is not significantly affected by humidity. Addition of silica fume lowers the acid resistance of these materials, suggesting that silica fume acts as inert filler.

4.6.3.2 Slurry Infiltrated Fibre Concrete (SIFCON)

It is a high performance fibre reinforced concrete with very high fibre content, up to 20 percent by volume depending on the type of fibres used and manufacturing method (Lankard and Newell, 1984). The matrix of this material has no coarse aggregate but a high cementitious content; however, it may contain fine sand and additives such as fly ash, microsilica, and latex emulsion (Naaman, 1991).

Furthermore, to investigate the effect of incorporating steel fibres on this type of materials, Balaguru and Kendzulak (1986) and Lankard (1985) have shown that in SIFCON the fibres are pre-placed in a mould to its full capacity and the corresponding fibre network is then infiltrated by cement-based slurry. The presence of fibres in SIFCON leads to an enhancement of ductility, as well as a reduction in crack width.

The use of a SIFCON matrix in over reinforced concrete beams can lead to ductility factors three to five times larger than control beams made from a plain concrete matrix (Naaman et al., 1990). They also observed that the use of such materials helps reduce crack widths in the tensile zone at least by one order of magnitude, and contributes to the spread of the zone of plasticity in the compression zone prior to failure.

The effect of using high volume of Class C fly ash (FA) on mechanical properties of autoclaved SIFCON (slurry infiltrated fibre concrete) has been investigated (Halit et al., 2006). Cement was replaced with up to 60% FA in SIFCON compositions and three different steel fibre volumes (2%, 6% and 10%) were used. Test results were presented in comparison with the control mix (0% FA and 0% fibre). Mechanical properties were positively affected almost at every FA replacement.

Moreover, by increasing the fibre volume, flexural strength and toughness were remarkably increased. This behaviour was more pronounced at 10% fibre volume. At this fibre volume ratio, flexural strength of 55 MPa could be achieved with 60% FA replacement.

4.6.3.3 Engineered Cementitious Composites (ECC)

Engineered Cementitious Composite (ECC) represents a unique type of high performance fibre reinforced cementitious composite (HPFRCC) which features high tensile ductility with moderate fibre volume fraction, typically 2% by volume (Li, 2003). The mixture design of current ECC contains controlled quantities and types of cement, sand, fly ash, water, chemical admixtures, and short, randomly oriented polyvinyl alcohol (PVA) fibre. ECC has been engineered to satisfy various field performance requirements such as high durability, or impact load resistance. Unlike ordinary concrete materials, ECC strain harden s after first cracking, similar to a ductile metal, and demonstrates a strain capacity of 300–500 times greater than normal and fibre reinforced concrete.

Even at large imposed deformation of several percent crack widths of ECC remain small, less than 80μm. (Li and Weimann, 2003). ECC has a tensile strain capacity of up to 6% and exhibits pseudo-strain hardening behaviour accompanied by multiple cracking. It also has high ultimate tensile strength (5-10 MPa), modulus of rupture (8-25 MPa), fracture toughness (25-30 kJ/m^2) and compressive strength (up to 80 MPa) and strain (0.6%). Due to its superior properties, the material can be used as a durable repair material (Li and Kamada, 2000)

4.6.3.4 Reactive Powder Concrete (RPC)

Reactive Powder Concrete RPC has been developed by the Scientific Division of Bouygues, at St Quentin en Yvelines in France. The material is characterised by high silica fume content and very low water to cement ratio. It exhibits very high mechanical and durability properties (Richard and Cheyrezy 1995). Compared to conventional concrete, the ductility estimated in terms of fracture energy is increased by one to two orders of magnitude, while the compressive strength values are in the range of 200 to 800 MPa. As reported by Richard and Cheyrezy (1995) the development of RPC was based on the following principles.

1. Improvement of homogeneity by elimination of coarse aggregates;
2. Enhancement of compacted density by optimization of the granular mixture, and application of pressure before and during setting.
3. Enhancement of the microstructure by post-set heat-treating.

4. Improvement of ductility by incorporating small-sized steel fibres

5. Maintaining mixing and casting procedures as close as possible to existing practice.

4.6.3.5 DSP Cementitious Materials

Aalborg Portland-Cement developed a new type of cement based materials. This class of materials is termed DSP, referring to Densified System containing homogenously arranged ultra fine Particles. It was made possible by superplasticizers and silica fume in systems that can be densely packed in a low stress field and with very low water content (Bache 1981). DSP belongs to a new class of materials formed from densely packed particles of a size ranging from 0.5 to 100μm, and homogeneously arranged ultra fine particles ranging in size from about 50Å to 0.5 μm and arranged in the spaces between the larger particles.

Dense packing of the particles (sand, cement and ultra-fine silica) together with fibres is essential for achieving the desired mechanical properties. It is also the prime feature of HPFRCCs materials. Materials such as DSP combine very densely packed cement particles (5-10μm) and ultra fine silica fume (0.1-0.2μm) filling the spaces between the cement particles and, normally densely arranged fibres (Bache, 1981; Bache, 1987).

The new binder is a very strong and brittle material with a compressive strength of 150 MPa – 270 MPa. Due to its brittleness, it is difficult to utilize this material effectively without the incorporation of fine, strong and stiff fibres. The fibres improve the tensile properties of DSP based matrix such as Densit®. Therefore, in accordance with the micro-mechanical model of strain hardening and tension softening of FRCs, the DSP can give the strong matrix a high degree of ductility by adding appropriate fibres (Karihaloo and Wang, 1997).

4.6.3.6 CARDIFRC®

Many studies have been conducted at CARDIFF University (Karihaloo and De Vriese 1999; Sullivan 1999; Karihaloo et al., 2000) using materials widely used in the UK concrete industry. The researchers selected two classes of HPFRCCs materials as the

main basis of experimental programme which are Reactive Powder Cement (RPC) and Densified System containing homogeneously arranged ultra-fine Particles (DSP) or Densit®. The mechanical properties were found to be inferior to those reported in the literature (Richard and Cheyrezy, 1995; Bache, 1981), and the workability of some mixes was poor. These attempts however provided valuable clues on how to improve the mixing and processing techniques in order to produce HPFRCCs similar to RPC and Densit® but whose mechanical performance even exceeded that of the original mixes. Another type of mix, a HPFRCC with 6 mm coarse aggregate, was also investigated (Benson, 1999). The workability of this mix was satisfactory but the mechanical properties were inferior to those achieved with mixes containing no coarse aggregate (Benson, 2003).

Therefore, to optimise the HPFRCC, further studies were continued at Cardiff. The aim was to achieve good workable mixes with a very low water/binder ratio and a high volume fraction of steel fibre, in order that the resulting concrete, in its hardened state, was very ductile with a relatively high tensile strength. This result was achieved by adding large amounts (up to 8 % by volume) of short steel fibres (6-13 mm long, 0.16 mm diameter) in a cementitious matrix densified by the use of silica fume. The matrix contains only very fine quartz sands (up to 2mm), instead of ordinary river sand and coarse aggregates. By optimising the grading of fine sands, the water demand was considerably reduced without affecting the workability of the mix.

As a result of many trial mixes and testing, the mixes shown in Table 4.1 are the optimised ones. Two different mixes (designated CARDIFRC®, Mix I and Mix II) of high-performance concrete differing mainly by the maximum size of quartz sand used in the mix have been developed using novel mixing procedures. These procedures are described in patent GB2391010. However, there are some differences in CARDIFRC® mix compared with RPC and DSP mixes. The two different types of fibre used in combination to the high volume fraction are adopted. This rather innovative technique was found to be quite beneficial to the load deflection response of the matrix in terms of both strength and ductility. The investigations showed also that a significant improvement in the performance of Mix I by the use of two grades of fine quartz sand (Table 4.1). Similarly, in Mix II in order to maximize the dry density of the mix, three grades of fine quartz were used.

This optimisation of grading of quartz sands used led to considerable reduction in the water demand without any loss in workability. It is reported by Karihaloo et al. (2001) that the produced material (CARDIFRC®) in its hardened state is characterised by very high compressive strength (in excess of 200 MPa), tensile /flexural strength (up to 30 MPa), high energy-absorption capacity (up to 20,000 J/m^2). Table 4.2 shows the material properties of CARDIFRC®.

Table 4.1 Mix proportions for CARDIFRC® Mix I and Mix II (per m^3) (Karihaloo et al., 2001)

Constituents (kg)	Mix I	Mix II
Cement	855	744
Microsilica	214	178
Quartz sand:		
9-300μm	470	166
250-600μm	470	-
212-1000μm	-	335
1-2 mm	-	672
Water	188	149
Superplasticizer	28	55
Fibres: -6 mm	390	351
-13 mm	78	117
Water/cement ratio	0.22	0.20
Water/binder ratio	0.18	0.16

Table 4.2 Typical material properties of CARDIFRC® Mix I and Mix II

Material properties	Mix I	Mix II
Indirect tensile strength (MPa)	28.6	21.4
Fracture energy (J/m^2)	22909	17875
Compressive strength (MPa)	207.0	185.0

4.6.3.6.1-The effect of high temperature curing conditions

It has been found that the elevated temperature and curing conditions activate the reaction between the calcium hydroxide formed during normal cement hydration and the silica fume contained in the mix and thus affects beneficially the early strength of concrete (Sullivan, 1999; and Neville, 1995). Typically, the remarkable strength properties observed in HPFRCCs are obtained by curing it at 90°C. For example, compressive strength of CARDIFRC® reaches up to 200 MPa when the specimens are cured at high temperature up to 90°C for only 7 days.

Moreover, an investigation was conducted by Zanni et al. (1996) to study the effect of heat treatment on the hydration of RPC. This investigation showed that silica fume consumption was highly dependent on heat treatment temperature and duration. It also proved that the crushed quartz reactivity was dependent on heat treatment and duration. Karihaloo and De Vriese (1999) showed that, the curing time of RPC specimens could be reduced from 28 to 16 days, when the specimens are cured under the following regime:

7 days	at	ambient temperature
3 days	at	90°C
7 days	at	ambient temperature

In order to reduce the curing time of the specimens Sullivan (1999) exposed RPC specimens to high temperature curing for the entire seven days at 90°C immediately after the moulds are stripped. The strengths attained by CARDIFRC® specimens cured at 90° C for seven days have been found to be the equivalent of standard 28-day water curing at 20° C (Alaee, 2002). To avoid any large thermal gradients, which will create a thermal shock, it is recommended that the specimens be left in the curing tank for 9 days. On the first day the temperature is increased gradually from 20° C to 90° C and on the last day it is decreased from 90° C to 20° C.

4.6.3.6.2 The effect of silica fume

Different kinds of cement replacement material are usually added to the concrete mixtures to improve their mechanical properties. Generally, silica fume is a fine powder whose particles are about 100 times smaller than cement. It is the one of the most popular pozzolans, whose addition to concrete mixes results in low porosity, low permeability and bleeding because the oxides (SiO_2) react with and consume calcium hydroxide, which is produced by the hydration of ordinary Portland cement. The main results of pozzolanic reactions are: lower heat liberation and strength development; lime-consuming activity; smaller pore size distribution.

The particles of silica fume pack tightly against the surface of the aggregate and fit in-between the cement particles, thus greatly improving packing. Neville (1995) reported that because the extremely fine particles of silica fume reduce the size and volume of voids near the surface of the aggregate, the so-called interface zone has improved properties with respect to microcracking and permeability.

The bond between the aggregate and the cement paste is improved, allowing the aggregate to participate better in stress transfer. Bhanjaa and Sengupta, (2005) showed that silica fume incorporation in concrete and with the initial filling of the voids by silica fume results in a significant improvement in the tensile strength of concrete, along with the compressive strength.

The main functions of silica fume in HPFRCCs as reported by Richard and Cheyrezy (1995) are:

- Filling the voids between the next larger class particles [cement]
- Enhancement of rheological characteristics by the lubrication effect resulting from the perfect spherical shape of the basic particles.
- Production of secondary hydrates by pozzolanic reaction with the lime resulting from primary hydration.

One of the main advantages of using silica fume particles with cement is to fill the spaces between the cement particles and thus achieving very dense packing system. Bache (1981) attributed these to the following:

1- The silica particles are smaller than even the finest cement we can produce by grinding and are therefore more conductive to dense packing into the spaces between the cement particles.

2- The silica particles, being formed by condensation from gas phase, are spherical in shape (unlike crushed cement particles, which are angular) and this makes the silica particles even more suitable for dense packing than very fine cement.

3- The particles are chemically less reactive than cement, which eliminates the problem of too rapid hardening encountered with very fine cement; in addition, the silica is likely to ensure the formation of a coherent structural skeleton between the cement particles, resulting in a fine dense microstructure.

Adding silica fume to HPFRCCs mixture can improve the bond by increasing the contact area between the fibre and the surrounding matrix. This introduction of fine microsilica particles will increase the density of the matrix, filling any pore spaces around the fibre. The increase in the surface contact area increases the pull-out force (Bache, 1981).

Recently, many studies have been conducted to evaluate the effect of microsilica on the mechanical properties of concrete mixture (Mazloom et al., 2004; Almusallam et al., 2004). The results proved that the microsilica plays a significant role in increasing the mechanical properties of concrete (compressive and splitting strengths and modulus of elasticity). Moreover, Yin and Shu (2004) reported that the incorporation of silica fume can effectively enhance the fibre–matrix interfacial properties, especially the fibre pullout energy. It is also concluded that in terms of the bond characteristics, the optimal silica fume content is between 20% and 30%, given the conditions of the experimental program.

The experimental investigation to evaluate the effect of different amounts of silica fume and water to the cement ratios (w/c) by Behnood and Ziari (2008) shows that the rates of strength loss for concrete containing 6% and 10% SF at 600^0C were 6.7% and 14.1% lower than those of the ordinary concrete. The dosage of SF had no significant effect on the relative residual compressive strength at 100 and 200^0C, whereas the amount of SF had considerable influence on the residual compressive strength above 300^0C, similar to the response at 600^0C. Another important property of microsilica is its pozzolanic behaviour. The material is extremely reactive, and hence can react with the surplus of calcium hydroxide, which in ordinary cement paste will crystallize out as a separate and relatively weak phase. The reaction of microsilica with the remaining calcium hydroxide, from the primary cement water reaction, results in the production of an extra C-S-H. The chemical representation of this process is shown below:

Primary reaction: Cement + Water

$$2C_3S + 6H \rightarrow C_3S_2H_3 + 3Ca(OH)_2 \qquad (4.5)$$

$$(C\text{-}S\text{-}H) + [CH]$$
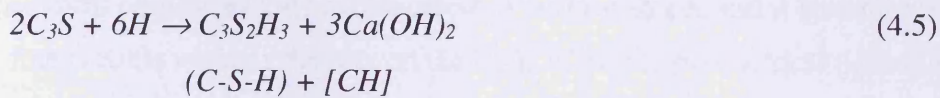
Secondary Reaction: *Silica + Calcium Hydroxide + Water*

$$S + CH + H \rightarrow C\text{-}S\text{-}H \qquad (4.6)$$

The extra production of C-S-H results in a microstructure which is very dense in the freshly mixed state and gets even denser during the succeeding hydration process. The effect of microsilica in the cement paste is shown in Figure 4.5.

(a) Cement paste   (b) DSP paste
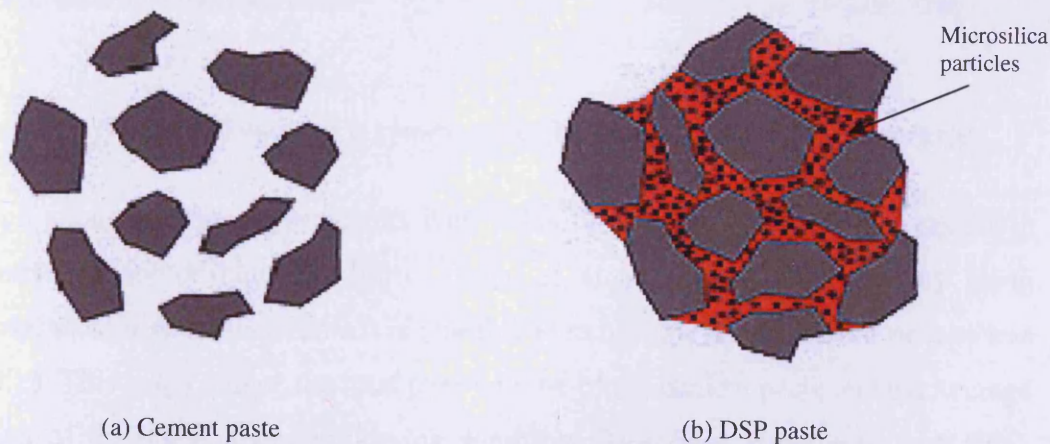
Figure 4.5 (a) Flocculated particles in ordinary cement paste. (b) Densely packed cement grains and microsilica in DSP paste

4.6.3.6.3 The effect of dispersing agent (Superplasticizer)

When a high volume of steel fibre and silica fume is incorporated in concrete, there will be a significant loss in the workability. In order to achieve adequate workability of the mix, superplasticizers are used. They are long and heavy molecules (Neville,1995) which wrap themselves around the cement particles and give them a highly negative electrical charge so that they repel each other. These results in deflocculation and dispersion of the cement particles and therefore, in high workability (Figure 4.6).

Superplasticizers are added to the CARDIFRC® matrix in order to achieve a very workable mix at low water/cement ratio, thus obtaining dense packing which give high strength and durable concrete. One of the main difficulties of achieving such a system, as described by Bache (1987) is the presence of surface forces. These forces interlock neighbouring particles, consequently counteracting mutual particle movement during mixing and shaping. However, effective dispersing agent such as, superplasticizer eliminates the locking effect of surface forces and it becomes possible to pack fine particle systems densely on the basis of purely geometrical principle.

Addition of Superplasticiser

(a)   (b)
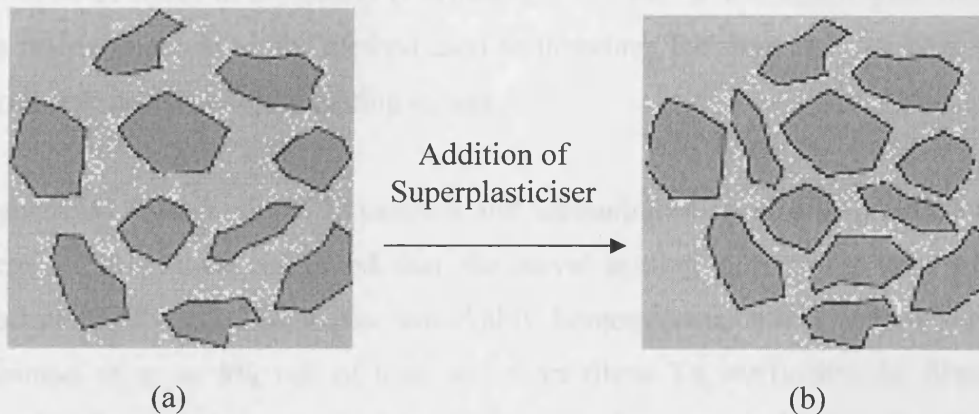
Figure 4.6 (a) Flocculated particles in cement paste. (b) Superplasticised cement particles

The combination of superplasticizers with silica fume in the concrete mix results in high strength and/or high durability. Dugat et al. (1996) reported that by using superplasticizers with silica fume it is possible to reduce the water/cement ratio to less than 0.15. This helps reduce the total pore volume of the cement paste and the average diameter of the pores, hence improving durability. Moreover, experience with RPC, DSP and CARDIFRC® showed remarkable strength properties when superplasticizers

and silica fume are incorporated in the original mix. In order to increase the workability of CARDIFRC® mixes, the amount of superplasticizer used in the material mix is somewhat higher than that of RPC and DSP mixes.

4.6.3.6.4 The effect of steel fibres

The incorporation of fibres in the CARDIFRC® matrix increases the tensile load-carrying capacity and turns an otherwise brittle material into a very ductile one. Furthermore, to prevent corrosion, brass-coated steel fibres (diameter 0.16 mm, 6 mm or 13 mm long) are used in CARDIFRC® mix. The use of long and short fibres was found necessary to improve the material properties, whilst minimising loss of workability. The short fibres prevent microcrack growth and coalescence (Mobasher et al., 1990; Tjiptobroto and Hansen, 1993) and provide a high tensile strength. Long fibres provide increased ductility, greater pullout strength and will bridge wider cracks (Sullivan, 1999).

4.6.3.6.4.1 Fibre distribution

The mechanical performance of any HPFRCC, depends to a high degree on even distribution of fibres in the matrix (Karihaloo et al., 2007). The distribution of fibres in the matrix depends on the method used to introduce the fibre into the bulk of the material and the shape of the casting mould.

Computerised Topography (CT) imaging and sectioning of specimens (Karihaloo and Jefferson, 2001) have confirmed that the novel mixing procedures used for the production CARDIFRC® ensures remarkably homogeneous mixes with a uniform distribution of up to 8% vol. of long and short fibres To verify that the fibres are uniformly distributed in a CARDIFRC® mix, Benson (2003) employed non-destructive and destructive testing techniques. CT results show that the fibres are nearly uniformly distributed with random orientation in the mixes. Destructive testing also confirmed these findings and showed that the fibre distribution was generally uniform.

4.6.3.6.4.2 Volume fraction of fibre

Generally, as the volume fraction of fibre increases and as the fibres are more uniformly dispersed, the growth of microcracks is hindered, and the localisation of

deformation is delayed with a consequent substantial increase in the tensile strength and strain capacities of the composite (Balaguru and Shah, 1992). The volume fraction of fibres in concrete affects both the fresh and hardened state. Hoy and Bartos (1999) reported that when higher volumes of steel fibre are added to concrete, there is a more significant loss of workability and greater chance that fibres will interlock. For these reasons, there is an optimum fibre content for any given fibre-matrix combination. Higher fibre contents will produce mixes which lack homogeneity and have poorer workability, while lower fibre contents will result in less efficient reinforcement.

By a careful selection of mix proportions, the optimum fibre content can be increased with a resulting performance improvement. Mobasher et al. (1990) carried out an experimental programme on the effect of fibre content on the fracture properties of concrete. They concluded that as the volume fraction of fibres increases the growth of microcracks was hindered through an arrest mechanism and the matrix fracture toughness was increased. The higher the volume fraction of fibres, the higher peak load, and the higher the matrix contribution and the higher the acoustic emission (AE) rate event count the lather means that there is a greater number of microcracks.

Karihaloo and De Vriese, (1999) investigated the influence of volume fraction of fibres on the mechanical properties of the RPC mix. The experimental programme revealed that the increase in the volume fraction of steel fibres V_f led to significant improvements in both the specific fracture energy and the splitting strength. Furthermore, Shannag and Hansen (2000) showed that incorporating large volume fractions of short steel fibres (more than 2% by volume) in DSP composites results in a dramatic increase in matrix tensile strength (up to 100%).

4.6.3.6.4.3 Aspect ratio of fibre (l/d)

The most important advantages of the incorporation of steel fibre into CARDIFRC® matrix is the improvement of major mechanical properties of such mix. Physically, the length divided by the diameter fibres is described as the aspect ratio; higher aspect ratio fibres perform better than lower aspect ones. Fanella and Naaman (1985) and Gopalaratnam and Shah (1986) found a monotonic increase in compressive strength and ductility when the aspect ratio increased from 47 to 100. Sullivan (1999) also

83

found that long fibres increased both the tensile strength and ductility of concrete. Karihaloo and De Vriese (1999) reported that an increase in fibre length – and consequently of aspect ratio- seems to be more effective than an increment only in volume fraction of fibres. The incorporation of long fibre (13 mm) in CARDIFRC® mixes is a primary reason for enhancing its ductility.

4.6.3.6.5 Constitutive description of CARDIFRC®

According to Karihaloo et al. (1996); Wang and Karihaloo (2000) and Karihaloo and Wang (2000) the strain hardening of HPFRCC results from the nucleation of microcracks under increased tensile/flexural stress. As mentioned in the literature, the assumptions have been made on their evolution but no experimental work was available to validate them. An experimental programme was implemented on CARDIFRC® specimens to quantify the increase in the crack density ω as a function of applied tensile stress σ and fibre parameters (Benson, 2003). The results reveal that the fracture process zone is affected by not one dominant crack but by many microcracks. In support of this, parallel cracks, crack branching, cracks linking-up and multiple cracking were all observed and recorded.

Moreover, as the active crack opens, evidence of fibre bridging was confirmed. It was also noted that not all cracks continued to propagate; some cracks became dormant since the failure plane will occur along the path of least resistance. Numerical expressions have been fitted to the test data to describe the behaviour of CARDIFRC in uniaxial tension.

Figure 4.7 shows the three regions predicted by the equations. Laboratory test work shows clear evidence that the linear elastic region is larger than theoretically predicted (Karihaloo and Wang, 2000), a smaller strain hardening region with a distinct plateau at the peak load followed by a gradual decrease in the stress after the peak load.

Stage I- Linear-elastic region

Applicable form 0 to200 microstrain (σ in MPa)

$$\sigma_1 = 0.046\varepsilon \qquad\qquad (4.7)$$

Stage II- Strain hardening region

Applicable form 200 to600 microstrain (σ in MPa)

$$\sigma = -4.34*10^{-10}\varepsilon^4 + 8.32*10^{-7}\varepsilon^3 - 6.03 \times 10^{-4}\varepsilon^2 - 0.199\ \varepsilon\text{-}12.62 \tag{4.8}$$

Stage III- Tension hardening region

Applicable from 0 to 6.5 mm (σ in MPa)

$$\sigma = 3.07 * 10^{-3} w^7 - 0.08\ w^6 + 0.82\ w^5 - 4.42\ w^4 + 12.80\ w^3 - 18.11\ w^2 +$$

$$5.73\ w + 12.89 \tag{4.9}$$
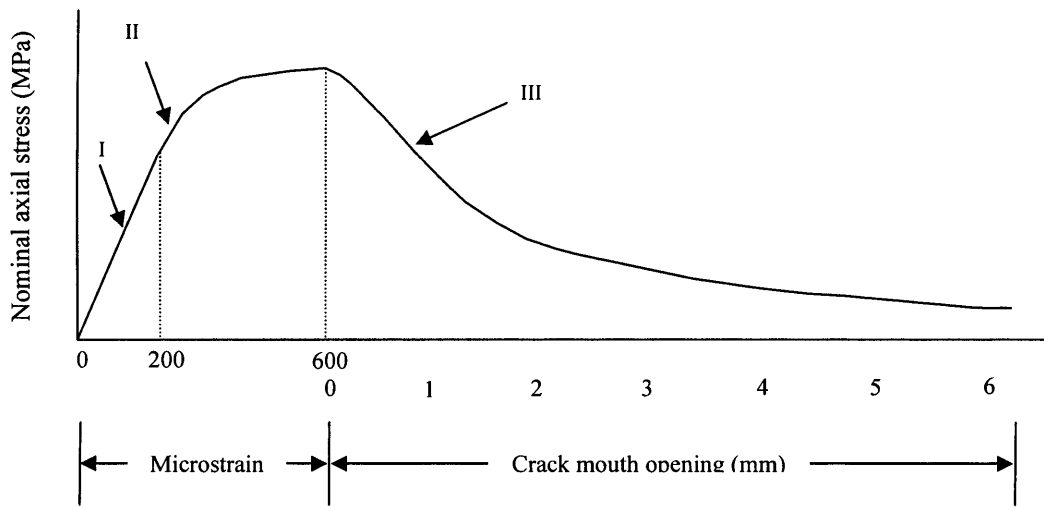
Figure 4.7 Complete pre- and post peak tensile curve for CARDIFRC®

4.7 Conclusion

As mentioned in the preceding literature review, HPFRCC materials have shown superior characteristics in terms of material properties. The mechanical and fracture properties of such materials reveal substantial improvements compared to other types of concrete mixes. Moreover, the improved and densified microstructure of these materials leads to a significant increase in their brittleness as well as the volume changes which occur during the hardening of material. However, only an insignificant improvement in the first crack strength, tensile strain capacity and peak load were observed. With the advent of special processing methods (novel mixing procedures) and the use of high volume fraction of steel fibre, concretes of high compressive, tensile strength as well as high energy absorption have been reported.

The produced material (CARDIFRC®) is characterized by strain hardening (multiple-cracking) followed by tension softening due to localization of cracks. This a new class of high performance fibre reinforced cementitious composite (designated CARDIFRC®) is an exciting durable material with great potential. In addition to the mechanical and fracture properties, Karihaloo et al. (2010) have found that superior CARDIFRC® has a very high limit of fatigue (85% of its monotonic flexural strength) without any visible cracks on the external surface. Furthermore, it was observed that using CARDIFRC® as a retrofitting material for concrete members exposed to thermal cycling enhanced the load serviceability and the stiffness of the concrete structure (Karihaloo et al., 2007). It has many potential applications and can be used for retrofitting (Alaee et al 2001; Karihaloo et al., 2001; Karihaloo et al., 2002), for durable and reliable joining of pre-cast concrete elements, for the construction of structures for the containment and retention of hazardous materials and for the protection of valuable civilian and military assets, offshore and marine structures, overlays on ordinary concrete subjected to chemical attack, water and sewerage pipes.

Chapter 5

Performance of NSC Bonded to CARDIFRC after Thermal Cycling

5.1 Introduction

This Chapter aims to investigate the effect of the thermal cycles on the mechanical properties of the normal strength of concrete and CARDIFRC® specimens and to evaluate the performance of normal strength concrete specimens retrofitted with CARDIFRC® using the wedge splitting test (WST) by investigating the interfacial fracture behavior of CARDIFRC® / concrete repair system (Tschegg, 1991). The main factors that affect the bonding between concrete and the retrofitted material will be examined (e.g. the climatic change (thermal cycles) and the roughness of the attached surfaces). The results of previous research (0, 30 and 90 thermal cycles), together with the experimental work (120 and 180 thermal cycles) conducted as a part of this research, will be discussed.

5.2 Mixing and Casting of CARDIFRC®

The CARDIFRC® mix used in this work is Mix I; the mix proportions are shown in Table 5.1. The mix was prepared according to the procedure given by Karihaloo et al. (2002). The mixing was done in a horizontal pan mixer.

Table 5.1 Mix proportions for CARDIFRC® Mix I per m³ (Karihaloo et al., 2002)

Constituents (kg)	Mix I
Cement	855
Micro-silica	214
Quartz sand: 9-300μm	470
Quartz sand: 250-600μm	470
Water	188
Super-plasticizer	28
Fibre: 6mm	390
Fibre: 13mm	78
Water/Cement ratio	0.22
Water/Binder ratio	0.18

The mixing procedure was started by adding the coarsest constituent (250-600 μm) to the micro-silica and mixed for two minutes. The second step was adding the next coarsest constituent (9-300 μm) and mixing for two minutes until a uniform distribution was achieved. In the next step, the next finest constituent (cement) was

added to the mixture and mixed for the same period. The fine sand and cement fill the gaps between the particles of the coarsest sand. In order to strengthen the mix and increase its energy absorption capacity, 13 mm and 6 mm brass coated steel fibres were added to the dry mixture. To achieve a good distribution of fibres in the mixture, these fibres were added to the mix as follows: first, 25 percent of the shorter fibres were passed through a vibrating sieve having an aperture size of 5 x 5 mm. The use of the sieve helps to separate the fibres and to avoid their clumping in the mix. The added fibres were mixed for two minutes. The next 25 percent of fibres were added and mixed. This step was repeated until all the 6 mm fibres had been added. The long fibres (13 mm) were then added in a similar stepwise manner using a 12 mm sieve.

In the last stage the mixture of water and two-thirds of the total super-plasticizer was added to the dry constituents according to the following sequence: first, one half of the mixture was added to the dry mix and mixed for two minutes; second, half of the remaining mixture was added and mixed for the same period; third, the step was repeated until the whole mixture had been added; finally, the remaining one-third of the super-plasticizer was added and mixed for three minutes. Following the mixing procedure, the mix was placed into the specimen moulds and vibrated on an electric vibration table at 50 Hz.

The specimens were divided into two groups. First, the test specimens that were needed to assess the mechanical strength of CARDIFRC® mix, i.e. compressive, tensile, flexural strengths, and modulus of elasticity, and comprised of fifteen 100x100x100 mm standard cubes, fifteen 100x200 mm cylinders, fifteen 100x100x500 mm beams, and three 150x300 mm cylinders. The second group of specimens was prepared to assess the fracture properties of CARDIFRC® mix bonded to parent concrete. It comprised of thirty six 200 x 200 x 98.5 mm half cubes (see Figure 5.1). Thereafter, the moulds were left at the room temperature for 24 hours before demoulding and placing in a hot curing tank.

5.3 Curing regime

The specimens were placed in a temperature controlled water tank and cured at $90^{\circ}C$ for 7 days. The high temperature can improve the microstructure of HPFRCC (Sullivan; 1999). It has also been found that due to this elevated temperature curing

regime, the total curing time can be reduced from 28 days to 7 days. To avoid any large thermal gradients, which will create a thermal shock, the specimens were actually left in the curing tank for 9 days. On the first day the temperature was increased gradually from 20° C to 90° C and on the last day it was decreased from 90° C to 20° C.

5.4 Normal Strength Concrete Mix

A large number of concrete mixes have been designed with different compressive strength for different grades. The NSC mix with the required compressive strength was chosen, the mix proportions that were used to prepare the test specimens in this work are cement: sand: coarse aggregate: water ratio of 1: 2: 2.5: 0.56. These ingredients were weighed and placed in plastic buckets prior to the mixing process. Cement, sand and aggregate were first mixed. Then water was added in an electrical horizontal rotating pan. After the mixing process was completed the fresh mix was transferred to the test specimen moulds.

The first group of specimens were used to determine the mechanical strength of hardened concrete, i.e. compressive, tensile, flexural strengths, and modulus of elasticity, and comprised of fifteen 100x100x100 mm standard cubes, fifteen 100x200 mm cylinders, fifteen 100x100x500 mm beams (five each for testing at 0, 120, and 180 thermal cycles), and three 150x300 mm cylinders (one each for testing at 0, 120, and 180 thermal cycles). The next group of specimens was prepared to assess the fracture properties of hardened concrete. It comprised of eighteen 200 x 200 x 200 mm cubes with a rectangular groove; they were cast in specially manufactured steel moulds for the WS test. To determine the fracture properties, half of the cubes were notched to a notch to depth ratio of 0.2 and the other half notched to a notch to depth ratio of 0.6 before they were thermally cycled and tested. The final group of specimens comprised of eighteen 200 x 200 x 98.5 mm half cubes. These half cubes were produced using 200x200x200 mm WS steel moulds partitioned with 3 mm sheet metal in the middle (Figure 5.1).

5.5 Preparation of WS bonded specimens

One day after casting of the different specimens of NSC, they were removed from the moulds and stored in a steel water tank for 28 days at 20^0C to achieve the maximum

concrete strength. Half cubes of CARDIFRC® were cast and cured as described before. After the curing stage, the contacting surfaces of the half cubes were cleaned and roughened to create a grid of grooves using an angle grinder. The grooves were approximately 3 mm deep at a spacing of 50 mm (Figure 5.1), and were now ready to be bonded together.
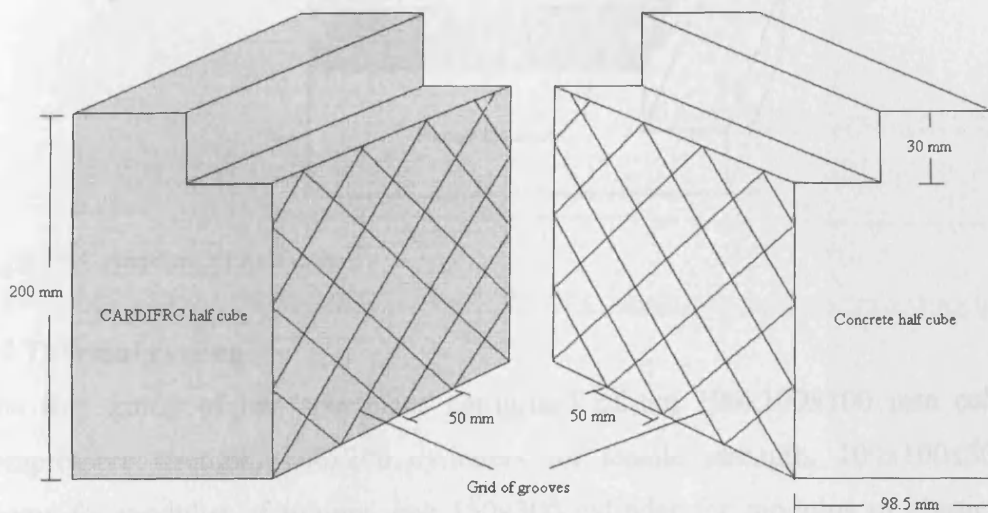
Figure 5.1 Configuration of NSC and CARDIFRC® specimens roughened and grooved surface

5.6 Bonding Process

As mentioned above, the joining surfaces of NSC and CARDIFRC® specimens were cleaned and roughened with an angle grinder to improve the bond and to create mechanical interlocking between the adhesive and the concrete. The rough, irregular and furrowed surface creates a structural morphology that allows the adhesive to penetrate into the irregularities, forming a strong interfacial layer (Farhat, 2004). The adhesive material consists of two parts which were thoroughly mixed and placed with a serrated trowel on the NSC specimen to a thickness of 3 mm, and applied also on CARDIFRC® half cube to cover the grooves. The CARDIFRC® half cube was placed on the concrete half cube and evenly pressed. Four small plastic spacers were fixed on the parent concrete to get a uniform adhesive thickness of 3 mm to complete the normal cube width 200 mm (98.5 + 98.5 + 3), see Figure 5.2. They were removed after the bonding material had hardened i.e. after approximately 3 to 4 hours. The bonded specimens were notched to a notch depth ratio 0.2 and 0.6 along the interface by a diamond saw with a blade thickness of 3 mm.

90
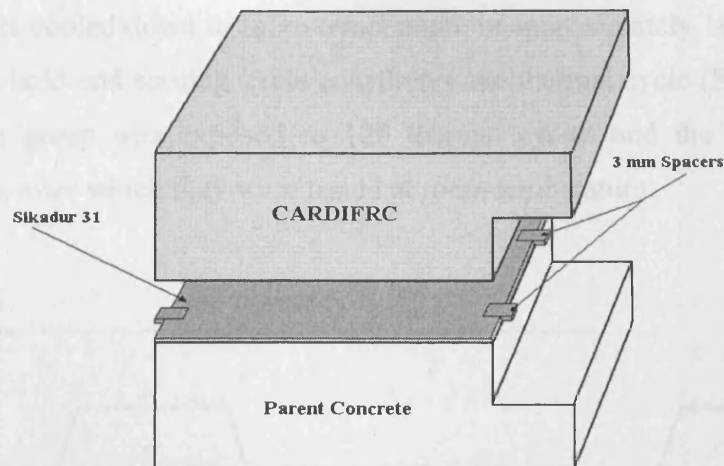
Figure 5.2 Bonding of half cubes

5.7 Thermal cycling

The first group of test specimens comprised of ten 100x100x100 mm cubes for compressive strength, 100x200 cylinders for tensile strength, 100x100x500 mm beams for modulus of rupture, one 150x300 cylinder for modulus of elasticity, six 200x200x200 mm cubes of control and CARDIFRC® bonded specimens with a notch to depth ratio of 0.2, and six 200x200x200 mm cubes of control and CARDIFRC® bonded specimens with a notch to depth ratio of 0.6. This group of specimens was not exposed to thermal cycling and was tested after the curing stage at room temperature.

The thermal cycling for NSC and CARDIFRC® specimens was conducted in two groups because of the capacity of the furnace. The second group of specimens was subjected to 120 thermal cycles and the third group to 180 thermal cycles. The second and third groups comprised of twenty 100x100x100 mm cubes for compressive strength, 100x200 mm cylinders for splitting strength, and 100x100x500 mm beams for modulus of rupture, four 150 x 300 mm cylinders for modulus of elasticity for NSC and CARDIFRC® mixes. twelve 200x200x200 mm cubes as control specimens and twelve 200x200x200 mm CARDIFRC® bonded to NSC half specimens with a notch to depth ratio of 0.2 and 0.6 for determining the fracture properties.

The specimens were placed in the electrical furnace and heated to maximum temperature of 90°C from the room temperature (about 25°C) for about 20 minutes. This was aimed to avoid any risk of the specimens being thermally shocked during

91

heating. The maximum temperature was maintained for eight hours before the specimens were cooled down to room temperature in approximately 16 hours. The 24 hours heating, hold and cooling cycle constitutes one thermal cycle (Figure 5.3). The first specimen group was exposed to 120 thermal cycles and the second to 180 thermal cycles, after which they were tested at room temperature.
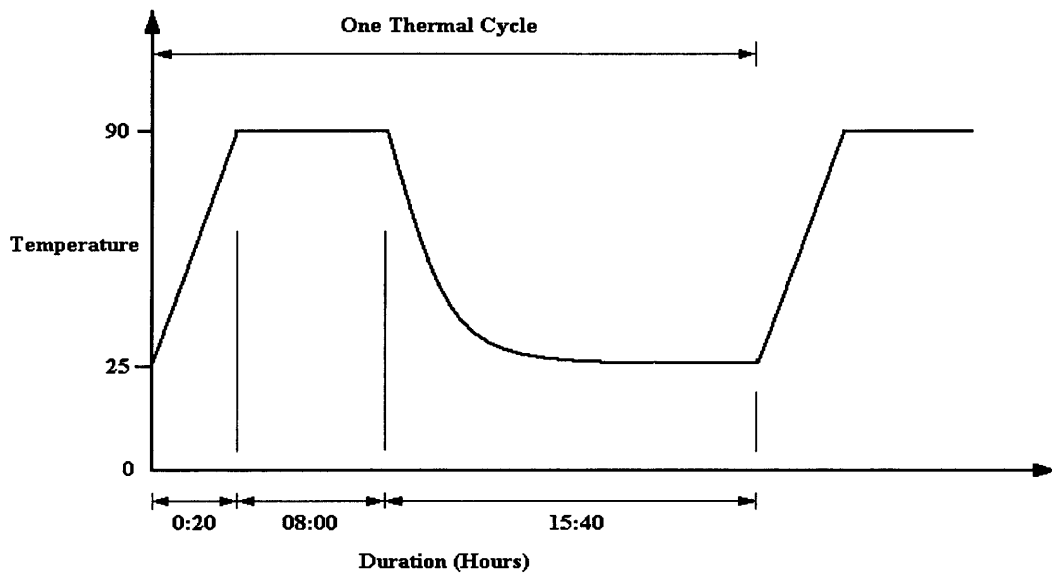
Figure 5.3 Schematic representation of the thermal cycle

5.8 Mechanical Tests

The mechanical tests were designed to evaluate the mechanical properties of normal strength concrete and CARDIFRC® specimens. The mechanical properties, namely the compressive and splitting strengths, modulus of rapture and modulus elasticity, were determined according to the relevant British Standards.

5.8.1 Compressive strength (f_c)

The compression test was performed in a FARNELL Compressive Test Machine. Fifteen 100 x 100 x 100 mm cubes of NSC and fifteen cubes of CARDIFRC® (five at 0, 120 and 180 thermal cycles each) were tested to determine the compressive strength according to BS 1881-116 1983. The test results of specimens subjected to 0, 120, and 180 thermal cycles are shown in Table 5.2a and 5.2b. The results reveal a significant increase in the compressive strength for cubes exposed to thermal cycling.

For NSC specimens, the compressive strength of 39.0 MPa at the room temperature increased to 44.2 MPa after 120 thermal cycles and then reduced slightly to 43.8 MPa after 180 thermal cycles. Thus, the total increase in the compressive strength was 12 percent after 180 thermal cycles.

The results reveal also an increase in the compressive strength f_c of CARDIFRC® cubes from198.0 MPa before heating to 206.5 MPa after 120 cycles and followed by a slight reduction to 205.0 MPa after 180 thermal cycles, giving a total increase of 3.5 percent in the compressive strength. The increase in compressive strength may be because the elevated temperatures assist further hydration (Zhang et al., 2002).

5.8.2 Splitting strength test after thermal cycles (f_t)

The splitting strength f_t of NSC specimens was determined according to BS 1881-117 1983. The test was performed also using a FARNELL Compressive Test Machine. Fifteen 100 x 200 mm cylinder specimens of each mix were tested and the splitting strength was calculated for each specimen. The specimens were placed horizontally with their axes between the machine platens with hard board strips inserted between the machine platens and the cylinders to insure that the whole length of the specimens is fully loaded. The cylinder failed by splitting along the vertical diameter and the splitting strength was determined as the follows:

$$f_t = \frac{2F}{\pi DL}$$
(5.1)

where F is the maximum failure load in (N), L is the length of the cylinder in (mm) and D is the diameter of the cylinder in (mm).

The results of the materials after thermal cycles are shown in Table 5.3a and 5.3 b. The splitting strength of NSC decreased from 3.83 MPa at room temperature to 3.5 MPa after 120 thermal cycles and a further slight decrease to reach a value of 3.4 MPa after 180 thermal cycles. Similarly, the splitting strength of CARDIFRC® specimens reduced from 32.2 MPa at zero cycles to 28.4 MPa after 120 thermal cycles with a further small decrease to 28.3 MPa after 180 thermal cycles giving a total decrease of 12 percent.

Table 5.2a The compressive strength results of NSC after 0, 120 and 180 thermal cycles

Material Type	Thermal Cycles	Specimens no.	Failure Load (kN)	Compressive Strength (MPa)	Mean compressive Strength (M Pa)	C O V %
NSC	0	1	394.7	39.4	39.0	2.3
		2	373.7	37.3		
		3	389.7	38.9		
		4	394.1	39.4		
		5	399.3	39.9		
	120	1	446.8	44.6	44.2	1.0
		2	442.0	44.2		
		3	441.8	44.1		
		4	435.5	43.5		
		5	445.1	44.5		
	180	1	433.0	43.3	43.8	1.36
		2	429.1	42.9		
		3	441.1	44.1		
		4	444.2	44.4		
		5	443.1	44.3		

Table 5.2b The compressive strength results of CARDIFRC® after 0, 120 and 180 thermal cycles

Material Type	Thermal Cycles	Specimens no.	Failure Load (kN)	Compressive Strength (MPa)	Mean compressive Strength (M Pa)	C O V %
CARDIFRC	0	1	1943	194.3	197.0	1.2
		2	1960	196.0		
		3	1993	199.3		
		4	2000	200.0		
		5	1953	195.3		
	120	1	2066	206.6	206.5	2.0
		2	2129	212.9		
		3	2073	207.3		
		4	1998	199.8		
		5	2061	206.1		
	180	1	2110	211.0	205.0	3.2
		2	2138	213.8		
		3	2019	202.0		
		4	1950	195.0		
		5	2032	203.2		

Table 5.3a The splitting strength of NSC after 0, 120 and 180 thermal cycles

Material Type	Thermal Cycles	Specimens no.	Failure Load (kN)	Splitting Strength (MPa)	Mean Splitting Strength (MPa)	C O V %
NSC	0	1	117.6	3.7		
		2	125.3	4.0		
		3	120.4	3.8	3.8	2.2
		4	118.6	3.8		
		5	119.7	3.8		
	120	1	110.3	3.5		
		2	109.2	3.4		
		3	109.5	3.5	3.5	1.0
		4	110.5	3.4		
		5	109.6	3.5		
	180	1	106.3	3.4		
		2	107.6	3.4		
		3	113.0	3.6	3.4	2.2
		4	109.4	3.5		
		5	108.3	3.4		

Table 5.3b The splitting strength of CARDIFRC® after 0, 120 and 180 thermal cycles

Material Type	Thermal Cycles	Specimens no.	Failure Load (kN)	Splitting Strength (MPa)	Mean Splitting Strength (MPa)	C O V %
CARDIFRC®	0	1	1003	31.9		
		2	998	31.8		
		3	1006	32.0	32.2	1.2
		4	1023	32.5		
		5	1029	32.8		
	120	1	898	28.6		
		2	891	28.4		
		3	903	28.7	28.4	1.6
		4	868	27.6		
		5	910	29.0		
	180	1	885	28.2		
		2	879	28.0		
		3	862	27.4	28.3	2.1
		4	917	29.2		
		5	901	28.7		

5.8.3 Modulus of rupture test after thermal cycles (MOR)

The modulus of rapture was measured according to BS 1881-118 1983 in four point bending. The test was performed in an AVERY-DENISON Type 7152 Servo-Hydraulic Testing Machine with load capacity of 600 kN. Fifteen 500 x 100 x 100 mm beams of NSC and the same number of CARDIFRC® specimens were tested. The test results are shown in Tables 5.4a and 5.4b. The maximum breaking loads were noted and the MOR was calculated as follows:

$$MOR = \frac{(F\,l)}{(d_1\,d_2^2)} \tag{5.2}$$

where F is the maximum failure load in N, d_1 and d_2 are the cross sectional dimensions of the beam in mm, and l is the distance between supports in mm.

The modulus of rapture was determined from the maximum failure load for each specimen. The results demonstrated an increase in the flexural strength for NSC from 4.6 MPa at room temperature to 7.3 MPa after 120 thermal cycles and with a further slight increase to 7.7 MPa after 180 thermal cycles. The MOR experiences a total increase of 68.2 percent. However, the results of MOR for CARDIFRC® specimens showed an increase from 37.0 MPa to 40.8 MPa after 120 thermal cycles and then a slight decrease to 38.4 MPa after 180 thermal cycles.

5.8.4 Modulus of Elasticity (E)

The modulus of elasticity of NSC and CARDIFRC® cylinders was calculated according to BS 1881-121 1983 at room temperature after the specimens were exposed to 0, 120 and 180 thermal cycles. Six 150 x 300 mm cylinder specimens for NSC and CARDIFRC were tested and the results are shown in Table 5.5.

The results show that the modulus of elasticity for NSC increases from 34.8 GPa to 35.1 GPa after 120 thermal cycles and then reduces to 32.6 GPa after 180 thermal cycles. For CARDIFRC® specimens, the modulus of elasticity increased slightly from 47.8 GPa at zero cycles to 48.3 GPa after 120 thermal cycles and then no significant effect of thermal cycling in the modulus of elasticity was observed after 180 thermal cycles.

Table 5.4a The flexural test results of NSC after 0, 120 and 180 thermal cycles

Material Type	Thermal Cycles	Specimens no.	Failure Load (kN)	MOR (MPa)	Mean MOR (MPa)	C O V %
NSC	0	1	10.4	4.0	4.6	5.0
		2	11.9	4.8		
		3	11.7	4.7		
		4	10.9	4.4		
		5	11.7	4.7		
	120	1	18.6	7.5	7.3	4.3
		2	19.4	7.8		
		3	17.9	7.3		
		4	17.3	7.0		
		5	17.5	7.1		
	180	1	21.0	8.5	7.7	5.9
		2	18.5	7.5		
		3	19.3	7.8		
		4	19.2	7.8		
		5	17.5	7.1		

Table 5.4b The flexural test results of CARDIFRC® after 0, 120 and 180 thermal cycles

Material Type	Thermal Cycles	Specimens no.	Failure Load (kN)	MOR (MPa)	Mean MOR (MPa)	C O V %
CARDIFRC®	0	1	88.8	35.9	37.0	2.8
		2	95.8	38.8		
		3	92.8	37.6		
		4	90.3	36.5		
		5	89.5	36.2		
	120	1	104.9	42.5	40.8	2.7
		2	97.5	39.5		
		3	103.0	41.7		
		4	99.8	40.4		
		5	98.7	40.0		
	180	1	96.3	39.0	38.4	4.3
		2	101.8	41.2		
		3	91.9	37.2		
		4	95.0	38.4		
		5	89.9	36.3		

Table 5.5 The effect of thermal cycling on modulus of elasticity of NSC and CARDIFRC®

Concrete Mix	E at 0 TC (GPa)	E at 120 TC (GPa)	E at 180 TC (GPa)
NSC	34.8	35.1	32.6
CARDIFRC®	47.8	48.3	48.2

The mechanical properties summarised in Table 5.6 for NSC indicate that f_c, MOR and E generally increase with the thermal cycling of the specimens because of further hydration of un-hydrated cement after 120 thermal cycles. The decrease in the strength and stiffness after 180 thermal cycles is most likely due to internal micro-cracks that were caused by thermal cycling. However, with different environmental conditions the splitting strength of NSC specimens reduced. The reduction in splitting strength is probably due to the effect of thermal cycling on the microstructure of the concrete by weakening the bond between the cement paste and the aggregate creating debonding interfacial cracks.

Table 5.6 The mechanical properties of NSC after different environmental conditions

Environmental Condition	Compressive Strength MPa	Splitting Strength MPa	Flexural Strength MPa	Modulus of Elasticity GPa
28 days at 20° C	39.0	3.8	4.6	34.8
120 days under TC	44.2	3.5	7.3	35.1
180 days under TC	43.8	3.4	7.7	32.6

5.9 Fracture tests

The fracture behaviour of control NSC specimens and NSC bonded to CARDIFRC® specimens after thermal cycling using the wedge splitting test (WST) are discussed in this section. The wedge splitting test is a very stable test which requires only a small amount of test material.

5.9.1 Test procedure

The test procedure is characterised by the simplicity of making and handling of specimens and by stable crack-growth conditions. The specimen shape, test configuration and load arrangement for control NSC specimens are shown in Figure 5.3 (see also Plates 5.1 and 5.2 for control and bonded specimens).

The control and retrofitted cube specimens 200 x 200 x 200 mm have an initial rectangular groove for the placement of two steel load transmission pieces fitted with roller bearings on either side. A steel wedge is placed between the roller bearings. A vertical force F_M on the wedge imparts a well-defined horizontal-force F_H to the bearings thus wedging open the starter crack. The test was carried out using a DARTEC closed loop machine (200 kN). The rate of loading was controlled by a crack mouth opening displacement (CMOD) gauge at a very low rate (0.0002 mm/s) so that the fracture occurred in a stable manner. During the propagation of the crack in the specimens, the deformation is measured by the crack mouth opening displacement (CMOD) along the line of application of the horizontal splitting force using this CMOD gauge. The vertical load F_M on the wedge was measured by a load cell between the wedge and the testing machine. The horizontal splitting force F_H was calculated with the aid of wedge angle θ.

$$F_H = \frac{F_M(1 - \mu \tan\theta)}{2\tan\theta(1 + \mu\cot\theta)} \approx \frac{F_M}{(1 + \mu\cot\theta)(2\tan\theta)} \tag{5.3}$$

where F_M is the vertical force on the bearings and μ is the coefficient of friction between the wedge and roller bearing. The manufacturer of roller bearings quotes μ between 0.1 and 0.5%. For $\theta = 15°$, (the half wedge angle for the WS used in this study) the contribution of $\mu \cot\theta$ in the previous expression is therefore between 0.40 and 1.9%. Therefore, F_H may be approximately expressed by

$$F_H \approx \frac{F_M}{2\tan\theta} \tag{5.4}$$

The area under the load-CMOD curve corresponds to the work done which is required to separate the specimens. Dividing this work by the fracture area or the ligament area that was intact before the test began yields the measured specific energy G_f. This value characterises the crack propagation resistance of the tested material and can be simply calculated as follows

$$G_f = \frac{1}{(W^* - a)B} \int F_H d(CMOD) \tag{5.5}$$

where, B is the specimen thickness, $W^* = W - d_n$ (see Figure 5.4c).

5.9.2 Control NSC specimens

The fracture behaviour of normal strength concrete under thermal cycling was evaluated using the WS test. Eighteen specimens with notch to depth ratios of 0.20 or 0.60 were tested at room temperature after different numbers of thermal cycles.
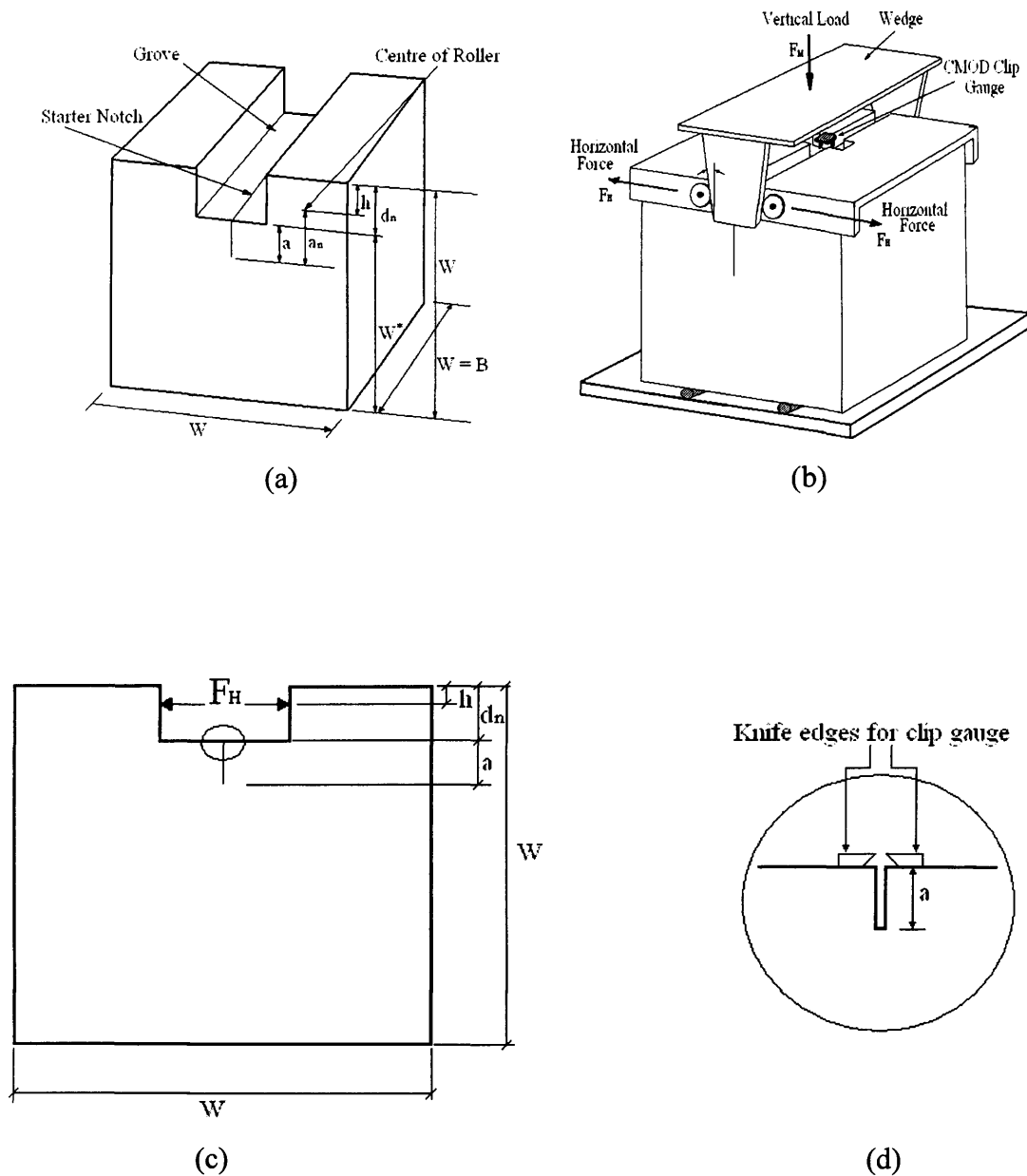
Figure 5.4 Configurations of WS test: (a) specimen shape, (b). loading arrangements, (c) the points of application of wedge force and (d) location of clip gauge for measuring CMOD
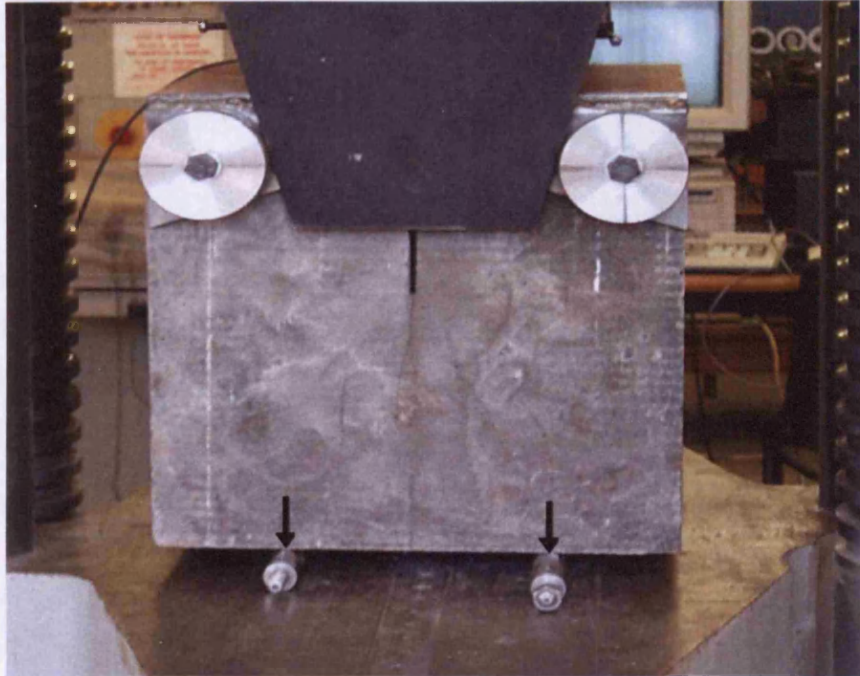
Plate 5.1 Wedge splitting test, showing the wedge mounted between two rollers bearing at each side of the specimen
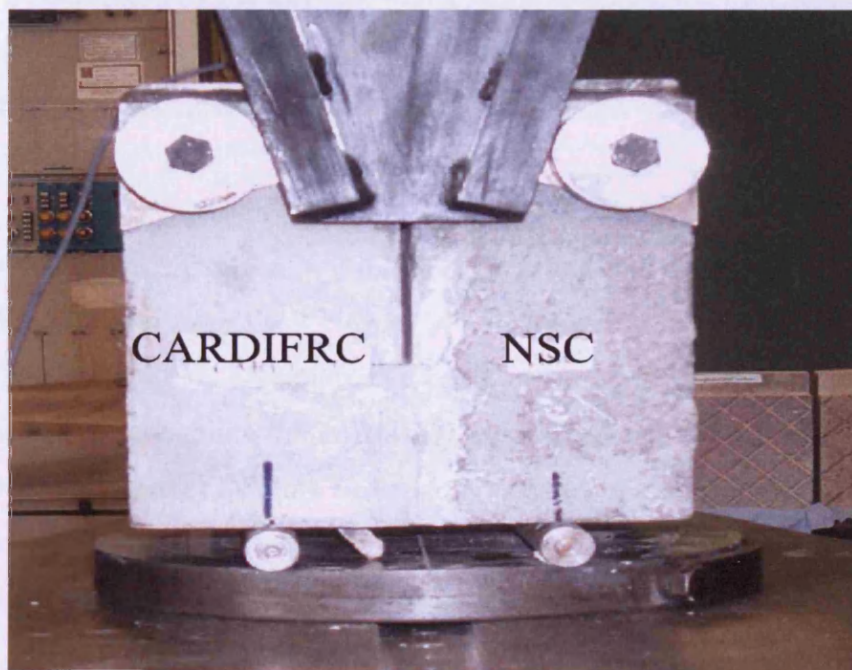
Plate 5.2 Wedge splitting test for bi-material system CARDIFRC®/NSC)

5.9.2.1 Measured fracture energy G_f

The measured specific fracture energy results for NSC specimens with the notch to depth ratios of 0.20 and 0.60 after 0, 120 and 180 thermal cycles are shown in Tables 5.7, 5.8 and 5.9, respectively. The fracture energy G_f (α) decreases as the notch to depth ratio α increases (see Figure 5.5a).

As can be seen in Table 5.7, the mean value of G_f decreases from 123.1 N/m for α = 0.20 to 116.6 N/m for α = 0.60. This is brought about by several factors. First, the propagating crack encounters resistance from more coarse aggregate particles for shorter initial notches. Second, the probability of flaws like voids, micro-cracks and bond cracks in the path of the growing crack increases with increasing ligament length (Karihaloo, 1995, and Nallathambi, 1986).

A similar trend for the variation of fracture energy with initial crack size has also been observed for test specimens after 120 and 180 thermal cycling (Figures 5.5b and 5.5c and Tables 5.8 and 5.9). It was observed that the crack path through the thickness of the NSC specimens was not straight. Moreover, it seems to be more tortuous for specimens with notch to depth ratio of 0.20. This variation in tortuosity with notch size may be explained by the fact that with a larger area available for crack extension, i.e. with small notch, the advancing crack front will encounter more coarse aggregates which are largely responsible for the tortuosity during the crack propagation (Sabir et al., 1997).

Based on the test results given in Tables 5.7, 5.8, and 5.9, after 120 thermal cycles, the G_f value increases from 123.1 N/m to 148.5 N/m for α = 0.2, and from 116.6 N/m to 134.6 N/m for α = 0.6. This may be a result of further hydration of cement paste, which gives extra strength to the interface to resist cracking. With further increase in the number of thermal cycles, the G_f value reduces to 137.2 N/m and 118.5 N/m for α = 0.2 and α = 0.6, respectively after 180 thermal cycles. The reduction could be due to the initiation of new micro-cracks at the interface.

Table 5.7 Wedge splitting test results of NSC after 0 thermal cycles

Material Type	Depth ratio	Specimens no.	Max.Load F_M (kN)	Max.Load F_H (kN)	Mean F_H (kN)	CMOD (mm)	G_f (N/m)	Mean G_f (N/m)
NSC	0.2	1	6.7	12.5	12.3	0.0384	124.3	123.1
		2	6.0	11.2	COV%	0.0845	107.3	COV%
		3	7.1	13.2	8.2	0.0405	137.8	12.4
	0.6	1	2.0	3.7	4.2	0.0514	111.4	116.6
		2	2.7	5.0	COV%	0.0782	122.6	COV%
		3	2.2	4.1	13.7	0.0591	115.7	29.7

Table 5.8 Wedge splitting test results of NSC after120 thermal cycles

Material Type	Depth Ratio	Specimens no.	Max.Load F_M (kN)	Max.Load F_H (kN)	Mean F_H (kN)	CMOD (mm)	G_f (N/m)	Mean G_f (N/m)
NSC	0.2	1	9.6	17.9	18.3	0.0537	138.7	148.5
		2	10.6	19.7	COV%	0.0584	179.6	COV%
		3	9.3	17.3	6.5	0.0383	127.2	18.5
	0.6	1	2.7	5.0	4.7	0.0958	138.8	134.6
		2	2.5	4.7	COV%	0.1559	129.9	COV%
		3	2.4	4.5	5.4	0.0958	135.0	3.3

Table 5.9 Wedge splitting test results of NSC after 180 thermal cycles

Material Type	Depth Ratio	Specimens no.	Max.Load F_M (kN)	Max.Load F_H (kN)	Mean F_H (kN)	CMOD (mm)	G_f (N/m)	Mean G_f (N/m)
NSC	0.2	1	10.6	19.7	18.1	0.0398	153.8	137.2
		2	10.0	18.6	COV%	0.0338	122.9	COV%
		3	8.7	16.2	6.5	0.0421	135.0	11.3
	0.6	1	2.4	4.5	4.7	0.0709	126.9	118.5
		2	2.5	4.7	COV%	0.0733	119.8	COV%
		3	2.7	5.0	5.2	0.0658	108.9	5.4
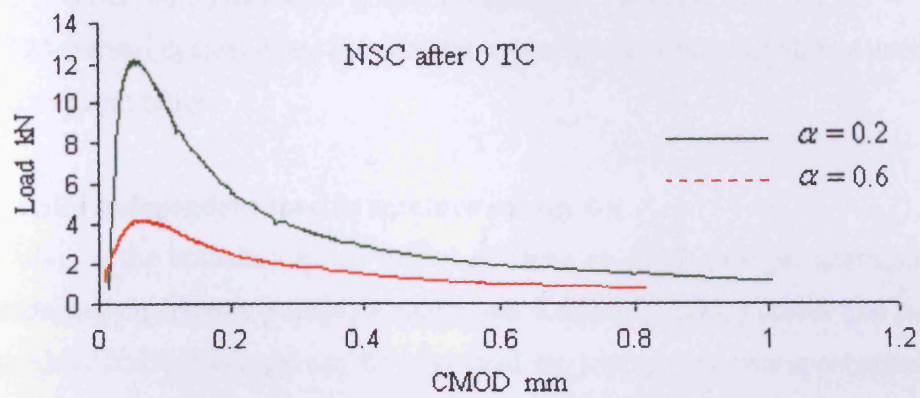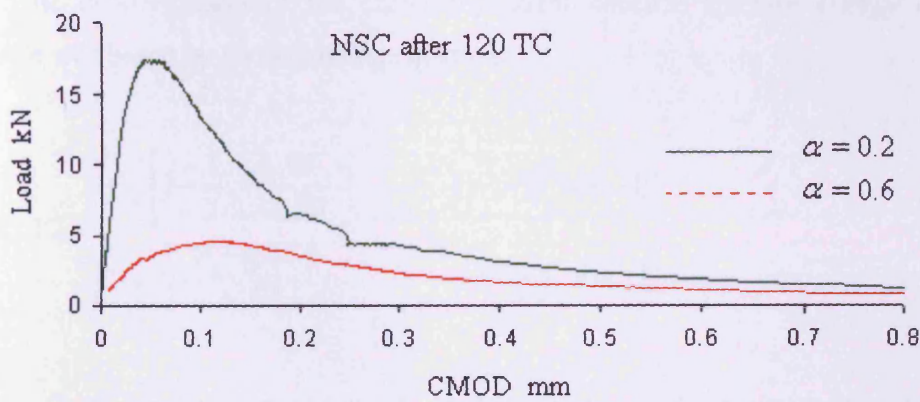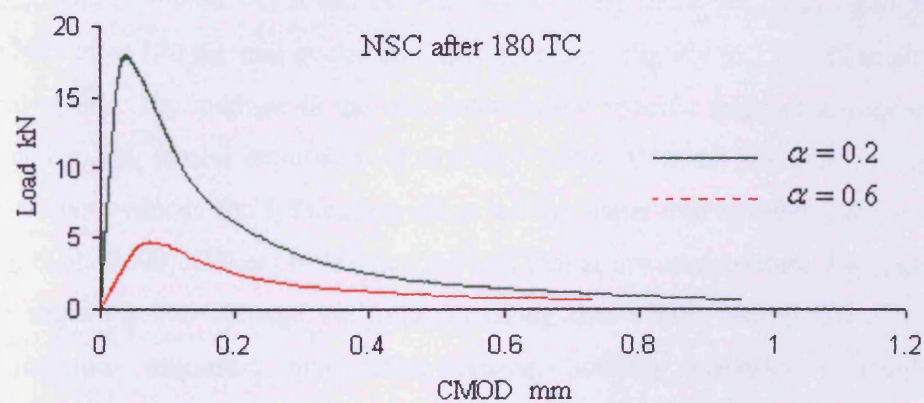
Figure 5.5 The influence of notch size on the load-CMOD curves, after: (a) zero thermal cycles (b) 120 thermal cycles (c) 180 thermal cycles

This leads to lowering the material resistance for cracking and makes it more brittle. The results also show that the maximum load for specimens with both depth ratios ($\alpha = 0.2$ and $\alpha = 0.6$) increases from 12.3 kN to 18.3 kN and from 4.2 kN to 4.7 kN after 120 thermal cycles. After 180 thermal cycles the peak remains almost unchanged with both depth ratios.

5.9.2.2 Size-independent specific fracture energy G_F

According to the boundary effect model of Duan et al. (2001) for determining the size-independent fracture energy, Abdalla and Karihaloo (2003) found that the size-independent fracture energy can be evaluated by testing just two specimens of the same size containing a shallow and deep starter notch (see § 3.6). Due to this reason the tests were conducted on WS specimens with $\alpha = 0.20$ and $\alpha = 0.60$ (Tables 5.7 to 5.9). The determination of the size-independent specific fracture energy G_F for concrete was based on the following equation:

$$G_f(a/W) = \begin{cases} G_F\left[1 - \dfrac{1}{2}\cdot\dfrac{a_l/W}{1-a/W}\right] & 1-a/W > a_l/W \\ G_F\cdot\dfrac{1}{2}\cdot\dfrac{(1-a/W)}{a_l/W} & 1-a/W \le a_l/W \end{cases} \tag{5.6}$$

Table 5.10 shows the results of the size-independent specific fracture energy G_F and transition ligament length a_l after thermal cycling obtained from the $G_f(\alpha)$ values for $\alpha = 0.20$ and $\alpha = 0.60$. As it can be seen, the G_F first increases from 129.7 N/m to 162.4 N/m after 120 thermal cycles and then decreases slightly to 155.9 N/m after 180 thermal cycles. The increase in the size-independent specific fracture energy may be attributed to the partial expulsion of capillary water. Gradual removal of capillary water further reduces the lubricating effect of the water and toughens the concrete (Zhang et al., 2000). Baker (1996) also showed that at low temperature, less than 120° C, the slight thermal damage via micro-cracking that occurs before full drying out with moisture migration and steam escape, actually provides a toughening mechanism.

The results show also that using the first of two equations (5.6) to determine G_F and a_l on the assumption that $1 - \dfrac{a}{W} > \dfrac{a_l}{W}$ is confirmed true after determining $\dfrac{a_l}{W}$ which is less than both $1 - \dfrac{a}{W}$, i.e. 0.8 and 0.4 after each thermal cycling stage.

Table 5.10 Size-independent fracture energy after 0, 120 and 180 thermal cycles

Thermal Cycles	G_F N/m	a_l mm	$\dfrac{a_l}{W}$
0 TC	129.7	16	0.08
120TC	162.4	27	0.13
180TC	155.9	38	0.19

Another factor that significantly contributes to the increase in G_F is the age of concrete specimens as pointed out by Petersson (1980). Temperature, which contributes to the hydration of the remaining unhydrated cement, densifies the cement matrix. The denser of the microstructure of normal concrete, the higher its crack resistance will be (Karihaloo, 1995). For more clarity, the measured and size – independent fracture energy for the NSC after different thermal cycles is plotted in Figure 5.6.
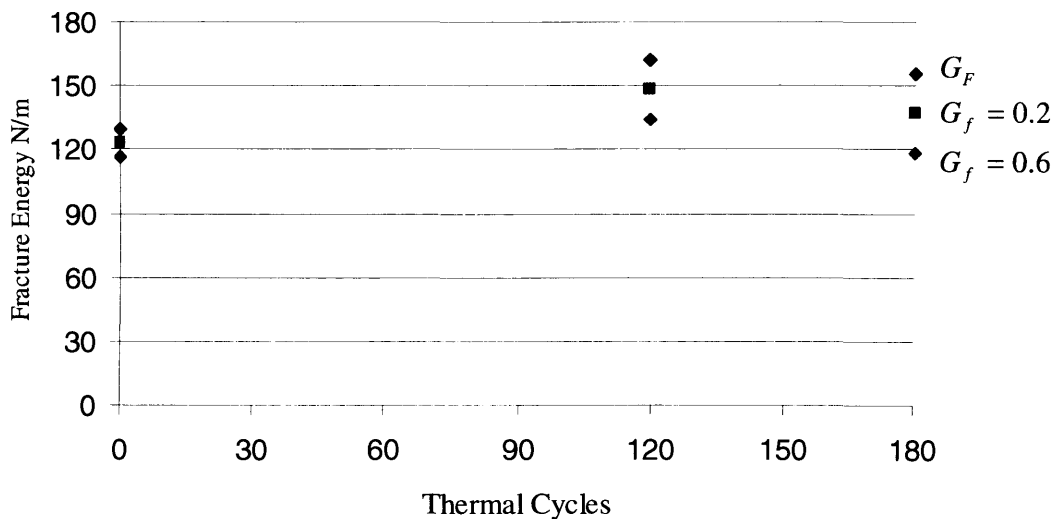
Figure 5.6 The effect of thermal cycling on measured and size-independent fracture energy of NSC

5.9.2.3 Brittleness

Brittleness is defined as the tendency for a material or structure to fracture abruptly before significant irreversible deformation occurs. Conversely, toughness characterises the capacity of structure to resist fracture. Hillerborg et al. (1976) proposed the characteristic length l_{ch} as a brittleness parameter for concrete

$$l_{ch} = \frac{G_F E_c}{f_t^2}$$

(5.7)

where f_t is the tensile strength of the concrete and G_F is the size-independent specific fracture energy. Because l_{ch} includes a combination of toughness, stiffness and strength parameters, the larger value the l_{ch} the less brittle or more ductile the concrete is. The results listed in Table 5.11 show that the characteristic length of normal concrete increases after 120 thermal cycles from 312.6 mm to 465.3 mm and then slightly reduces to 439.6 mm after 180 thermal cycles. The decrease that is observed in l_{ch} after 180 thermal cycles is mainly due to thermally induced microcracks.

Table 5.11 Characteristic length l_{ch} of NSC after 0, 120 and 180 thermal cycles

Thermal cycles	0	120	180
l_{ch} (mm)	308.1	465.3	439.6

5.9.3 CARDIFRC®/NSC bonded system

To evaluate the performance of CARDIFRC®/NSC bonded system, the WST procedure (Chapter 3) was again adopted. This section presents the test results of CARDIFRC® bonded to NSC specimens using the WS test (Tschegg and Stanzel, 1991). The fracture behaviour of CARDIFRC®/concrete bonded system was investigated, and the main factors that affect the bond properties of interfaces, such as the roughness of the mating surfaces and thermal cycling have been evaluated. The WS test was performed in a similar manner to that of NSC (see Figure 5.7).
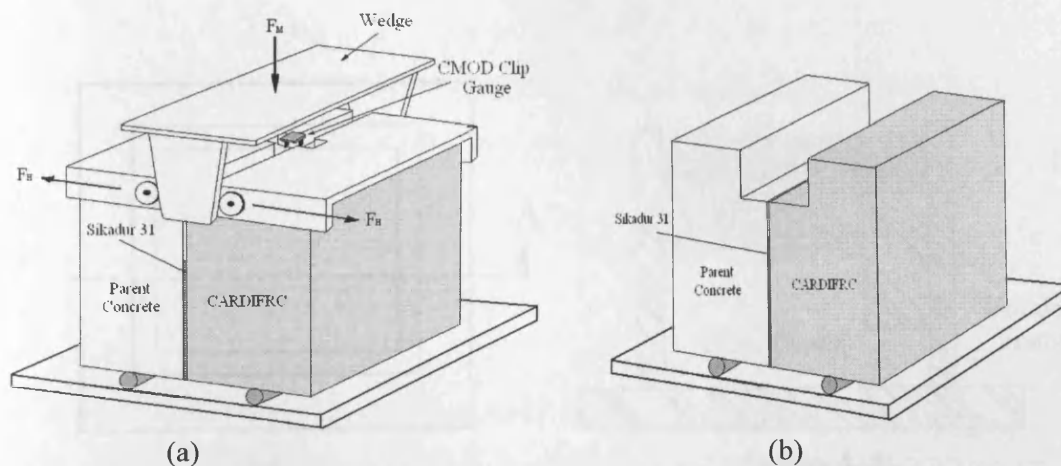
Figure 5.7 Configuration of bonded specimens: (a) Loading arrangements and (b) wedge splitting specimen of bonded system

5.9.3.1 Direct wet casting

The casting of wet CARDIFRC® directly on to NSC has been explored previously but the results showed that the bond between the two materials (CARDIFRC® / NSC) (Farhat, 2004) was very weak. The specimens split apart when the applied load was still in the elastic stage. This is a result of the casting configuration whereby the specimens are cast horizontally and thus no mechanical interlocking had been achieved (Figure 5.8).Our results confirm those of Farhat (2004), namely that the crack goes straight through the interface with a slight kink into the normal concrete half of the specimens. It was found by inspection that more than 30 percent of the failure occurred in the normal strength concrete and the remainder in the interface, so that the maximum load and fracture energy for the bonded specimens is lower than those of the NSC control specimens (see Table 5.12)

Table 5.12a NSC control specimens compared with bonded specimens (direct casting)

	Specimens	Max Load (kN)	Average load (kN)	CMOD (mm)	G_f (N/m)	Average G_f (N/m)	Failure Location
Bonded	1	4.9	5.0	0.032	26.0	27.0	I/C
	2	5.1		0.02	28.0		I/C
Control	1	6.1	6.1	-	95.6	95.6	C

I/C Crack starts at the interface and propagates slightly into concrete.
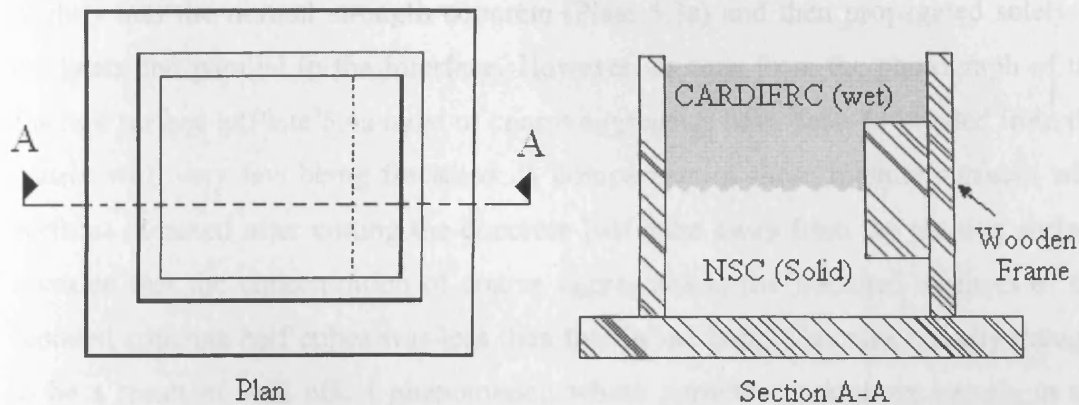
Figure 5.8 Direct casting technique

5.9.3.2 Adhesive bonding

The WS test results for normal strength concrete half cubes adhesively bonded to CARDIFRC® half cube show that there are no signs of interfacial fracture or delamination either at the interface between the adhesive and the parent concrete or between the CARDIFRC® and the adhesive. Generally, in the bonded specimens the crack always propagated in the parent concrete after initiating at the starter notch corner and kinking towards the parent concrete. However, in some specimens failure propagated along the interface, but this was found to be as a result of inadequate preparation of the mating surfaces.

5.9.3.2.1 Influence of surface preparation

The following sections highlight the influence of surface preparation of both parent concrete and the repair material.

5.9.3.2.1.1 Repair material (CARDIFRC®)

In order to enhance mechanical interlocking with the adhesive, it was decided to slightly roughen the mating surface of the CARDIFRC® half cube with an angle grinder. The tests showed that the surface roughening of CARDIFRC®, and not only the parent concrete, is very important to prevent abrupt delamination failure (Farhat, 2004).

5.9.3.2.1.2 Parent concrete

The results showed that a crack emanated from a starter notch corner and kinked slightly into the normal strength concrete (Plate 5.3a) and then propagated solely in the latter and parallel to the interface. However, as seen from the photograph of the fracture surface in Plate 5.4a most of coarse aggregates have been de-bonded from the matrix with very few being fractured. A comparison of these fracture surfaces with surfaces obtained after cutting the concrete half cube away from the matting surface revealed that the concentration of coarse aggregates in the fractured surfaces of the repaired concrete half cubes was less than that in the bulk. This was initially thought to be a result of wall effect phenomenon where particles pack more loosely in the immediate vicinity of a mould wall than away from it (Farhat, 2004).

5.9.3.2.1.3 Surface improvement

To overcome the aforementioned problem, it was proposed to improve the bonding technique in order to achieve a more ductile and stronger bonded system. Since the previous results recorded that a crack emanating from a starter notch corner always propagated in the region of the parent concrete adjacent to the interface, it was likely that a thin cement film formed there during casting. Therefore, it was decided to remove this film from the bonding surface of the concrete specimens with a grinder until the aggregate became visible before applying the adhesive to it.

This additional surface preparation of the mating surfaces of the concrete half cubes was undertaken before bonding them to CARDIFRC® half cubes. Therefore, to remove any trapped air, CARDIFRC® half cube was slightly pressed on to the adhesive. The influence of the additional surface preparation on the fracture behaviour was investigated by Farhat (2004) and the results are shown in Table 5.12. As seen from Plate 5.3b the crack emanating from the starter notch corner kinked towards the concrete with a kink angle of about $10°$ to $20°$ and then propagated in the concrete close to the interface. It is clear that both the maximum load and fracture energy increased substantially after the removal of cement film and the fracture surfaces of complete specimens exhibited higher irregularity (Plat 5.4b). As seen from the test results, it was concluded that the removal of the thin film layer of cement paste from the joining surface of the NSC (parent concrete) is essential to obtain a strong and tough repairing system.

(a)   (b)
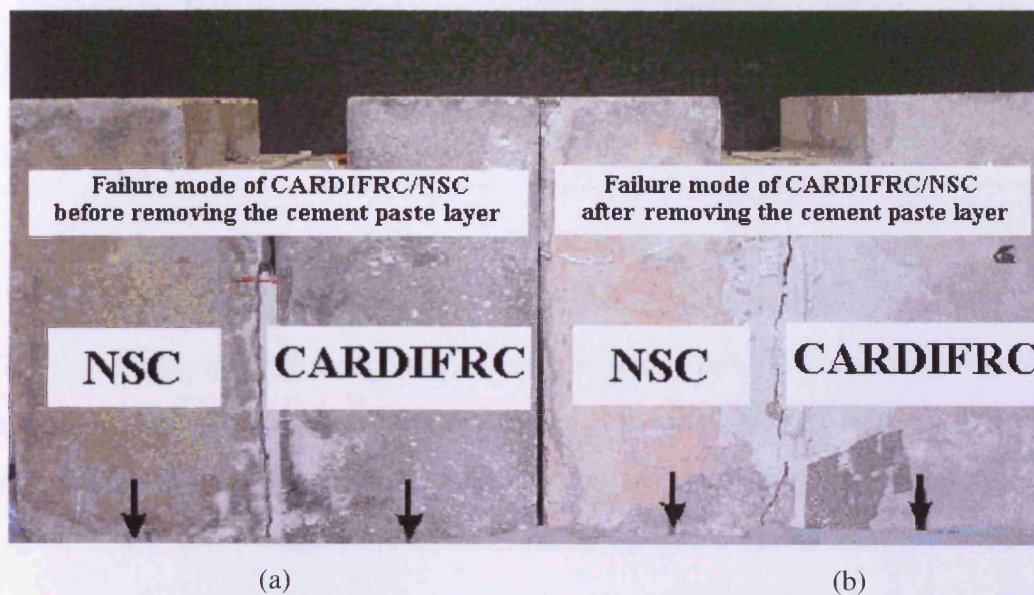
Plate 5.3 The effect of cement paste film on the failure mode of CARDIFRC®/NSC, (a) before, (b) after removal of film

(a)   (b)
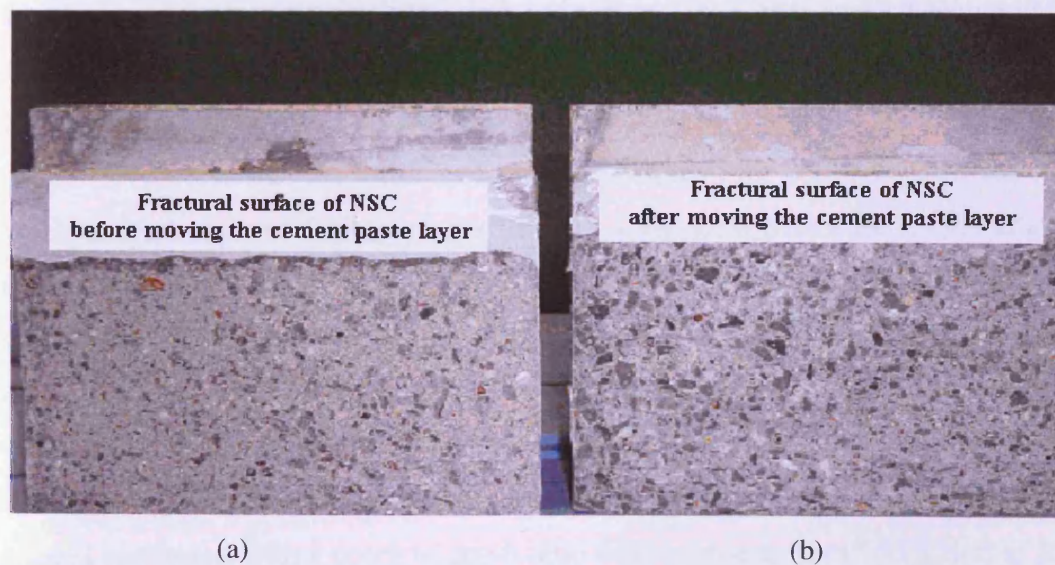
Plate 5.4 The effect of cement paste film on the fractured surface of CARDIFRC®/NSC: (a) before, (b) after removal of film.

Table 5.13 WS test results of NSC adhesively bonded to CARDIFRC®

Type of specimens	Specimens	Max. Load	CMOD	Failure location	G_f (N/m)
Bonded	Before removing the cement paste film	10.0	0.025	CF	39.0
	After removing the cement paste film	13.5	0.045	NSC	94.0
Control	-	11.4	0.050	-	98.0

5.9.3.2.2 Effect of thermal cycling

The test results of NSC bonded specimens exposed only to room temperature are shown in Table 5.13. The results reveal that the crack started at the starter notch corner and propagated in the parent concrete at an angle of 13° to 19° for $\alpha = 0.20$, and 10° to 15° for $\alpha = 0.60$. Visual observation showed a variation of fracture energy measurements $G_f(\alpha)$ with the notch of depth ratios of 0.20 and 0.60 similar to the WS test of control specimens (Figure 5.9a).

The specific fracture energy and the maximum load of bonded specimens revealed a decrease with increasing notch to depth ratio from 100.3 N/m to 87.9 N/m and from 15.5 kN to 4.1 kN. This behaviour was observed in all of NSC specimens bonded to CARDIFRC® exposed to 120 and 180 thermal cycling (Figures 5.9b and 5.9c). The results reveal also that the mean value of the peak load for bonded specimens with a notch to depth ratio of 0.20 increases from 15.5 kN for 0 cycles to17.3 kN after 120 thermal cycles and then drops to 13.9 kN after 180 thermal cycles, giving a total decrease of 10 percent. The results showed that NSC bonded specimens behaved as the control NSC specimens.

Tables 5.14, 5.15 and 5.16 also show that the measured fracture energy G_f for NSC bonded specimens with a notch to depth ratio 0.20 increases from 100.3 N/m to 150.8 N/m after 120 thermal cycles, thereafter, the G_f decreases to 134.0 N/m after 180 thermal cycles. Similar behavior was also observed in bonded specimens with a notch to depth ratio 0.60 and those of control specimens exposed to the same number of thermal cycles.

Table 5.14 WS results of CARDIFRC® / NSC after 0 thermal cycles

Material Type	Depth Ratio	Specimens no.	Max.Load F_M (kN)	Max.Load F_H (kN)	Mean F_H (kN)	CMOD (mm)	G_f (N/m)	Mean G_f (N/m)
NSC bonded to CARDIFRC	0.2	1	8.5	15.8	15.5	0.0279	95.8	100.3
		2	8.4	15.6	Cov%	0.0336	98.7	Cov%
		3	8.1	15.1	2.3	0.0381	106.5	5.5
	0.6	1	2.2	4.1	4.1	0.0527	82.8	87.9
		2	2.2	4.1	Cov%	0.0734	101.0	Cov%
		3	2.3	4.3	3.7	0.0565	80.1	12.9

Table 5.15 WS results of CARDIFRC® / NSC after 120 thermal cycles

Material Type	Depth Ratio	Specimens no.	Max. Load F_M (kN)	Max. Load F_H (kN)	Mean F_H (kN)	CMOD (mm)	G_f (N/m)	Mean G_f (N/m)
NSC bonded to CARDIFRC	0.2	1	9.9	18.4	17.3	0.0361	143.2	150.8
		2	9.0	16.8	COV%	0.0389	139.6	COV%
		3	9.0	16.8	5.5	0.0534	169.6	10.8
	0.6	1	2.8	5.2	5.4	0.1045	139.3	133.1
		2	2.7	5.0	COV%	0.0937	123.0	COV%
		3	3.2	6.0	9.8	0.1051	137.1	6.6

Table 5.16 WS results of CARDIFRC® / NSC after 180 thermal cycles

Material Type	Depth Ratio	Specimens no.	Max. Load F_M (kN)	Max.Load F_H (kN)	Mean F_H (kN)	CMOD (mm)	G_f (N/m)	Mean G_f (N/m)
NSC bonded to CARDIFRC	0.2	1	8.1	15.1	13.9	0.0651	139.2	134.0
		2	7.3	13.6	COV%	0.1092	129.5	COV%
		3	7.0	13.1	6.9	0.0507	133.4	3.6
	0.6	1	2.4	4.5	3.9	0.0912	118.9	115.8
		2	2.1	3.9	COV%	0.1029	119.8	COV%
		3	2.1	3.9	8.3	0.0834	108.9	5.2

NSC with CARDIFRC after 0 TC

(a)

NSC with CARDIRC after120 TC

(b)

NSC with CARDIFRC after 180 TC
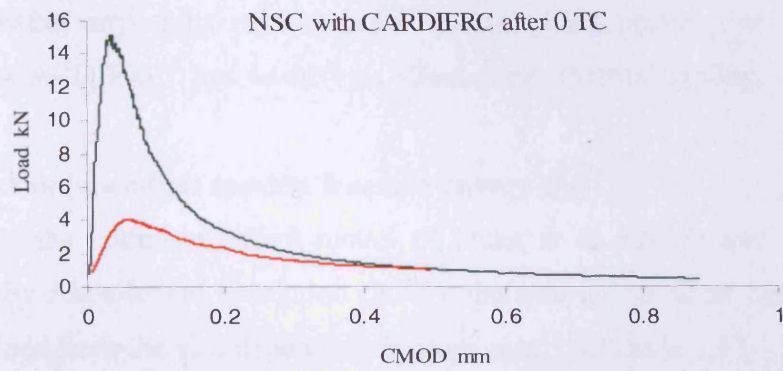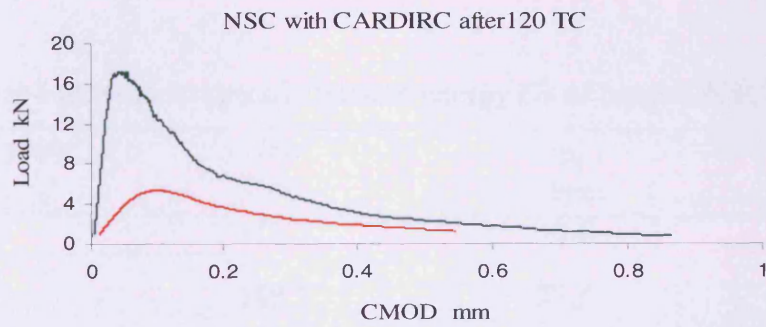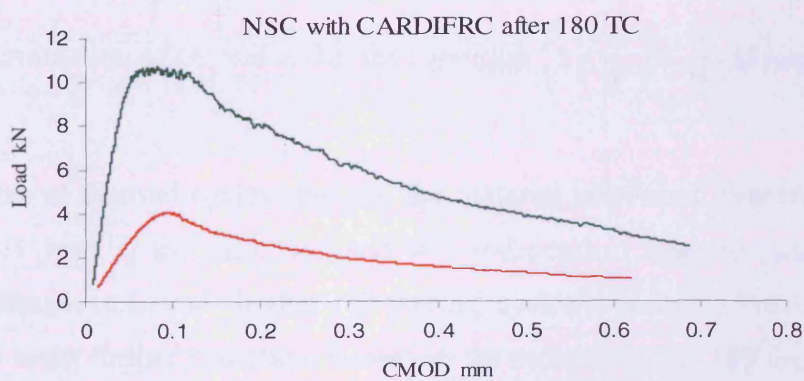
(c)

Figure 5.9 The affect of notch size on the load – CMOD curves of bonded NSC specimens, after; (a) zero thermal cycles, (b) 120 thermal cycles and (c) 180 thermal cycles

114

Generally, the results show that there is no significant effect caused by the thermal cycling on the failure mode; all failures took place in the NSC (parent concrete) without showing any signs of interfacial fracture. This proves that the repairing system with CARDIFRC® has no adverse effect due to thermal cycling.

5.9.3.2.3 Size-independent specific fracture energy G_F

According to the boundary effect model of Duan et al. (2001) and its additional verification by Abdalla and Karihaloo (2003), the size independent specific fracture energy obtained from the size dependent fracture energies (Table 5.13 – Table 5.15) is given in Table 5.17. It can be seen that the size independent fracture energy of bonded specimens increases from 112.7N/m at room temperature to 168.5 N/m after 120 thermal cycles and then decreases to 152.2 N/m after 180 thermal cycles.

Table 5.17 Size-independent specific fracture energy G_F of bonded NSC specimens

Thermal Cycles	G_F N/m	a_l mm	$\dfrac{a_l}{W}$
0 TC	112.7	35.0	0.18
120TC	168.5	33.5	0.17
180TC	152.2	38.2	0.19

Again, the first of the two equations (5.6) has been used and it has been confirmed after the determination of G_F and a_l that the condition $\left(1 - \dfrac{a}{W}\right) < \dfrac{a_l}{W}$ is indeed satisfied.

As the number of thermal cycles changes, the material behaviour also changes. This can be clearly seen in the measured and size independent fracture energy (Figure 5.10). The increase in G_f and G_F after 120 thermal cycles is probably because elevated temperatures assist further hydration. However, the reduction after 180 thermal cycles is due to the stress generated at the interface between the aggregate and the hardened cement paste which allow initiation of more microcracks (Farhat, 2004).
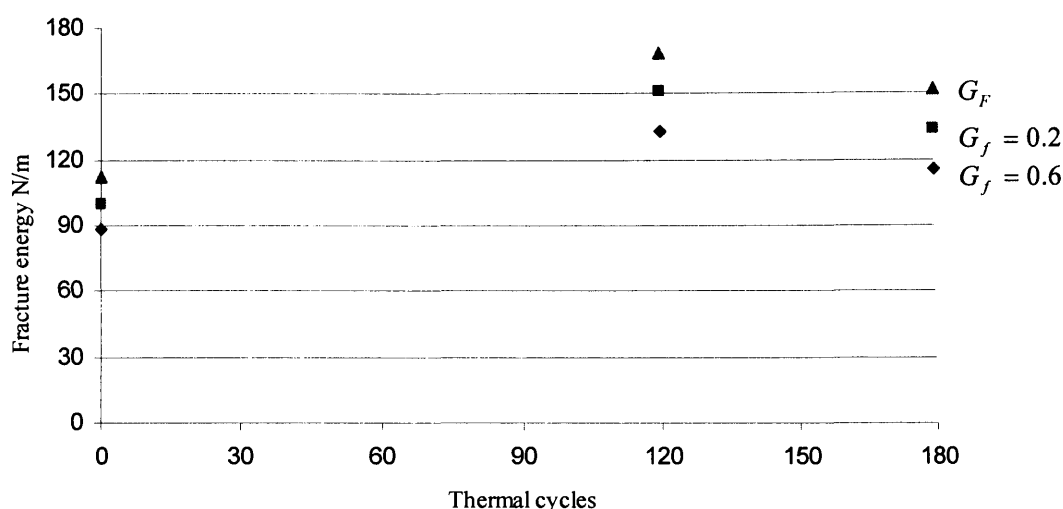
Figure 5.10 The effect of thermal cycling on measured and size independent fracture energy of CARDIFRC® / NSC bonded system

5.10 Comparison of the results

5.10.1 Specimens exposed to 0 thermal cycles

Both control and bonded specimens test results show clearly that the failure took place in the normal strength concrete, and the fracture mode is quasi-brittle. The load-CMOD curves for control and bonded specimens for $\alpha = 0.20$ and $\alpha = 0.60$ after 0 thermal cycles shown in Figures 5.11a and 5.12a reveal as expected, that the stiffness and the maximum load for bonded specimens with a notch to depth ratio of 0.20 increases compared to the control specimens and the mean value of the maximum load for bonded specimens is 15.5 kN, whereas it is only 12.3 kN for control specimens. Therefore, a total increase in the mean value of the maximum load of bonded specimens for $\alpha = 0.20$ is 26 percent (see Table 5.18). For specimens with depth ratio of 0.60, the mean value of the maximum load seems to remain unchanged.

5.10.2 Specimens exposed to 120 thermal cycles

The topical load-CMOD curves for both control and bonded NSC specimens for $\alpha = 0.20$ $\alpha = 0.60$ after 120 thermal cycles are plotted in Figures 5.11b and 5.12b. As can be seen, the maximum failure load for bonded and control specimens with a notch to depth of 0.20 is nearly the same but the mean value of maximum failure load for $\alpha = 0.60$ increases slightly from 4.7 kN for control specimens to 5.4 kN for CARDIFRC® bonded specimens, giving a total increase of 12 percent (see Table 5.17).

116

5.10.3 Specimens exposed to 180 thermal cycles

Figures 5.11c and 5.12c show the load-CMOD curves for control and CARDIFRC®
bonded specimens with a notch to depth ratio of 0.20 and 0.6 respectively. It can be
seen that the maximum failure load decreases from 18.1 kN for the control specimens
to 13.9 kN for the bonded one, giving an decrease in the maximum load of 23 percent.
Similarly, the mean values of the maximum load for control and bonded specimens
with depth ratio 0.60 are reduced from 4.7 kN for control specimens to 3.9 kN for
bonded one.

Generally, the results indicate that the bonded specimens are somewhat stronger
compared with the control one at room temperature. The bonding of NSC with
CARDIFRC® system reveal that the peak load has improved, the pre-peak non-
linearity reduced and the post-peak behavior is steeper However, after 120 and 180
thermal cycles, the strength of bonded specimens decreased slightly for both notch to
depth ratios 0.20 and 0.60 (Table 5.18). It was also found that the fracture energy
value G_f decreases compared with control specimens. The reduction of G_f value could
be due to fact that the crack path in such bonded specimens is less tortuous than that
in the control specimens.

Table 5.18 The effect of thermal cycling on failure load of control and repairing NSC
specimens

Number of thermal cycles	The mean of maximum failure load (kN)				Increases / Decrease in failure load of bonded relative to control (%)	
	Control specimens		Bonded specimens			
	0.2	0.6	0.2	0.6	0.2	0.6
0	12.34	4.30	15.55	4.15	26.01	-3.48
120	18.35	4.75	17.31	5.34	-5.66	12.42
180	18.18	4.75	13.94	4.15	-23.32	-12.63
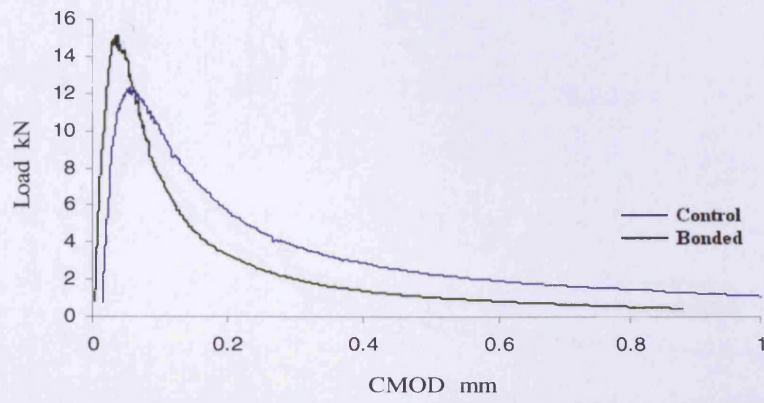
(a)
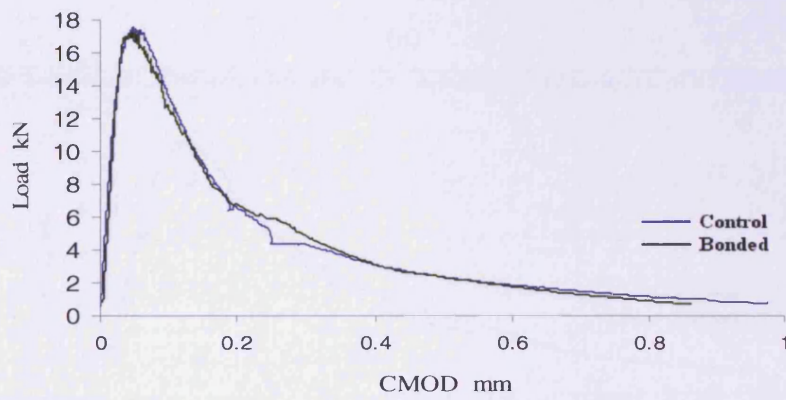
(b)
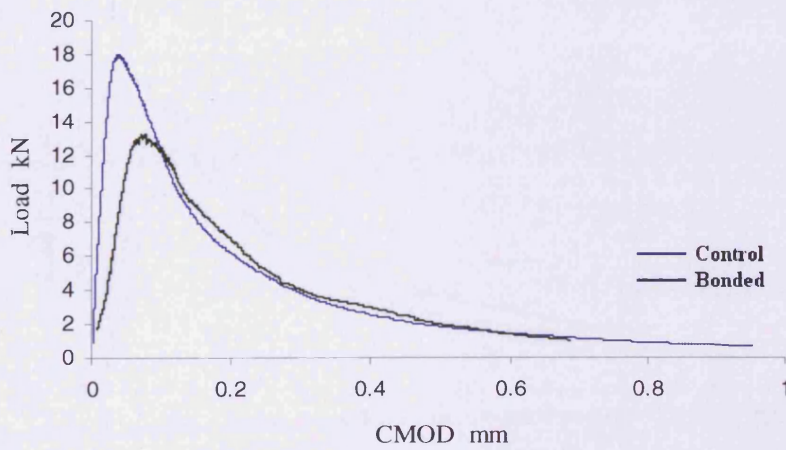
(c)

Figure 5.11 Load-CMOD curves for control and bonded NSC specimens with α = 0.20, after; (a) zero thermal cycles, (b) 120 thermal cycles and (c) 180 thermal cycles
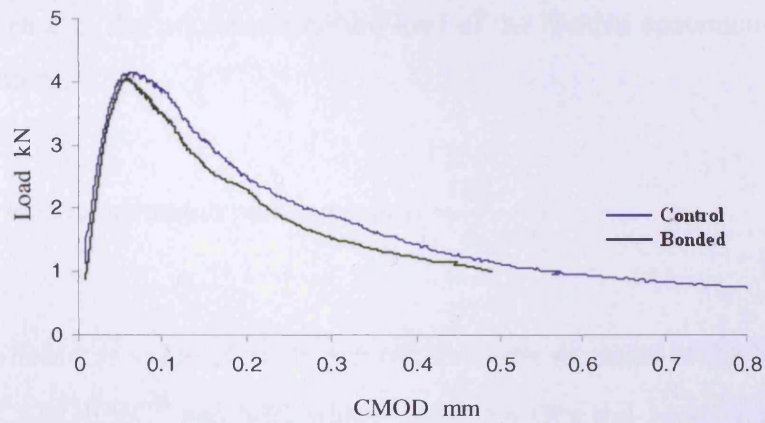
(a)
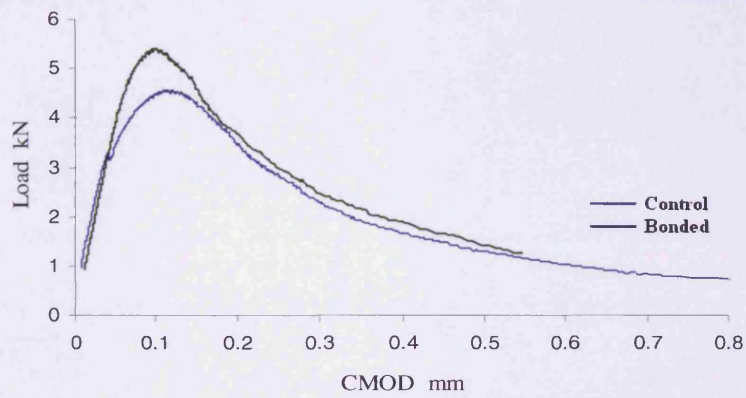
(b)
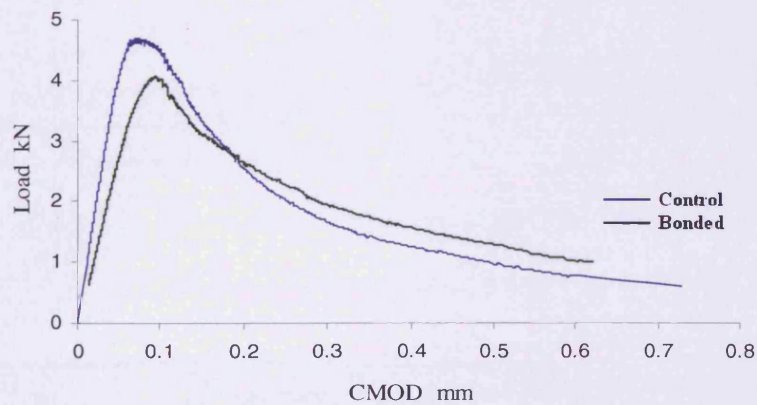
(c)

Figure 5.12 Load-CMOD curves for control and bonded NSC specimens with α = 0.60, after; (a) zero thermal cycles, (b) 120 thermal cycles and (c) 180 thermal cycles

Following Farhat (2004) steps that were used in the LEFM analysis of the bi-material system were discussed in Chapter 3. A simple explanation is provided here for the observed increase in the maximum failure load of the bonded specimens over that of control specimens.

The Dundurs elastic mismatch parameter is $\alpha = \dfrac{E_1 - E_2}{E_1 + E_2}$ (5.8)

where, α the measures value of mismatch of the elastic modulus of the bimaterials ,E_1 and E_2 for CARDIFRC$^®$ and NSC which equal 47.8 GPa and 34.81 GPa, respectively. With $\alpha = 0.20$ and the second Dundurs parameter β is $\approx$ zero. Substituting β in equation (3.38) gives (with subscript "*com*" referring to the campanile)

$$G_{com} = \frac{1}{E_*} k_*^2$$ (5.9)

where

$$\frac{1}{E_*} = \frac{1}{2}\left(\frac{1}{E_1} + \frac{1}{E_2}\right)$$ (5.10)

Since $E_* = E_{Com}$ and E_1 and E_2 are equal to E_{NSC} and $E_{CARDIFRC}$

$$G_{com} = \frac{1}{2}\left(\frac{1}{E_{NSC}} + \frac{1}{E_{CARDIFRC}}\right) k_*^2$$ (5.11)

Thus

$$k_* = \sqrt{\frac{2G_{com}}{\dfrac{1}{E_{NSC}} + \dfrac{1}{E_{CARDIFRC}}}} = \sqrt{\frac{2G_{com}\, E_{NSC}\, E_{CARDIFRC}}{\left(E_{CARDIFRC} + E_{NSC}\right)}}$$ (5.12)

Since G_F of NSC is roughly equal to G_{com} and k_I of NSC is equal to $\sqrt{E_{NSC}G_F}$, at the same level of applied k_I, the ratio $\sqrt{2E_{CARDIFRC}/(E_{CARDIFRC} + E_{NSC})}$ is given below (Table 5.19).

Table 5.19 The value of ($\sqrt{(2E_{CARDIFRC})/(E_{CARDIFRC} + E_{NSC})}$) compares with the number of thermal cycles

Thermal cycles	0 TC	30 TC	90 TC	120 TC	180 TC
$\sqrt{\dfrac{2E_{CARDIFRC}}{E_{CARDIFRC} + E_{NSC}}}$	1.1	1.08	1.08	1.07	1.09

As a result, it follows from (5.12)

$$k_* > k_I$$

This means that the maximum load level corresponding to the initiation of crack growth must be larger in the bonded system ($P_{* max}$) than solid NSC (P_{max}).

5.11 Influence of increased thermal cycling on NSC and CARDIFRC®

5.11.1 Mechanical properties

This section summarizes the effect of increased thermal cycling on the mechanical properties of NSC and CARDIFRC®, including previous results (0, 30, and 90 thermal cycles), together with the results reported above. The summary is shown in Figures 5.13, 5.14 and Table 5.19. It can be seen the compressive and splitting strengths of NSC show a slight change with the number of thermal cycles but the values do not drop below that at room temperature even after 180 thermal cycles. However, MOR of NSC reveals a further increase with the thermal cycling. The modulus of elasticity on the other hand can be regarded as practically unchanged.

The specimens of CARDIFRC® behaved similar to those of NSC specimens after the different thermal cycles (Figure 5.14). The results reveal that all mechanical properties of CARDIFRC® followed the same trend that was observed in the mechanical properties of NSC.
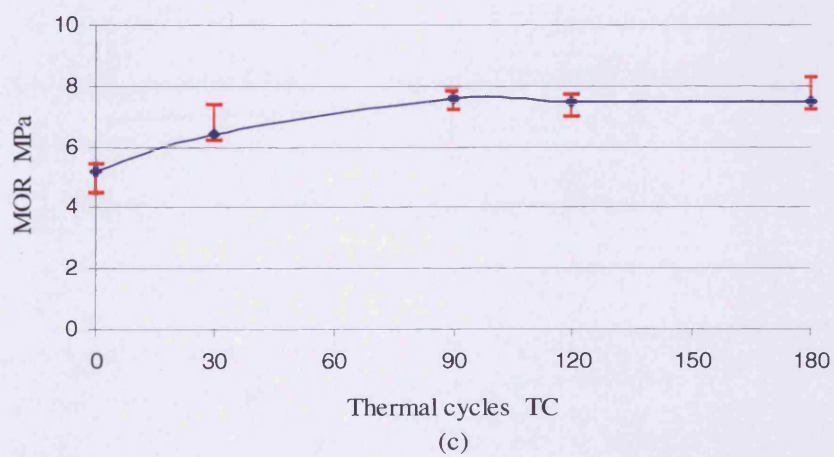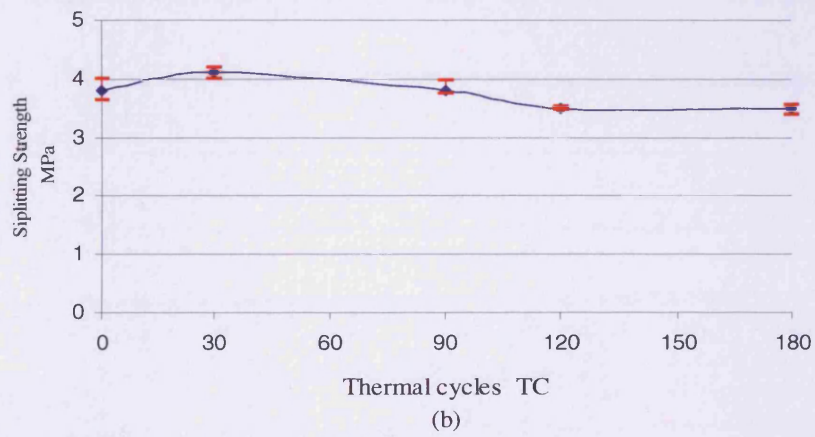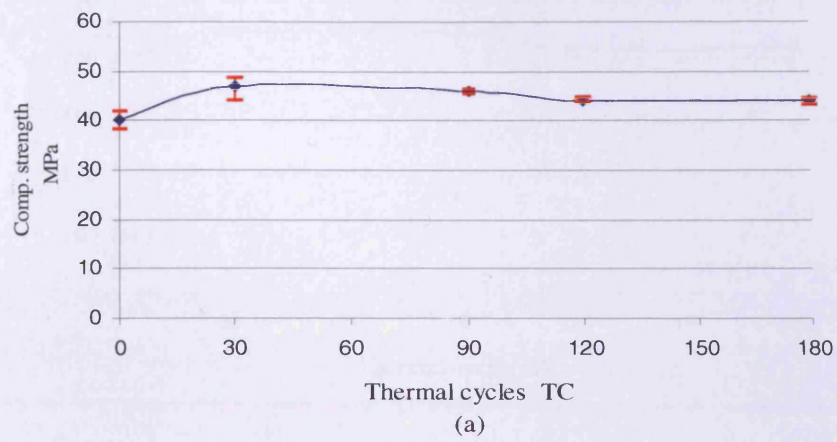
Figure 5.13 Influence of thermal cycling on (a) the compressive strength of NSC (b) the splitting strength of NSC (c) the modulus of rapture of NSC

122
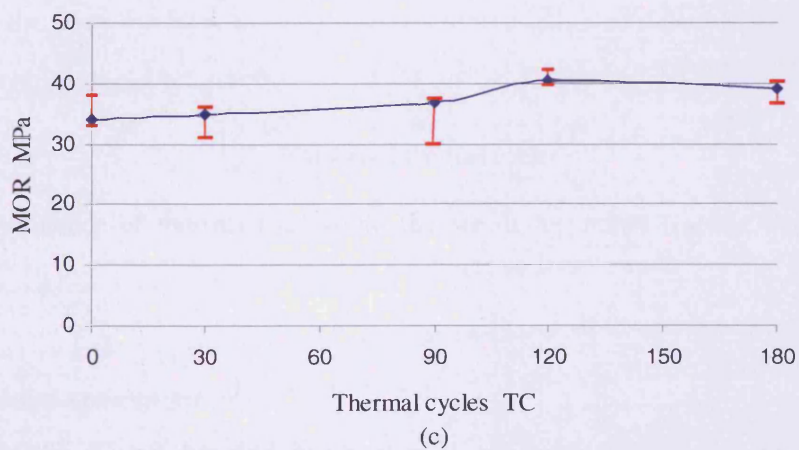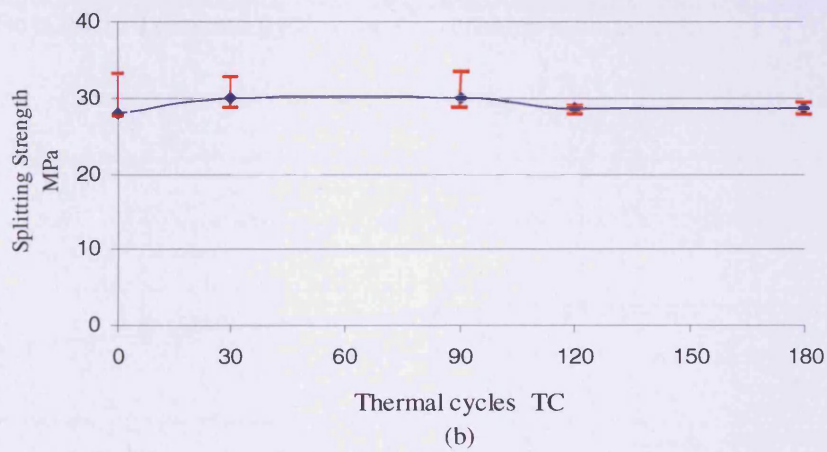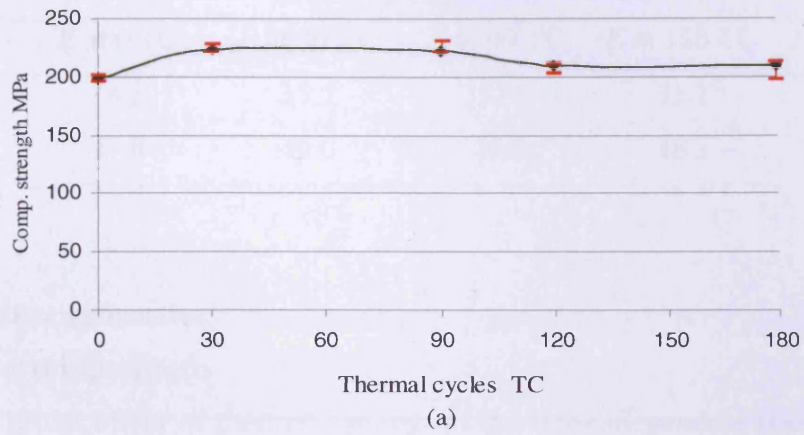
Figure 5.14 Influence of thermal cycling on (a) the compressive strength of CARDIFRC® (b) the splitting strength of CARDIFRC® (c) the modulus of rapture of CARDIFRC®

123

Table 5.20 The influence of thermal cycling on the modulus of elasticity of NSC and CARDIFRC®

Mix type	E at 0 TC	E at 30 TC	E at 90 TC	E at 120 TC	E at 180 TC
NSC	34.8	35.2	35.50	35.1	32.6
CARDIFRC	47.8	49.0	49.0	48.3	48.2

5.11.2 Fracture properties

5.11.2.1 Control specimens

The results of the effect of thermal cycling on the size-independent fracture energy are shown in Figure 5.15. As the number of thermal cycles increases the G_F value increases. Beyond 120 thermal cycles the G_F remains unchanged.
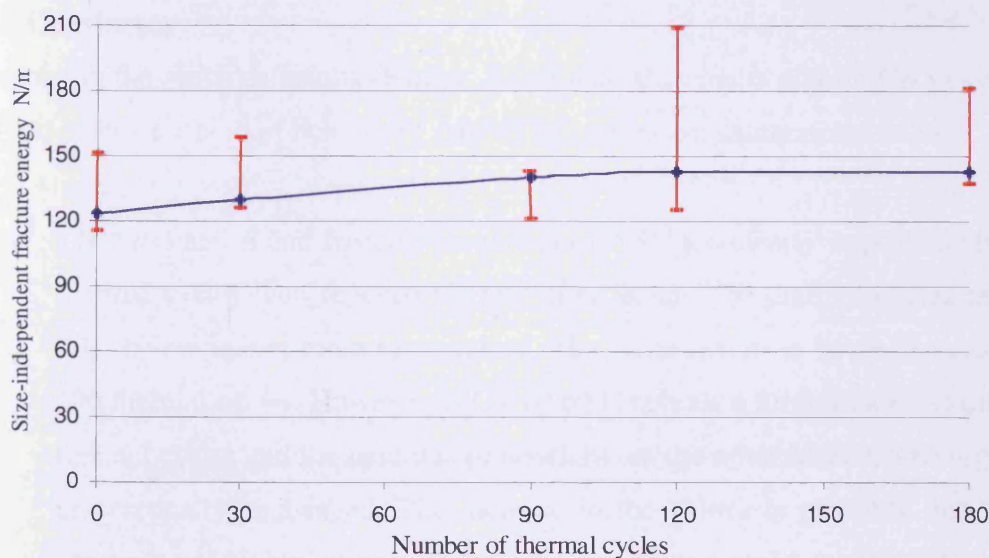
Figure 5.15 Influence of thermal cycling on the size-independent fracture energy of NSC specimens

5.11.2.2 Bonded specimens

As expected, the G_F of bonded specimens is affected by the thermal cycling; it increases gradually and then decreases after 120 thermal cycles, but it never falls below the value at 0 cycles.
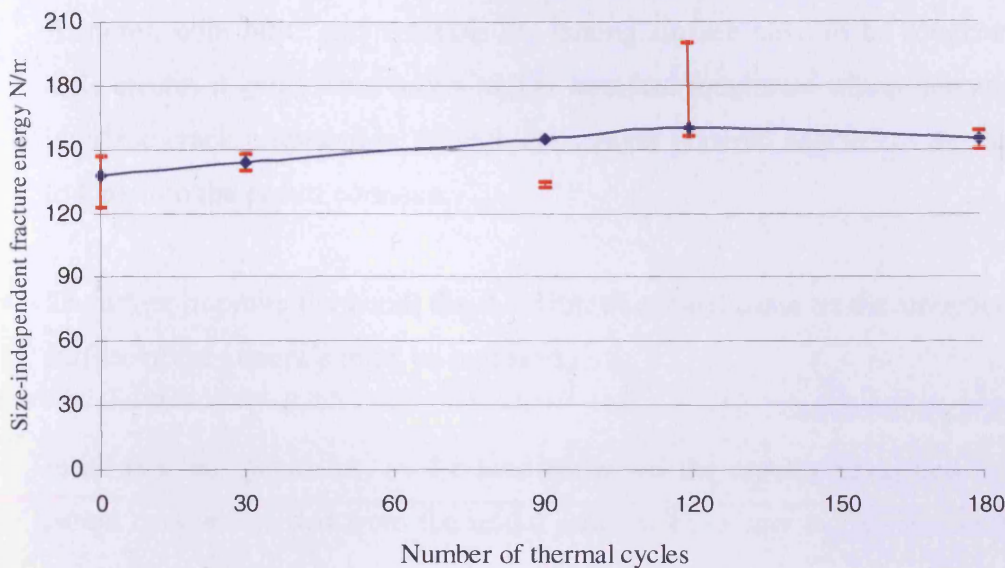
Figure 5.16 Influence of thermal cycling on the size-independent fracture energy of NSC bonded specimens

5.12 Conclusion

Combining the previous results (Farhat, 2004) with the results reported in this study, the test results for both of NSC and CARDIFRC mixes are summarized below.

- The mechanical and fracture properties of NSC are clearly improved after 30 thermal cycles then reduced slightly after 90 and120 thermal cycles but not drop below that at room temperature. The values seem to be unchanged after 180 thermal cycles. However, MOR of NSC reveals a further increase after 90 thermal cycles and the modulus of elasticity on the other hand can be regarded as practically unchanged. The increase in the values is probably due to the continuity of hydration process, and the reduction may be regarded due to the initiation of new microcracks between the cement paste and the aggregate.

- The mechanical properties of CARDIFRC® followed the same trend that was observed in the mechanical properties of NSC with a further increase after 90 thermal cycles. This increase could be due to continued hydration of unhydrated cement, and the presence of microsilica which activates the secondary reaction.

- To avoid any deterioration in the repair system (delamination or interfacial fracture), both NSC and CARDIFRC mating surface have to be roughened. This creates a good bond and a higher interface toughness which delays the interface crack propagation through the weaker material and forces the crack to kink into the parent concrete.

- To further improve the bond, the thin film of cement paste on the smooth cast surface of the concrete must be removed.

- In all bonded specimens, as the load increased the crack propagation in the parent concrete started from the initial notch without any visual deterioration or bond degradation.

- Both the measured fracture energy (G_f) and the size-independent specific fracture energy (G_F) of control and bonded specimens follow the same trend where the values decreased as the notch to depth ratio increased.

- Generally, the repairing system of normal strength concrete with CARDIFRC is more successful when the adhesive bonding technique is used.

Chapter 6

Performance of HSC Bonded to CARDIFRC after Thermal Cycling

6.1 Introduction

In Chapter 5, the mechanical and fracture properties of control and CARDIFRC® bonded to NSC specimens after different thermal cycles were investigated. This chapter discusses only the results of control and CARDIFRC® bonded to HSC specimens under 0, 120 and 180 thermal cycles. The bonding technique and the thermal cycling are similar to those used in Chapter 5. The mechanical properties of high strength concrete were measured according to relevant British Standards, and the fracture behavior was evaluated from WS test based on load- CMOD curves for both control and bonded specimens, through visual observations, measured and size-independent fracture energy.

6.2 Control specimens

To evaluate the mechanical properties and the behavior of HSC after various thermal cycles, fifteen 100x100x100 mm cubes were tested to determine the compressive strength (five each at 0, 120, and 180 cycles), fifteen 100x200 mm cylinders and fifteen 100x100x500 mm beams for splitting strength and modulus of rapture. Three 150x300 mm cylinders were used to determine the modulus of elasticity (one at 0, 120, 180 cycles each). For the determination of fracture behaviour eighteen 200x200x200 mm cubes were used. These cubes were notched using a diamond saw to a notch to depth ratio of 0.2 or 0.6. The specimens were tested at room temperature by WS test as in § 5.7 after various thermal cycles.

6.2.1 Mix proportion of HSC

HSC mixes are generally characterized by low water/binder ratios, high content of cement, and the presence of various chemical and mineral admixtures (Mehta and Aitcin, 1990). The mix that was used in this study was chosen based on previous work carried out by other researchers in the same laboratory (Taylor et, al., 1997; Abousaif, 1997; Farhat, 2004). The proportions of HSC mix are shown in Table 6.1

Table 6.1 Mix Proportions of HSC

Material type	Cement	Sand	Aggregate	Micro-Silica	Super-plasticizer	W/b ratio
Mix proportion	1	1.32	2.21	0.11	1.8 %	0.22

The materials used in the HSC mix were as follows:

- Cement: Blue circle OPC (BS12: 1996 compliant).
- Fine aggregate: Local sea dredged sand.
- Coarse aggregate: Local crushed limestone with $d_a = 10$ mm.
- Micro-silica (SF): Elkem micro silica undensified 983.
- Superplasticizer (sp): Adoflow extra (consisted of sodium salts of sulphonated naphthalene formaldehyde condensate and lignosulphonic acid).

The dry materials were mixed first, then the water was added gradually to the mix while the mixer was in operation, following that the superplasticizer was added to achieve the required workability. After a few minutes from the completion of the mixing process, the fresh concrete mix was cast into the specified test specimen moulds.

6.2.2 Mechanical properties

The mechanical properties (the compressive, splitting and flexural strengths and the modulus of elasticity) were determined at room temperature according to relevant British Standards after 0, 120, and 180 thermal cycles. The results of experimental tests are discussed in the following sections.

6.2.2.1 Compressive strength f_c

The results of cube crushing tests are shown in Table 6.2. The compressive strength increased from 103.1 MPa to 124.7 MPa after 120 thermal cycles and then dropped to reach a value of 118.7 MPa after 180 cycles. Therefore, the total increase in the compressive strength was 15.13 percent after the final thermal cycles compared with the room temperature value. As discussed before in § 5.8.1 the significant increase in the compressive strength may be due further hydration caused by thermal cycling and the effect of age of the concrete specimens (see later in Table 6.6).

Table 6.2 Compressive strength of HSC after different thermal cycles

Thermal cycle	Specimens no.	Failure Load (kN)	Compressive Strength (MPa)	Mean value of comp. Strength (MPa)	C O V %
0	1	1026	102.6		
	2	1110	111.0		
	3	992	99.2	103.1	4.0
	4	998	99.8		
	5	1028	102.8		
120	1	1248	124.8		
	2	1211	121.1		
	3	1294	129.4	124.7	2.4
	4	1222	122.2		
	5	1260	126.0		
180	1	1167	116.7		
	2	1150	115.0		
	3	1227	122.7	118.7	2.4
	4	1213	121.3		
	5	1177	117.7		

6.2.2.2 Splitting strength f_t

Table 6.3 shows the splitting strength results under different thermal cycling. It can be seen that the splitting strength decreased from 7.6 MPa to 6.6 MPa after 120 thermal cycles and then reduced further to 5.7 MPa after 180 cycles. (The effect of age on the splitting strength is also shown in Table 6.6).

6.2.2.3 Modulus of rupture (MOR)

The test results of modulus of rupture after 0, 120 180 thermal cycles are shown in Table 6.4. The results show no significant change in the modulus of rupture after 120 thermal cycles but a slight decrease from 11.3 MPa to 10.9 MPa after 180 thermal cycles. This reduction is owing to the formation of new microcracks.

6.2.2.4 Modulus of elasticity

The value of modulus of elasticity was determined according to BS 1881 – 121 1983. It was calculated after different thermal cycling (Table 6.5). The results showed that the E increases slightly from 44.3 GPa at no cycles to 45.6 GPa after 120 thermal cycles and then decreases to 44.5 GPa after 180 thermal cycles.

Table 6.3 Splitting strength of HSC after different thermal cycles

Thermal cycles	Specimens no.	Failure Load (kN)	Splitting Strength (MPa)	Mean value of splitting Strength (MPa)	C O V %
0	1	246.0	7.8		
	2	235.9	7.5		
	3	232.6	7.4	7.6	2.5
	4	238.5	7.6		
	5	249.5	7.9		
120	1	206.5	6.6		
	2	210.8	6.7		
	3	202.2	6.4	6.6	1.4
	4	206.4	6.6		
	5	209.6	6.8		
180	1	186.0	5.9		
	2	179.3	5.7		
	3	171.5	5.5	5.7	2.8
	4	184.3	5.9		
	5	182.1	5.8		

Table 6.4 Flexural strength test of HSC after different thermal cycling

Thermal cycles	Specimens no.	Breaking Load (kN)	MOR (MPa)	Mean value of MOR (MPa)	C O V %
0	1	27.32	11.0		
	2	29.85	12.1		
	3	27.39	11.1	11.2	4.00
	4	27.90	11.3		
	5	26.58	10.8		
120	1	29.23	11.8		
	2	27.41	11.1		
	3	28.92	11.7	11.3	3.7
	4	26.47	10.7		
	5	27.52	11.1		
180	1	26.43	10.7		
	2	25.70	10.4		
	3	26.55	10.7	10.9	3.5
	4	28.30	11.5		
	5	27.70	11.2		

6.5 The effect of thermal cycles on the Modulus of elasticity of HSC

Thermal Cycles	0	120	180
Modulus of Elasticity (GPa)	44.3	45.6	44.5

Table 6.6 The effect of different environmental conditions and age on f_c, f_t and MOR

Environmental condition	Compressive strength (MPa)	Splitting Strength (MPa)	Flexural Strength (MPa)
28 days at 20°C	103.1	7.6	11.2
120 days at 20°C	108.1	7.8	11.3
120 TC	124.7	6.6	11.3
180 TC	118.7	5.7	10.9

6.2.3 Fracture properties

Based on load – CMOD curves, the fracture behaviour of HSC was evaluated. It was obtained by using the WS test (see § 5.9.1). The fracture properties of concrete were evaluated according to load – CMOD curve and using the area under the curve divided by the ligament area to yield the measured fracture energy of concrete.

6.2.3.1 Measured fracture energy G_f

The load-CMOD curves for HSC and NSC show that both NSC and HSC behaved as expected and similar to those results obtained previously by Farhat (2004). The failure mode of HSC specimens was more brittle than NSC specimens. This is due to the compact nature of HSC matrix and interface which decreases the toughness (Gettu, et al., 1990).

Several investigations have revealed that cracks in HSC develop through the coarse aggregate, giving a smooth fracture surface. However, in NSC the cracks grow around the aggregates, therefore leading to more tortuous fracture path and a rough fracture surface. As can be seen in Figure 6.1, the post peak response seems to be steeper for HSC than that of NSC. This due the strong interface and the smaller process zone in front of the initial crack tip.

The variation in crack pattern can be caused by the homogeneity and the strength of the interfacial zone of HSC (Tasdemir et al., 1996). The thermal cycling of HSC specimens was performed in a similar manner to the NSC specimens (see § 5.7). After the WS specimens were exposed to the required thermal cycles, they were cooled naturally for 24 hours and then tested at room temperature using a DARTEC closed loop machine (600 kN).
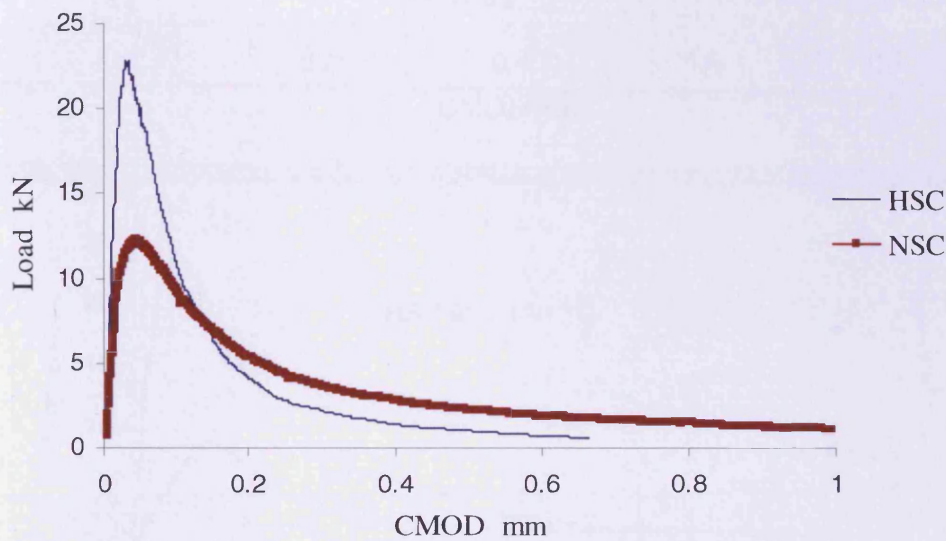
Figure 6.1 Comparison of Load-CMOD curves for HSC and NSC specimens with a notch to depth ratio of 0.20.

The results of the measured fracture energy for HSC with notch to depth ratios of 0.20 and 0.60 after 0, 120 and 180 thermal cycles are shown in Figures 6.2a, 6.2b, and 6.2c, respectively. The measured G_f (α) for specimens after zero thermal cycles decreases from115.2 N/m α = 0.20 to 104.5 N/m for α = 0.60 (Table 6.7). It can also be seen that the failure load decreases as α increases. Furthermore, the mean value of the peak load for HSC specimens decreases from 24.1 kN with a notch to depth ratio of 0.20 to 6.9 kN with a notch to depth ratio of 0.60. A similar trend was observed for the results of the mean value of the failure load and fracture energy for HSC specimens for α = 0.20 and α = 0.60 after 120 and 180 thermal cycles (Tables 6.8 and 6.9).
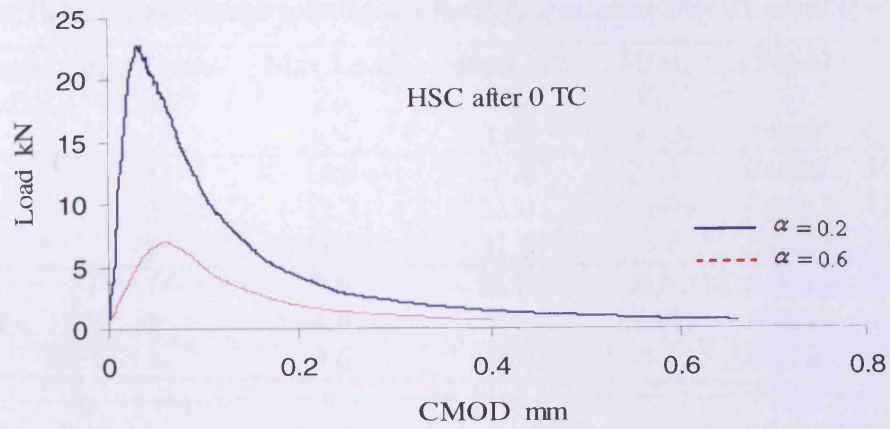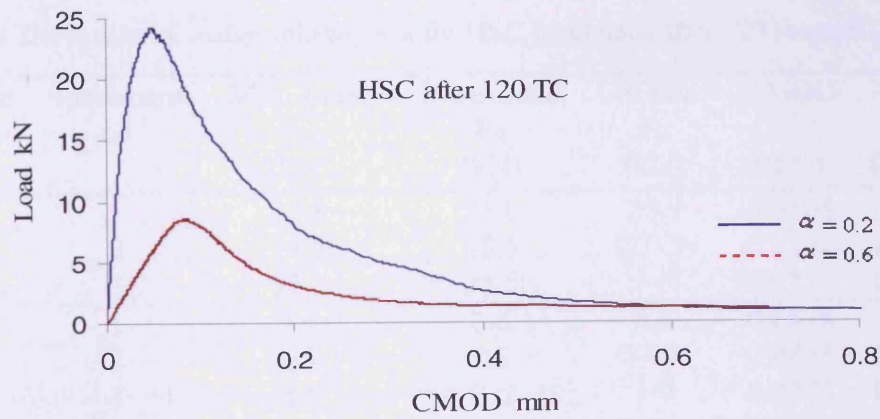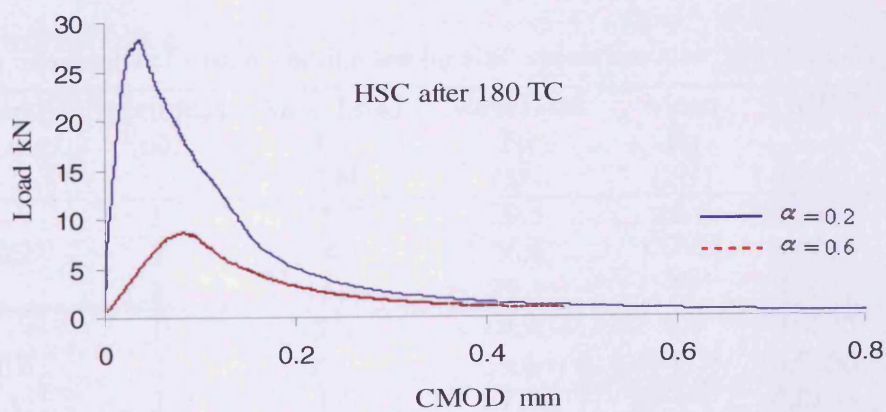
Figure 6.2 The influence of notch size on the load-CMOD curves of HSC specimens, after:
(a) zero thermal cycles (b) 120 thermal cycles (c) 180 thermal cycles

Table 6.7 The results of wedge splitting test for HSC specimens after 0 thermal cycles

Material Type	Depth Ratio	Specimens no.	Max.Load F_M (kN)	Max.Load F_H (kN)	Mean F_H (kN)	CMOD (mm)	G_f (N/m)	Mean G_f (N/m)
HSC	0.2	1	14.9	27.8	24.1	0.0227	100.4	115.2
		2	12.3	23.0	Cov%	0.0363	123.5	Cov%
		3	11.5	21.5	13.5	0.0367	121.8	11.1
	0.6	1	3.6	6.7	6.9	0.0623	115.4	104.5
		2	4.0	7.5	Cov%	0.0643	103.5	Cov%
		3	3.6	6.7	6.8	0.0665	94.7	9.9

Table 6.8 The results of wedge splitting test for HSC specimens after 120 thermal cycles

Material Type	Depth Ratio	Specimens no.	Max. Load F_M (kN)	Max. Load F_H (kN)	Mean F_H (kN)	CMOD (mm)	G_f (N/m)	Mean G_f (N/m)
HSC	0.2	1	13.8	25.8	25.9	0.0608	166.8	150.7
		2	14.2	26.5	COV%	0.0241	152.3	COV%
		3	13.7	25.5	1.9	0.0329	133.1	11.2
	0.6	1	4.6	8.6	8.6	0.0838	151.6	133.8
		2	4.7	8.8	COV%	0.0855	130.3	COV%
		3	4.6	8.6	1.8	0.0775	119.7	12.1

Table 6.9 The results of wedge splitting test for HSC specimens after 180 thermal cycles

Material Type	Depth Ratio	Specimens no.	Max. Load F_M (kN	Max. Load F_H (kN	Mean F_H (kN)	CMOD (mm)	G_f (N/m)	Mean G_f (N/m)
HSC	0.2	1	15.8	29.5	28.5	0.0397	145.4	145.6
		2	14.3	26.6	COV%	0.0321	140.3	COV%
		3	15.8	29.5	5.8	0.0516	151.2	3.7
	0.6	1	5.0	9.3	8.6	0.0845	127.6	127.9
		2	4.9	9.1	COV%	0.0900	138.5	COV%
		3	4.0	7.4	12.4	0.0803	117.8	8.0

The results reveal that the fracture energy for specimens with a notch to depth ratio of 0.20 increases from 115.2 N/m to 150.7 N/m after 120 thermal cycles and then decreases slightly to 145.6 N/m after 180 thermal cycles. Similarly, the G_f of specimens with $\alpha = 0.60$ increases from104.5 N/m at a room temperature to 133.8 N/m after 120 thermal cycles, then drops to reach a value of 127.9 N/m.

However, as the number of thermal cycles increases, the mean value of the ultimate load of the specimens with notch to depth ratios of 0.20 and 0.60 also increases. This is most likely due to the presence of microsilica that activates the secondary reaction and leads to an increase in strength.

6.2.3.2 Size-independent fracture energy G_F

The size-independent specific fracture energy G_F for HSC was determined using the equation (3.31), and the results of G_F are shown in Table 6.10. As can be seen, the values of size-independent fracture energy and the transition ligament length increase with increasing number of thermal cycles.

The G_F value increases from 125.9 N/m to 167.5 N/m after 120 thermal cycles, thereafter, the fracture energy reduces slightly to 163.3 N/m, giving a total increase of 29.7 percent. It can be summarized that 120 thermal cycles do not affect the ductility of HSC specimens, whereas there is an insignificant decrease after 180 thermal cycles (Figure 6.3). This might be due to the initiation of microcracks at the interfaces between cement paste and coarse aggregates (Farhat, 2004).

Table 6.10 Size-independent fracture specific energy for HSC specimens after different TC

Thermal cycling	0 TC	120 TC	180 TC
G_F (N/m)	125.9	167.5	163.3
a_l (mm)	27	32	34

Fracture Energy N/m

200

160

120

80

40

0

0   30   60   90   120   150   180

Thermal Cycles

G_F

$G_f = 0.2$

$G_f = 0.6$
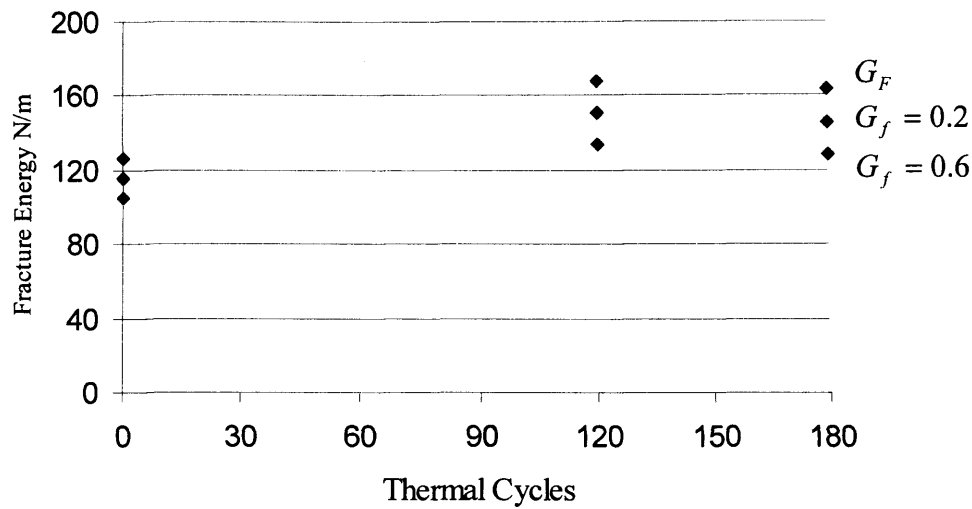
Figure 6.3 The influence of thermal cycling on the measured and size-independent fracture energy of HSC.

6.2.3.3 Brittleness

The characteristic length l_{ch} is an indication of the brittleness of the mix according to Hillerborg et al. (1976). Its can be determined using equation (5.7) (see § 5.9.2.3). The values of characteristic length after different thermal cycles are shown in Table 6.11. The results reveal clearly that the value of l_{ch} increases with the number of thermal cycles. This behaviour of HSC specimens was also observed in NSC specimens exposed to the same number of thermal cycles.

Table 6.11 The effect of thermal cycling on the l_{ch} for HSC

Thermal cycles	0 TC	120 TC	180 TC
l_{ch} (mm)	95.2	176.0	220.2

6.3 HSC bonded specimens

The casting of CARDIFRC® and HSC half cubes and bonding process was performed in an identical manner to that described in Chapter 5. Wedge splitting test of CARDIFRC® bonded to HSC half cubes using only the adhesive bonding technique will be described in this section. The main factors that affect the bonding system, such as the thermal cycling, roughness of the mating surface of the parent concrete will be

highlighted. The parameters that affect the repairing system, such as the maximum failure load, failure modes, measured fracture energy and size-independent specific fracture energy will be discussed.

6.3.1 Adhesive bonding

The results illustrate the feasibility of bonding HSC with CARDIFRC® using an adhesive bonding technique. CARDIFRC® half cubes were bonded on to HSC half cubes using a thixotropic epoxy adhesive, Sikadur®31 in the same way that was used in Chapter 5 with NSC specimens.

6.3.1.1 Influence of surface preparation
6.3.1.1.1 Parent concrete (HSC)

Based on Farhat (2004), the test results revealed that a crack started from a corner of the initial notch and kinked slightly into the HSC specimen and thereafter propagated solely in the latter and almost parallel to the interface before removing a cement film (Plate 6.1a). However, as it can be seen from the photograph of the fracture surfaces in Plate 6.2a there are very few coarse aggregates on the surface.

A comparison was made with fractured surfaces obtained after cutting the specimens away from the mating surface. This showed that the concentration of coarse aggregates in the fractured surfaces of the bonded concrete is less than that in the bulk and revealed also that the fracture surfaces of complete specimen exhibited higher irregularity and the number of fractured coarse aggregate was much larger.

According to Farhat (2004) results, this difference manifests in the mechanical data listed in Table 6.12. The data show that the measured specific fracture energy for the complete HSC specimen is 72 N/m, whereas the bonded HSC specimen is only 40.8 N/m. The results indicate that the failure of this bonded system can be regarded more brittle than that of the control specimen, and therefore the bonding technique needs to be modified.
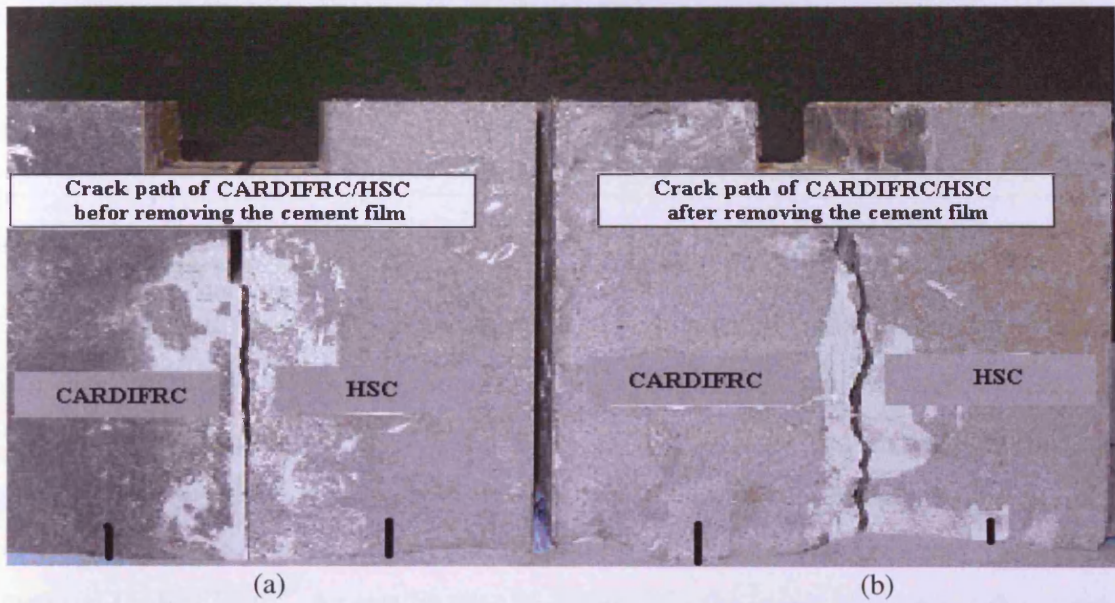
Plate 6.1 The effect of cement paste film on the failure mode of CARDIFRC®/HSC, (a) before, (b) after the removal of film
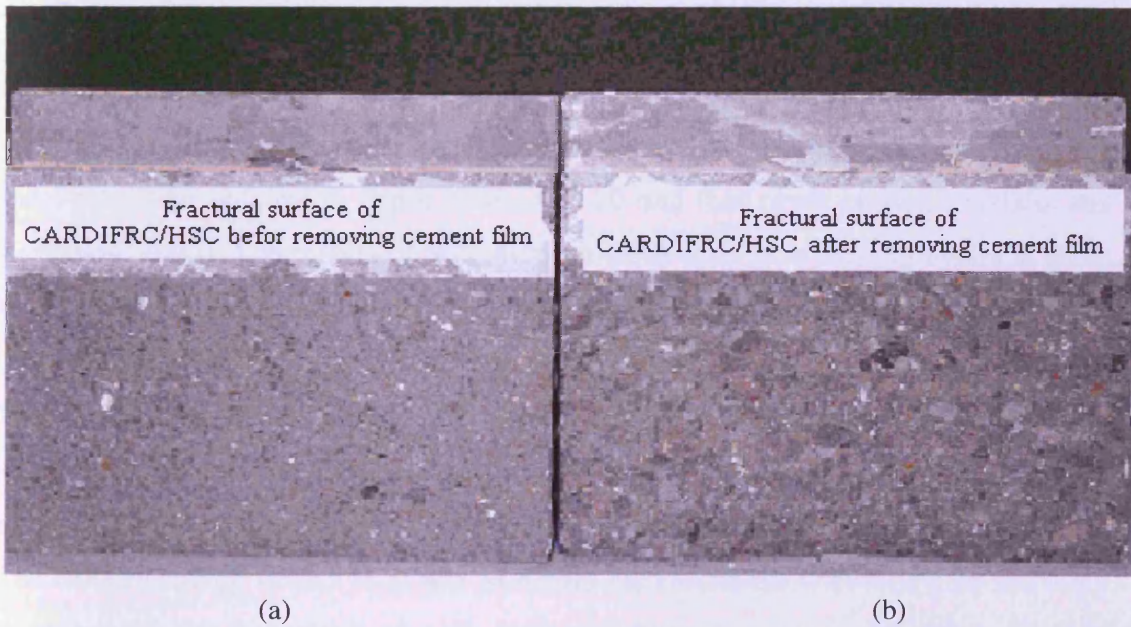
Plate 6.2 The effect of cement paste film on the fractured surface of CARDIFRC®/HSC, (a) before, (b) after the removal of film

Table 6.12 Trial WS results of CARDIFRC®/HSC with α=0.30 (adhesive bonding)

Type		Specimen	Max Load (kN)	Average (kN)	*CMOD* (mm)	G_f (N/m)	Average G_f (N/m)
Bonded	Before	1	14.0	14.5	0.025	35.6	40.8
		2	15.1		0.027	46.0	
	After	1	18.2	18.2	0.037	68.3	68.3
Control		1	17.3	17.3	0.032	72.0	72.0

6.3.1.1.2 Surface improvement

To avoid the problem maintained above, it was recommended to use a similar bonding technique that applied on CARDIFRC®/NSC bonded system (see § 5.9.3.2.1.3), which incorporated the removal of a cement paste film from the mating surface of the HSC half cubes. The results of this additional treatment were encouraging. The adhesive adhered firmly to the parent concrete and the repair material CARDIFRC®. As can be seen in Plate 6.1b, the crack initiating at the starter notch corner, kinked towards the HSC, with a kink angle of about 10° and propagated thereafter in the HSC half close to the interface. The fractured surface of the bonded HSC specimen after the removal of the cement film exhibited higher irregularity than the one before (Plate 6.2b).

6.3.1.2 Influence of notch size

To evaluate the size-independent specific fracture energy G_F for bonded HSC specimens, two notches to depth ratios of 0.20 and 0.60 were chosen (Abdalla and Karihaloo, 2003). The results of WS test specimens after zero thermal cycles at room temperature are presented in Figure 6.4. In these specimens, a crack started at a corner of the starter notch and always kinked into the parent concrete at an angle of about 11° for specimens with a notch to depth ratio of 0.20 and about 8° for specimens with a notch to depth ratio of 0.60. The maximum failure load of bonded specimens with a notch to depth ratio of 0.20 is 11.25kN, but only 3.5 kN for specimens with α = 0.60. The fracture energy is 62.5 N/m and 54.4 N/m for specimens with α of 0.20 and 0.60, respectively. The variations of peak load and fracture energy with notch size are almost similar to those of control HSC specimens exposed to 120 and 180 thermal cycles.

6.3.1.3 Influence of thermal cycling

The results of thermal cycling on the bonded specimens after exposure to different thermal cycles are presented in Tables 6.13, 6.14 and 6.15. The results show that the crack initiated at the corner of starter notch and propagated into the HSC half cubes close to the interface with an angle of about $11°$ and $8°$ for specimens with $\alpha = 0.20$ and $\alpha = 0.60$, respectively. The failure mechanism for bonded HSC/CARDIFRC® specimens is similar to those of bonded CARDIFRC® /NSC specimens.

As can be seen, the mean value of the failure load decreases from 11.2 kN to 7.9 kN after 120 thermal cycles for specimens with $\alpha = 0.20$ and from 3.5 kN to 2.3 kN for specimens with notch to depth ratio 0.60. With a further increase in the thermal cycles to 180 the peak load increases slightly to 9.2 kN and 5.0 kN for $\alpha = 0.20$ and $\alpha = 0.20$ respectively.

The results also show that the fracture energy increases with thermal cycling; from room temperature to 120 thermal cycles the fracture energy increases from 62.5 N/m to 77.1 N/m and then reduces to 66.2 N/m after 180 thermal cycles for specimens with $\alpha = 0.20$. Similar trend has been observed for specimens with a notch to depth ratio of 0.60.

6.3.1.3.1 Size independent specific fracture energy

Table 6.16 shows the size independent specific fracture energy G_F and the transition ligament length a_l for CARDIFRC® / HSC specimens obtained using equation (3.31). The results reveal that the G_F for CARDIFRC® bonded to HSC specimens increases from 70.6 N/m at room temperature to 92.0 N/m after 120 thermal cycles. With a further increase in the thermal cycles to 180 the size independent specific fracture energy drops to 72.5 N/m (Figure 6.5) which is still higher than the room temperature value.

140

Table 6.13 Wedge splitting test results of CARDIFRC® / HSC after 0 thermal cycles

Material Type	Depth Ratio	Specimens no.	Max.Load F_M (kN)	Max.Load F_H (kN)	Mean F_H (kN)	CMOD (mm)	G_f (N/m)	Mean G_f (N/m)
HSC bonded to CARDIFRC	0.2	1	7.5	14.0	11.2	0.0217	63.9	62.5
		2	7.0	13.0	Cov%	0.0410	56.2	Cov%
		3	3.6	6.7	34.8	0.0824	67.5	9.2
	0.6	1	1.6	3.00	3.5	0.0408	52.8	54.4
		2	1.8	3.3	Cov%	0.0332	51.4	Cov%
		3	2.3	4.3	19.1	0.0507	59.1	7.4

Table 6.14 Wedge splitting test results of CARDIFRC® / HSC after 120 thermal cycles

Material Type	Depth Ratio	Specimens no.	Max.Load F_M (kN)	Max.Load F_H (kN)	Mean F_H (kN)	CMOD (mm)	G_f (N/m)	Mean G_f (N/m)
HSC bonded to CARDIFRC	0.2	1	4.2	7.8	7.9	0.0880	70.4	77.1
		2	4.3	8.0	COV%	0.0709	83.9	COV%
		3	0.0	0.0	2.4	0.0000	0.00	12.3
	0.6	1	1.2	2.2	2.3	0.1166	66.2	62.3
		2	1.1	2.0	COV%	0.1291	65.1	COV%
		3	1.5	2.8	16.8	0.1349	55.6	9.3

Table 6.15 Wedge splitting test results of CARDIFRC® / HSC after 180 thermal cycles

Material Type	Depth Ratio	Specimens no.	Max. Load F_M (kN)	Max. Load F_H (kN)	Mean F_H (kN)	CMOD (mm)	G_f (N/m)	Mean G_f (N/m)
HSC bonded to CARDIFRC	0.2	1	4.9	9.1	9.2	0.0301	58.9	66.2
		2	5.0	9.3	COV%	0.0257	73.6	COV%
		3	0.0	0.0	2.8	0.0000	0.00	15.7
	0.6	1	2.6	4.8	5.0	0.0558	58.1	57.9
		2	2.8	5.2	COV%	0.0534	57.8	COV%
		3	0.0	0.0	4.0	0.0000	0.00	0.5
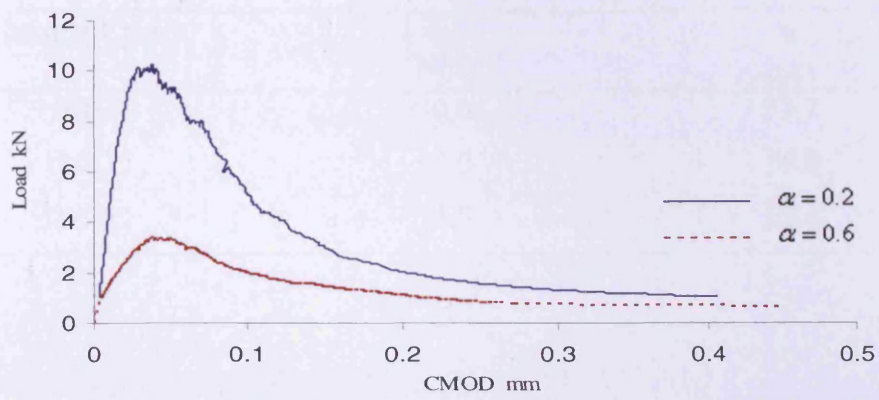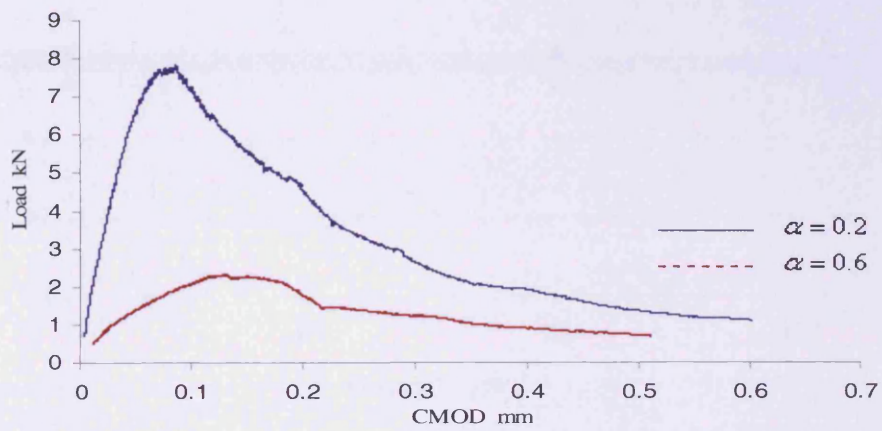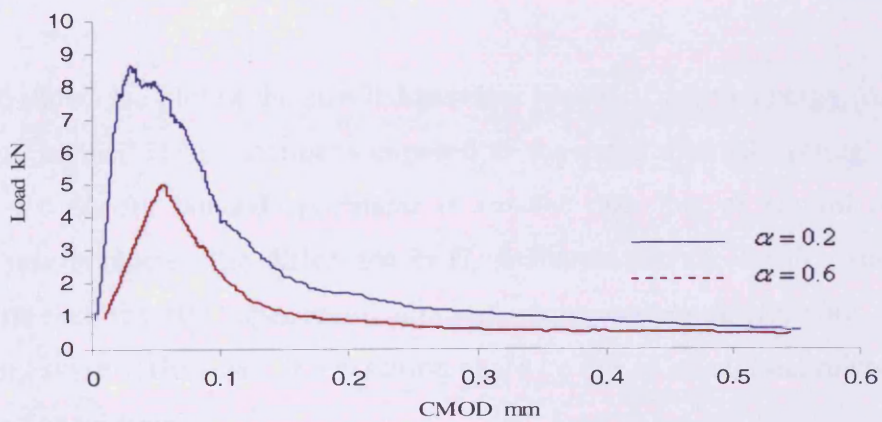
Figure 6.4 The influence of notch size on the load – CMOD curve of bonded HSC specimens after: (a) zero thermal cycles (b) 120 thermal cycles (c) 180 thermal cycles

Table 6.16 The effect of thermal cycles on size independent specific fracture energy

Thermal Cycles	G_F N/m	a_l mm
0 TC	70.6	37.7
120TC	92.0	50.0
180TC	74.5	35.6
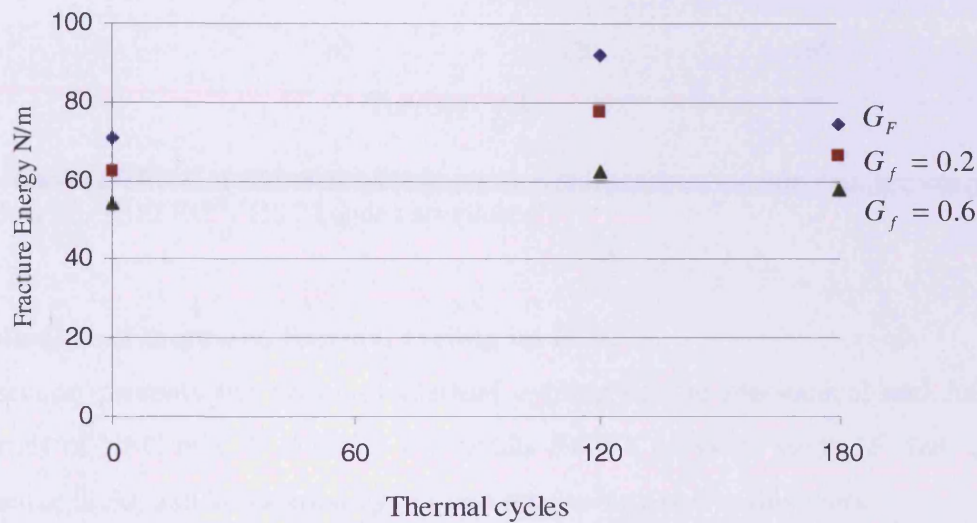
Figure 6.5 The effect of thermal cycles on measured and size independent specific fracture energy of CARDIFRC® / HSC specimens

Figure 6.6 shows the plot of the size-independent specific fracture energy for both the control and bonded HSC specimens exposed to the same thermal cycling. It can be seen that the G_F for bonded specimens is smaller than that of control one at all thermal cycle numbers. The difference in G_F indicates that the bonded specimen is more brittle than the HSC specimens, although there was no deterioration visible in the bonding system. However, the variation could be due to an internal microcracking in HSC half specimens.
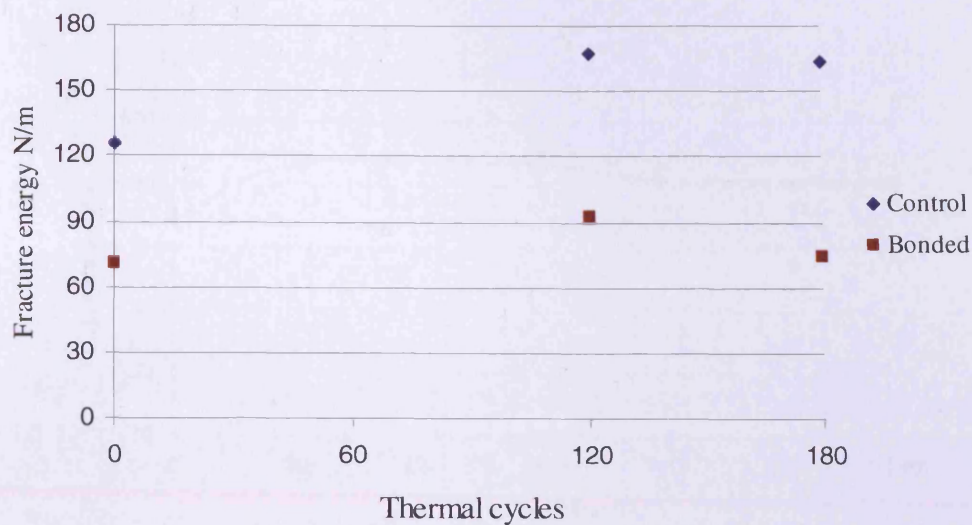
Figure 6.6 The effect of thermal cycling on size-independent specific fracture energy of control and CARDIFRC® / HSC bonded specimens

6.4 Influence of increased thermal cycling on HSC

This section presents the effect of thermal cycling on the mechanical and fracture properties of HSC mix. It includes the results from a previous study (Farhat, 2004) obtained at 0, 30, and 90 thermal cycles and results obtained in this work.

6.4.1 Mechanical properties

The results of the mechanical properties after different thermal cycling are shown in Table 6.16 and Figures 6.7, 6.8, and 6.9. The values of compressive and splitting strength increase in the first stage of thermal cycling and then decrease gradually as the thermal cycling is increased. The modulus of rupture on the other hand remains practically unchanged.

Table 6.17 The effect of thermal cycling on the modulus of elasticity value

Thermal cycles	0 TC	30 TC	90 TC	120 TC	180 TC
E value (GPa)	45.7	48.7	46.5	45.6	44.5
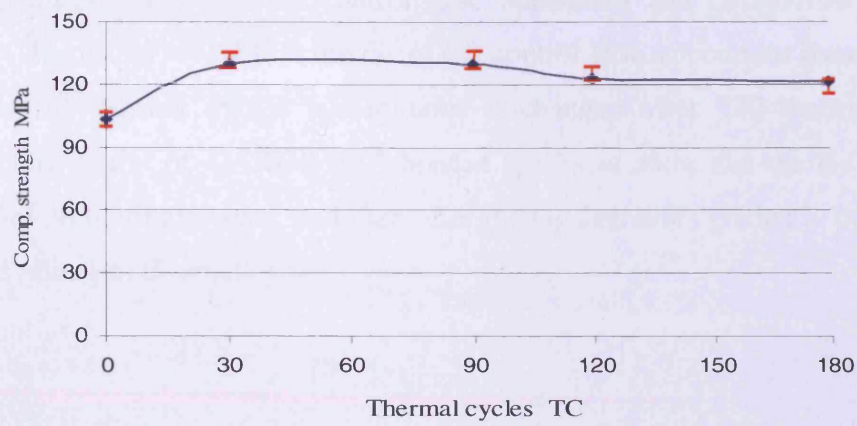
Figure6.7 Influence of thermal cycling on the compressive strength of HSC
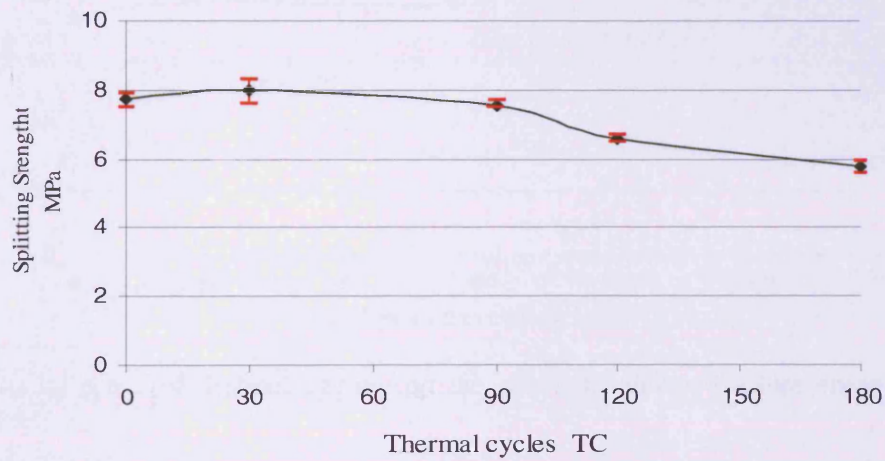
Figure 6.8 Influence of thermal cycling on the splitting strength of HSC
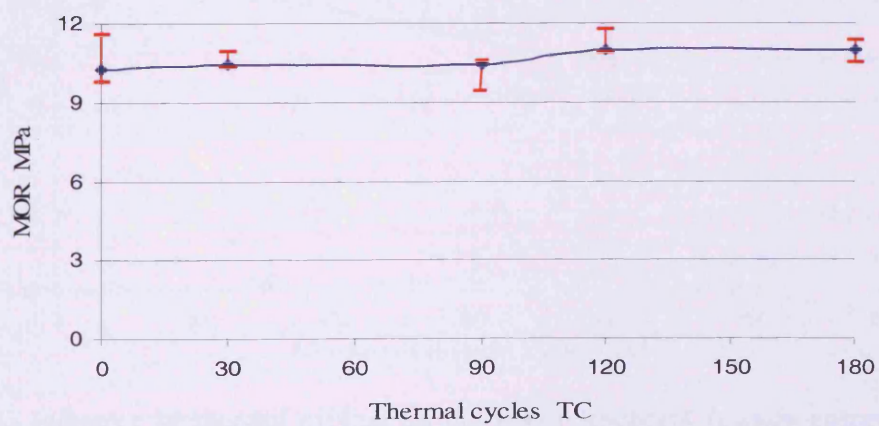
Figure 6.9 Influence of thermal cycling on the modulus of rapture of HSC

145

6.4.2 Fracture properties

Figures 6.10 and 6.11 present the effect of thermal cycling on size-independent specific fracture energy (G_F) of control HSC specimens and CARDIFRC® bonded specimens. The results reveal that the G_F of the control HSC specimens increases with the number of thermal cycles but remains unchanged after 120 thermal cycles. However, the results of CARDIFRC® bonded specimens show that the G_F increases slightly after 30 thermal cycles, and thereafter the G_F decreases gradually but remains unchanged after 120 thermal cycles.
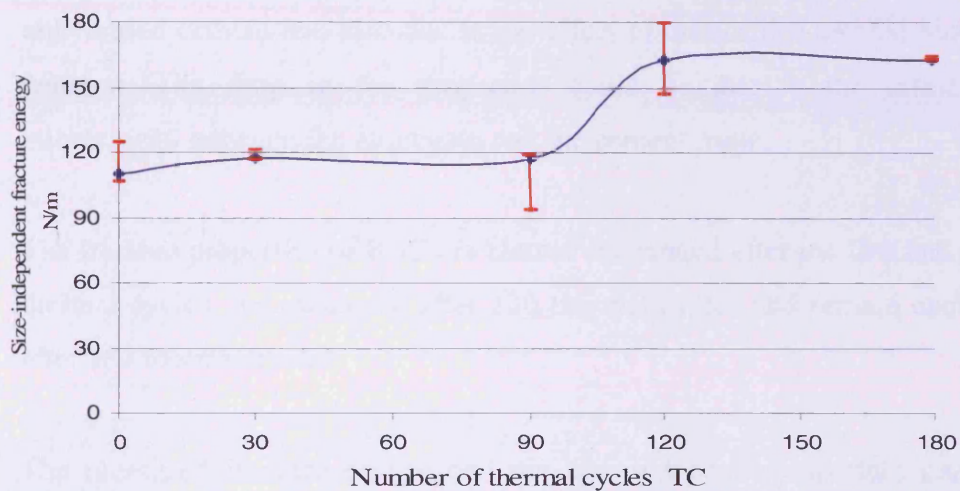
Figure 6.10 Influence of thermal cycling on the size-independent fracture energy of HSC specimens
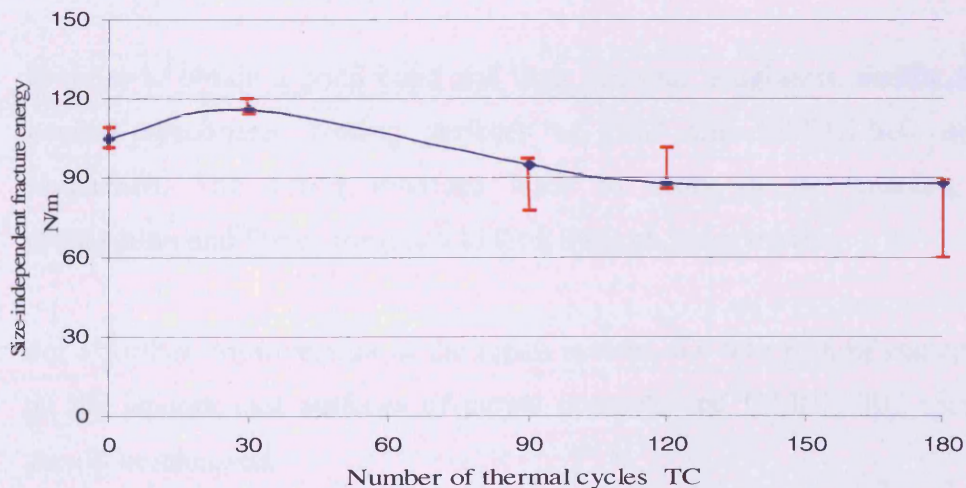
Figure 6.11 Influence of thermal cycling on the size-independent fracture energy of HSC bonded specimens

146

6.5 Conclusion

All high strength concrete (control and bonded) specimens have been exposed to hot climate represented by the thermal cycling programme. The previous test results and the results reported in this research lead to the following conclusions.

- The mechanical properties are increased after 30 thermal cycles but not so after 90 and 120 thermal cycles. After 180 thermal cycles the values remain unchanged. On the other hand, a further increase in MOR and modulus of elasticity was observed after 90 and 120 thermal cycles. As mentioned before, this increase in the values is probably due the continued hydration of unhydrated cement and also due to the effect of microsilica created secondary reaction. The drop in the properties could be due to the initiation of microcracks between the aggregate and the cement paste.

- The fracture properties of HSC are almost unchanged after the first and second thermal cycles, but enhanced after 120 thermal cycles and remain unchanged after 180 thermal cycles.

- The measured fracture energy and the size independent fracture energy of control and bonded specimens change with the thermal cycling and with the notch to depth ratio.

- In order to obtain a good bond and high interface toughness, similar to NSC bonded specimens, mating surfaces of HSC and CARDIFRC must be roughened. The strong interface leads to delay in the interface crack propagation and forces the crack to kink through the concrete.

- For a further improvement in the repair system, the thin film of cement paste on the smooth cast surfaces of parent concrete and CARDIFRC specimens should be removed.

- No visual deterioration or degradation has been observed after the bonded specimens were exposed to the thermal cycling. This is due to the good thermal compatibility between the parent concrete and CARDIFRC.

- Repairing of high strength concrete with CARDIFRC is more successful when the adhesive bonding technique is used.

Chapter 7

Retrofitting of Reinforced Concrete Beams with CARDIFRC after Thermal Cycling

7.1 Introduction

This chapter aims to evaluate the performance of reinforced concrete beams retrofitted with CARDIFRC® in hot climatic conditions. The retrofitted RC beams have been subjected to a number of thermal cycles, each thermal cycle including a temperature rise period of 20 min from the room temperature which is 25° C to 90° C, a dwell period of 8 hours at 90° C, and a cooling period of 16 hours from 90° C to 25° C (see § 5.7).

7.2 Beam Preparation

Fifty four under-reinforced concrete beams were cast, of which 36 beams were retrofitted with CARDIFRC® strips and eighteen left as control beams. Along with these beams, nine 100x 200 mm cylinders and nine 100 x 100 x 100 mm cubes were also cast. The beams, cylinders and cubes were cast at room temperature and then allowed to cure in a water tank for 28 days. The proportions of cement: fine aggregate: coarse aggregate in the concrete mix were 1:1.8:2.8 by weight and the water cement ratio was 0.50. The concrete mix used ordinary Portland cement and the maximum aggregate size was 10mm.

Two different reinforced concrete beams have been investigated in this study: beams without shear reinforcement, which were designed to fail in flexure or in shear, and beams with sufficient shear reinforcement. The former, reinforced with a single 12 mm rebar, were 1000 mm long, 100 mm wide and 150 mm deep (Figure 7.1a). The remaining beams were provided with shear stirrups in their shear spans (Figure 7.1b). According to the British Standard BS8110 the beams were over-designed for shear to prevent brittle failure due to the increased shear load on the strengthened beam so the flexural behaviour could be observed throughout the loading up to failure. Shear reinforcement consisted of 6 mm deformed bars placed at 65 mm spacing (Figure 7.1b).

Two types of configuration of retrofitting were investigated; one strip bonded on the tension face and three strips (one bonded on the tension face and the others on the vertical sides). These strips completely covered each side of the beam (Figure 7.2).

149
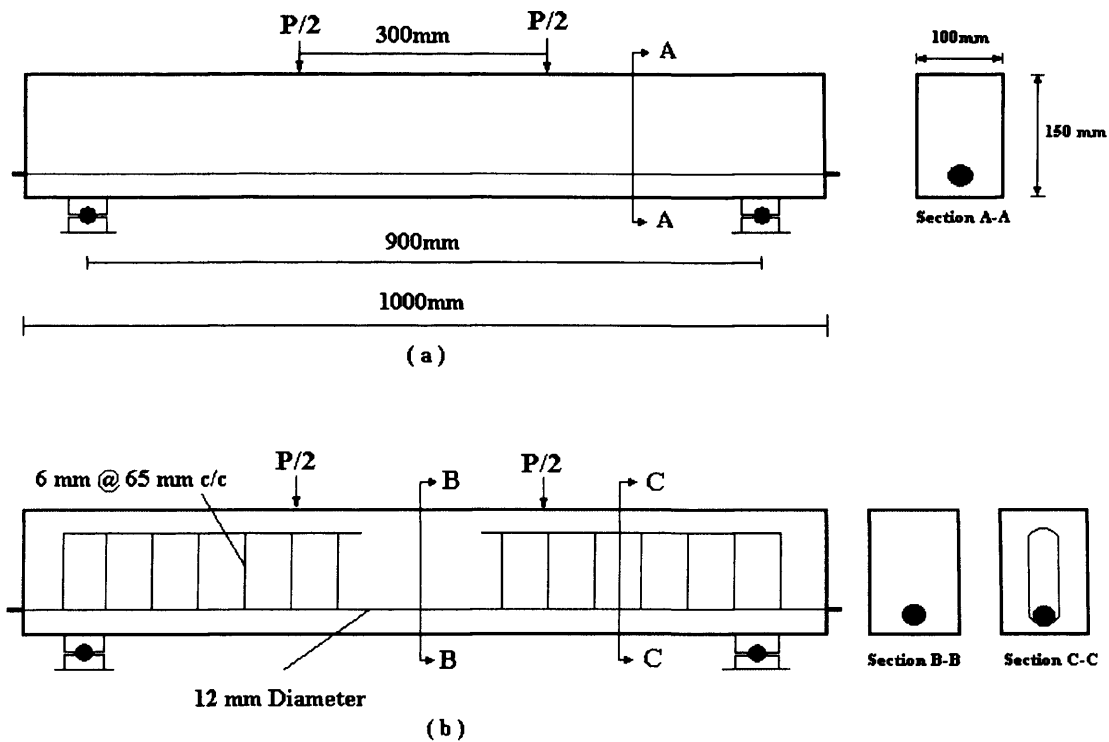
Figure 7.1 Beam details (a) Explanation of beam dimensions and internal steel reinforcement, (b) Beam with sufficient shear reinforcement

7.3 Preparation of CARDIFRC® strips

The steel moulds 1030 mm long, 100 mm wide and 16-20 mm border height were cleaned and oiled, Figure 7.3. The retrofit material CARDIFRC® was cast as flat strips in these steel moulds. The moulds were filled on a non- magnetic vibrating table at 50 Hz frequency and smoothed over using a float. The strips were left to dry in the moulds for 24 hours at room temperature before de-moulding, thereafter the strips were allowed to cure in hot curing bath at 90° C for a further 7 days. A gradual increase in temperature from ambient to 90° C and vice versa was found important to avoid any thermal gradients. For that reason the retrofitting strips were left in the bath for a total period 9 days, on the first day the water temperature was increased gradually from $20^{\circ}C$ to $90^{\circ}C$ and on the ninth day it was reduced from $90^{\circ}C$ to $20^{\circ}C$.
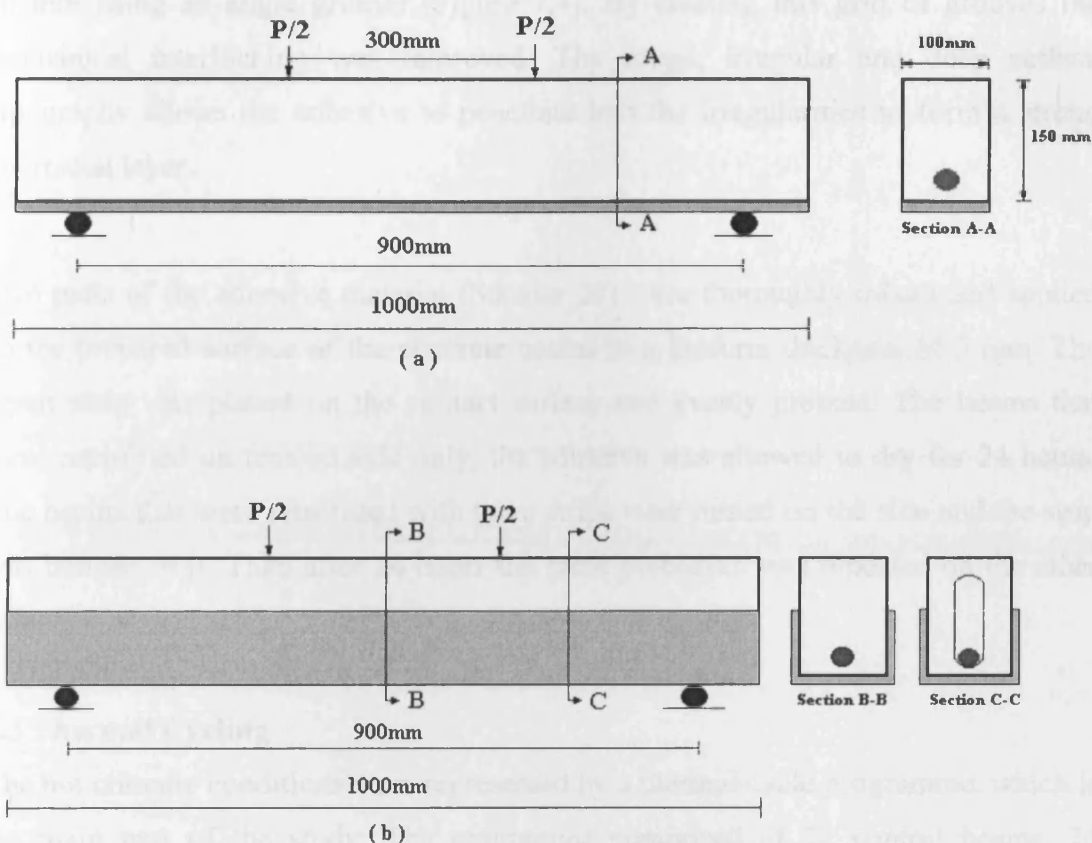
Figure 7.2 CARDIFRC® strip configuration: (a) One retrofitted strip bonded on tension face (b) Three retrofitted strips bonded; one on tension side and two on vertical sides
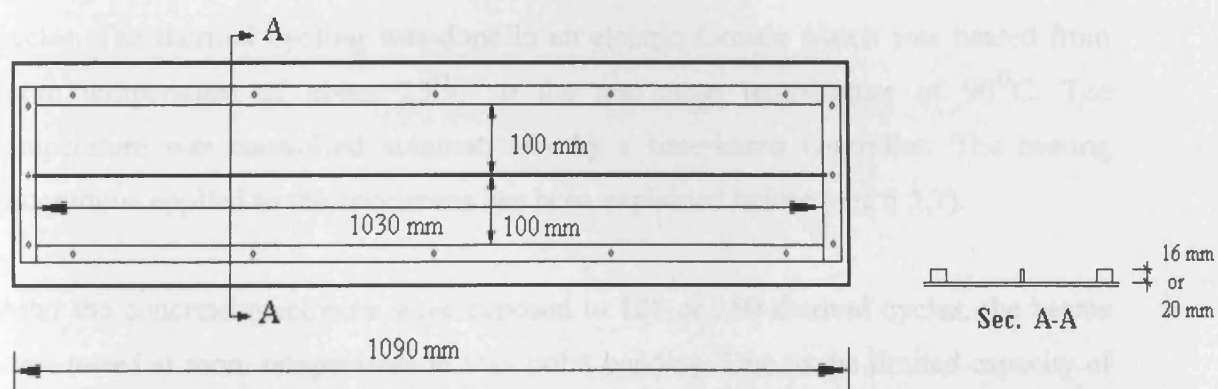
Figure 7.3 Steel moulds to cast two CARDIFRC® strips, 16 or 20 mm thick

7.4 Retrofitting Procedure

Thirty six beams were retrofitted with CARDIFRC® strips and epoxy-based adhesive (Sikadur 31). Before bonding the retrofitting strips to the parent concrete, the contact surfaces of the concrete specimens and CARDIFRC® strips were carefully cleaned

and roughened by creating a grid of grooves approximately 3 mm deep at a spacing of 50 mm using an angle grinder (Figure 7.4). By creating this grid of grooves the mechanical interlocking was improved. The rough, irregular and deep surface topography allows the adhesive to penetrate into the irregularities to form a strong interfacial layer.

Two parts of the adhesive material (Sikadur 31) were thoroughly mixed and applied on the prepared surface of the concrete beams to a uniform thickness of 3 mm. The repair strip was placed on the contact surface and evenly pressed. The beams that were retrofitted on tension side only, the adhesive was allowed to dry for 24 hours. The beams that were retrofitted with three strips were turned on the side and the strip was bonded to it. Then after 24 hours the same procedure was repeated on the other side.

7.5 Thermal Cycling

The hot climatic conditions were represented by a thermal cycle programme, which is the main part of the study. The programme comprised of 12 control beams, 24 retrofitted RC beams, six (100 x 100 x 100 mm) cubes for compressive strength and six (100 x 200 mm) cylinders for splitting test. One half of these beams and test specimens were subjected to120 thermal cycles and the remaining half to180 thermal cycles. The thermal cycling was done in an electric furnace which was heated from room temperature of about 25^OC to the maximum temperature of 90^OC. The temperature was controlled automatically by a time-based controller. The heating programme applied to the specimens has been explained before (see § 5.7).

After the concrete specimens were exposed to 120 or 180 thermal cycles, the beams were tested at room temperature in four point bending. Due to the limited capacity of the furnace, it was not possible to accommodate all beams at once. Therefore each half of the beams and test specimens was placed in the furnace and exposed to 120 or 180 thermal cycles, respectively.
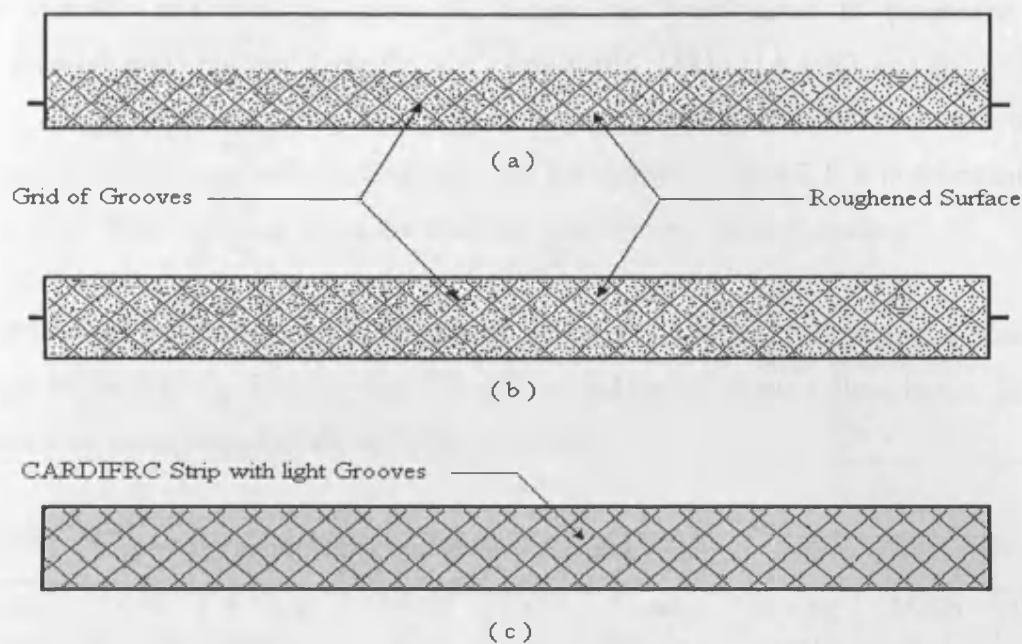
Figure 7.4 Roughened and grooved beam and strip surfaces (a) Vertical face (b) Tension side and (c) CARDIFRC® strip surface

7.6 Test Procedure

All beams were tested under four-point loading as a simply supported beam on 900 mm clear span. The loading points were 300 mm apart (Figure 7.5). Five transducers were placed on each side to record the deflection of the beam at different points along its span. The transducers were SOLARTON type ACR-25 and DCR-15 LVDTs. Two aluminium bars were designed with total of ten slots to hold the transducers and fixed on each side of the beam at the mid height (Figure 7.5). The load was controlled by the movement of the actuator with a starting loading rate 0.01 mm/sec; it was increased to 0.04 mm/sec when the load exceeded the peak load.
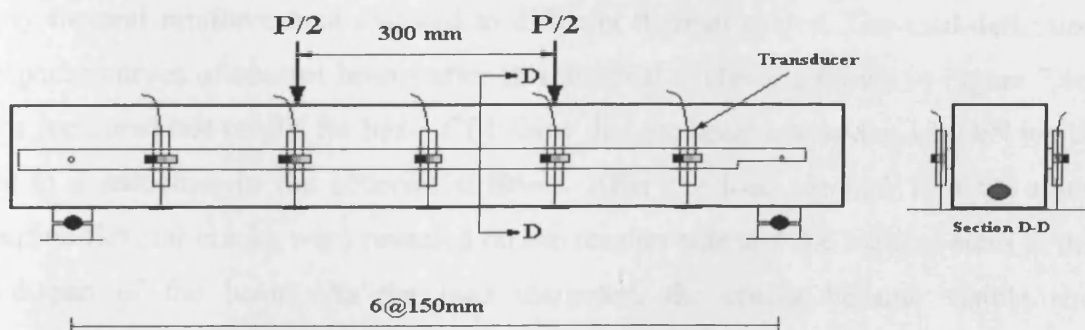
Figure 7.5 Arrangement of transducers and load points

153

7.7 Test Results

The concrete mix used to make the beams has been tested to determine the compressive and splitting strengths according to BC 1881- 116 1983 and BC 1881 – 117 1983, respectively. The results from three cubes 100x100x100 mm and three cylinders 100x200 mm at each thermal cycle are shown in Table 7.1. It is seen that the compressive and splitting strengths decrease slightly with thermal cycling.

The results of 18 control and 36 retrofitted beams at 0, 120 and 180 thermal cycles are shown in Tables 7.2, 7.3, 7.4 and 7.5 with an indication of the failure mode. These results will be presented in the subsequent sections.

Table 7.1 Compressive and splitting strengths of concrete mix

Thermal Cycles	Load Failure F_c (kN)	Comp. Strength f_c(MPa)	Mean of f_c (MPa)	COV %	Load Failure F_t (kN)	Splitting Strength f_t(MPa)	Mean of f_t (MPa)	COV %
0	554	55.4	55.93	0.8	148.2	4.72	4.61	2.5
	564	56.4			146.2	4.66		
	560	56.0			139.8	4.45		
120	528	52.8	54.12	1.8	136.8	4.35	4.26	1.7
	549	54.9			131.0	4.17		
	548	54.8			133.0	4.26		
180	525	52.5	53.06	0.8	125.3	3.99	3.99	0.4
	532	53.2			124.8	3.97		
	535	53.5			125.9	4.01		

7.8.1 Control beams

7.8.1.1 Beams without shear reinforcement.

Figure 7.6 shows the measured load versus deflection curves for control beams with only flexural reinforcement exposed to different thermal cycles. The load-deflection response curves of control beams after zero thermal cycles are shown in Figure 7.6a. The measured test results for beam CF1 show that the beam cracked at 12.0 kN which led to a reduction in the concrete stiffness. After the load reached 16.0 kN some hairline flexural cracks were revealed on the tension side and the vertical sides at the mid-span of the beam. As the load increased, the cracks became visible and propagated towards the compressive zone.

Thereafter, a group of these cracks propagated diagonally towards the support and created a shear failure, while the flexural cracks progressively closed. At a load carrying capacity of 49.58 kN and a mid span deflection of 3.60mm the trend changed with a local drop in the load displacement response. This reduction was attributed to the yielding of the steel. Thereafter, due to the strain hardening behaviour of steel the load again increased. When the load carrying capacity reached 52.66 kN and mid-span deflection of 9.0 mm a sudden drop in the load was observed, this is due to shear failure.

A similar trend was observed on beam CF2, the crack initiated at the same load as that of CF1. When the load capacity exceeded 15.5 kN the flexural cracks appeared on the bottom side of the beam. With an increase in the load, the cracks become more visible. However, after the load carrying capacity reached 50.01 kN and the mid-span deflection exceeded 4.7 mm a slight drop was observed, this coincides with the onset of the yielding of steel. Thereafter, due to the strain hardening of the steel, the load was still increasing. At 49.5 kN one of the cracks propagated diagonally from the support towards the load point, this crack started to open until the beam failed in combination of flexural and shear failure mode with a maximum load carrying capacity of 52.88 kN and a mid-span deflection of 9.2 mm.

Load-mid span deflection curve for beam CF3 presented a different behaviour, where the crack initiated at the mid span at load capacity of 11.00 kN. At a load of 14.5 kN the crack appeared on the tension side and both of vertical sides of the beam. As the load was increased the crack became visible and propagated towards the compression zone. When load capacity reached 24.5 kN a shear crack appeared near to the left support and then propagated up to the load point. This crack started to open while the other flexural cracks progressively closed until the beam failed in shear mode with a maximum load capacity of 35.24 kN.

The response of the beams exposed to 120 thermal cycles is presented in Figure 7.6b. The test results for beam CF4 revealed that after the load reached 16.0 kN some hairline flexural cracks appeared at the middle third of the beam. As the load was further increased, a diagonal crack was initiated close to the support and then

propagated towards the point load creating a shear crack which led to a decrease in the stiffness of concrete. When the load exceeded 48.9 kN and mid-span deflection of 3.9 mm, a slight drop in the load-deflection curve was observed. This is due to the fact that the yielding of steel started at this stage. Because of the strain hardening behavior of the steel, the load increased again. Finally, the beam CF4 failed in a shear mode with a maximum load of 49.7 kN and mid-span deflection of 4.4 mm.

The other two beams CF5 and CF6 followed the same trend and failed in a combination of flexural and shear modes. The cracks started growly on the tension side of the beams at load of 14.0 kN and 15.0 kN respectively. At load of 18.5 kN for CF5 and 19.0 kN for CF6 the flexural cracks propagated in the vertical sides towards the compressive zone. When the load carrying capacity of beam CF5 and CF6 reached 48.5 kN and 54.8 kN and the mid-span deflection exceeded 4.1 mm and 3.5 mm respectively, a drop in the load-deflection curves was observed. This is due to the fact that the yield of steel started at this point. The two beams failed with a maximum load of 50.7 kN and 54.8 kN, respectively.

For the beams that were tested after 180 thermal cycles, the measured load deflection curves are shown in Figure 7.6c. It can be seen that beams CF7 and CF8 exhibited the same behaviour, where both beams failed in shear mode (Plate 7.1) with a similar maximum load of 47.5 kN. The load-deflection curve for both beams showed that the failure happened suddenly, it can be attributed to a high reduction in the concrete stiffness due to an increase in the number of microcracks in the concrete after the thermal cycling. The beam CF9 failed in a combination of flexural and shear modes with a maximum load of 53.2 kN and behaved similar to those beams that were exposed 0 and 120 thermal cycles.

156
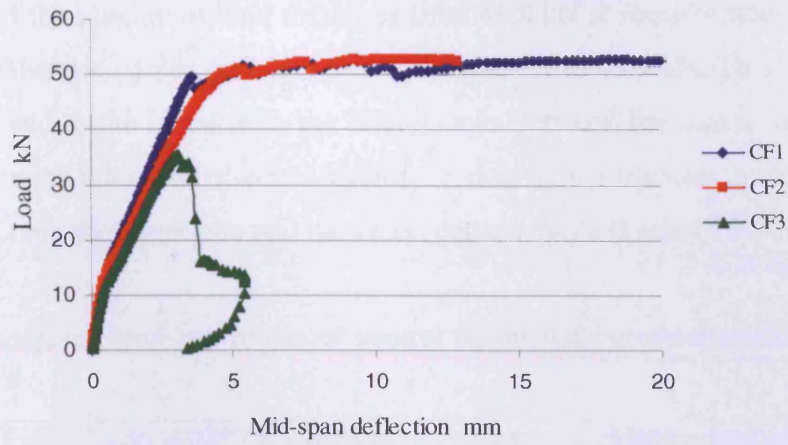
(a)
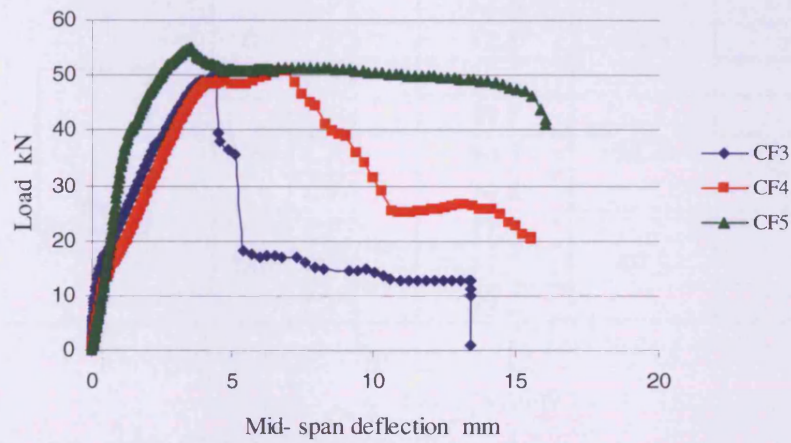
(b)
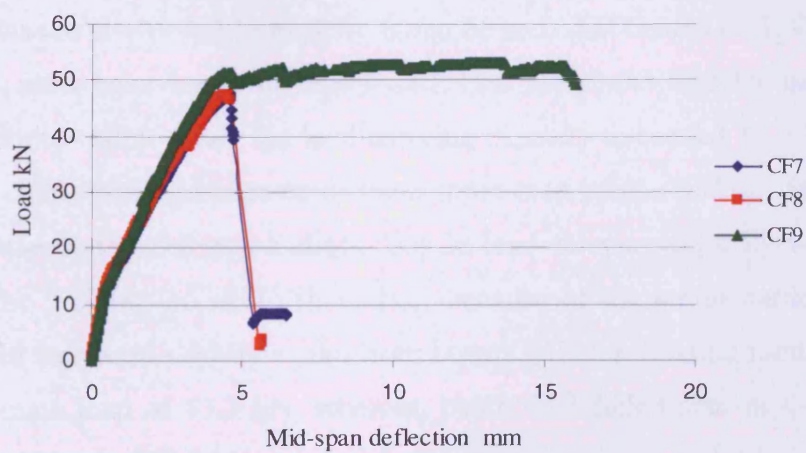
(c)

Figure 7.6 Load Deflection responses of control beams without shear reinforcement, after (a) zero thermal cycles (b) 120 thermal cycles and (c) 180 thermal cycles

A comparison has been made between the mean value of the ultimate load of the beams exposed to 0, 120 and 180 thermal cycles (Table 7.2). The results show that the mean value of the maximum load increases from 46.8 kN at room temperature to 51.7 kN after 120 thermal cycles and then decreases slightly to 49.4 kN. This phenomenon can be attributed to the increase in the microcracks between the coarse aggregate and the cement paste after 120 thermal cycles or due to the stresses generated at the interface between the aggregate and hardened cement paste (Farhat 2004).

Table 7.2 Four point bend test results of control beams without shear reinforcement after thermal cycling

Type	Configuration	TC	Beam no.	Max Load (kN)	Mean Load (kN)	Failure Mode
Control beam		0	CF1	52.6	46.8	S
			CF2	52.8		F&S
			CF3	35.2		S
		120	CF4	49.7	51.7	S
			CF5	50.7		F&S
			CF6	54.8		F&S
		180	CF7	47.7	49.5	S
			CF8	47.7		F&S
			CF9	53.2		S

7.8.1.2 Beams with sufficient shear reinforcement

The test results of control beams with sufficient shear reinforcement after zero thermal cycles are shown in Figure 7.7a. It can be seen that beams CS1, CS2 and CS3 followed the same behaviour. For beams CS1, CS2 the cracks initiated on the tension side and become visible when the load carrying capacity exceeded 15.0 kN and then the flexural cracks propagated towards the compression zone. At about 51.0 kN and a mid-span deflection of 5.0 mm a slight drop in load carrying capacity was observed caused by the yielding of steel. Thereafter, because of the strain hardening of the steel, the load increased slightly again. Both beams failed in flexural mode (Plate 7.2) with an ultimate load of 53.3 kN, whereas, beam CS3 failed also in flexural mode with maximum load of 52.6 kN.

For beams exposed to 120 thermal cycles, the typical load-deflection behavior can be seen in Figure 7.7b. The results of the beams are similar to each other; the beams cracked in flexure in the middle third of the tension face when the load achieved 15.0 kN. These flexural cracks led to a reduction in the concrete stiffness. At about 50.6 kN for beams CS4 and CS5 and a mid-span deflection which exceeded 5.2 mm and 4.0 mm respectively, the load decreased due to the yielding of steel, whereas the load for beam CS6 reduced when it is about 52.1 kN and a mid-span deflection of 4.0 mm. Thereafter, the load carrying capacity increased slightly, because of the strain hardening behaviour of the steel. The beams failed with flexural mode at ultimate loads of 53.8 kN, 54.6 kN and 55.2 kN, respectively.

Figure 7.7c shows the load deflection response of beams tested after 180 thermal cycles. The test results reveal that the beams CS7, CS8 and CS9 behaved similar to those beams exposed to 120 thermal cycles, however with quite a difference in the ultimate load. These beams also failed in the flexural mode with a maximum load carrying capacity of 54.3 kN for CS7, and 54.0 kN for CS8, while the ultimate load for CS9 was 48.3 kN.

The results which are included in Table 7.3 reveal that the effect of thermal cycling on the ultimate load of control beams with shear reinforcement is very small. Moreover, the mean value of the maximum load for beams tested at room temperature is 53.0 kN, and after 120 thermal cycles increased to 54.5 kN. With a further increase in the thermal cycles to 180 the mean value of the maximum load reduced slightly to 52.2 kN.

Plat 7.1: Typical shear failure in control beams reinforced only in flexure

Plat 7.2: Typical flexural failure in control beams reinforced in shear and flexure
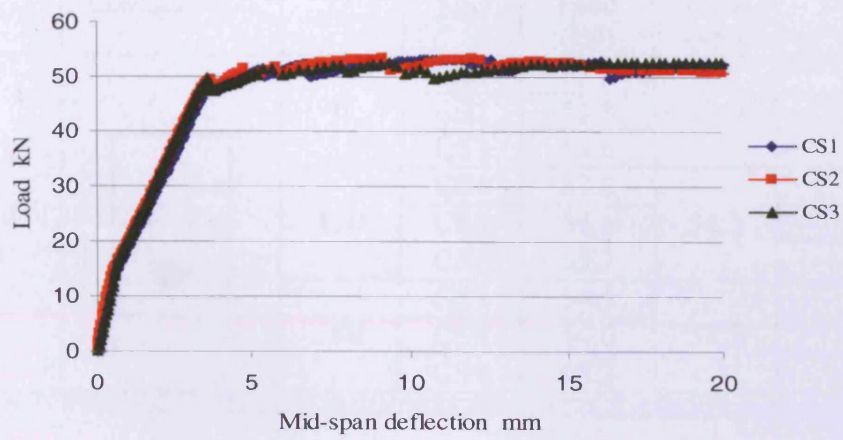
(a)
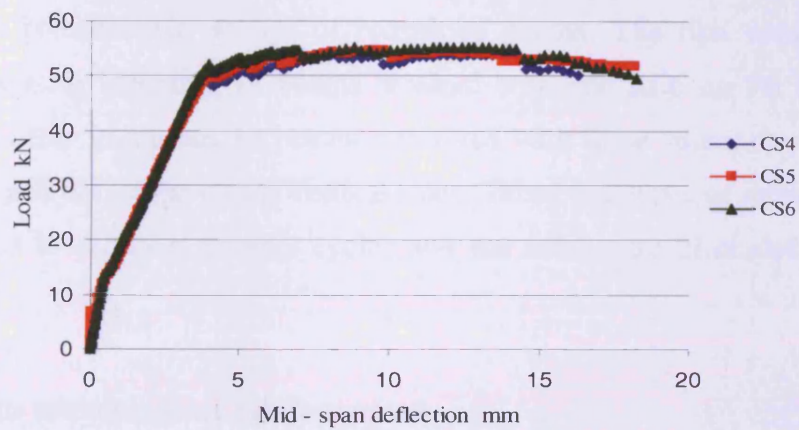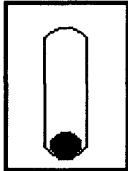
(b)
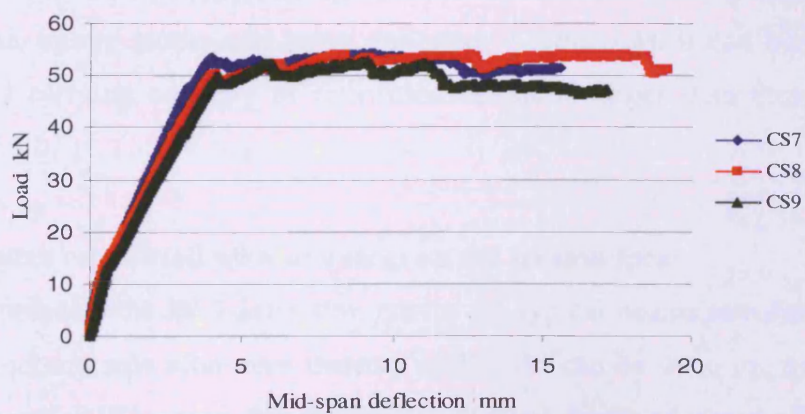
(c)

Figure 7.7 Load Deflection responses of control beams with sufficient shear reinforcement, after (a) zero thermal cycles (b) 120 thermal cycles and (c) 180 thermal cycles

161

Table 7.3 Four point test results of control beams with sufficient shear reinforcement after thermal cycling

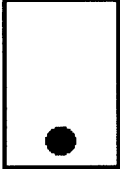| Type	Configuration	TC	Beam No.	Max Load (kN)	Mean Load (kN)	Failure Mode
Control beam		0	CS1	53.3	53.0	F
			CS2	53.3		F
			CS3	52.6		F
		120	CS4	53.8	54.5	F
			CS5	54.6		F
			CS6	55.2		F
		180	CS7	54.3	52.2	F
			CS8	54.0		F
			CS9	48.3		F

7.8.2 Retrofitted beams

This section presents two groups of retrofitted beams. The first configuration of retrofitting system including 18 beams repaired with one strip on the tension side, whereas the other group has 18 beams retrofitted with three strips, one strip on the tension face and two strips on the vertical sides. These two types of retrofitted beams were exposed to different thermal cycles and the results are discussed in the next sections.
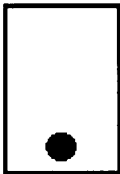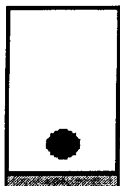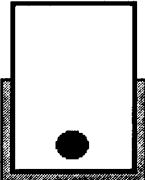
7.8.2.1 Beams without shear reinforcement

To evaluate the efficiency of the repairing system on the beams reinforced only in the flexure, there are some parameters that should be considered such as thermal cycling, ultimate load, failure mode, and beam deflection (Table 7.4). It can be seen clearly that the load carrying capacity of retrofitted beams is larger than those of control beams.

7.8.2.1.1 Beams retrofitted with one strip on the tension face

Figure 7.8a presents the load deflection curves for typical beams retrofitted with one strip on the bottom side after zero thermal cycles. As can be seen, the measured test results for beam R1F1 show that the initial flexural crack appeared after the load reached 42.0 kN. The crack started in the tension strip and then propagated through the concrete towards the compressive zone.

Table 7.4 Four point test results for control and retrofitted beams without shear reinforcement after thermal cycling (TC)

Type of beams	Configuration	TC	Beam no.	Max Load P kN	Mean Load P kN	Increase or Decrease in P relative to 0 TC %	$\delta_{(P=20)}$ (mm)	$\delta_{(P=30)}$ (mm)	Failure Mode
Control		0	CF1	52.6	46.9	-	1.008	1.855	S
			CF2	52.9			1.995	2.191	F&S
			CF3	35.2			1.359	2.314	S
		120	CF4	49.8	51.7	10.2	0.719	1.585	S
			CF5	50.7			1.195	2.068	F&S
			CF6	54.8			0.657	0.905	F&S
		180	CF7	47.5	49.4	5.3	1.217	2.198	S
			CF8	53.2			1.070	1.863	F&S
			CF9	47.5			1.158	2.112	S
Retrofitted		0	R1F1	60.2	59.7	-	0.658	0.888	F
			R1F2	61.9			0.615	0.800	S
			R1F3	57.2			0.565	0.802	F&S
		120	R1F4	64.5	60.0	0.5	0.565	0.755	F&S
			R1F5	54.8			0.645	0.905	F&F
			R1F6	60.8			0.663	0.909	F
		180	R1F7	58.5	59.8	0.1	0.669	0.931	F&S
			R1F8	61.5			0.648	0.901	F
			R1F9	59.5			0.661	0.916	F&S
		0	R3F1	103.2	95.1	-	0.530	0.765	F
			R3F2	90.8			0.558	0.765	F
			R3F3	91.3			0.610	0.804	F
		120	R3F4	88.4	91.4	-3.4	0.571	0.779	F
			R3F5	86.5			0.596	0.829	F
			R3F6	99.5			0.528	0.722	F
		180	R3F7	78.4	79.2	-16.7	0.632	0.883	F
			R3F8	68.6			0.568	0.816	F
			R3F9	90.8			0.587	0.815	F

163

As the load was increased, this crack opened more and became the dominant crack whereas some other cracks with different directions initiated as the load was further increased. Beam R1F1 failed in flexural mode with a maximum load of 60.2 kN (Plate 7.3), while beam R1F2 and R1F3 behaved similar to beam R1F1 where the loading stage of beams R1F2 and R1F3 started with a constant stiffness until the load exceeded 45.0 kN at which the stiffness slightly decreased and hairline cracks started to appear in the strip at the mid-span of the beams and then propagated to the concrete. At a load of 52.0 kN a diagonal crack started opening to create a shear crack which progressed diagonally toward the load point. As can be seen in Figure 7.8a, beam R1F2 failed in shear mode with peak load of 61.9 kN and beam R1F3 failed in a combination of flexural and shear modes with a maximum load of 57.2 kN (Plate 7.4).

Figure 7.8b shows the test results of retrofitted beams exposed to 120 thermal cycles. In beams R1F4 and R1F5, the flexural crack initiated in the middle of the beam when the load exceeded 45.0 kN and started to become visible after the load reached 50.0 kN at a mid-span deflection of about 1.4 m and 1.8 mm, respectively. The crack initiated in the tension strip then propagated through the beam towards the compressive zone. As the beam carried more load with reduced stiffness, a reduction in load was observed at about 64.5 kN and mid-span deflection of 3.4 mm for R1F4, then the load dropped to 30.0 kN. This change in the curve was influenced by a shear crack which started opening near to the support and then moved up towards the load point. Both beams failed in a combination of flexural and shear modes with an ultimate load of 64.5 kN and 54.8 kN, respectively.

Beam R1F6 followed the same response where the beam cracked under the load point at load of 41.0 kN. As the load was further increased the crack continued to propagate and the number of cracks increased in different directions. When the load achieved the maximum value of 60.8 kN and mid-span deflection of 3.8 mm the load versus deflection curve dropped slightly to 55.0 kN and then failed in flexural mode.

The load versus mid-span deflection response of beams tested after 180 thermal cycles are shown in Figure 7.8c. A crack appeared at a load of 46.0 kN in the bottom strip and then propagated to the compression side. With further increase in the load, other cracks initiated horizontally and diagonally at the middle of the beams.

164

Beams R1F7 and R1F9 failed in combination of flexural and shear modes with a maximum load of 58.5 kN and 59.5 kN respectively, whereas beam R1F8 failed in flexural mode with an ultimate load of 61.5 kN.

(a)

(b)

(c)

Figure 7.8 Load-Deflection response of beams without shear reinforcement retrofitted with one strip on the tension side, after: (a) zero thermal cycles, (b) 120 thermal cycles, and (c) 180 thermal cycles
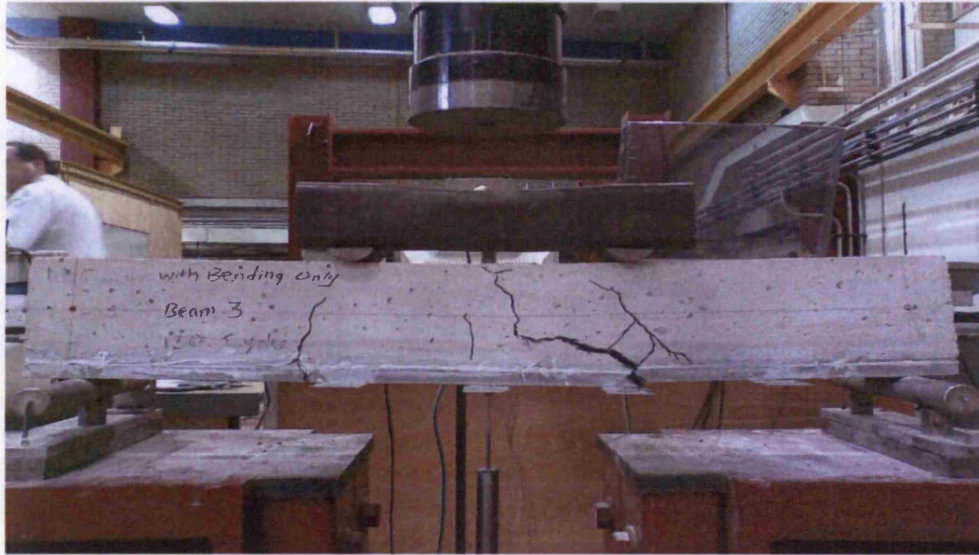
Plate 7.3 Typical flexural failure of retrofitted beam with one strip in the bottom and without shear reinforcement

Plate 7.4 Combination shear and flexural failure of retrofitted beam on tension face and without shear reinforce

The results of the retrofitted beams with one strip in tension face revealed that there is no damage in the repairing system or any debonding. As thermal cycling increased the mean value of the load carrying capacity seems to be unchanged. This is due to stability of concrete stiffness which is attributed to the non- thermal cycling effect on the microstructure of the concrete beams.

7.8.2.1.2 Beams retrofitted with three long strips

The retrofitting configuration using three strips has been explained before (Figure 7.2b); it consists of one strip bonded to the bottom side and another two strips retrofitted on the vertical sides. The beams were placed in the electrical furnace for the required thermal cycles. Thereafter, three beams were tested at room temperature, three after 120 thermal cycles and the remaining three tested after 180 thermal cycles.

The test results for beams not exposed to thermal cycles are shown in Figure 7.9a. The load deflection response of beams R3F1, R3F2 and R3F3 exhibited the same behavior. In the first stage of loading the initial crack appeared when the load exceeded 89.0 kN. It was located in the middle third and under the load point regions (Plate 7.5). The beams failed in pure flexure where the peak load for beam R3F1 reached 103.2 kN, then the load-deflection curve started to descend gently, and the ultimate loads of beams R3F2 and R3F3 were 90.8 kN and 91.3 kN, respectively. As can be seen in Table 7.4, the mean value of the maximum load increased from 46.9 kN for control beams to 95.1 kN for retrofitted beams with three strips.

Figure 7.9b presents the load versus mid-span deflection response of the next three beams exposed to 120 thermal cycles. The behaviour of the beams is almost similar to those exposed to no thermal cycles, where the beams exhibited a linear elastic behavior up to 60.0 kN followed by a deviation in the load-deflection curve caused be the initiation of the crack. For beams R3F4 and R3F5, the crack started to become visible in the bottom strip after the load reached of 84.5 kN with mid-span deflection of 2.3 mm and 2.6 mm, the crack propagated through the vertical strips towards the compressive region. The maximum load carrying capacity for beams R3F4 and R3F5 was 88.4 kN and 86.5 kN, respectively, whereas beam R3F6 carried more load than the other two beams; it failed in pure flexure with an ultimate load of 99.4 kN.

As can be seen in Table 7.4, the mean value of the peak load increased from 51.7 kN for control beams to 91.4 kN for bonded beams after exposure to the same number of thermal cycles.

The load-deflection response of beams retrofitted with three strips on the tension face and the vertical sides after 180 Thermal cycles is shown in Figure 7.9c. In the early stage of loading, two beams R3F7 and R3F8 cracked at about of 63.5 kN, the crack appeared in the tension face strip at the mid-span region and then propagated to the sides towards the compression zone. With a further increase in the load, the crack opened gradually until the load carrying capacity reached the maximum. Thereafter, the load-deflection curve started to descend gently; both beams failed in the flexural mode with an ultimate load of 78.4 kN and 68.6 kN. The beam R3F9 followed the same trend as the other two but it failed with a maximum load capacity of 90.8 kN.

From Table 7.4, the mean value of the ultimate load of the beams after 180 thermal cycles increased from 49.4 kN for control beams to 79.2 kN for retrofitted beams with three strips. Furthermore, due to thermal cycling, there were no significant effects observed on the repairing system, and also no debonding failure was revealed.
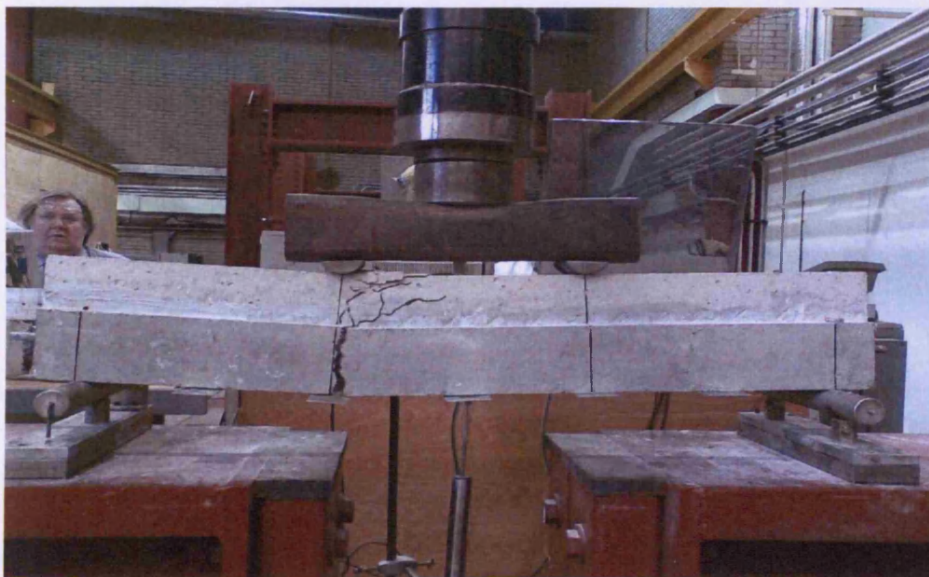
Plate 7.5 Flexure failure of retrofitted beam with three strips and without shear reinforcement
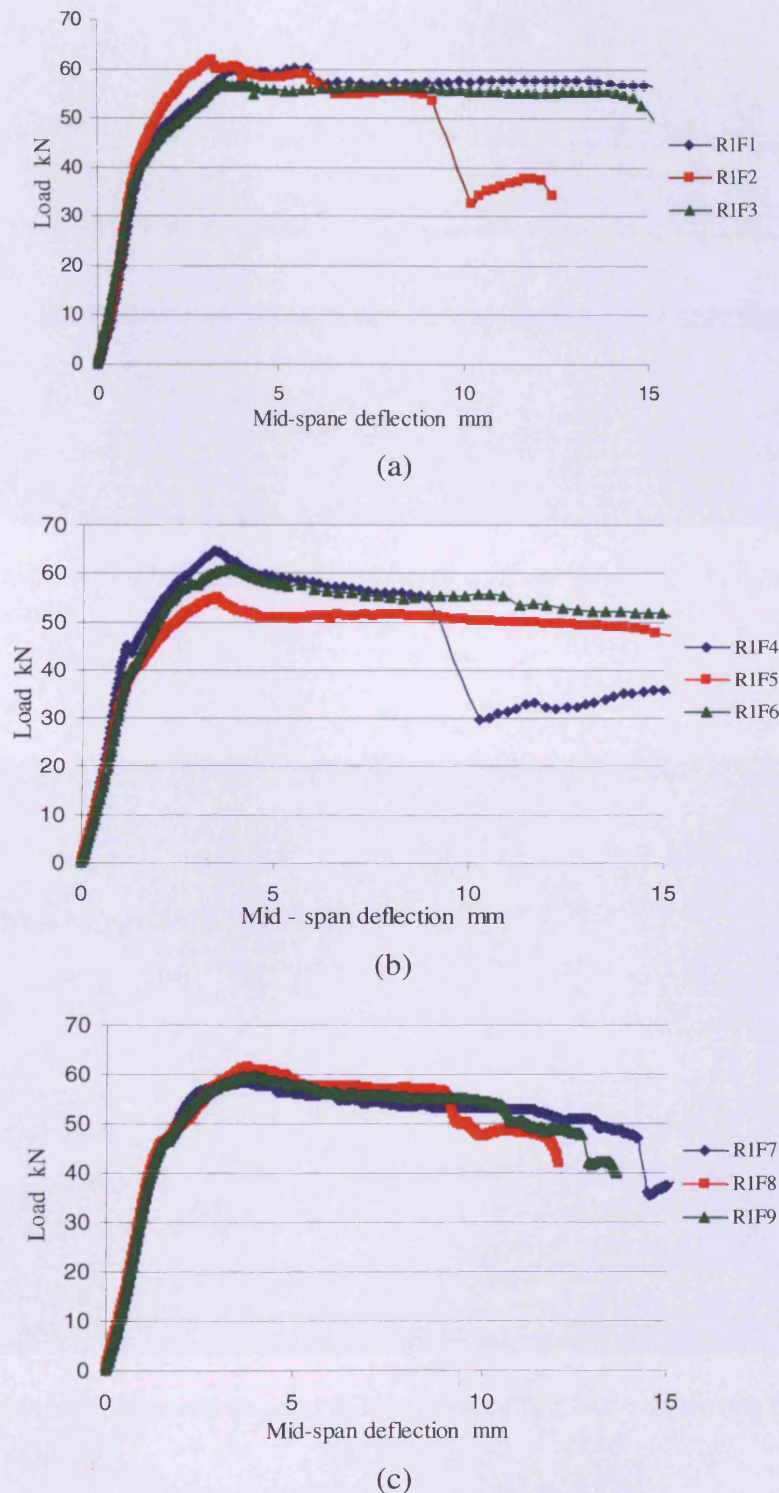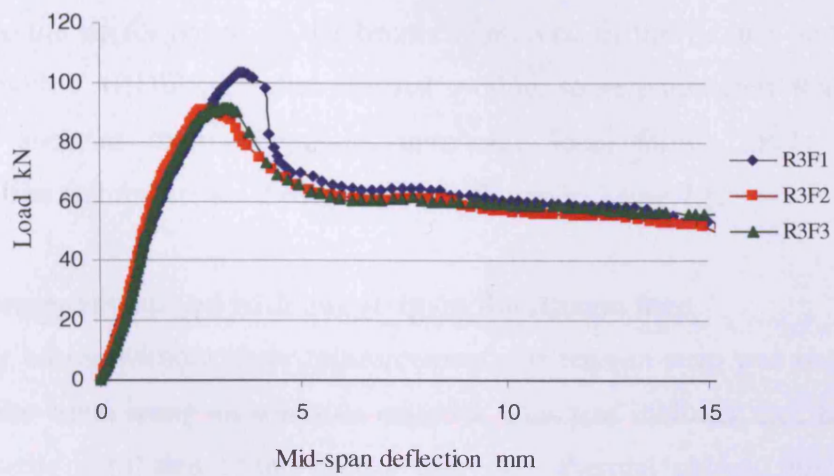
(a)
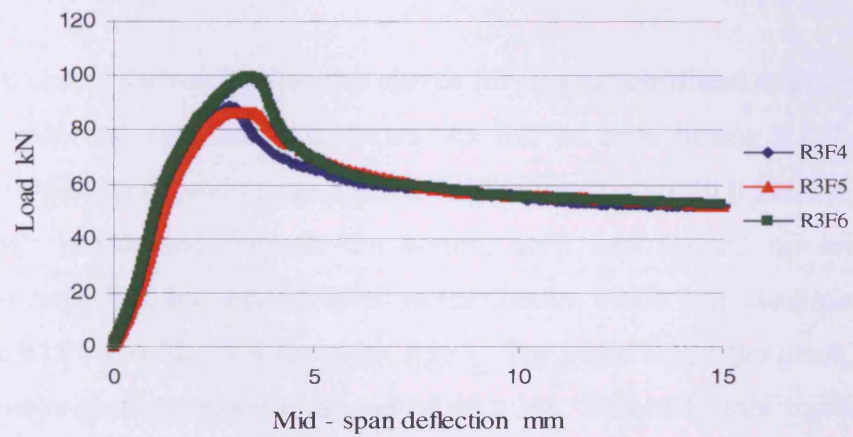
(b)
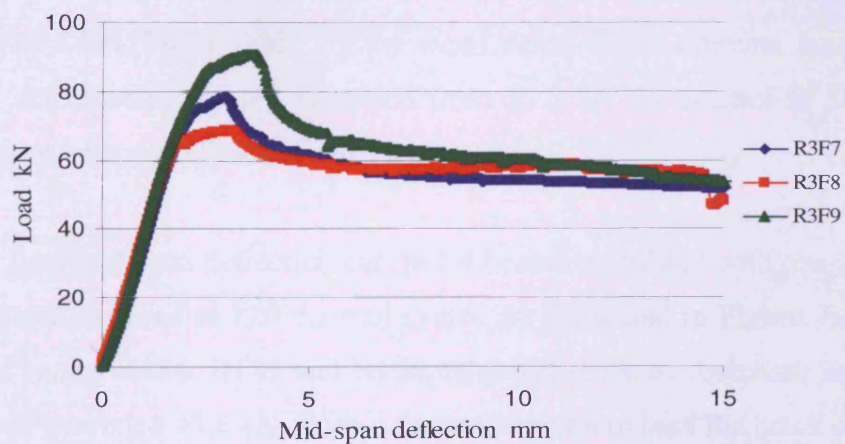
(c)

Figure 7.9 Load-Deflection responses of beams without shear reinforcement retrofitted with three strips, one the tension side, and two in vertical sides after: (a) zero thermal cycles, (b) 120 thermal cycles, and (c) 180 thermal cycles

169

7.8.2.2 Beams with sufficient shear reinforcement

To evaluate the performance of the beams reinforced in the flexure and shear and retrofitted with CARDIFRC® after thermal cycling, some parameters that should be considered such as thermal cycling, maximum load, failure mode, and beam deflection. The test results for these beams are shown in Table 7.5.
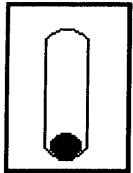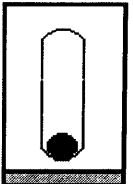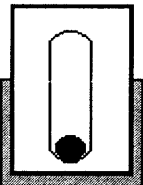
7.8.2.2.1 Beams retrofitted with one strip on the tension face

As with the beams without shear reinforcement, the tension strip was bonded on the bottom of the beam using an adhesive material. This part includes nine beams, three of which were retrofitted beams tested after zero thermal cycles, three after 120 thermal cycles, and the remaining three beams after 180 thermal cycles.

Figure 7.10a shows the load-deflection curves for beams retrofitted with one strip on the bottom side and exposed to 0 cycles. As can be seen beams R1S1and R1S3 followed a similar trend and cracked when the load exceeded 40.0 kN. At load 55.5 kN the crack propagated through the bottom strip and moved up towards the compression zone. The two beams failed in the flexure mode with maximum load of 59.6 kN for R1S1 and 52.5 kN for beam R1S3. For beam R1S2 the crack started in the region under the load point at a load of 42.0 kN. With a further increase in the load a shear crack initiated near to the support and caused a slight drop in the load with a reduction in stiffness. The beam failed in shear at a maximum load carrying capacity of 65.5 kN. From Table 7.5 the mean value of the ultimate load of beams tested after zero thermal cycles increased from 53.0 kN for control to 59.2 kN for retrofitted ones with a total increase of 11 percent.

The typical load-mid span deflection curves for beams retrofitted with one strip on the bottom side and exposed to 120 thermal cycles are presented in Figure 7.10b. It can be seen that beams R1S4, R1S5 and R1S6 exhibited the same behavior and cracked when the load exceeded 45.0 kN. With a further increase in load the crack opened and propagated through the sides towards the compression zone. At a load of 55.0 kN the top fibres of beams between the load points were crushed and some of cracks initiated horizontally and diagonally in the middle third of the beams. The beams failed in the flexural mode with a maximum load of 61.0 kN, 59.5 kN and 63.8 kN, respectively.

Table 7.5 Four point test results for control and retrofitted beams with sufficient shear reinforcement after thermal cycling (TC)

Type of beams	Configuration	TC	Beam no.	Max Load P (kN)	Mean Load P (kN)	Increase or Decrease in P relative to 0 TC %	$\delta_{(P=20)}$ (mm)	$\delta_{(P=30)}$ (mm)	Failure mode
Control		0	CS1	53.3	53.0	-	1.105	1.999	F
			CS2	53.3			1.021	1.898	F
			CS3	52.6			1.002	1.855	F
		120	CS4	53.8	54.5	2.8	1.130	2.057	F
			CS5	54.6			1.216	2.055	F
			CS6	55.2			1.059	1.985	F
		180	CS7	53.5	53.5	0.9	1.113	1.883	F
			CS8	54.2			1.168	2.123	F
			CS9	52.8			1.285	2.183	F
Retrofitted		0	R1S1	59.6	59.2	-	0.668	0.916	F
			R1S2	65.5			0.525	0.755	S
			R1S3	52.5			0.478	0.725	F
		120	R1S4	61.0	61.4	3.7	0.622	0.865	F
			R1S5	59.5			0.533	0.735	F
			R1S6	63.8			0.655	0.931	F
		180	R1S7	59.9	58.0	-2.0	0.656	0.933	F
			R1S8	62.7			0.609	0.882	F
			R1S9	51.4			0.570	0.844	F
		0	R3S1	87.8	88.9	-	0.598	0.790	F
			R3S2	96.7			0.537	0.728	F
			R3S3	82.4			0.665	0.888	F
		120	R3S4	79.5	91.1	2.5	0.529	0.716	F
			R3S5	102.2			0.523	0.699	F
			R3S6	91.8			0.601	0.792	F
		180	R3S7	90.2	88.7	-0.2	0.544	0.793	F
			R3S8	86.9			0.571	0.807	F
			R3S9	89.0			0.565	0.813	F

The mean value of the maximum load carrying capacity of the beams increased from 54.5 kN for control beams to 61.4 kN for retrofitted beams which were exposed to the same number of thermal cycles.

Figure 7.10c explains the test results of three retrofitted beams exposed to 180 thermal cycles. As shown in the Figure, the response of beams R1S7 and R1S8 is very similar to those exposed to120 thermal cycles. The beams failed in flexure with a maximum failure load of 59.9 kN and 62.7 kN, respectively. However, beam R1S9 carried a lower load than the other beams; it failed in the flexure mode with maximum load of 51.4 kN. As can be seen from Table 7.5 after 180 thermal cycles the mean value of the failure load of the beams increases from 53.5 kN for control to 58.0 kN for retrofitted beams giving a total increase of 8.5 percent.

7.8.2.2.2 Beams retrofitted with three long strips

Nine beams were retrofitted with three continuous strip bonded on the bottom and vertical sides. The three sides of the beams were fully covered by the strips. The beams were exposed to different thermal cycling thereafter; three beams were tested after no thermal exposure, three after 120 thermal cycles, and the remaining three beams tested after 180 thermal cycles. The plots of the load-displacement curves of beams retrofitted with three strips can be seen in Figure 7.11.

The load versus the mid-span deflection curves for beams R3S1, R3S2 and R3S3 exposed to no thermal cycles are shown in Figure 7.11a. The beam behaviour is similar to each other, with the crack becoming visible when the load reached 85.0 kN. The crack initiated near the middle of the tension strip and propagated up through the vertical strip towards the compression zone. It was possible to see the steel fibre in the bottom strip. After the load carrying capacity exceeded the peak, the load-deflection curves dropped gradually. The beams failed in flexure with an ultimate load of 87.8 kN, 96.7 kN, and 82.4 kN, respectively. The mean value of the ultimate load of retrofitted beams was about 67 percent higher than that of control beams (Table 7.5).
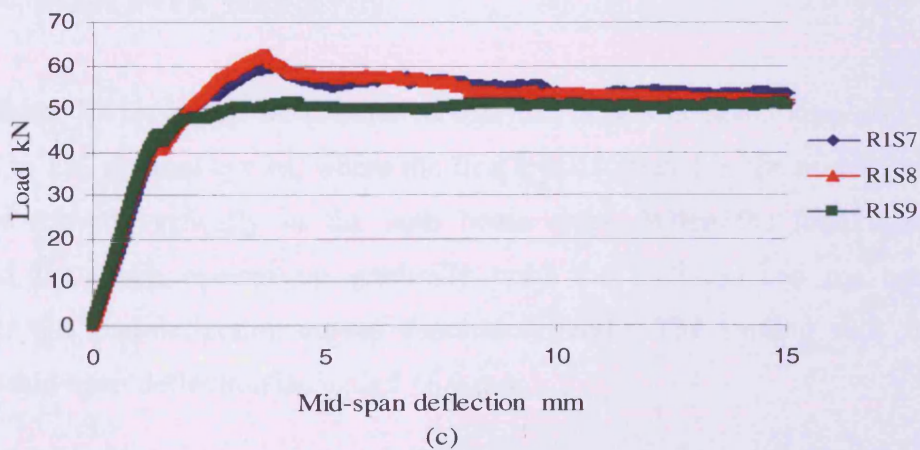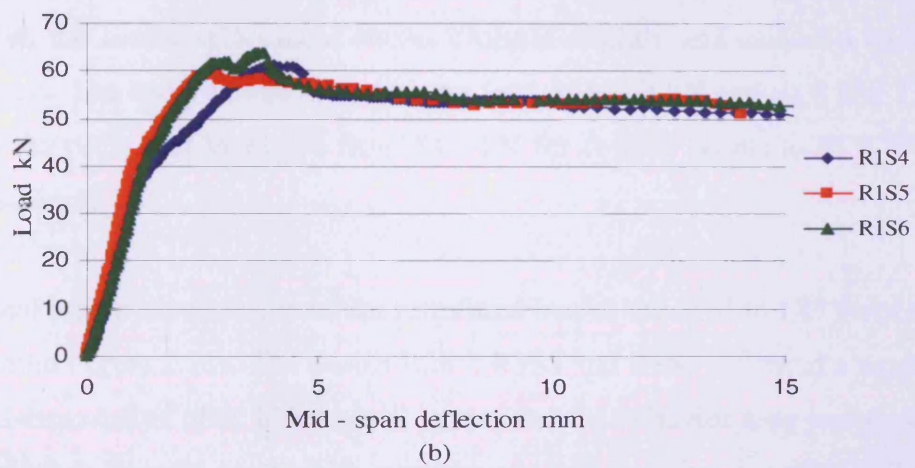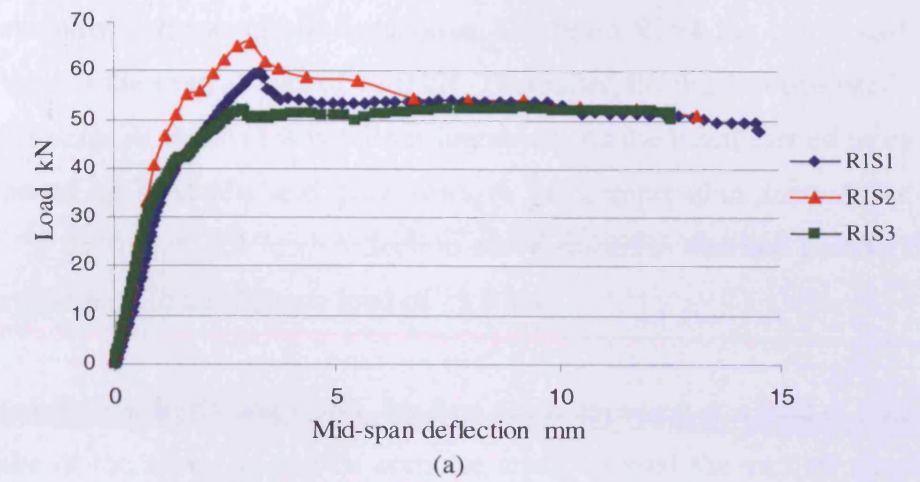
Figure 7.10 Load-Deflection response of beams with sufficient shear reinforcement retrofitted with one strip in the tension side, after: (a) zero thermal cycles, (b) 120 thermal cycles, and (c) 180 thermal cycles

173

The load-deflection response of the beams tested after 120 thermal cycles is shown in Figure 7.11b. The test results revealed that at the early stage of loading, the three beams exhibited a linear elastic behaviour. For beam R3S4 the crack started in the middle third of the span at load of 72.0 kN. Thereafter, the crack propagated vertically in the side strips as the load was further increased. As the beam carried more load the crack opened up gradually and grew towards the compression zone. After the load reached the maximum, the load-deflection curve started to descend gently. The beam failed in flexure with an ultimate load of 79.5 kN.

Of the two beams R3S5 and R3S6, the first crack appeared at a load of 90.0 kN near the middle of the span. As can be seen the crack crossed the vertical strips in both sides of the beams and opened up gradually until the load exceeded the peak. Thereafter, the load-displacement curves dropped slightly and caused a reduction in the stiffness. The beam failure occurred at a load of 102.2 kN and 91.8 kN. The mean value of the peak load increased from 54.5 kN for control beams to 91.1 kN for the retrofitted ones.

The typical load-deflection curves for retrofitted beams exposed to 180 thermal cycles are shown in Figure 7.11c. The beams R3S7, R3S8 and R3S9 followed a similar trend to those beams tested after 120 thermal cycles and the behavior also was similar. The beams failed in flexural mode with a maximum load carrying capacity of 90.23 kN, 86.93 kN, and 88.99 kN, respectively.

From Figure 7.11c, it can be concluded that the beams behaved similarly to those exposed to 120 thermal cycles, where the first crack initiated in the middle third span and then moved vertically to the both beam sides. When the load was further increased the crack opened up gradually until the load reached the maximum, thereafter the load-deflection curves descended gently. The loading was continued until the mid-span deflection exceeded 16.0 mm.
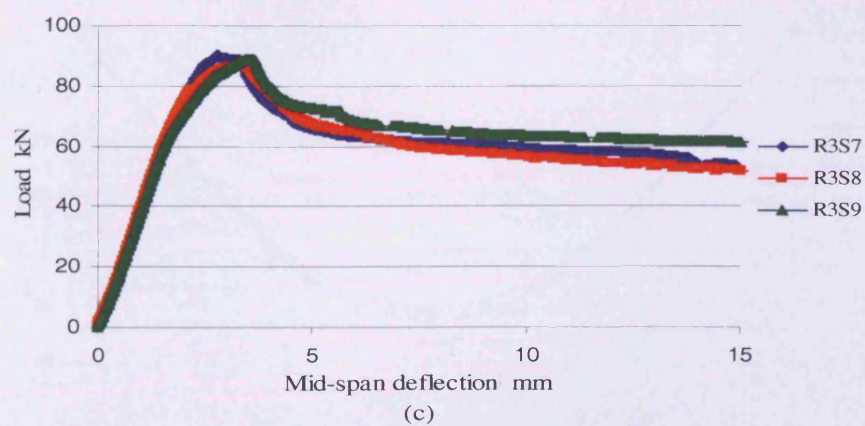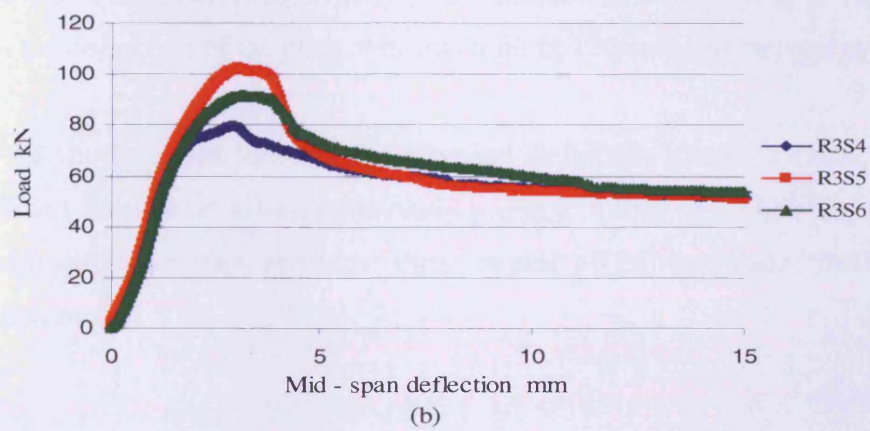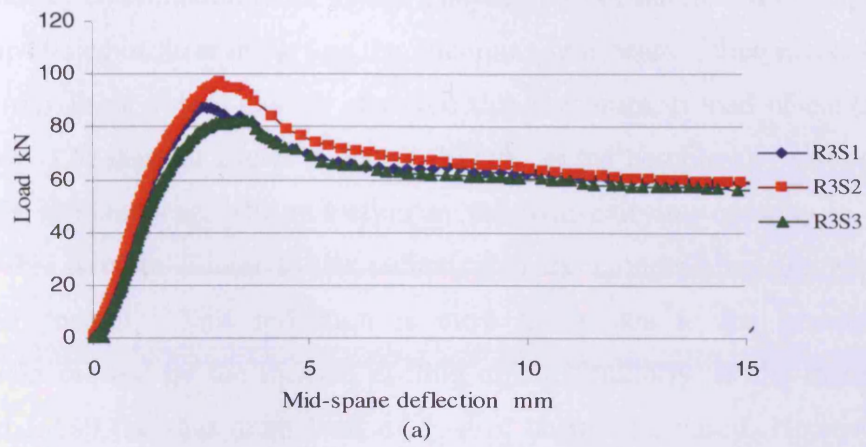
Figure 7.11 Load-Deflection responses of beams with sufficient shear reinforcement retrofitted with one strip in the tension face, and two in the vertical side, after: (a) zero thermal cycles, (b) 120 thermal cycles, and (c) 180 thermal cycles

7.9 Discussion

The test results revealed that the control beams reinforced in flexure only exhibited a shear mode or combination mode (shear and flexural) of failure. Of the eight beams, four beams failed in shear mode and the remaining four beams failed in a combination mode. From Table 7.4, it can be observed that the ultimate load of control beams exposed to 120 thermal cycles reduced slightly as the compressive strength of the beam mix also reduced. The reduction in the load carrying capacity is about 2.9 percent; this is quite similar to the reduction in the compressive strength which is equal 3.2 percent. This reduction is most likely due to the presence of the microcracks created by the thermal cycling effect. Similarly, as the thermal cycles increased to180 the maximum load of control beams decreased. However, due to decrease in the load carrying capacity and concrete stiffness of the control beams, the mid span deflection increased slightly after different thermal cycling. Figure 7.12 compares the deflection of the control beams after 0, 120 and 180 thermal cycles.

Figure 7.13 shows a comparison of the typical deflection shapes of retrofitted and control beams tested after different thermal cycling at a load of 20 kN. The retrofitted beams with only one strip exhibited three modes of failure (shear, flexure and a combination mode).
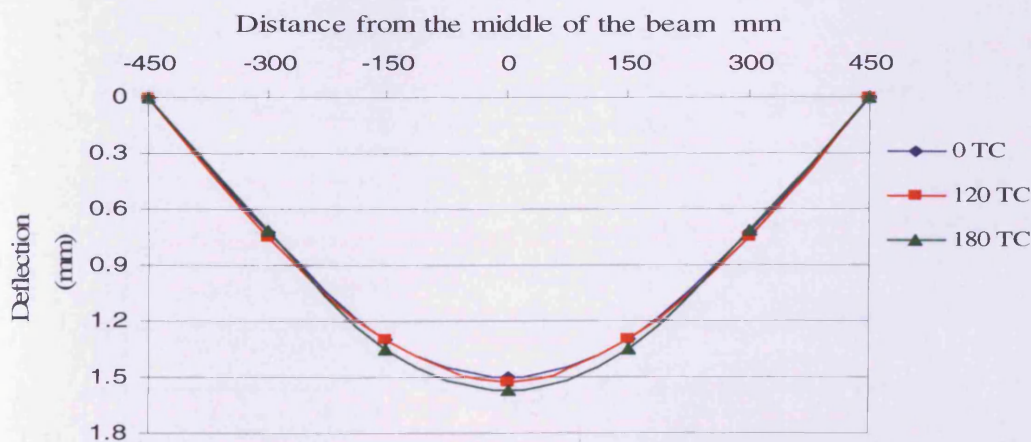
Figure 7.12 Typical deflections of control beams without shear reinforcement exposed to 0, 120 and 180 thermal cycles
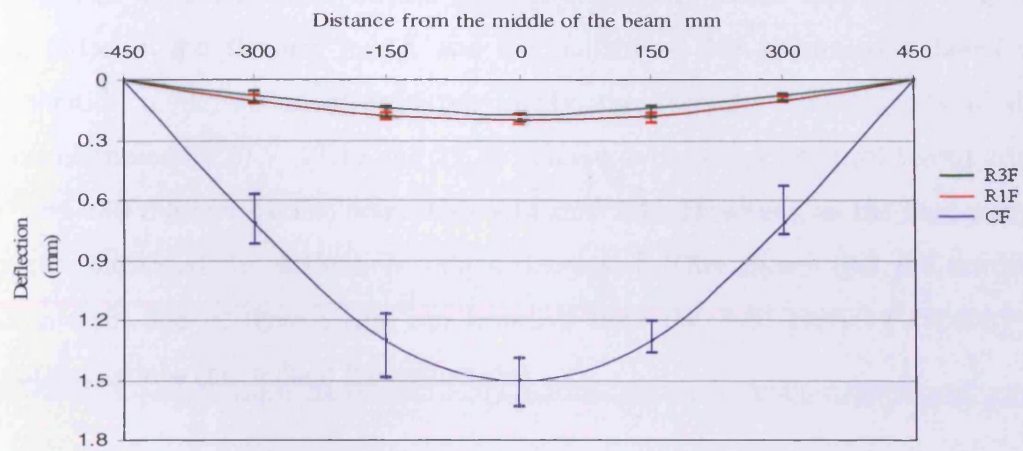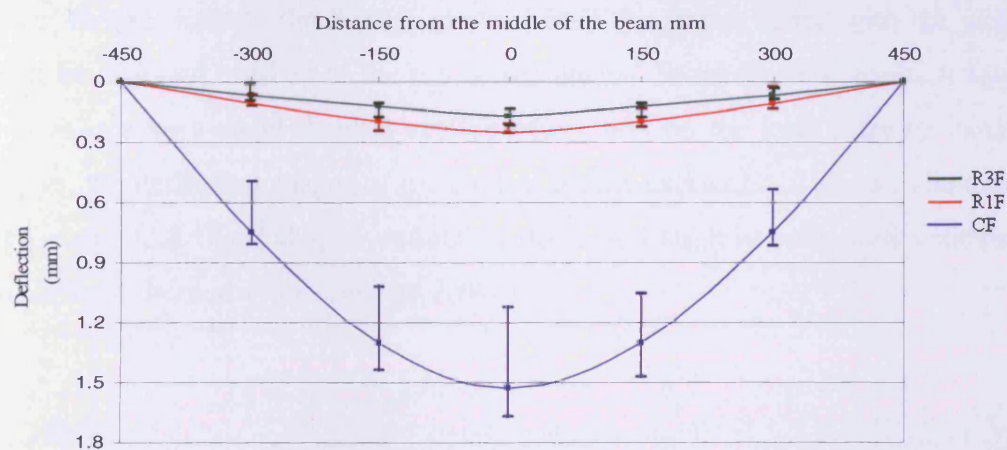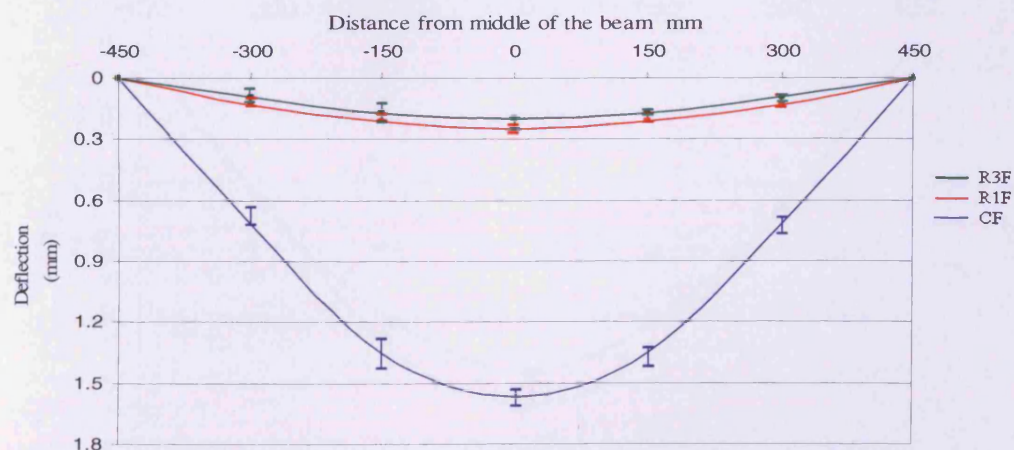
Figure 7.13 Typical deflection of beams without shear reinforcement retrofitted with one strip on tension face and three continual strips bonded on the bottom and vertical sides compared with that of control beams at 20 kN, after; (a) zero thermal cycles, (b) after 120 thermal cycles and (c) after 180 thermal cycles

Of the nine test beams, one beam failed in shear because the flexural strength at the mid-span of the beam exceeded the shear strength near to the support, and three of them failed in the flexural mode, and the remaining five beams were failed in a combination mode. As mentioned previously, the carrying load capacity of these beams increased by 27.7, 17.19 and 21.39 percent over those of control beams after 0, 120 and 180 thermal cycles, respectively (Table 7.4). However, as the load carrying capacity increased the deflection values decreased. This shows that the retrofitted system with one or three strips can improve both the load carrying capacity and flexural response (i.e. reduce the deflection).

The failure mode of control beams reinforced in flexure and shear exhibited only one mode of failure, namely the flexure mode, where the beams failed with the yield of steel in tension and crushed at the top of the beams. From the test results it follows that there is a very small thermal cycling effect was on the load carrying capacity. However, the deflection shapes of the control beams exposed to 120 and 180 thermal cycles reveal that the mid-span deflection decreased slightly compared with beams exposed to no thermal cycles (Figure 7.14).
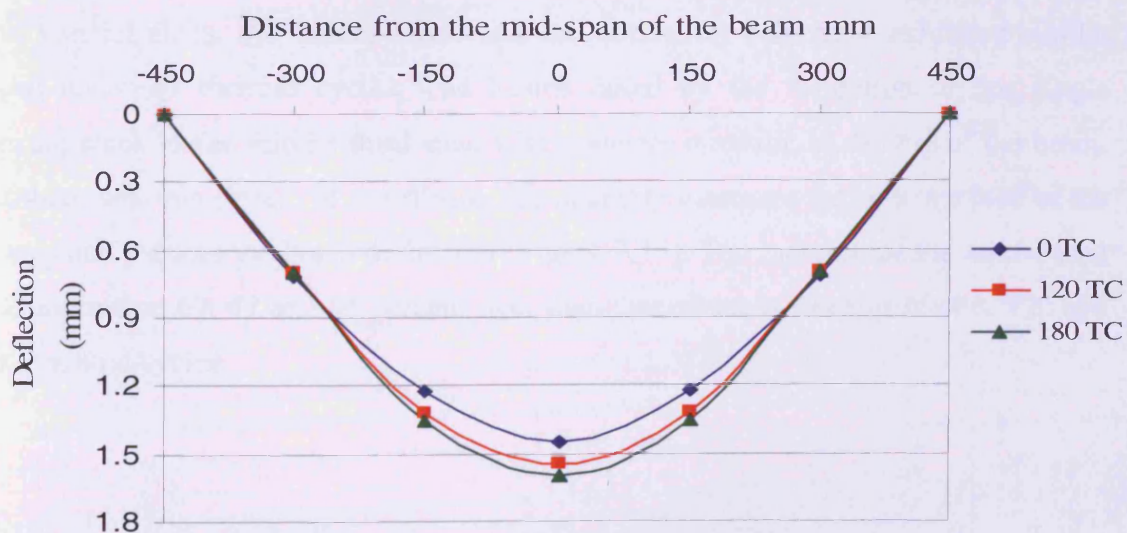
Figure 7.14 Typical deflections of control beams with sufficient shear reinforcement exposed to 0, 120 and 180 thermal cycles

As can be seen from Table 7.5, all beams retrofitted with one strip on the bottom side and tested after different thermal cycling failed in pure flexure except one beam which failed in shear and was exposed to no thermal cycles. Generally, there is no sign of deterioration in the repairing system and the flexural failure that was observed in the beams occurred in the middle third of the span and then extended towards the concrete top fibre between the load points. As mentioned earlier, the mean value of the ultimate load of retrofitted beams is higher than the control beams. The configuration that uses one strip bonded to the tension faces not only improves the load carrying capacity, but also increases the concrete stiffness and reduces the crack opening.

The results revealed also that the mean value of the maximum load of retrofitted beams compared with control beams increased from 53.05 kN to 59.18 kN, from 54.56 kN to 61.42 kN and from 53.47 kN to 58.01 kN for beams tested after 0, 120 and 180 cycles, respectively. Moreover, the mean value of the failure load of retrofitted beams increased slightly from 59.18 kN to 61.42 kN after 120 thermal cycles, and then decreased to 58.01 kN, giving a total decrease in failure load of 1.97 percent after 180 thermal cycles.

With regard to the beams retrofitted with three continuous strips bonded to the bottom and vertical sides, the failure mode and the deflection behaviour exhibited similar trend under all thermal cycles. The beams failed by the formation of one single flexure crack in the middle third span with concrete crushing in the top of the beam. Furthermore, this system of retrofitting considerably increases the ultimate load of the beams and reduces the beam deflection (Figure 7.15). The increase of the failure load was more than 67, 67 and 65 percent over than that of control beams after 0, 120 and 180 thermal cycles.
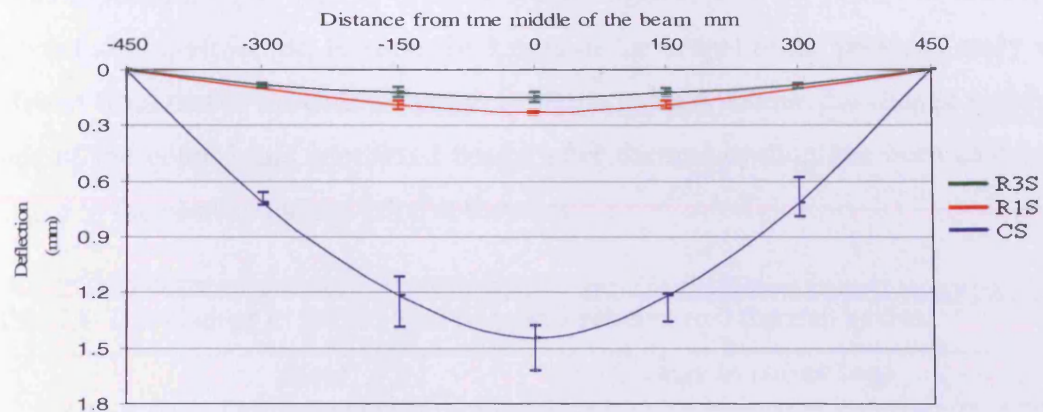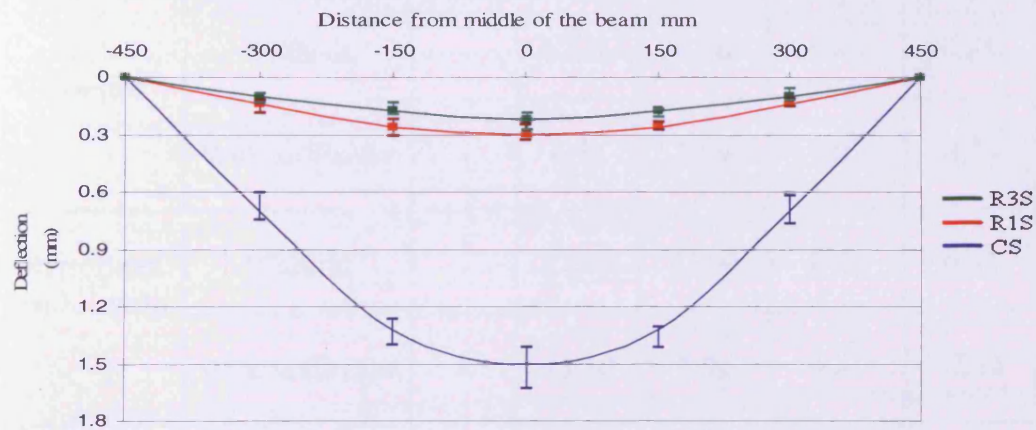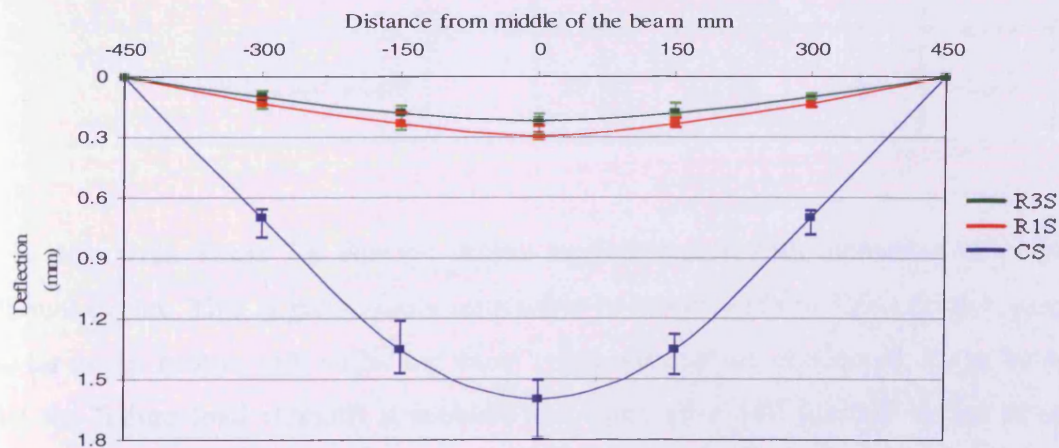
Figure 7.15 Typical deflection of beams with sufficient shear reinforcement retrofitted with one strip on tension face and three continual strips on the bottom and vertical sides compared with that of control beams at 20 kN, after; (a) zero thermal cycles, (b) after 120 thermal cycles and (c) after 180 thermal cycles

7.10 Influence of increased thermal cycling on the control and retrofitted beams

This section will give an overview of the results of a previous study (Farhat, 2004) on beams exposed to 0, 30 and 90 thermal cycles, together with the results of the beams reported above. However, because the length of the beams in the previous study was different from that in the present study, 1100mm against 900mm the change in failure loads of the control and retrofitted beams after thermal cycling has been calculated relative to the corresponding value at 0 cycles.

Table 7.6 The change in failure load of beams relative to 0 thermal cycles.

Beam type	Shear Reinforcement	% Change in failure load				
		0 TC	30TC	90TC	120TC	180TC
Control	Without	-	17.36	4.26	9.46	5.55
	With sufficient	-	4.38	3.79	2.85	0.79
Retrofitted with 1 strip	Without	-	27.05	13.90	0.43	0.32
	With sufficient	-	12.10	1.09	3.61	-2.14
Retrofitted with 3 strips	without	-	18.40	15.76	-3.83	-16.63
	With sufficient	-	18.66	12.13	2.48	-0.27

It is clear from Table 7.6 that the failure load decreases with increasing number of thermal cycles. This is particularly noticeable in beams without shear reinforcement. As far as the beams with sufficient shear reinforcement are concerned, it can be said that the failure load remains practically the same after 180 thermal cycles as at 0 thermal cycles.

7.11 Conclusion

The repairing technique using CARDIFRC strips in hot dry regions has been tested. The effect of high temperature environments on the maximum load and failure mode of the RC beams retrofitted with CARDIFRC strips in both tension and vertical sides was evaluated. From the results of previous tests and present study the following conclusions can be drawn.

- The thermal cycling enhances the ultimate load of the control beams. This is due to the hydration of the remaining unhydrated cement.

- There is considerable improvement in the mechanical properties of concrete beams, namely in the compressive and tensile strengths after exposure to 30 thermal cycles. There is a slight reduction thereafter but not below that at room temperature even after 180 thermal cycles.

- The retrofitting technique using CARDIFRC strips bonded externally to the tension side of the beams substantially improves the load carrying capacity and the serviceability of concrete beams compared with the control ones. In the hot climate conditions the maximum load of such beams increased slightly.

- To prevent any shear failure in the beams retrofitted on the tension side, two CARDIFRC strips can be bonded on the vertical sides. The additional retrofitting strips can increase the ultimate load by up to 50 percent and reduce slightly the deflection of the beams.

- The failure load of the beams retrofitted with three strips and exposed to thermal cycling are substantially improved, the failure load increased by up to 45 and 50 percent after 120 and 180 thermal cycles, respectively.

- To improve the flexural behaviour of the concrete beams, retrofitting RC beams with CARDIFRC using one strip bonded on the tension side and two strips bonded to the vertical sides is a promising externally bonded system.

- No visual deterioration or bond degradation has been observed after the retrofitted beams were exposed to the thermal cycling. This is due to the good thermal compatibility between the concrete beams and CARDIFRC. Therefore, this retrofitting technique can be successfully used in hot environmental conditions.

Chapter 8

Analysis of Reinforced Concrete Beams Retrofitted with CARDIFRC

8.1 Introduction

The previous Chapter investigated experimentally the behaviour of RC beams retrofitted with CARDIFRC® strips. The results showed clearly the viability and effectiveness of this new retrofitting technique. A parametric study is also essential to correlate the experimental results, and thus to quantify the general structural behaviour. This chapter introduces an analytical model based on fracture mechanics concepts. This model will be used to predict the maximum resistance moment of the retrofitted beams. It was originally developed by Alaee and Karihaloo (2003b) and mimics the initiation and growth of the flexural crack that eventually leads to the failure of the retrofitted beam. The results of this model will be compared with those of the current test data, and conclusions will be reported.

8.2 Constitutive relations

8.2.1 Concrete

The response of a structure under load depends to a large extent on the stress-strain relation of the constituent materials and the magnitude of stress. Since concrete is used mostly in compression, the stress-strain relation in compression is of primary interest. The concrete stress-strain relation exhibits a nearly linear elastic response up to about 30 % of the compressive strength. This is followed by gradual softening up to the concrete compressive strength, when the material stiffness momentarily drops to zero. Beyond the compressive strength, the concrete exhibits strain softening until failure takes place by crushing (Figure 8.1).

In the present study, the distribution of concrete stresses in compression zone was found from the following stress-strain curve for concrete (CEB-FIP code 1990)

$$\sigma_c = \frac{\dfrac{E_c}{E_{c1}} \cdot \dfrac{\varepsilon_c}{\varepsilon_{c1}}}{1 + \left(\dfrac{E_c}{E_{c1}} - 2\right)} \cdot f_{cm} \qquad \text{for } \varepsilon_c < \varepsilon_{cu} \qquad (8.1)$$

where f_{cm} is the mean value of compressive strength of cylindrical specimens (150 mm diameter and 300 mm height) E_c is the tangent modulus, ε_{c1} is 0.0022, E_{c1} is the secant modulus from the origin to the peak compressive stress and ε_{cu} : ultimate strain.
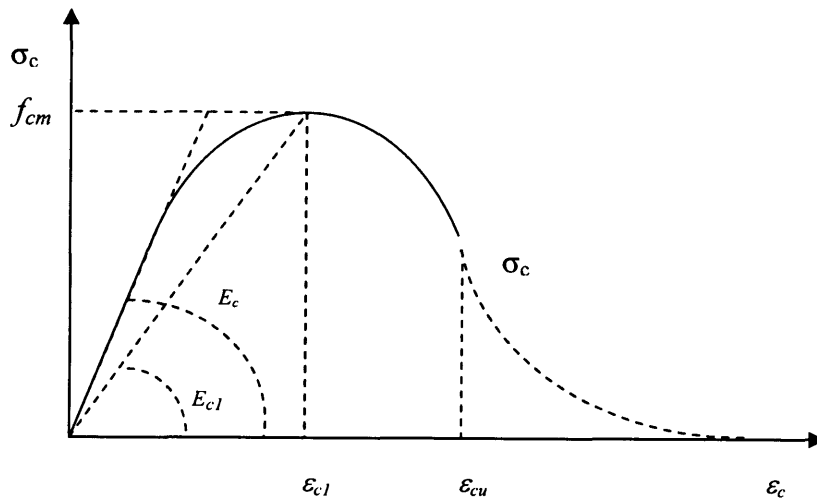
Figure 8.1 Stress-strain diagram for concrete in compression

The cylindrical compressive strength f_{cm} can be determined from the cube compressive strength f_{cu} using Table 2.1.1 (CEB-FIP). The tangent modulus E_c and the ultimate strain of concrete ε_{cu} can also be calculated from the compressive strength of concrete using Table 2.1.7 (CEB-FIP). Table 8.1 shows the values of these parameters used in the model.

Table 8.1 Assumed parameters for modelling the compressive strength behaviour of concrete

TC	F_{cu} N/mm^2	f_{cm} N/mm^2	E_c kN/mm^2	E_{c1} kN/mm^2	ε_{c1} -	ε_{cu} -
0	39.0	39.6	36.2	21.5	0.0022	0.0033
120	44.2	43.5	37.3	23.8	0.0022	0.0034
180	43.8	43.3	37.2	23.7	0.0022	0.0032

Although the tensile strength of concrete is usually ignored in the design of reinforced concrete flexural members, the concrete in between the cracks does contribute to the beam stiffness, and hence influences the moment-curvature relationship. The behaviour of concrete in tension is divided into two stages; un-cracked and cracked sections. For the un-cracked section, the concrete exhibits linear elastic stress-strain behaviour until 90 percent of the ultimate tensile stress f_{ctm}, the slope of the curve then changes to account for pre-peak micro-cracking (Figure 8.2a).

$$\sigma_1 = E_c \varepsilon_{ct} \qquad\qquad \varepsilon_{ct} \leq \varepsilon_1 \qquad\qquad (8.2)$$

185

$$\sigma_2 = f_{ctm} - \frac{0.1 f_{ctm}}{0.00015 - (0.9 f_{ctm} / E)} . (0.00015 - \varepsilon_{ct}) \qquad \varepsilon_l < \varepsilon_{ct} < \varepsilon_m \qquad (8.3)$$

where

ε_{ct}: tensile strain at which the tensile stress has to be calculated

ε_l: tensile strain according to Figure 8.2.

ε_m: tensile stain at maximum tensile stress

f_{ctm}: direct tensile strength which is estimated to be 90 percent of splitting tensile strength.
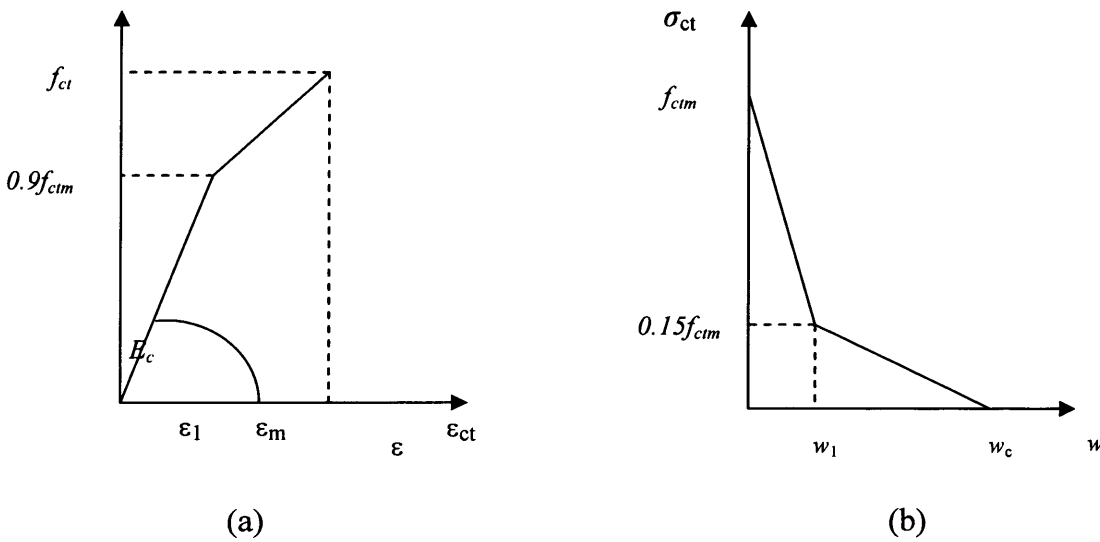
Figure 8.2 Stress-strain and stress-crack opening diagrams for concrete in tension: (a) pre-cracking region and (b) post-cracking region.

Cracked section starts beyond the maximum tensile strength. For this section a bilinear softening relation is recommended. The concrete between the cracks still carries a certain amount of stress and this is the so-called tension softening behaviour. Figure 8.2b shows the tension softening behaviour of concrete. The descending curve changes slop when the tensile stress in concrete reaches 15 percent of the tensile strength of the section. The initial steep part of this curve is primarily a result extensive post-peak micro-cracking, while the more gradual tail part is primarily a result of aggregate interlock (Karihaloo, 1995)

$$\sigma_1 = f_{ctm} \left(1 - 0.85 \frac{w}{w_1} \right) \qquad w \leq w_1 \qquad (8.4)$$

$$\sigma_2 = \frac{0.15 \, f_{ctm}}{w_c - w_1}(w_c - w) \qquad\qquad w_1 < w < w_c \qquad\qquad (8.5)$$

and

$$w_1 = \frac{G_F - 0.075 w_c f_{ctm}}{0.5 f_{ctm}} \qquad\qquad\qquad (8.6)$$

where

w: crack opening at which the stress has to be calculated

w_1: crack opening according to Figure 8.2b

w_c: crack opening at the termination of tension softening

α_F: coefficient depends on the maximum aggregate size d_{max} from Table 2.1.3 of CEB-FIP

G_F: specific fracture energy, calculated using the maximum aggregate size and the compressive strength of concrete from Tables 2.1.8 and 2.1.4 of CEB-FIP 1990.

Table 8.2 Assumed parameters for modelling the tensile strength behaviour of concrete

TC	f_{ctm} MPa	G_F N/m	w_1 mm	w_c mm
0	3.5	66.4	0.0197	0.125
120	3.1	71.5	0.0266	0.125
180	3.1	71.3	0.0271	0.125

8.2.2 Steel reinforcement

To determine the mechanical properties of steel, namely the yield stress and modulus of elasticity, three lengths of reinforced steel bar (50 mm each) were tested in the laboratory. Table 8.3 shows the characteristics of stress-strain diagram of these specimens. Using the average values of test results, i.e. the yield stress and modulus of elasticity- a perfect elasto-plastic diagram was assumed for steel reinforcing bar, as shown in Figure 8.3, ignoring the obvious strain hardening from the 0.2 % proof stress to the ultimate strength.

Table 8.3 Tensile test results of steel reinforcing bar

Diameter mm	Area mm²	0.2% Proof f_{yk}		Ultimate		Elongation		Elastic Modulus E_S GPa
		Load kN	Stress MPa	Load kN	Stress MPa	mm	%	
12	113.1	58.5	517.2	65.4	578.2	15.3	30.6	200.0
12	113.1	54.2	479.2	67.3	595.0	15.8	31.6	198.8
12	113.1	53.8	475.7	67.8	599.5	14.7	29.4	201.5
Average Values		55.5	490.7	66.8	590.9	15.3	30.5	200.1
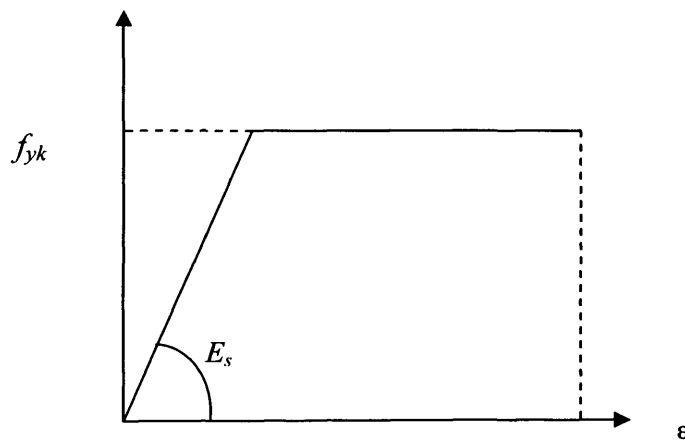
Figure 8.3 Stress-strain diagram for steel

8.2.3 CARDIFRC®

As mentioned in § 4.6.3.6.5, numerical expressions have been fitted to the tensile test data to describe the behaviour of CARDIFRC® in uniaxial tension. The constitutive behaviour of CARDIFRC® thus can be classified into two sections (i.e. un-cracked and cracked). For un-cracked section, the stress-strain curve was divided into two stages: linear elastic (stage I) and strain hardening (stage II). As can be seen in Figure 8.4, the stress-strain curve is linear up to the tensile strength of the matrix, this stress can be determined by the following linear equation

$$\sigma_1 = 0.046\varepsilon \qquad 0 < \varepsilon < 200 \text{ microstrain} \qquad (8.7)$$

The stress for strain hardening region (stage II) can be determined by the following equation:

$$\sigma_2 = -4.34 \times 10^{-10} \varepsilon^4 + 8.32 \times 10^{-7} \varepsilon^3 - 6.03 \times 10^{-4} \varepsilon^2 - 0.199 \varepsilon - 12.62$$

$200 < \varepsilon < 600$ microstrain (8.8)

Finally, the stress for (cracked section) tension softening region (Stage III), can be determined by the following equation:

$$\sigma = 3.07 \times 10^{-3} w^7 - 0.08 \ w^6 + 0.82 \ w^5 - 4.42 \ w^4 + 12.79 \ w^3 - 18.11 \ w^2$$
$$+5.73 \ w + 12.89 \qquad\qquad 0 < w < 6.5 \text{ mm} \qquad (8.9)$$
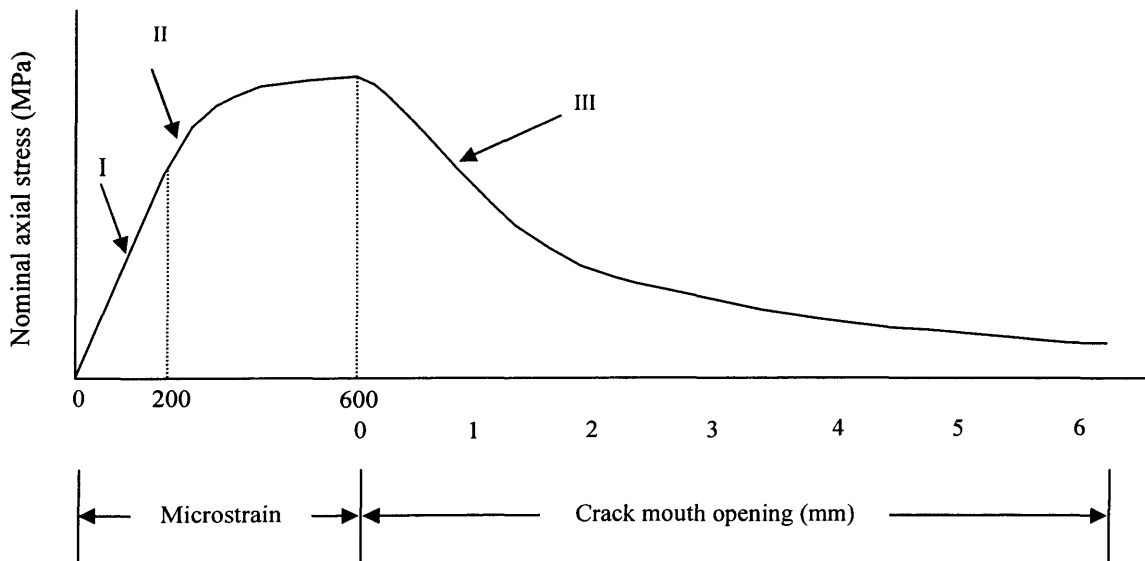
Figure 8.4 Complete pre- and post peak tensile curve for CARDIFRC® (After Benson, 2003)

8.3 Analytical model based on fracture mechanics concept

The analytical model is based on the fracture mechanics concepts. It mimics the initiation and growth of the flexural crack that eventually leads to the failure of the retrofitted beam. To model the response of a structure based on fracture mechanics, it is important to have a good knowledge of the details of the formation and propagation of cracks in the structure.

8.3.1 Sequence of crack growth

This section reviews the initiation and the propagation process that occurred in the beams retrofitted with CARDIFRC strips after they were loaded. The beams were loaded to failure. As the applied load was increased, the cracks in the tension strip became visible (Figure. 8.5a) and then grew through the beam (Figure 8.5b). One of these cracks in the tension strip opened and with a further increase in load this crack opened further and propagated into the beam (Figure 8.5c). Even after thermal cycling none of the test beams showed any indication of this crack branching into the interface. The main crack and the other cracks that formed in the tension strip, continued to open until the peak load was reached (Figure. 8.5d).

However, no attempt was made to measure the crack mouth opening displacement at the maximum load because it was too small for accurate measurement. The approximate load levels corresponding to the above sequence of crack growth are shown schematically in Figure. 8.5e.

For beams retrofitted with a tension strip and side strips, the load increased further until the crack in the tension strip extended along the side strips (Figure 8.6a). However, the crack was still within the side strips when the maximum load was reached (Figure 8.6b). It extended beyond the side strips and into the concrete beam after the attainment of the maximum load. The approximate load levels are shown schematically in Figure. 8.6c.
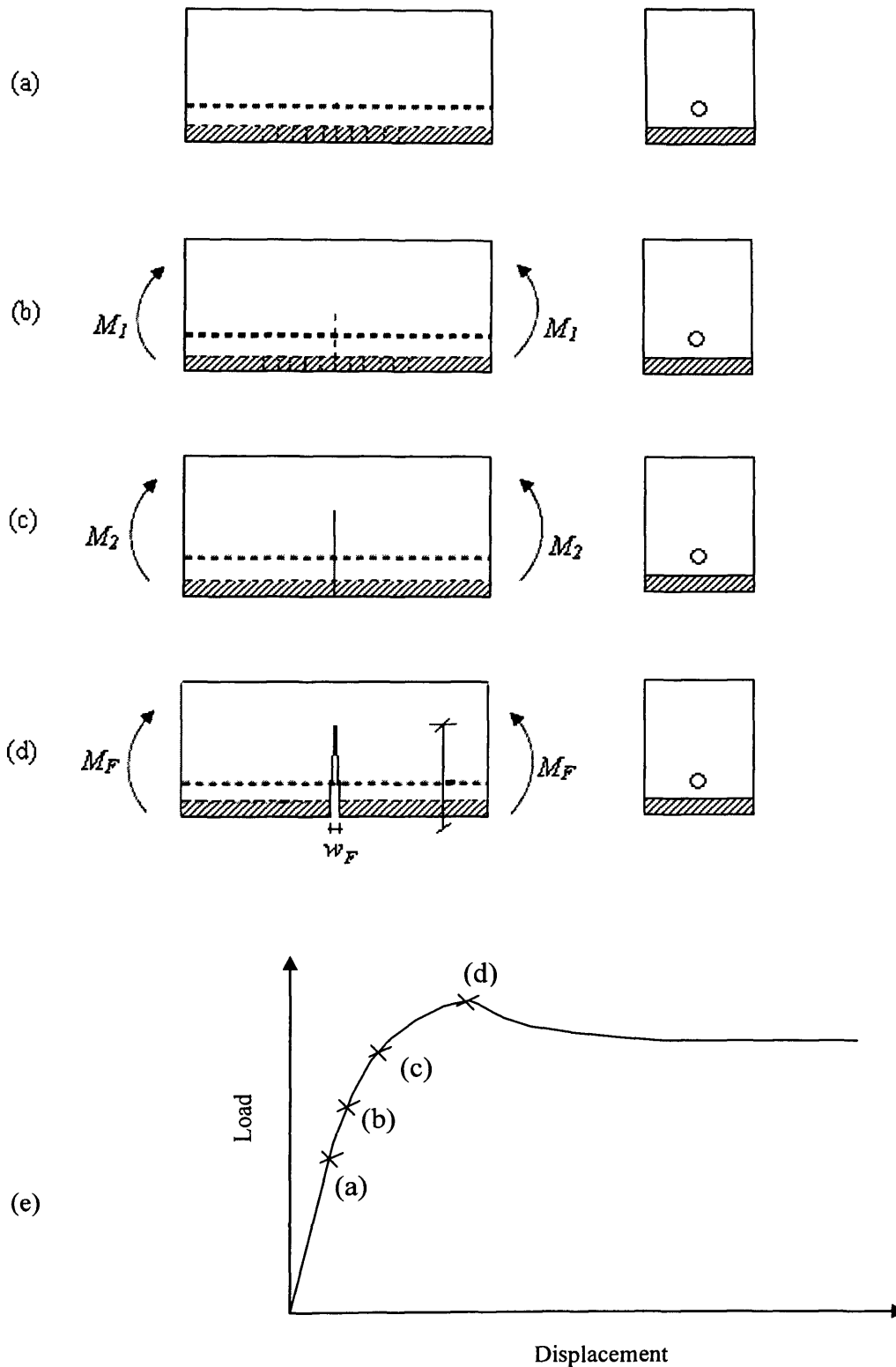
Figure 8.5 Sequence of crack growth in the middle part of the beams retrofitted with one strip: (a) Crack initiation in the middle of the strip, (b) The crack propagated into the beam, (c) propagation and penetration of the dominant crack into the beam, (d) opening of the dominant crack, and (e) load levels corresponding to the observed crack growth sequence (After Alaee and Karihaloo, 2003b)
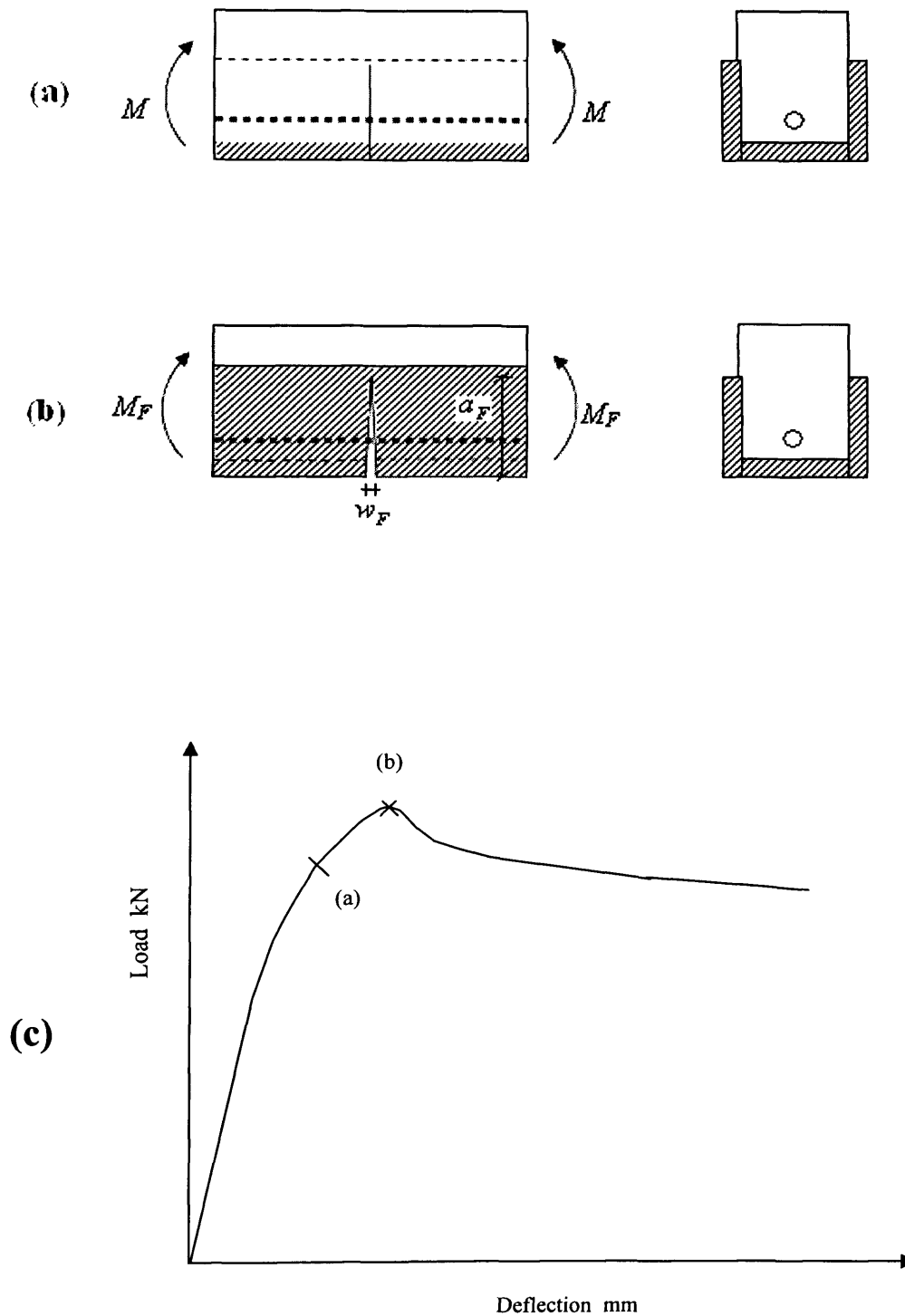
Figure 8.6 Cracking in middle part of beams retrofitted with three strips: (a) when the crack penetrated into tension strip. For clarity side strip is not shown. Note that stages (a) and (b) of Figure 8.5 are obscured by side strips; (b) at maximum load, and(c) load levels corresponding to stages (a) and (b). (After Alaee and Karihaloo, 2003b)

8.3.2 Modelling of dominant flexural crack

Following Alaee and Karihaloo (2003b) we consider the free body diagram of a part of the retrofitted beam containing the dominant flexural crack and study the effect of different loads acting on it. Figure 8.7 shows that only the moment due to the applied load tends to open the crack. However, there are three different loads which tend to close the crack as shown in the free body diagram. The first load is due to the bridging force across the crack faces from the reinforcing steel at the level of reinforcement, the second is from the post-peak tension softening response of concrete distributed along the process zone, and the third is from the bridging stresses in the retrofit strips assumed to be concentrated at the mid-thickness of the strip because of its thickness.

The computations are simplified by assuming that the crack profile is always linear. Therefore, a crack can be specified by its depth a and the opening w at its mouth. To calculate the moment resistance of the retrofitted beam M_F, the condition of the dominant crack at the ultimate load is important. In fact, M_F cannot be found, unless the crack depth (a_F) and the crack mouth opening at the maximum load (w_F) are calculated.

The bridging force from steel F_S is the most significant closing force on the crack faces. There is no definite relationship between the geometrical properties of the crack (w and a) and the bridging force in steel. On the other hand, there are some empirical relations, which will be discussed later. Figure 8.7a shows that concrete is capable of carrying residual tensile stresses, even after the attainment of its tensile strength, thanks to its tension softening behaviour. The amount of the stress transmitted along the crack faces depends upon the crack opening; it decreases with an increase in the crack opening. As shown in Figure 8.7a, the residual tensile stress in concrete σ_c, acts as a closure pressure on the dominant crack faces. It varies from f_{ctm} (the tensile strength of concrete) at the crack tip, to nothing where the crack opening equals to the critical crack opening of concrete w_c. If the crack mouth opening w and the crack depth a are given (Figure. 8.7), the distribution of this bridging stress can be easily worked out from the tension softening diagram of concrete (Figure 8.2b).
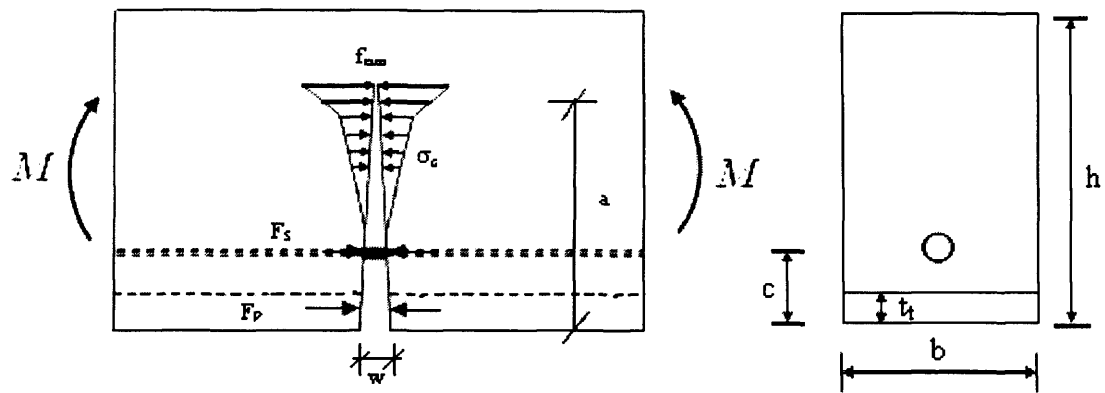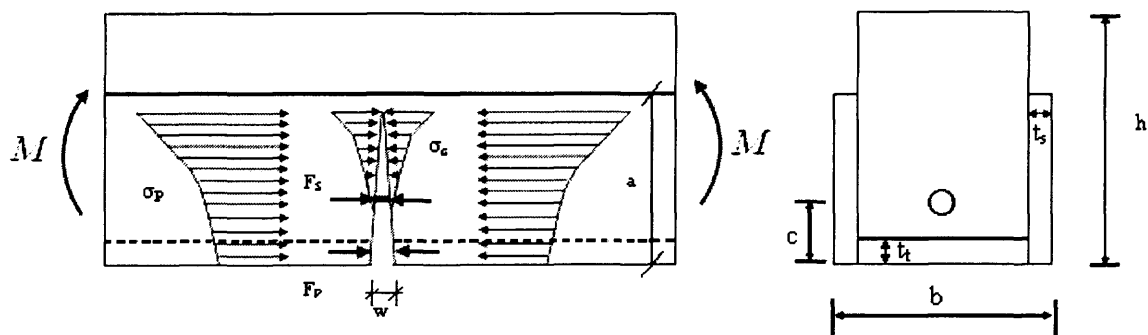
Figure 8.7 Free body diagram of dominant flexural crack in retrofitted beams. Beams retrofitted with (a) one tension strip, and (b) one tension strip and two side strips. (After Alaee and Karihaloo, 2003b)
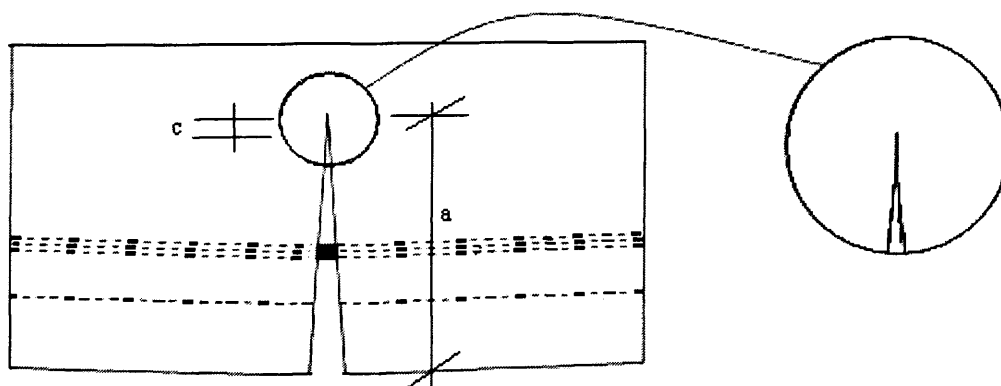
Figure 8.8 Smooth closure of crack faces. (After Alaee and Karihaloo, 2003b)

The effect of the retrofit strips on the dominant crack is very similar to that of the concrete. CARDIFRC® with its tension softening behaviour produces a closure pressure on the crack faces, which again is a function of the crack opening (Figure. 8.7b). Therefore, because there is a relation between the applied moment M to the crack depth a and crack mouth opening w, the compatibility conditions and the relations introduced in section 3.8.1 shall be used.

8.3.3 The condition of smooth closure of crack faces

Referring to the free body diagram shown in Figure 8.7, the resistance to crack opening consists of three different components. The first component is from the bridging force across the crack faces due to the reinforcing steel, the second one from the post-peak tension softening response of concrete, and the third is due to the bridging stresses in the retrofit strips. The closure pressure exerted counteracts the opening action of the applied moment M. Barenblatt (1959) reported that the stress at the crack tip is finite and the net stress intensity factor at the crack tip must vanish as shown in Figure 8.8. In fact, this requires that the crack faces close smoothly near the tip (Figure 3.5). It seems to contradict the assumption of linear crack profile.

However, Alaee and Karihaloo (2003b) have shown that the inclusion of non-zero K_I at the crack tip, implied by non-smooth closure of crack tip faces introduces an error of less than 1 percent. We shall therefore assume $K_I = 0$ at the crack tip. The net K_I at the crack tip is obtained by superimposing the stress intensity factors produced at the crack tip by the applied moment (K_{IM}), and the closure forces exerted by steel (K_{IS}), concrete (K_{Iconc}), tension retrofit strips $(K_{I(t-strip)})$, and side retrofit strips $(K_{I(s-strip)})$ (if they are used). The condition of finite stress at the crack tip, i.e. $K_I = 0$ is therefore

$$K_{IM} - K_{IS} - K_{Iconc} - K_{I(t-strip)} - K_{I(s-strip)} = 0 \qquad (8.10)$$

The various stress intensity factors appearing in the above equation will be calculated in the following sub-sections.

8.3.3.1. Stress Intensity factor due to the applied moment K_{IM}

As mentioned in § 3.8.1 (Equation 3.49) the stress intensity factor produced at the crack tip by the moment M is (Guinea et al., 1998)

$$K_{IM}(\xi) = \frac{M}{h^{3/2}b} Y_M(\xi) \tag{8.11}$$

where ξ is the ratio of the depth of the crack to the height of the beam a/h, b is the width of the beam and $Y_M(\xi)$ is

$$Y_M(\xi) = \frac{6\xi^{1/2}(1.99 + 0.83\xi - 0.31\xi^2 + 0.14\xi^3)}{(1-\xi)^{3/2}(1+3\xi)} \tag{8.12}$$

Substitution of (8.12) into (8.11) gives

$$K_{IM} = \frac{M}{h^{3/2}b}\left[\frac{6\xi^{1/2}(1.99 + 0.83\xi - 0.31\xi^2 + 0.14\xi^3)}{(1-\xi)^{3/2}(1+3\xi)}\right] \tag{8.13}$$

8.3.3.2. Stress Intensity factor due to the steel force

Similarly, from equation (3.50) the stress intensity factor produced at the crack tip by the concentrated steel force F_S is (Tada et al., 1985)

$$K_{IS}(\xi) = \frac{F_S}{h^{1/2}b} Y_S(\xi, \beta) \tag{8.14}$$

where $\beta = c/h$, c is the distance from the centre of the reinforcing bar to the bottom of the beam and the function $Y_S(\xi, \beta)$ is given by

$$Y_S(\xi, \beta) = \left\{ \begin{array}{l} \dfrac{3.52(1-\beta/\xi)}{(1-\xi)^{3/2}} - \dfrac{4.35 - 5.28\beta/\xi}{(1-\xi)^{1/2}} \\[2mm] + \left[\dfrac{1.30 - 0.30(\beta/\xi)^{3/2}}{(1-(\beta/\xi)^2)^{1/2}} + 0.83 - 1.76\beta/\xi\right]\left[1-(1-\beta/\xi)\xi\right] \end{array} \right\} \dfrac{2}{\sqrt{\pi\xi}} \tag{8.15}$$

196

8.3.3.3 Stress intensity factor due to the residual tensile stress of concrete K_{Iconc}

To determine the stress intensity factor at the crack tip produced by the residual tensile stress of concrete, this stress is discretized into infinitely many concentrated forces. Each force is applied over small crack segments of length dy at a distance $y(=y^*h)$ from the bottom of the crack (see Figure 8.9). The magnitude of each force is

$$dF_c = \sigma_c \ (w_y) \ bdy \equiv \sigma_c \ (w_y) \ bhdy^* \tag{8.16}$$

where

$$w_y = w(1-y/a) = w(1-y^*/\xi) \tag{8.17}$$

In the above equations, w_y is the crack opening at the level of the point load dF_c. Now, using equation (8.14) the stress intensity factor produced by this point load can be calculated

$$dK_{Iconc} = \frac{\sigma_c (w_y)bh}{h^{1/2}b} Y_S (\xi, y^*) dy^* \tag{8.18}$$
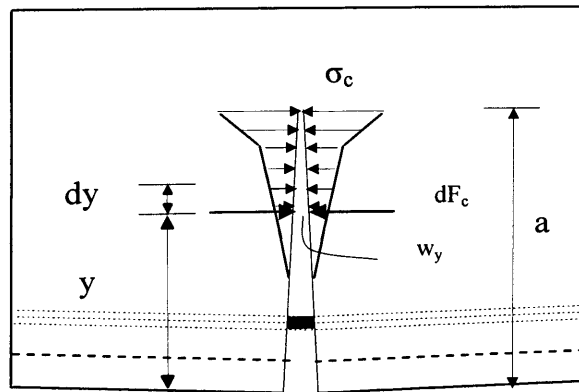
Figure 8.9 Towards the discretisation of the bridging stresses in concrete (After Alaee and Karihaloo, 2003b)

The relation in equation (8.18) is integrated over the length of the crack in concrete (i.e. excluding the retrofit strip)

$$K_{Iconc}(\xi) = \int_{t_t/h}^{\xi} \sigma_C(w_y) h^{1/2} Y_S(\xi, y^*) \, dy^*$$
(8.19)

where t_t is the thickness of the retrofit strip and $Y_S(\xi, y^*)$ is

$$Y_S(\xi, y^*) = \left\{ \begin{array}{l} \dfrac{3.52(1 - y^*/\xi)}{(1-\xi)^{3/2}} - \dfrac{4.35 - 5.28 y^*/\xi}{(1-\xi)^{1/2}} \\[3mm] + \left[\dfrac{1.30 - 0.30\,(y^*/\xi)^{3/2}}{(1-(y^*/\xi)^2)^{1/2}} + 0.83 - 1.76 y^*/\xi \right]\left[1-(1-y^*/\xi)\xi \right] \end{array} \right\} \dfrac{2}{\sqrt{\pi\xi}}$$
(8.20)

8.3.3.4. Stress intensity factor due to the closure force of tension strip $K_{I(t\text{-}strip)}$

To determine $K_{I(t\text{-}strip)}$ the magnitude of the closure force F_P exerted by the tension retrofit strip is calculated using the corresponding crack opening w_P at the level of F_P

$$F_P = \sigma_P(w_P) b t_t$$
(8.21)

where w_P can be calculated from the following equation:

$$w_P = w(1 - t_t/2a) \equiv w\{1 - t_t/(2h\xi)\}$$
(8.22)

Substitution of (8.21) into (8.14) gives the stress intensity factor produced at the crack tip by the closure force exerted by the tension strip

$$K_{I(t-strip)}(\xi) = \frac{\sigma_P(w_P) t_t}{h^{1/2}} Y_S\left(\xi, \frac{t_t}{2h}\right)$$
(8.23)

where the geometry function $Y_S\left(\xi, \dfrac{t_t}{2h}\right)$ is

198

$$Y_S(\xi, \frac{t_t}{2h}) = \left\{ \begin{array}{l} \dfrac{3.52(1-t_t/2h\xi)}{(1-\xi)^{3/2}} - \dfrac{4.35-5.28\,t_t/2h\xi}{(1-\xi)^{1/2}} \\[4mm] + \left[\dfrac{1.30-0.30(t_t/2h\xi)^{3/2}}{(1-(t_t/2h\xi)^2)^{1/2}} + 0.83-1.76t_t/2h\xi \right]\left[1-(1-t_t/2h\xi)\xi\right] \end{array} \right\} \dfrac{2}{\sqrt{\pi\xi}}$$

(8.24)

8.3.3.5 Stress intensity factor due to the closure force of side strip $K_{I(s-strip)}$

The stress intensity factor produced at the crack tip by the closing force of the side strips can be calculated in the same manner as K_{Iconc}. Dividing each of the side strips into infinitesimal elements of height $dy(=hdy^*)$, the closure force on each element of the two side strips is

$$dF_{SP} = 2\sigma_P\,(w_y)\,t_S\,dy \equiv 2\,\sigma_P\,(w_y)t_S\,hdy^* \qquad (8.25)$$

where t_S is the thickness of the side strip, w_y is the crack opening at the level of the closure force dF_{SP}

$$w_y = w(1-y/a) = w(1-y^*/\xi) \qquad (8.26)$$

Substitution of (8.25) into (8.14) gives the stress intensity factor produced by this point load at the crack tip

$$dK_{I(s-strip)} = \frac{2\sigma_P(w_y)t_S h^{1/2}}{b} Y_S(\xi, y^*)dy^* \qquad (8.27)$$

To calculate $K_{I(s-strip)}$, this relation is integrated as follows:

$$K_{I(s-strip)}(\xi) = \int_0^\alpha \frac{2\sigma_P(w_y)t_S h^{1/2}}{b} Y_S(\xi, y^*)dy^* \qquad (8.28)$$

where α is min $\{\xi, h_s/h\}$(i.e. the smaller of α or h_S), h_s is the height of the side strips. The choice of the upper limit of integration is dictated to the fact that, when the crack depth exceeds the height of the side strip, the side strips do not exert any closure pressure over the part of the crack that is beyond the side strips. The geometry function $Y_S(\xi, y^*)$ is

$$Y_S(\xi, y^*) = \left\{ \begin{array}{l} \dfrac{3.52(1 - y^*/\xi)}{(1-\xi)^{3/2}} - \dfrac{4.35 - 5.28 y^*/\xi}{(1-\xi)^{1/2}} \\[4mm] + \left[\dfrac{1.30 - 0.30(y^*/\xi)^{3/2}}{(1 - (y^*/\xi)^2)^{1/2}} + 0.83 - 1.76 y^*/\xi \right]\left[1 - (1 - y^*/\xi)\xi\right] \end{array} \right\} \dfrac{2}{\sqrt{\pi\xi}} \qquad (8.29)$$

Finally, substitution of (8.13), (8.14), (8.19), (8.23), and (8.28) into (8.10) gives

$$\frac{M}{h^{3/2}b} Y_M(\xi) - \frac{F_S}{h^{1/2}b} Y_S(\xi, \beta) - \int_{t_i/h}^{\xi} \sigma_c(w_y) h^{1/2} Y_S(\xi, y^*) dy^* - \frac{\sigma_P(w_P)}{h^{1/2}} Y_S(\xi, \frac{t_t}{2h}) -$$

$$\int_0^\alpha \frac{2\sigma_P(w_y) t_s h^{1/2}}{b} Y_S(\xi, y^*) dy^* = 0 \qquad (8.30)$$

8.3.4 Crack opening compatibility equation

In addition to the condition of smooth closure of crack faces at its tip, we must consider the compatibility of crack opening displacement of a retrofitted beam (Leung, 1998). The crack opening displacement can again be written as the vectorial sum of the contribution from the applied bending moment and the closure forces exerted by steel, concrete and retrofit strips. The compatibility condition of the crack opening need be satisfied only at the level of the steel reinforcement, because of the assumed known (i.e. linear) variation along the length of the crack:

$$(w_S)_M - (w_S)_S - (w_S)_{conc} - (w_S)_{t-strip} - (w_S)_{s-strip} = w_S \qquad (8.31)$$

where $(w_S)_i$ are the crack opening displacement at the level of the steel bar produced by the applied bending moment and the closure forces exerted by steel, concrete, tension strip, and side strips, respectively. Note that the crack opening w_s at the level of the reinforcement is not known, but is to be determined. Each term in the left hand side of (8.31) can be expressed in terms of the corresponding compliance coefficients (see § 3.8.1).

For instance, the crack opening at the level of the steel bar produced by the applied moment is

$$(w_S)_M = \lambda_{SM} M \qquad\qquad (8.32)$$

where λ_{SM} (compliance coefficient) is the crack opening at the level of steel when a unit bending moment is applied to the crack. The compliance coefficients can be computed from energy principles and Clapeyron's theorem (see § 3.8.1). The following sections present the relations for the computation of the required compliance coefficients.

8.3.4.1 Compliance coefficient due to a unit moment λ_{SM}

The derivation of the compliance coefficient due to a unit moment has been presented in § 3.8.1.Equation (3.53) from that section can be rewritten as (Bosco and Carpinteri, 1992)

$$\lambda_{SM} = \frac{2}{hbE} \int_{\beta}^{\xi} Y_M(x).Y_S(x,\beta)dx \qquad\qquad (8.33)$$

where E is the Young modulus of concrete, and $Y_M(x)$ and $Y_S(x, \beta)$ are the geometry functions given by (8.12) and (8.15) respe ctively. The crack opening due to the applied moment is obtained by substituting equation (8.33) into (8.32).

$$(w_S)_M = \frac{2M}{hbE} \int_{\beta}^{\xi} Y_M(x).Y_S(x,\beta)dx \qquad\qquad (8.34)$$

8.3.4.2 Compliance coefficient due to a unit steel force λ_{SS}

Similarly, the compliance coefficient due to a unit steel force is given by (Bosco and Carpinteri, 1992)

$$\lambda_{SS} = \frac{2}{bE} \int_{\beta}^{\xi} Y_S^2(x,\beta)dx \qquad\qquad (8.35)$$

The crack opening $(w_S)_S$ is then obtained as

$$(w_S)_S = \lambda_{SS} F_S \qquad\qquad (8.36)$$

8.3.4.3 Compliance coefficient due to a unit tensile force in concrete λ_{SConc}

To work out the crack opening at the level of the steel bar produced by tension softening of concrete $(w_S)_{conc}$, the continuous closure stresses exerted by concrete is again discretized into infinitely many concentrated loads dF_c, each acting on an infinitesimal crack length dy (see Figure 8.9). The crack opening $(w_S)_{dF_c}$ produced by one of these concentrated loads is calculated by using the compliance method. The corresponding compliance coefficient λ_{S-dF_c} can again be computed from energy principles (Bosco and Carpinteri, 1992) considering the point load dF_c acting simultaneously with the steel force F_S

$$\lambda_{S-dF_c} = \frac{2}{E} \int_{\beta^*}^{\alpha} Y_S(x,\beta) Y_S(x,y^*)\, dy^*$$ (8.37)

where β^* is max $\{y^*, \beta\}$ (i.e. the larger of y and c). Multiplying this compliance factor by dF_c from equation (8.16) gives

$$(w_S)_{dF_c} = \frac{2\sigma_c(w_y)h\,dy^*}{E} \int_{\beta^*}^{\xi} Y_S(x,\beta) Y_S(x,y^*)\,dy^*$$ (8.38)

To calculate the crack opening at the level of reinforcement due to the tension softening of concrete, equation (8.38) is integrated over the length of the crack in concrete

$$(w_S)_{conc} = \int_{t_1/h}^{\xi} \left\{ \frac{2\sigma_c(w_y)h}{E} \int_{\beta^*}^{\xi} Y_S(x,\beta) Y_S(x,y^*)\,dx \right\} dy^*$$

$$(w_S)_{conc} = \int_{t_1/h}^{\xi} \left\{ \frac{-\sigma_c(w_y)h}{E} \int_{\beta^*}^{\xi} Y_S(x,\beta) Y_S(x,y^*)\,dx \right\} dy^*$$ (8.39)

8.3.4.4 Compliance coefficient due to a unit force in retrofit tension strip $\lambda_{S(t-strip)}$

Using the same procedure as above, the compliance coefficient due to a unit force in the tension retrofit strip $\lambda_{S-(t-strip)}$ can be written as

$$\lambda_{S-(t-strip)} = \frac{2}{Eb} \int_{\beta}^{\xi} Y_S(x,\beta) Y_S\left(x, \frac{t_t}{2h}\right) dx$$ (8.40)

Multiplying this compliance factor by F_P from equation (8.21) gives

$$(w_S)_{l-strip} = \frac{2\sigma_P(w_P)t_l}{E} \int_\beta^\xi Y_S(x,\beta)Y_S\left(x,\frac{t_l}{2h}\right)dx \tag{8.41}$$

8.3.4.5 Compliance coefficient due to a unit force in retrofit side strips $\lambda_{S-(s-strip)}$

To calculate $(w_S)_{S-strip}$, exactly the same procedure as that adopted for concrete is followed. Equation (8.37) in this case becomes

$$\lambda_{S-dF_{SP}} = \frac{2}{Eb} \int_{\beta^*}^\xi Y_S(x,\beta)Y_S(x,y^*)dx \tag{8.42}$$

Multiplying this compliance coefficient by the magnitude of the point load dF_{SP} from equation (8.25) gives the crack opening produced by this point load

$$(w_S)_{dF_{SP}} = \frac{4\sigma_P(w_y)t_s h}{Eb}dy^* \int_{\beta^*}^\xi Y_S(x,\beta)Y_S(x,y^*)dx \tag{8.43}$$

Again, to compute the crack opening at the level of steel due to the forces exerted by the side strips, equation (8.43) is integrated over the length of the cracked side strips

$$(w_S)_{S-strip} = \frac{4t_s h}{Eb} \int_0^\alpha \left\{ \sigma_P(w_y) \int_{\beta^*}^\xi Y_S(x,\beta)y_S(x,y^*)dx \right\}dy^* \tag{8.44}$$

All the crack openings mentioned in the right hand side of equation (8.31) have now been expressed in terms of the corresponding forces and the geometry of the crack and the beam, and of the Young modulus of concrete

$$\frac{2M}{hbE} \int_\beta^\xi Y_M(x).Y_S(x,\beta)dx - \frac{2F_S}{bE} \int_\beta^\xi Y_S^2(x,\beta)dx$$

$$-\frac{2h}{E} \int_{t_l/h}^\xi \left\{ \sigma_c(w_y) \int_{\beta^*}^\xi Y_S(x,\beta)Y_S(x,y^*)dx \right\}dy^* - \frac{2\sigma_P(w_P)t_l}{E} \int_\beta^\xi Y_S(w,\beta)Y_S\left(x,\frac{t_l}{2h}\right)dx -$$

$$\frac{4t_s h}{Eb} \int_0^\alpha \left\{ \sigma_P(w_y) \int_{\beta^*}^\xi Y_S(x,\beta)y_S(x,y^*)dx \right\}dy^* = w_S \tag{8.45}$$

It should mentioned that the constitutive relation of CARDIFRC® (post-peak response) and the material properties of concrete and steel described earlier in this chapter will be used. The bridging closure forces exerted by concrete and CARDIFRC® strips can be easily worked out from the corresponding relations. However, the relationship between the geometrical properties of a crack and the bridging force exerted by steel crossing it is quite complicated and this will be discussed in the next section.

8.3.5 Bridging force exerted by steel F_S

The bridging force from steel F_S is a very significant closing force on the crack faces.

There is no definite relationship between the geometrical properties of the crack (w and a) and the bridging force in steel. However, some semi-theoretical and empirical formulas have been proposed and will be presented in the following.

8.3.5.1 Carpinteri's approximation

Bosco and Carpinteri (1992) assumed that the displacement discontinuity in a cracked cross section at the level of reinforcement is zero up to the moment of yielding or slippage of the reinforcement. They considered a rigid perfectly plastic behaviour of the reinforcement and obtained the moment at plastic flow or slippage.

In fact, they assumed that the reinforcement steel yields as soon as the crack at this level starts to open. It is obvious that this simplifying assumption will overestimate the moment resistance of the beam. According to this assumption, the bridging force exerted by steel is simply

$$F_S = A_S f_y \tag{8.46}$$

where f_y is the yield stress of the reinforcing bar and A_S the area of steel. The steel force is therefore uncoupled from the crack opening displacement at the level of steel.

8.3.5.2 Kaar's formula

In another study, Kaar and Mattock (1963) expressed the tensile stress in steel as a function of the crack width w_S at the level of deformed bar reinforcement

$$f_S = \frac{F_S}{A_S} = \frac{11876.5 w_S}{A^{1/4}} \tag{8.47}$$

where A is the area of concrete surrounding each bar ($A = A_e/n$, where n is the number of bars) (see Figure 8.10)

$$A_e = 2(h-d)$$
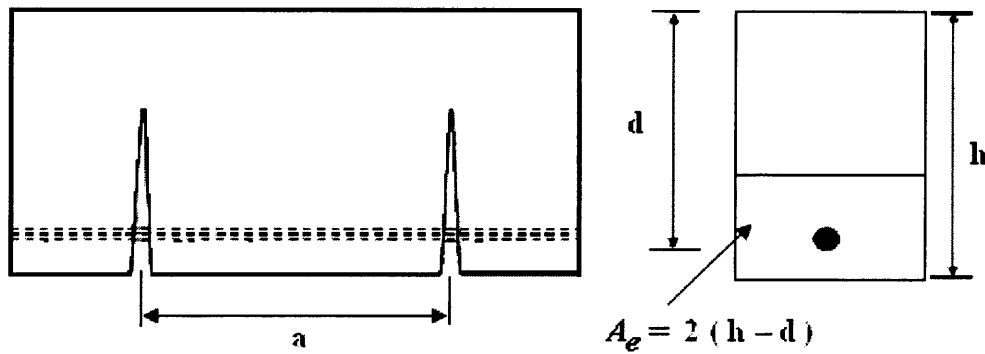
Figure 8.10 Cracking of a reinforced concrete member under flexure (After Park and Paulay 1975)

Alaee and Karihaloo (2003b) used the aforementioned Carpinteri's approximation and Kaar's formula and concluded that none of these has been found to be consistent with their test results. They found that the model results based on Carpinteri's approximation were higher than the test results and those based on the Kaar's formula were significantly lower. Moreover, their analysis showed that the crack opening at the maximum load was not zero as Carpinteri assumes or as large as Kaar proposes.

8.3.5.3 Modified Kaar's formula

Lange-Kornbak and Karihaloo (1999) conducted an experimental study and compared the test results with approximate nonlinear fracture mechanical prediction of the ultimate capacity of three-point bend, singly-reinforced concrete beams. They found that Kaar's formula (8.47) overestimates the crack opening by the factor of 3.5 to 4. Alaee and Karihaloo (2003b) further improved Kaar's formula by calibrating the results against the test data by a least squares fit. This calibration suggested the

following relationship between the tensile stress in steel and the crack width at the level of deformed bar

$$f_S = \frac{F_S}{A_S} = \frac{4.8 \times 11876.5 w_S}{A^{1/4}} \tag{8.48}$$

Due to the similarity between the test beams in Alaee and Karihaloo (2003b) and those in the present study, equation (8.48) will be used in the analysis as the bridging force of steel.

8.3.6 Evaluation of moment resistance of the beams

From above the fracture mechanics approach, it is clear that two equations should be simultaneously satisfied for a flexural crack; the equation of smooth closure of the crack faces (8.30) and the equation of the crack opening compatibility (8.45). The unknown parameters appearing in these equations are the crack depth a, the crack mouth opening w and the applied moment M. To determine these unknowns the following three-step procedure was followed:

- First, the equation of smooth closure of the crack faces (8.30) was solved for a wide range of crack depths and crack mouth openings, and the corresponding moment M was calculated. The results of this step are denoted by the set $\{a_i, w_i, M_i\}$

- Second, the equation of the crack opening compatibility (8.45) was solved for the same ranges of values of a and w. The results of this step are denoted by the set $\{a_j, w_j, M_j\}$

- The results of the previous two steps were compared and the intersection of these two sets identified. This set satisfies both the smooth closure condition (8.30) and the crack opening compatibility equation (8.45). These results are denoted by the set $\{a_k, w_k, M_k\}$

From the set of values identified in the previous step, the maximum moment was selected ($M_{k\,max}$) and denoted M_F. The moment M_F is the moment resistance of the
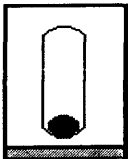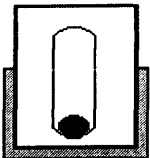
beam, and the corresponding crack length a_F and crack mouth opening w_F describe how deep the crack has penetrated into the beam at the maximum load, and how far it has opened.

A flowchart of the above procedure is given in Appendix C.

8.3.7 Model results

The method described in the previous section has been applied to the critical sections of all test beams (i.e. the section in which the dominant flexural crack forms). The moment resistance M_F, crack mouth opening w_F and crack depth a_F of the beams at the peak load have been calculated. The model results for the retrofitted beams (beams retrofitted with one strip on the tension face and beams retrofitted with one strip on the tension face, two continuous strips on the sides) after, 0, 120 and 180 thermal cycles are given in Table 8.4. Comparisons have been made between the moment resistances of the beams predicted by the model with the mean values of the maximum moment of experimental results and shown in Figures 8.11 and 8.12.

Table 8.4 Crack opening w_F, crack depth a_F and the moment resistance M_F of the beams at the maximum load predicted by the model after 0, 120 and 180 thermal cycles.

Retrofitting Configuration	Thermal cycles Number	a (mm)	w (mm)	M_{model} (kNm)	F_{test} mean (kNm)	M_{test} mean (kNm)
	0	78	0.23	8.8	59.2	8.9
	120	78	0.23	8.8	61.4	9.2
	180	78	0.24	8.8	58.0	8.7
	0	116	0.17	13.9	89.0	13.3
	120	118	0.21	14.0	91.1	13.7
	180	116	0.18	13.9	88.7	13.3
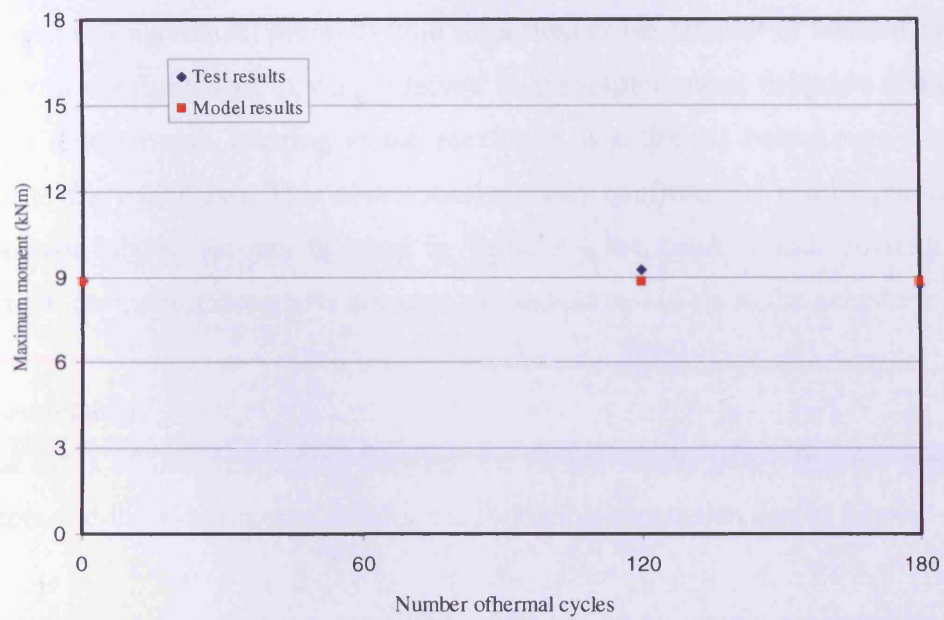
Figure 8.11 Comparison of the moment resistance of RC beams retrofitted with one strip on the tension side with the prediction of the model after a number of thermal cycles.
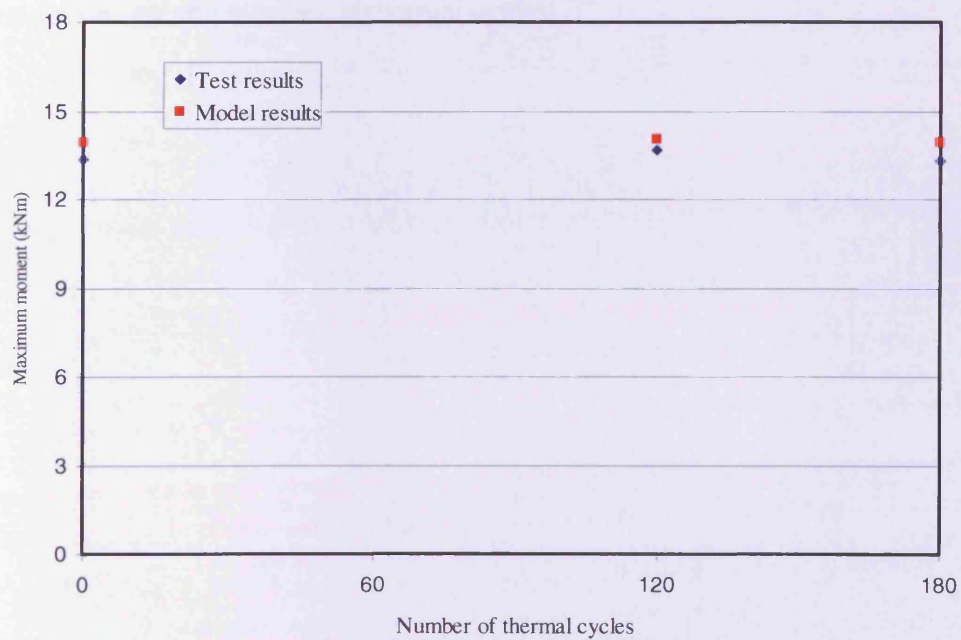
Figure 8.12 Comparison of the moment resistance of RC beams retrofitted with three strips (one on the tension side and two on the vertical sides) with the prediction of the model after a number of thermal cycles.

208

It is seen that the model results are in excellent agreement with the test results. Moreover, this agreement seems to hold regardless of the number of thermal cycles or the retrofit configuration. It was observed in the experimental program (Chapter 7) that the crack mouth opening at the maximum load for all beams was finite and visible to the naked eye. This observation actually confirms the results predicted by the present model. As can be seen in Table 8.4 the crack mouth opening at the maximum moment resistance is not zero and should be visible to the naked eye.

8.4 Conclusion

On the basis of the comparison between the model results using fracture mechanics concepts and the experimental results, the following conclusion can be drawn.

The moment resistance of the retrofitted beams can be accurately predicted by using a fracture mechanics model. This model follows the propagation of the flexural crack which eventually leads to the failure of the retrofitted beams. The results of this model were found to be in excellent agreement with the test results irrespective of the retrofit configuration and the number of thermal cycles.

Chapter 9

Conclusions

9.1 Conclusions

The conclusions that are a part of the investigation have been drawn and reported at the end of each Chapter. This Chapter therefore provides a brief and succinct summary of the major conclusions.

- The mechanical properties of BMC NSC and CARDIFRC® mixes are negligibly affected by thermal cycles up to 80 and 90 below those at room temperature, but after 120 they differ... This increase in the properties after 120 ... could be attributed to the continued hydration process of the ... a slight reduction after 180 ... with 120 thermal cycles ... might be due to the ... The most ... CARDIFRC® decreased, significant deterioration due to ... ... NSC and HSC ... fracture energy G_f and the ... ... after 120 thermal cycles and ... after 180 thermal cycles. The increase in their ... after ... thermal cycles is probably due to the partial morphological ...

- To compare the crack between the adhesive and cracked concrete and in several combinations of materials ... when CARDIFRC® and the crack ... 90°C and 120°C ... the period in which should be ... Modelling such a ... is therefore unlikely, the aggregate, thus initially a rough ... to micro ... is higher interface roughness than ... to reduce the interface crack ... having the crack to ... the ... through the ... concrete ...

9.1 Conclusions

The conclusions of each aspect of the investigation have been drawn and reported at the end of each Chapter. This Chapter therefore provides a brief and succinct summary of these major conclusions

- The mechanical properties of NSC, HSC and CARDIFRC® mixes are improved after 120 thermal cycles and do not fall below those at room temperature even after 180 thermal cycles. This increase in the properties after 120 thermal cycles could be attributed to the continued hydration process of the remaining unhydrated cement and the presence of micro-silica that activates the secondary reaction. However, the slight reduction after 180 thermal cycles (in compression with 120 thermal cycles) might be due to the initiation of microcracks between the cement paste and aggregate. The steel fibres in CARDIFRC® counteract any possible deterioration due to microcracking.

- A significant increase in the fracture properties of NSC and HSC mixes (measured fracture energy $G_f(\alpha)$, size-independent fracture energy G_F and the brittleness) was observed. They are increased slightly after 120 thermal cycles and seem to be unchanged after 180 thermal cycles. The increase in these properties after 120 thermal cycles is probably due to the partial expulsion of capillary water.

- To improve the bond between the adhesive and parent concrete, and to prevent delamination or interfacial fracture, both CARDIFRC® and the parent concrete (NSC and HSC) mating surfaces must be roughened. Moreover, the thin film of cement paste on the smooth cast surface of the parent concrete should be removed. Removing such a film will therefore expose the aggregate, thus creating a rough surface. The rough substrate surface leads to higher interface toughness which prevents interface crack propagation, forcing the crack to kink into the weaker material and to eventually propagate through the parent concrete.

- The wedge splitting test a very useful and easy technique to evaluate the bond performance of NSC and HSC repaired with CARDIFRC®. By incorporating CARDIFRC® as a retrofitting material, it has been found to be a successful material for repairing NSC and HSC.

- The size-independent fracture energy G_F of NSC and HSC / bonded specimens after thermal cycling follows a similar trend to that of control specimens; the G_F increases gradually up to 120 cycles and then drops slightly after 180 cycles.

- The ultimate load and the measured fracture energy of both the control and bonded specimens changed with the change of the notch to depth ratio. Therefore, the fracture energy and maximum load decrease as the notch to depth ratio increases.

- No visual deterioration or bond degradation was observed after thermal cycling of the CARDIFRC® bonded specimens attesting to the good thermal compatibility between the CARDIFRC® and concrete.

- Both the mechanical and fracture properties of the NSC, HSC and CARDIFRC® mixes experienced only a slight reduction even after 180 thermal cycles but the values did not drop below those at the room temperature.

- The maximum failure loads of reinforced concrete beams are enhanced after exposure to a hot dry regime. The increase in the load carrying capacity after the thermal cycling is due to the activation of the hydration of the unhydrated cement.

- In order to improve the ultimate load and the serviceability of the RC beam, retrofitting with CARDIFRC® strips bonded to the tension face is promising. The increase in maximum load carrying capacity of the beams can be up to 11 percent at room temperature. With thermal cycling the failure load of such

beams can increase by up to 12 and 9 percent after 120 and 180 thermal cycles, respectively

- To prevent shear failure and also for further improvement in the maximum load carrying capacity and stiffness, it is suggested that CARDIFRC® strips should also be bonded to the sides of the beams. This additional retrofitting can enhance the failure load by up to 67 percent at room temperature. With temperature cycling, the ultimate load can be increased to 67 percent after 120 and 65 percent after 180 cycles. Therefore, the room temperature figure provides a safe value for design at elevated temperature.

- No bond degradation was observed in the retrofitted beams after the thermal cycling. Therefore, the results show that using CARDIFRC strips bonded externally to the RC beams is a successful technique and can be applied even in hot environment. This is due to the good thermal compatibility between the CARDIFRC® and concrete

- The analytical model for the prediction of the moment resistance of the retrofitted beams is based on the fracture mechanics concepts. This model mimics the growth of the flexural crack that eventually leads to the failure of the retrofitted beam. The results of this model are found to be in excellent agreement with the test results

List of References

References

Abdalla, H. M. and Karihaloo B. L. (2003). Determination of size-independent specific fracture energy of concrete from three-point bend and wedg splitting tests, *Magazine of Concrete Research*, 55 (2), pp. 133-141.

Abdelhady, H., Hamdy, S., Abdelrahman, A. and Tamere, E. (2006). Performance of reinforced concrete beams strengthened by hybrid FRP laminates. *Cement and Concrete Composites* 28. pp. 906–913.

Abousaif H. E. (1997). Damage and fracture behaviour of concrete, *PhD, Thesis, Division of Civil Engineering*, School of Engineering, Cardiff University, Wales.

ACI (1994). Guide for the use of silica fume in concrete, Detroit, *Committee 363 American Concrete Institute.*

ACI (1996). State-of-the-art report on fibre reinforced concrete, *Manual of concrete Practice*, (ACI 544.1R-96).

ACI (2001). Guide for the Design and Construction of Externally Bonded FRP System for Strengthening Concrete Structure, *Committee 440 Draft Document, American Concrete Institute*, Farmington Hills, MI, USA.

Adhikary, B. and Mutsuyoshi, H. (2005). Shear strengthening of RC beams with web-bonded continuous steel plates, *Construction and Building Materials* 20, pp. 296-307.

Alaee, F. (2002). Retrofitting of concrete structures using high performance fibre reinforced composite (HPFRCC), *PhD. Thesis, Cardiff University. UK.*

Alaee, F., Benson, S. and Karihaloo, B. L. (2001). Strengthening of RC beams with High Performance Cementations Composites, *Proceedings International Conference on Civil Engineering*, Technical Committee ICCE (eds), Interline Publishing, abaangalore, India, pp 1-13.

Alaee, F. and Karihaloo, B. L. (2003a). Retrofitting of Reinforced Concrete Beams with CARDIFRC. *Journal of Composites for Construction*, 7 (3), pp.174-186.

Alaee, F. and Karihaloo, B. L. (2003b). A fracture model for flexural failure of beams retrofitted with CARDIFRC®. *ASCE Journal of Engineering Mechanics*, 129 (9), pp. 1028-1038.

Al-Sulaimani, G. J., Sharif, A., Basunbul, I. A., Balush, M. H. and Ghaleb, B. N. (1994). Shear repair for reinforced concrete by fibreglass plate bonding, *ACI Structural Journal*, 91 (3), pp. 458-464.

Almusallam, A. A., Beshr, H. B., Maslehuddin, M. and Al-Amoudi O S., (2004). Effect of silica fume on the mechanical properties of low quality coarse aggregate, *concrete Cement & Concrete Composite*s, V 26, pp. 891–900.

Almusallam, H. (2006). Load–deflection behaviour of RC beams strengthened with GFRP sheets subjected to different environmental. *Conditions Cement & Concrete Composites*. 28. pp. 879–889.

Almusallam, T., Al-Salloum, Y. and Alsayed, S. (2001). Behaviour of concrete cylinders confined with GFRP sheets in severe environmental conditions. *Proceedings of the third international conference on concrete under severe conditions*. Canada, June 2001 .pp. 1723–1729.

Anthony E. and Newman K. (1965). The structure of concrete and its behaviour under load, *Proceeding of an International Conference*, London

Appa Rao, G. and Raghu Prasad, B. K. (2002). Fracture energy and softening behaviour of high-strength concrete, *Cement and Concrete Research*, Vol.32, pp. 247–252.

Arslan G., Sevuk, F. and Ekiz, I. (2006). Steel plate contribution to load-carrying capacity of retrofitted RC beams, *Construction and Building Materials* 22 (2008) 143–153.

Bache, H. H. (1981). Densified cement ultra-fine particle-based materials, *CBL Report No, 40, Aalborg Portland*, Denmark, pp. 35.

Bache, H.H. (1987). Introduction to compact reinforced composite, Nord. *Concrete Research*. V.6, pp. 19–33.

Baker, G. (1996). The effect of exposure to elevated temperature on the fracture energy of plain concrete, *RIELM Materials and Structures*, 29, pp. 383-388.

Bakis, C., Bank, L., Brown, V., Cosenza, E., Davalos, J., Machida, A., Rizkalla, S. and Triantafillou, T. (2002). Fibre reinforced polymer composites for construction-state-of the-art review, *Journal of Composites for Construction*, 6 92), pp. 73-87.

Balaguru, P. N. and Kendzulak, J. (1986). Flexural behaviour of slurry infiltrated fibre concrete (SIFCON) made by using condensed silica fume, In Fly Ash, Silica Fume, Slag and natural Pozzolans in Concrete, *SP-91, ACI, Detroit*, pp. 1215-1229.

Balaguru, P. N. and Shah, S. P. (1992). Fibre-Reinforced Cement Composites, *McGraw-Hill, New York.*

Banthia, N. and Nandakumar, N. (2000). Crack growth resistance of hybrid fibre reinforced cement composites, *Cement & Concrete Composites*, pp.3–9.

Barenblatt, G. I. (1959). On equilibrium cracks forming during brittle fracture (in Russian), *Prikladnaya Matematika I Mekhanika* (P M M), 23, pp. 434-444.

Barluenga, G. and Olivares, F. H. (2007). Cracking control of concretes modified with short AR-glass fibres at early age. Experimental results on standard concrete and SCC, *Cement and Concrete Research*, (37), pp. 1624–1638.

Baruch, G. (1998). *Climate Considerations in Building and Urban Design*, Published on January 6th 1998 by Wiley.

Barnes, R. A. and Geoffrey C. M. (2004). Strengthening of reinforced concrete beams in shear by the use of externally bonded steel plates: *Part 1-Experimental programme Construction and Building Materials*, 20 (2006) 396–402

Bazant, Z. P. and Oh, B. H. (1988). Crack band theory for fracture of concrete, *Materials and Structures*, 16, pp. 155-157.

Behnood, A. and Ziari, H. (2008). Effects of silica fume addition and water to cement ratio on the properties of high-strength concrete after exposure to high temperatures, *Cement & Concrete Composites*, V 30, pp. 106–112.

Benson, S. D. P. (1999). Retrofitting damaged reinforced concrete flexural members with HPFRCC, *MEng Thesis, Cardiff University, UK*.

Benson, S. D. P. (2003). CARDIFRC-Development and constitutive behaviour, PhD. *Thesis, Cardiff University, UK*.

Bentur, A. and Mindess, S. (1986). The effect of concrete strength on crack patterns, *Cement and Concrete Research*, 16, pp. 59-66.

Bertero, V. V. and Polivka, M. (1972). Influence of thermal exposure on mechanical characteristics of concrete, *International Seminar on Concrete for Nuclear Research*, American concrete Institute, Detroit, ACI Special Publication 1 (34), pp. 505-531.

Berwanger, C. and Sarkar, X. (1973). Effective of temperature and age on thermal expansion and modulus of elasticity of concrete, Behaviour of concrete under temperature extremes, SP-39, *American Concrete Institute*, Farmington Hills, pp. 1-22.

Beshr, H, Almusallam, A., and Maslehuddin, M. (2003). Effect of coarse aggregate quality on the mechanical properties of high strength concrete. *Construction and Building Materials*, V 17 pp. 97–103.

Bhanjaa, S. and Sengupta, B., (2005). Influence of silica fume on the tensile strength of concrete, *Cement and Concrete Research*, Vol. 35 pp. 743–747

Bilby B L., Cottrell, A. H. and Swinden K. H. (1963). The spread of plastic yield from a notch, *Preceedings of Royal Society*, London, A272, pp. 304-314.

Birchall, J. D., Howard, A. J., and Kendall, K. (1981) Flexural strength and porosity of cements, *Nature*, 289, pp. 388-390.

Bonfiglioli, B. and Pascale, G. (2004). Dynamic Assessment of Reinforced Concrete Beams Repaired with Externally Bonded FRP Sheets. *Mechanics of Composite Materials*. Vol. 42. No. 1, pp. 3-20.

Bosco, C. and Carpinteri, A. (1992). Fracture mechanics evaluation of minimum reinforcement in concrete structure, *In Application of Fracture Mechanics to Reinforced Concrete, Proc Int. Workshop*, Turin, Italy (1990), Carpinteri, A. (ed), Elsevier, London, pp. 347-377.

Bosco, C., Carpinteri, A. and Debernardi P. G. (1990a). Fracture of reinforced concrete scale effect and snab-pack instability, *Presented at the International Conference on Fracture and Damage of concrete and Rock.* 4-6 July 1988, Vienna, Austria, Engineering Fracture Mechanics, 35 (4-5), pp. 665-677.

Bosco, C., Carpinteri, A. and Debernardi P. G. (1990b). Minimum reinforcement in high strength concrete, *ASCE Journal of Structural Engineering*, 116, pp. 427-437.

Broek, D. (1978). *Elementary Fracture Mechanics*, Sijthoff and Noordhoof, The Netherlands.

Broek, D. (1989). *The practical Use of Fracture Mechanics*, Kluwer Academic Published, The Netherlands.

Brown W. E. and Srawley J. E. (1966). Plane strain crack toughness testing of high strength materials, *Special Technical Publication STP410 American Society for Testing and Material (ASTM)*, Philadelphia, p. 163.

Bruhwiler, E., Denarie, E. and Putallaz, J. C. (2005). Instandsetzung einer Betonbrucke mit ultrahochleistungsfähigem Faserfeinkornbeton (UHLFB). (Rehabilitation of a concrete bridge with UHPFRC). *Beton- und Stahlbetonbau*, 100(9): 822–7.

Bruhwiler, E. and Wittmann, F. H. (1990). The wedg splitting test, a new method of performing stable fracture mechanics test, *Engineering Fracture Mechanics*, 35, pp. 117-126.

Burak, F., Kamile, T., and Bulent, B. (2009). Effects of fibre type and matrix structure on the mechanical performance of self-compacting micro-concrete composites, *Cement and Concrete Research*, pp. 1023–103.

Buyukozturk O. and Hearing B. (1998). Failure behaviour of pre-cracked concrete beams retrofitted with FRP, *Journal of Composites for Construction*, 2 (3), pp. 138-144.

Carlos, A. Coronado, M. and Maria M. Lopez (2005). Sensitivity analysis of reinforced concrete beams strengthened with FRP laminates, *Cement & Concrete Composites* 28, pp. 102–114.

Casanova, P., Rossi, P., Schaller, I. (1996). Can steel fibres replace transverse reinforcement in reinforced concrete beams, *ACI Mater. J*, pp. 341–354.

Castillo, C. and Durrani, A. J. (1990). Effect of transient high temperature on high strength concrete, *ACI Materials Journal*, 87, (1), pp. 47-53.

CER-FIP Model Code, First Draft, (1990), Lausanne, Switzerland.

Chaallal, O., Nollet, M. and Perraton, D. (1998). Shear strengthening of RC beams by externally bonded side CFRP strips. *Journal of Composites Construction* 2.

Cheng, F., Kodur, V. and Wang, T., (2004). Stress- Strain Curves for High Strength Concrete at Elevated Temperature, *Journal of Materials in Civil Engineering*, ASCE/January /February 2004, pp 84-90.

Cucchiara, C., Mendola, L., Papia, M. (2004). Effectiveness of stirrups and steel fibres as shear reinforcement, *Cement and Concrete Composites*, pp. 777–786.

Duan, K., Hu, X. Z. and Wittmann, F. H. (2001). Boundary effect on concrete fracture induced by non-constant fracture energy distribution, In Borst, R. D., Mazars, J., Pijaudier - Cabot G. and Van Mier J. M. (editors), *Fracture Mechanics of Concrete Structures* (Proc. FRAMCOS-4), 49-55. A. A. Balkema Publishers, The Netherland.

Dugat, J., Roux, N. and Bernier, G. (1996). Mechanical properties of reactive powder concretes (RPC), *Materials and Structures*, 29, pp. 233-240.

Dugdale, D. S. (1960). Yielding of steel sheets containing slits, *Journal of the Mechanics and Physics of Solids*, 8 , pp. 100-104.

Emmons, P. H. (1994). *Concrete Repair and Maintenance*, Concrete Rublishers and Consultants, Kingston.

England, A. H. (1965) A crack between dissimilar media, *Journal of Applied Mechanics*, 32, pp. 400-402.

Ewalds, H. L. and Wanhill, R. J. (1985). *Fracture Mechanics*, Edward Arnold, UK and Delftse Uitgevers Maatschappj, The Netherlands (co-publishers).

Fanella, D. A. and Naaman, A. E. (1985). Stress-strain properties of fibre reinforced mortar in compression, *Journal of the American Concrete Institute*, 82 (4), pp. 475-483.

Farhat A. F. (2004). Performance of concrete structures retrofitted with CARDIFRC after thermal cycling, *PhD Thesis, Cardiff University, UK*.

Gamage, J., l-Mahaidi, R. and Wong, M. (2006) Bond characteristics of CFRP plated concrete members under elevated temperatures. *Composite Structures V.75* pp. 199–205.

Ganga-Rao, H., Barger, J. (2001). Aging of bond between FRP and concrete cubes. In: *Proceedings of the international conference on FRP composite in civil engineering*. Hong Kong, vol. 2; pp. 1569-1578.

Gao, B., Leung, K. and Kim, J. K. (2007). Failure diagrams of FRP strengthened RC beams. *Composite Structures* 77 (2007) pp.493-508.

Gettu, R., Bazant, Z. P. and Karr, M. E. (1990). Fracture properties and brittleness of high strength concrete, *ACI Material Journal*, 87, pp. 608-618.

Gonzalo, B. (2009). Fibre–matrix interaction at early ages of concrete with short fibres, *Cement and Concrete Research*. 40 (5), May 2010, pp. 802-809.

Gopalaratnam, V. S. and Shah, S. P. (1986). Properties of steel fibre reinforced concrete subjected to impact loading, *Journal of the American Concrete Institute*, 83 (1) pp. 117-126.

Grace, N. and Grace, M. (2001). Durability evaluation of CFRP strengthened beams. *Third international conference composites in construction.* France, July 2001. pp. 391–396.

Griffith A. A. (1920). The phenomena of rapture and flow in the solids, *Philosophical Transactions of Royal Society*, London, A221, pp. 163-198.

Guinea, G. V., Pastor, J. Y., Planas, J. and Elices M. (1998). Stress intensity factor compliance and CMOD for a general three-point bending beam, *International Journal of Fracture,* 89,pp. 103-116.

Habel, K., Denarie, E. and Bruhwiler, E. (2007). Experimental investigation of composite "UHPFRC-concrete" members, *ACI Structure J*, 104(1) pp. 93–101.

Hadi, M. (2003). Retrofitting of shear failed reinforced concrete beams. *Composite Structures* 62 (2003) 1-6.

Halit, Y. N., Huseyin, Y., Serdar, A., and Bulent B. (2006). Autoclaved SIFCON with high volume Class C fly ash binder phase, *Cement and Concrete Research,* 36, pp. 481 – 486

Hammil, N. (1999). Retrofitting damaged reinforced concrete flexural members with high performance fibre reinforced concrete, *MEng Thesis*, University of Wales, Cardiff.

Harmuth H. (1995). Investigation of the adherence and the fracture behaviour of polymer cement concrete, *Cement and Concrete Research*, 25 (3), pp. 497-502.

Hedong, N. and Zhishen, W. (2006). Effects of FRP-Concrete Interface Bond Properties on the Performance of RC Beams Strengthened in Flexure with Externally Bonded FRP Sheets. *Journal of Materials in Civil Engineering*, pp. 723-731.

Hillerborg A., Modeer M. and Petersson P. E. (1976). Analysis of crack formation and crack growth in concrete by means of fracture mechanics and finite elements, *Cement and Concrete Research*, 6, pp. 773-782.

Hoy, C. W. and Bartos, P. J. (1999). Interaction and packing of fibres: Effects on the mixing process, *In High Performance Fibre Reinforced Cement Composites (HPFRCC3)*, Reinhardt H. W. and Naaman A. E. (eds), RILEM Publications, pp. 181-191.

Hsuan, T., Fu-Ming, L. and Yih-Yuan, J. (2004). Non-linear finite element analysis of reinforced concrete beams strengthened by fibre reinforced plastics. *Composite Structures* 63. pp. 271–281.

Hu, X. Z. (1990). Fracture process zone and strain softening in cementitious materials, *ETH Building Materials Report NO. 1*, ETH, Switzerland. (AEDIFICATIO Publishers, Freiburg, 1995).

Hu, X. Z. and Wittmann, F. H. (1992). Fracture energy and fracture process zone, *Materials and Structures*, 25, pp. 319-326.

Hu, X. Z. and Wittmann, F. H. (2000). Size effect on toughness induced by crack close to free surface, *Engineering Fracture Mechanics*, 65, pp. 209-211.

Hutchinson, J. W., Mear, M. E., and Rice, J. R. (1987). Crack paralleling an interface between dissimilar materials, *Journal of Applied Mechanics*, 54, pp. 828-832.

Inglis, C. E. (1913). Stress in plate due to the presence of cracks and sharp corners, *Transactions of the Institution of Naval Architects*, pp. 219-241.

Islam M.R. Mansur M.A. and Maalej M. (2005). Shear strengthening of RC deep beams using externally bonded FRP systems, *Cement and Concrete Composites*, 27 (3), pp. 413-420.

Irhouma, A. M., Ayari, M. L. and Robinson, L. C. (1998). Effect of low temperature on fracture energy of concrete joints and repair material, *In Fracture Mechanics of Concrete Structures Volume III,* Mihashi, H., Rokugo, K. (eds) AEDIFICATIO Publishers, Freiburg, Germany, pp. 1593-1604.

Irwin, G. R. (1957). Analysis of stresses and strain near the end of a crack traversing a plate, *ASME Journal of Applied Mechanics*, 24, pp. 361-364.

Islam, M., Mansur, M., Maalej, M. (2005). Shear strengthening of RC deep beams using externally bonded FRP systems. *Cement & Concrete Composites* 27 (2005) pp. 413–420.

Jennings, H. M. (1991). Advanced cement-Based matrices for composites, in high Performance Fibre Reinforced Cement Composites, *Proceedings of International RILEM/ACI Workshop*, Reinhardt H. W. and Naaman A. E. (eds), Mains, Germany, pp. 3-17.

Jones, R., Swamy, R., Bloxham, J. and Bouderbalah, A. (1980). Composite Behaviour of Concrete Beams with Epoxy Bonded External Reinforcement, *International Journal of Cement Composites and Lightweight Concrete*, 2 (2). Pp. 91-107.

Jones, R., Swamy, R. and Sharif, A. (1988). Plate Separation and Anchorage of Reinforced Concrete Beams Strengthened by Epoxy-bonded steel Plate, *Structural Engineer (London)*, 66(5), pp. 85-94.

Kaar P. H. and Mattock, A. H. (1963). High strength bar as concrete reinforcement, Part 4, Control of Cracking, *Journal of the PCA Research and Development Laboratories*, 7 (1), pp. 15-38.

Karbhari, V., (1998) Material and Design Considerations in FRP Rehabilitation of Concrete Structures, *In Fracture Mechanics of Concrete Structures, vol. 3*, Mihashi H., Rogugom K. (eds)., AEDIFICATIO Publishers, pp. 1805-1816.

Karbhari, V., Rivera, J., and Dutta, P. (2000). Effect of short-term freeze-thaw cycling on composite confined concrete. *Composites for Construction*. 4 (4), pp.191-197.

Karihaloo, B. L. (1995). *Fracture Mechanical and Structural Concrete*, Addison Wesley Longman, London.

Karihaloo B. L., Abdalla, H. M. and Imjai, T. (2003). A simple method for determining the true specific fracture energy of concrete, *Magazine of Concrete Research*, 55 (5), pp. 471-481.

Karihaloo, B. L, Alaee, F. J., and Benson, S. D. (2001). A new Technique for Retrofitting Damaged Concrete Structures, *Concrete Communication Conference*, pp.293-304.

Karihaloo, B. L., Alaee, F. J. and Benson, S. (2002). A new Technique for Retrofitting Damaged Concrete Structures, *Proceedings of the Institution of Civil Engineer, Building & Structures,* 154(4), pp. 309-318.

Karihaloo, B. L., Benson, S., Didiuk, P., Fraser, S., Hamill, N. and Jenkins T. (2000). Retrofitting Damaged RC Beams with High-performance Fibre-reinforced Concrete. *Proceedings of the Tenth Annual BCA, British Cement Association,* Birmingham University, pp. 153-164.

Karihaloo, B. L and De Vriese, K. M. (1999). Short-fibre reinforced reactive powder concrete, *Proceedings of Concrete Communication Conference*, British Cement Association, pp. 67-77.

Karihaloo, B. L., Farhat, F. A., Nicolaides, D. and Kanellopoulos, A. (2007). High performance fibre-reinforced cementitious composite (CARDIFRC)- Performance and application to retrofitting, *Engineering Fracture Mechanics,* 74, pp. 151-167.

Karihaloo, B. L. and Jefferson, A. D. (2001). Looking into concrete, *Magazine of Concrete Research,* 53 (2), pp. 135-147.

Karihaloo, B. L., Nicolaides, D. and Kanellopoulos, A. (2010). Fatigue life and self-induced volumetric change of CARDIFRC, *Magazine of Concrete Research,* (in press).

Karihaloo, B. L. and Wang, J. (1997). Micromechanical modelling of strain hardening and tension softening in cementitious composites, *Computational Mechanics,* 19, pp. 453-462.

Karihaloo, B. L. and Wang, J. (2000). Mechanical of fibre-reinforced cementitious composites, *Computers and Structures,* 76, pp. 19-34.

Karihaloo, B. L., Wang J., and Grzybowski, M. (1996). Doubly periodic arrays of bridged crack and short fibre-reinforced cementitious composites, *Journal of the Mechanics and Physics of Solids,* 44 (10), pp. 1565-1586.

Kaufmann, J. and Hesselbarth, D. (2007). High performance composites in spun-cast elements, *Cement & Concrete Composites,* pp. 713-722.

Knott, J. F. (1973). *Fundamental of Fracture Mechanics,* Butterworths, London.

Kunieda, M, Kurihara, N., Uchida, Y. and Rokugo, K. (2000). Application of tension softening diagrams to valuation of bond properties at concrete interface, *Engineering Fracture Mechanics,* 65, pp. 299-315.

Lange-Kornback, D. (1997). The role of brittleness in the fracture of lain and reinforced concrete, *PhD. Thesis,* University of Sydney.

Lange-Kornback, D. and Karihaloo, B. L. (1997). Tension softening of fibre-reinforced cementitious composites, *Cement and Concrete Composites,* 19, pp. 315-328.

Lange-Kornback, D. and Karihaloo, B. L. (1999). Fracture mechanical prediction of transitional failure and strength of singly reinforced beams, *In Minimum Reinforcement in Concrete Members*, ESIS Publication 24, Carpinteri, A. (ed), Elsevier, London, pp. 31-42.

Lankard, D. R. (1985). Slurry infiltrated fibre concrete (SIFCON): *properties and applications, Materials Research Society*, 42, pp. 227-286.

Lankard, D. R. and Newell, J. K. (1984). Preparation of highly reinforced steel fibre reinforced concrete composites, *ACI Special Publication, SP-81, American Concrete Institute*, Detroit, pp. 286-306.

Lee, H. and Hausmann, L. (2004) Structural repair and strengthening of damaged RC beams with sprayed FRP. *Composite Structures* **63**. pp. 201–209.

Leung, C. K. (1998). Delamination failure in concrete beams retrofitted with a bonded plate, *In Fracture Mechanics of Concrete Structures Volume III*, Mihashi, H., Rokugo, K. (eds), AEDIFCATIO Publishers, Freiburg, Germany, pp. 1783-1792.

Leung, H., Balendran, R. and Lim, C. (2001). Flexural capacity of strengthened concrete beam exposed to different environmental conditions. *Proceedings of the international conference of FRP composites in civil engineering*. China, 2001. pp. 1597–1606.

Lewis, J. A. and Kriven, W. M. (1993). Microstructure property relationships in Macro-Defect-Free Cement, *MRS Bulletin*, pp. 72-77.

Li, V. C. (1992). A simplified micromechanical model of compressive strength of fibre reinforced cementitious composites, *Cement and Concrete Composites*, 14, pp. 131-141.

Li, V.C. (2003). On engineered cementitious composites (ECC), a review of the material and its applications, *J. Adv. Concrete Technol.*, 1(3), pp.215 – 230.

Li, V. C. and Kamada, T. (2000). The effects of surface preparation on the fracture behaviour of ECC/concrete repair system, *Cement & Concrete Composites*, 22, pp. 423-431.

Li, V. and Kanda, T (1998). Interface property and apparent strength of a high strength hydrophilic fibre in cement matrix. *ASCE J Mater Civil Eng* 1998; 10(1):5–13.

Li, V. C., Kong, H. and Chan, Y. (1998). Development of self-compacting engineered cementitious composites. In: *Proceedings of the International Workshop on Self-Compacting Composites*, Kochi, Japan. 1998. pp. 46-59.

Li, V. C., Kong, H., and Bike S. G. (2003). Constitutive rheological control to develop a self-consolidating engineered cementitious composite reinforced with hydrophilic poly(vinyl alcohol) fibres, *Cement and Concrete Composites*, 25, pp. 333-341.

Li, V. C., Lim, Y. M. and Foremsky, D. J. (1995). Interfacial fracture toughness of concrete repair materials, *Proceedings of Mechanics of Concrete Structures II* Wittman F. H. (ed), AEDIFCATIO Publishers, pp. 1329-1344.

Li, V. C., Wang, Y. and Backer, S. (1991). A micromechanical model of tension softening and bridging toughening of short random fibre reinforced brittle matrix composites, *Journal of Mechanics and Physics of Solids*, 39 (50), pp. 607-625.

Li, V. C. and Weimann, M. B. (2003). Drying shrinkage and crack width of ECC, *Brittle Matrix Composites 7, Warsaw, Poland*, pp. 37–46.

Lim, Y. M. and Li, V. C. (1997). Durable repair of aged infrastructures using trapping mechanism of engineering cementitious composites, *Journal of Cement and Concrete Composites*, 19 (4), pp. 373-385.

Macdonald, M. D. and Calder, A. J. (1982). Bonded steel plating strengthening concrete structures, *International Journal of Adhesion and Adhesives*, 2(2), pp. 119-127.

Mansur, M.A., Chin, M.S. and Wee, T.H. (1997). Stress–strain relationship of confined high strength plain and fibre concrete, *J Mater Civil Eng,* 51(05), pp.353–563.

Mazloom, M., Ramezanianpour, A. A. and Brooks, J.J. (2004). Effect of silica fume on mechanical properties of high-strength, *Concrete Cement & Concrete Composites*, V 26 pp. 347–357.

Mehta, P. K. (1999). Advancements in concrete technology. *Concrete Int*, pp. 69–76.

Mehta, P.K. and Aitcin, P.C. (1990). Micro-structural basis of selection of materials and mix proportions for high strength concrete, *HSC International Symposium on Utilization on High Strength Concrete*, vol. 2. Berkeley, CA.

Meier, U., (1997). Post strengthening by continues fibre laminates in Europe, non-metallic (FRP) reinforcement for concrete structures, *Japan Concrete Institute*, 1 pp. 41-56.

Meier, U., Deuring, M., Meier, H. and Schwegler, G. (1992). Strengthening of structures with CFRP laminates: Research and application in Switzerland, *Advanced Composites Materials in Bridges and Structures*. Canadian Society for civil Engineering, pp. 243-251.

Meier, U. and Kaiser, H. (1991). Strengthening of structures with GFRP laminates, *Advanced Composites Materials in Civil Engineering Structures*, ASCE, New York, pp. 224-232.

Mobasher, B., Stang, H. and Shah, S. P. (1990). Microcracking in fibre reinforced concrete, *Cement and Concrete Research*, 20, pp. 665-676.

Mustafa, S. and Li, V. C. (2007). Durability of mechanically loaded engineered cementitious composites under highly alkaline environments, *Cement & Concrete Composites*, 30 (2008) 72–81.

Myers, J., Murthy, S. and Micelli, F. (2001). Effect of combined environmental cycles on the bond of FRP sheets to concrete. *Proceedings composites in construction, international conference*. Portugal, October 2001.

Naaman, A. E. (1991). SIFCON: tailored properties for structural performance, in High Performance Fibre Reinforced Cement Composites, *Proceedings of the International RILM/ACI Workshop*, Rrinhardt, H. W., and Naaman A. F. (eds), Mains, Germany, pp. 18-38.

Naaman, A.E. and Reinhardt, H. W. (2003). High performance fibre reinforced cement composites HPFRCC-4: International workshop Ann Arbor, Michigan, June (2003), *Cement & Concrete Composites* 26 (2004) 757–759.

Naaman, A. E. and Reinhardt, H. W. (2004). High performance fibre reinforced cement composites HPFRCC-4, *Cement & Concrete Composites* 26 pp. 757–759.

Naaman, A. E., Rrinhardt, H. W. and Fritz, C. (1990). Reinforced concrete beams using SIFCON as a matrix, *Darmstadter Massivbau Report*, Germany, 85 pages.

Naaman, A. E. and Shah, S. P. (1976). Pull-out mechanism in steel fibre reinforced concrete, *ASE Journal of the Structural Division*, 102 (ST8), pp. 1537-1548.

Nabil, F., Wael, F., George, A. (2004). Development and Application of Innovative Triaxially Braided Ductile FRP Fabric for Strengthening Concrete Beams. *Composite Structures.* **64**. (2004) 521–530.

Nanni, A. (1995). Concrete repair with externally bonded FRP reinforcement: examples from *Japan. Journal Concrete International.* **97**. pp. 22-26.

Neville, A. M. (1995). Properties of Concrete 4th Edn., Longman Group, *UK and New York: John Wiley & Sons*.

Nollet, M., Perraton, D. and Chaallal, O. (1999). Flexural behaviour of CFRP strengthened RC beams under room and freezing temperatures. *Proceedings of eighth international conference on structural faults & Repairs*, p.7.

Okamura, H., Watanabe, K. and Takano, T. (1973). Applications of the compliance concepts in fracture mechanics. *ASTM STP 536*, pp. 423-438.

Okamura, H., Watanabe, K. and Takano, T. (1975). Deformation and strength of cracked member under bending moment and axial force. *Engineering Fracture Mechanics*, 7, pp. 531-539.

Park, P., and Paulay, T. (1975). Reinforced Concrete Structure, *Wiley-Interscience, New York*, pp. 769.

Petersson, P. E. (1980). Fracture energy of concrete, Practical performance and experimental results. *Cement and Concrete Research*, 10, pp. 91-101.

Rahimi, H. and Hutchinson, A. (2001). Concrete beams Strengthened with Externally Bonded FRP Plates, *Journal of Composites for Construction* 5 (1), pp. 44-56.

Raghu Prasad, B. K., Bharatkumar, B. H., Ramachandra, D. S., Narayanan, R. and Gopalakrishnan, S. (2005). Fracture Mechanics Model for Analysis of Plain and Reinforced High-Performance Concrete Beams, *Engineering Mechanics*, Vol. 131, No. 8, ©ASCE, ISSN 0733-9399/831–838.

Ramakrishnan, V. (1995). Concrete fibre composites for the twenty-first century, *Real World Concrete, Singh*, G (editor), Elsevier Science Ltd, UK, pp. 111-144.

Ramesh, K., Seshu, D.R., and Prabhakar, M. (2003). Constitutive behaviour of confined fibre reinforced concrete under axial compression, *Cement & Concrete Composites*, 25 pp. 343–350.

Reinhardt, H. W. (1991). Fibres and cement, a useful co-operation: Introductory note, High Performance Fibre Reinforced Cement Composites, *Proceedings of the International RILEM/ACI Workshop*, Reinhardt, H. W., & Naaman, A. E. (eds), Mains, Germany.

Ricardo, A. E. and Marta, S.L. (2006). Fracture parameters for high-performance concrete, *Cement and Concrete Research*, Vol. 36, pp. 576 – 583.

Rice, J. R. (1998). Elastic fracture mechanics concepts for interfacial cracks, *Journal of Applied Mechanics*, Transactions ASME, 55, pp. 98-103.

Rice, J. R. and Shih G. C. (1965). Plane problems of cracks in dissimilar media, *Journal of Applied Mechanics*, pp. 418-423.

Richard, P. and Cheyrezy, M. H. (1994). Reactive powder concrete with high ductility and 200-800 MPa compressive strength, *ACI Spring Cnvention, San Francisco, USA*.

Richard, P. and Cheyrezy, M. H. (1995). Composition of reactive powder concrete, *Cement and Concrete Research*, 25 (7), pp. 1501-1511.

RILEM Committee FMC 50. (1985). Determination of the fracture energy of mortar and concrete by means of the three-point bend tests on notched beams, *Materials and Structures*, 18, pp. 285-290.

Romualdi, J. P. and Batson, G. P. (1963). Mechanics of crack arrest in concrete, *J Engineering*, pp.147–168.

Rossi, P., Bruhwiler, E., Chhuy, S., Jenq, Y. S. and Shah S. P. (1991). Fracture properties of concrete as determined by means of wedg splitting test and tapered double cantilever beam test, In Shah S. P. and Carpinteri A. (editors), *Fracture Mechanics Test Methods for Concrete*, Chapman & Hall, London, pp. 87-128.

Saad M., Abo-El- Enein S. A. Hanna, G. B. and Kotkata, M. F. (1996). Effect of temperature on physical and chemical properties of concrete containing silica fume, *Cement and Concrete Research*, 26 (5), pp. 669-675.

Sabir, B. B., Wild, S., and Asili, M. (1997). On the tortuosity of the fracture surface in concrete, *Cement and Concrete Research*, 27, pp. 785-795.

Santos, R. S., Rodrigues, F. A., Segre, N. and Joekes, I. (1999). The Macro-defect free cements influence of poly (vinyl alcohol), cement type, and silica fume, *Cement and Concrete Research*, V 29, pp. 747–751

Schneider, U. (1976). Behaviour of concrete under thermal steady state and non- steady state condition, *Fire and Materials*, 1, pp. 103-115.

Sen, R., Mullins, G., Shahawy, M. and Spain, J. (2000).Durability of CFRP/epoxy/Concrete bond, Composites in the Transportation Industry, *Proceedings of the ACUN-2 International Composite Conference*, University of South Wales. Australia.

Shah, S. P., Peled, A., Aldea, C. M. and Akkaya, Y. (1999). Scope of high performance fibre reinforced cement composites, *In Third International Workshop on high performance Fibre Reinforced Cement composites* (HPRCC3), Reinhardt, H. W., &Naaman, A. E. (eds), Mains, Germany, pp. 113-129.

Shah, S. P., Swartz, S. E. and Ouyang, C. (1995). *Fracture Mechanics of Concrete:* Applications of Fracture Mechanics to Concrete, Rock and other Quasi-brittle Material, John Wiley and Sons, USA.

Shah, S. P. and Young, J. F. (1990). Current research at the NSF Science and Technology Centre for Advanced Cement-Based Materials, *American Ceramic Society Bulletin*, pp. 1319-1331.

Shang, H. and Song, Y. (2006) Experimental study of strength and deformation of plain concrete under biaxial compression after freezing and thawing cycles. *Cement and Concrete Research. V.36* pp. 1857-1864.

Shannag, M. J. and Hansen, W. (2000). Tensile property of fibre-reinforced very high strength mortar, *Magazine of Concrete Research*, 52 (2), pp. 101-108.

Sharif, A., Al-Sulaimani, G., Basunbul, I., Baluch M., and Husain, M. (1995). Strengthening of Shear-damaged RC Beams by External Bonding of Steel Plates, *Magazine of Concrete Research*, 47(173). pp. 329-334.

Shih, C. F. and Asaro, R. (1988). Elastic-plastic analysis of cracks on biomaterial interfaces; part 1: small scale yielding, *Journal of Applied Mechanics*, 55, pp. 299-316.

Soroka, I. and Jaigermann, C. (1984). Deterioration and Durability of concrete in Hot Climate. *Proceedings of RILEM Seminar on the Durability of Concrete Structures under Normal Outdoors Exposure*, Hanover, FRG, pp. 52-60.

Soroushian, P. and Elzafraney, M. (2004). Damage effects on concrete performance and microstructure, *Cement & Concrete Composites*, pp. 853–859.

Sullivan, A. P. (1999). The effect of hydrothermal curing at 90^0C and the use of 12 mm steel fibres on reactive powder concrete, *MSc. Thesis, Cardiff University*.

Sun, W., Zhang, Y., Yan, H., and Mu, R. (1999).Damage and damage resistance of high strength concrete under the action of load and freeze–thaw cycles, *Cement and Concrete Research V.29* pp.1519–1523.

Sundarraja, M. C. and Rajamohan, S. (2007). Strengthening of RC beams in shear using GFRP inclined strips, *Construction and Building Materials,* 23, pp. 856 – 864.

Swamy, R. N. (1992). Fibre reinforced cement and concrete, *Proceedings of the Fourth RILEM International Symposium*, pp. 1347.

Swamy, R., Jones, R. and Bloxham, J. (1987). Structural Behaviour of Reinforced Concrete Beams Strengthened by Epoxy-bonded Steel Plates. *The Structural Engineer,* 65(2), pp. 59-68.

Tada, H., Paris, P. and Irwin, G. (1985). The Stress Analysis of Cracks Handbook, *Del Research Corporation,* St. Louis, Missouri, Part 2 pp. 16-17.

Tarek, H. (2006). Load deflection behaviour of RC beams strengthened with GFRP sheets subjected to different environmental conditions. *Cement & Concrete Composites* 28 (2006) pp. 879–889.

Tasdemir, C., Tasdemir, M. A., Lydon, F. D. and Barr, B. I. (1996). Effects silica fume and aggregate size on the brittleness of concrete, *Cement and Concrete Research*, V 26(1), pp. 63-68.

Teng, J., Chen, J., Smith, S., and Lam, L. (2002). FRP Strengthened RC Structures, *John Wiley & Sons Ltd*, Chichester, UK.

Tjiptobroto, P. and Hansen, W. (1993). Tension strain hardening and multiple cracking in high-performance cement-based composites containing discontinuous fibre, *ACI Materials Journal*, 90 (1), pp.16-25.

Triantafillou, T. C. and Plevris, N (1992). Strengthening of RC beams with epoxy-bonded fibre composites materials, *Materials and Structures*, 25 (148), pp. 201-211.

Tschegg, E. K. (1991). A new equipment for fracture tests on concrete, *Material Testing*, pp. 338-342.

Tschegg, E. K. (1997). An efficient fracture test method for bituminous and layer bonds, Mechanical tests for Biuminous Materials, *Proceeding of Fifth International RILEM Symposium*, Di Benedetto, H. and Francken, L. (ed), pp. 405-411.

Tschegg, E. K., Rotter, H. M., Roelfstra, P. E., Bourgund, U. and Jussel, P. (1995). Fracture mechanical behaviour of aggregate-cement matrix interfaces, *Journal of Materials in Civil Engineering*, pp. 199-203.

Tschegg, E. K. and Stanzel, S. E. (1991). Adhesive powder measurements of bonds between old and new concrete, *Journal of Materials Science*, 26, pp. 5189-5194.

Uomoto T, Nishimura T. (1999). Deterioration of aramid, glass and carbon fibres due to alkali acid and water in different temperatures. *Proceedings of the fourth international symposium on fibre reinforced polymer reinforcement for reinforced concrete structures*, Baltimore; 1999. pp. 515-522.

Van Mier, J. G. (1997). Fracture Processes of Concrete, CRC Press.

Wang, J. and Karihaloo, B. L. (2000). Material instability in the tensile response of short-fibre-reinforced quasi-brittle composites, *Archives of Mechanics*, 52, pp.839-855.

Williams, M. L. (1959). The stress around a fault or crack in dissimilar media, *Bulletin of the Seismological Society of American*, 49, pp. 199-204.

Williams, B., Bisby, L. Green, M. and Kodur, V. (2003). An investigation of the fibre behaviour of FRP strengthened reinforced concrete beams. *Proceeding of the 10th International Conference on Structural Faults and Repair*. London, CD ROM.

Wu, C. (2000). Micromechanical tailoring of PVA-ECC for structural applications. *PhD dissertation*.

Yang, Q. and Zhu, B. (2005). Effect of steel fibre on the deicer-scaling resistance of concrete, *Cement and Concrete Research*, pp. 2360 – 2363.

Yining, D. and Wolfgang, K. (2000). Compressive stress-strain relationship of steel fibre-reinforced concrete at early age, *Cement and Concrete Research*, pp. 1573-1579.

Yin-Wen, C. and Shu-Hsien, C., (2004). Effect of silica fume on steel fibre bond characteristics in reactive powder concrete, *Cement and Concrete Research*, Vol. 34 pp.1167–1172.

Zanni, H., Cheyrezy, M., Maret, V., Philipot, S. and Nieto, P. (1996). Investigation of hydration and pozzolanic reaction in reactive powder concrete (RPC) using ^{29}Si NMR, *Cement and Concrete Research*, 26 (1), pp. 93-100.

Zhang, Z., Bicanic, N., Pearce, C. and Balabanic, (2000). Residual fracture properties of normal and high strength concrete subjected to elevated temperature, *Magazine of Concrete Research*, 52, pp. 123-136.

Zhang, Z., Bicanic, N., Pearce, C. and Philipot, D. (2002). Relationship between brittleness and moisture loss of concrete exposed to high temperature, *Cement and Concrete Research*, 32, pp. 363-371.

Zhen, M. and Chung, D. (2000). Effects of temperature and stress on the interface between concrete and its fibre-matrix composite retrofit, Studies by electrical resistance measurement, *Cement and Concrete Research*, 30, pp. 799-802.

Ziraba, Y. N., Baluch, M. B., Basunbul, I. A., Sharif, A. M., Azad, A. K., and Al-Sulaimani, G. J. (1994). Guideline toward the design of reinforced concrete beams with external plates. *ACI Structural Journal.* **91**(6) pp.639-646.

Appendices

Appendix A

Product information sheets

Blue Circle Cement

Blue Circle

Ordinary Portland cement

1.

2.

Blue Circle ordinary Portland cement (OPC) is a general purpose cement which complies with the requirements for ordinary Portland cement in BS12 'Portland cements'. It is a quality assured product covered by the Cement Industry Quality Assurance Scheme independently monitored by the British Standards Institution (BSI QAS 2420/47).

TYPICAL PROPERTIES			
Surface Area	(m²/kg)		320 to 390
Setting Time			
Initial	(mins)		80 to 180
Final	(mins)		140 to 240
BS4550 Concrete			
Compressive Strength			
(N/mm²)	3 day		20 to 27
	7 day		30 to 37
	28 day		40 to 47
Apparent particle			
density	(kg/m³)		3080 to 3140
Bulk density	(kg/m³)		
	Aerated		1000 to 1300
	Settled		1300 to 1450
Colour	—Y value		27.5 to 39.0
Sulphate	—SO_3	(%)	2.5 to 3.5
Chloride	—Cl	(%)	Less than 0.03
Alkali	—Eq Na_2O	(%)	0.45 to 0.90
Silica	—SiO_2	(%)	19.5 to 21.0
Lime	—CaO	(%)	63.5 to 66.0
Tricalcium Silicate	—C_3S	(%)	45.0 to 60.0
Dicalcium Silicate	—C_2S	(%)	12.5 to 25.0
Tricalcium Aluminate	—C_3A	(%)	7.0 to 12.0
Tetracalcium Aluminoferrite	—C_4AF	(%)	6.0 to 10.0

APPLICATIONS:

a) For concrete, mortar or grout in a wide range of end-uses, from the small D-I-Y job to the largest civil engineering project.

b) For durable concrete and masonry construction with the option of a variety of attractive surface finishes.

To achieve optimum performance from Blue Circle ordinary Portland cement in concrete, mortar or grout, it is essential that it is correctly specified and used. Attention should be given to an adequate cement content, a water/cement ratio as low as possible consistent with satisfactory placing and thorough compaction and to adequate curing. Reference should be made to the following documents:

BS5328: 1981 — 'Methods for specifying concrete including ready-mixed concrete'.
BS8110: Part 1: 1985 - 'Structural use of concrete'.
BS5628: Part 3: 1985 - 'Use of Masonry'.

It is recommended that
- Blue Circle Sulfacrete should be used where increased resistance to sulphates is required.
- Blue Circle Lightning high alumina cement should be used to give heat-resisting and refractory properties.
Blue Circle Walcrete may be used as an alternative to produce high performance mortars.

PROPERTIES

a) Grey colour.

b) Consistent strength which exceeds the minimum requirements in BS12 by a considerable margin.

c) Compatible with admixtures such as air-entraining agents and workability aids, with cement replacement materials such as pulverized-fuel ash and ground granulated blastfurnace slag and with pigments. Trial mixes are recommended to determine the optimum mix proportions.

AVAILABILITY

Blue Circle OPC is available throughout the United Kingdom in bulk and paper bags (20 to the tonne).

TECHNICAL SUPPORT

Further information or advice on Blue Circle OPC and other Blue Circle cements can be obtained from the Technical Representative at the addresses listed overleaf.

HEALTH AND SAFETY

Contact with cement mixed with water or body fluids (eg sweat or eye fluid) or with concrete or mortar should be avoided as it may cause irritation, dermatitis or burns.

If such contact occurs the affected area should be washed without delay with plenty of clean water. In case of eye contact seek immediate medical advice.

Refer to the Blue Circle Portland Cement Health and Safety Information Sheet.

Photographs courtesy of
1. British Cement Association
2. British Cement Association

1. Identification of the Substance and Company

Product name: *Elkem Microsilica* ®

Address/Phone No.:
Elkem ASA,
Materials
P.O.Box 8126 Vaagsbygd
N-4602 Kristiansand S., Norway
Telephone: + 47 38 01 75 00
Telefax: + 47 38 01 49 70

Contact person: Tore Danielssen

Emergency Phone No.:   Not applicable

2. Composition/Information on Ingredients

Synonyms:
Microsilica, Silica powder, Amorphous silica,

Silicon dioxide powder, condensed SiO_2-fume, Silica fume.

CAS No.:   69012-64-2
EINECS No.:   273-761-1

HAZARDOUS INGREDIENT(S):   None
Symbol: None
R and S Phrases: None

Constituents (analysis):

	Weight%
Silicon dioxide (SiO_2) amorphous	85-98
Iron oxide (Fe_2O_3)	max.3.0
Aluminium oxide (Al_2O_3)	max.1.5
Calcium oxide (CaO)	max.0.7
Magnesium oxide (MgO)	max.2.0
Sodium oxide (Na_2O)	max.1.0
Potassium oxide (K_2O)	max.3.0
Carbon (C)	max.3.0

DATA SHEET

ADOFLOW EXTRA
Super Plasticiser for Concrete and Mortar

cription

uid plasticiser and water reducing agent which imparts extremely high workability when added to a concrete mix or a cementitious grout. Being a highly ive deflocculating agent it disperses cement paste into its primary particles significantly increasing the flow characteristics of the paste.

efits

nables concrete to achieve high compaction with minimal or no ibration or tamping.

creases flow characteristics of concrete to assist with difficult pours.

- Permits significant reduction in water content of normal workability concrete with consequent reduction in water/cement ratio to produce higher early and ultimate strengths.

tion

timum addition rate of ADOFLOW EXTRA is best determined after preliminary trials with the actual concrete under consideration. As a guide for carrying als an addition rate of 0.5 litres to 1.5 litres per 100 kilos Portland cement is recommended. Where high early and ultimate strength concrete is required, itating a steep reduction in water/cement ratio, the addition rate of ADOFLOW EXTRA may be increased up to 2.0 litres per 100 kilos Portland cement.

ng

FLOW EXTRA is best added during the mixing cycle preferably at the same time as the water. Alternatively it may be added to a normal concrete mix just o the pour allowing for a further mixing cycle of at least 2 minutes.

cal Comparisons

llowing data is typical of what can be expected when comparing a concrete mix with the inclusion of ADOFLOW EXTRA to a control mix.

Workability Self Compacting Concrete

ggregate/Cement Ratio 5.2:1
- W/C Ratio - Control Mix 0.58
- W/C Ratio - Test Mix 0.58

FLOW EXTRA - Test Mix 1.0 litre per 100 kg OPC

ump - Control Mix 50 mm
- Slump - Test Mix Collapse

pressive Strength - Test Mix:

days: 102 % of control
- 28 days: 103 % of control

Early & Ultimate Strength Concrete

ggregate/Cement Ratio 5.2:1
- W/C Ratio - Control Mix 0.58
- W/C Ratio - Test Mix 0.47

FLOW EXTRA - Test Mix 1.25 litre per 100 kg OPC

ump - Control Mix 50 mm
- Slump - Test Mix 50 mm

pressive Strength - Test Mix

ay: 180 % of control
- 7 days: 144 % of control
- 28 days: 135 % of control

ge & Shelf Life

at temperatures above freezing but not above 28° C in dry condition and under cover. Should freezing occur, completely thaw ial and then mix thoroughly before use. In these circumstances shelf life is indefinite.

ification Clause

LOW EXTRA manufactured by ADOMAST Building Chemicals Ltd shall be added to the concrete mix in accordance with the manufacturers endation.

th & Safety

LOW EXTRA is non-hazardous in normal use. If splashes should affect the eyes bathe immediately with copious quantities of clean water and then iately seek medical advice. Reference should be made to the separate Health and Safety literature.

ABCD 394 ISSUE: 4
ISSUED: JAN 1997

Sikadur 31
Thixotropic epoxy adhesive

Technical Data Sheet

Description
Sikadur 31 is a two component system, both components being thixotropic and containing fillers. The resin component is white and the hardener component black, ultimately producing a grey colour when mixed.

USES

Sikadur 31 is free of solvents.

Sikadur 31 will bond and fill virtually all building materials.

Sikadur 31 can be used for example to bond the following materials:

Concrete	Metals	Non-siliconised ceramics (slip bricks)
Asbestos	Stoneware	Cast asphalt
Wood	Glass	Polyester and epoxy components

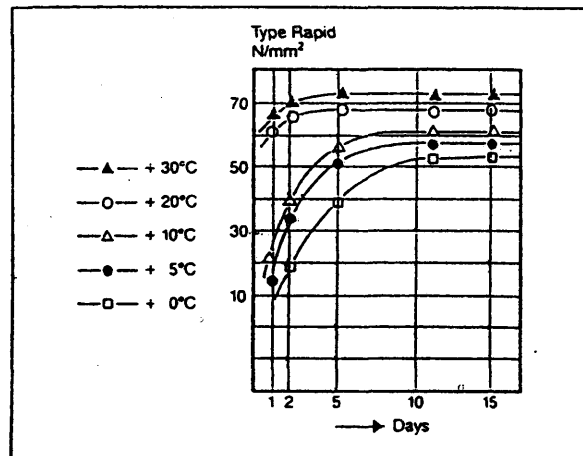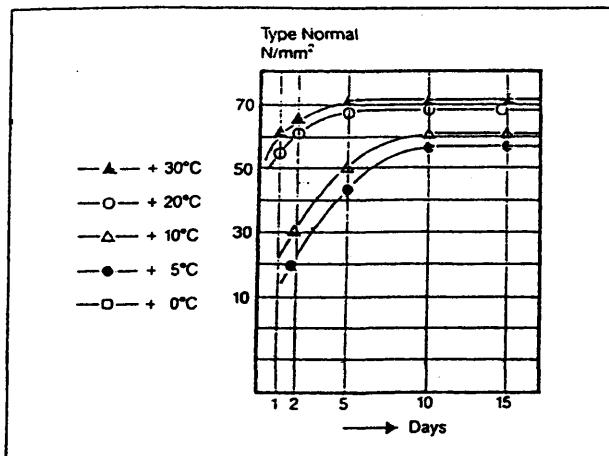Sikadur 31 resists the attack of a wide range of chemicals, solvents, etc.

Sikadur 31 is supplied in two grades: Normal and Rapid, and can be used in wet/damp or dry condition (no standing water), so enabling it to be used in most conditions within a temperature range of 0°C to 30°C. For structural strengthening please contact Sika's Specialist Engineering Division, for the appropriate materials and specification.

ADVANTAGES

* Colour coded components for thorough mixing

* Thixotropic – can be used on vertical and horizontal surfaces

* Outstanding adhesion – bonds to virtually all building surfaces

* Moisture tolerant – work can be carried out even in damp or wet conditions

* Rapid grade available for use at temperatures down to 0°C

* Sikadur 31 is approved for contact with potable water (WFBS No. 92 06505)

* High resistance to water absorption and creep

TECHNICAL DATA†

Grade	Normal	Rapid
Colour	Grey	Grey
Density	1.5 kg/litre	1.5 kg/litre
Pot life 30°C	20 mins.	–
20°C	40 mins	10 mins
10°C	1½ hours	30 mins
5°C	3½ hours	1 hour
0°C	–	1¼ hours
Tack Free	12 hours (at 20°C)	8 hours (20°C)
Shrinkage	Negligible	
Tensile strength*	14.8 N/mm²	
Flexural strength*	36 N/mm²	
Compressive strength	70–90 N/mm²	

Shear strength in excess of 21 N/mm² (3,000 psi)

E. Modulus	$7-7.5 \times 10^4$ kg/cm²
Storage life (minimum)	12 months in original containers at 5°C to 25°C
Application ranges	Rapid 0°C to 15°C Normal 5°C to 30°C

*Tested to B.S. 6319 (20°C cure)

Adhesion
(DIN 53232) to concrete: approx 3.5–4.5 N/mm
to grit blasted steel: approx 14 N/mm

(BS 6319: Part 4) Slant/Shear Test Sikadur 31: N/mm²

†Typical values

Type Normal N/mm²
—▲— + 30°C
—O— + 20°C
—△— + 10°C
—●— + 5°C
—□— + 0°C

Type Rapid N/mm²
—▲— + 30°C
—O— + 20°C
—△— + 10°C
—●— + 5°C
—□— + 0°C

SURFACE PREPARATION

All surfaces must be clean, sound and free from any dust, ice, oils, grease or other surface contaminants.

Concrete/Mortar Brickwork: Mechanically abrade the surface with a needle gun, mechanical wire brush, sandblast or grind. All surface laitence must be removed. Cement and concrete should be at least 4 weeks old.

Metals: Remove any paints, oils, grease, rust and oxide films by grit blasting. Where required apply one coat of **Friazinc R** or **Icosit EG1** as a primer/travel coat (refer to separate technical information sheet). **Sikadur 31** may be applied after approximately 8 hours. Note: In the event of extended waiting times, the surface of the **Friazinc R** or **Icosit EG1** should be thoroughly cleaned with fresh water.

Plastic components (epoxy, polyester), abrade and rinse with **Sikadur Cleaner.**

APPLICATION

Mix all of Part A (white resin) with all of Part B (black hardener) until an even grey colour is obtained. Mix well using a spatula or low speed drill and paddle.

Apply by trowel, serrated spreader, spatula or stiff brush (minimum thickness 1mm, maximum thickness per layer 30mm). Work the Sikadur 31 well into the substrate, especially if the substrate is damp.

Bond any subsequent materials onto the Sikadur 31 whilst it is still tacky.

Clean all tools, equipment with **Sikadur Cleaner** (flammable) whilst the resin is still soft. Hardened **Sikadur 31** can only be removed mechanically. **Do not part mix packs of Sikadur 31.**

Consumption guide *(does not allow for surface texture and wastage)*
1kg=approx 41 cubic inches or 666cc

Thickness of **Sikadur 31**	Kg/m² approx
2mm	3.0
4mm	6.0
10mm	15.0

PACKAGING

Sikadur 31 Normal: 1kg and 5kg
Sikadur 31 Rapid: 1kg and 5kg
Sikadur Cleaner: 5 litres and 25 litres and 200 litres (flammable).

Please consult our technical sales department for further information.

Sika Limited
Watchmead, Welwyn Garden City, Hertfordshire, AL7 1BQ Fax: 0707 329129
Telephone: 0707 329241

Appendix B

Load-CMOD curves for control and CARDIFRC bonded specimens

Control NSC
after 0 TC
$\alpha = 0.2$

Control NSC
after 0 TC
$\alpha = 0.6$

Control NSC
after 120 TC
$\alpha = 0.2$

Control NSC
after 120 TC
$\alpha = 0.6$

Control NSC
after 180 TC
$\alpha = 0.2$

Control NSC
after 180 TC
$\alpha = 0.6$

NSC bonded to CARDIFRC
after 0 TC
$\alpha = 0.2$

NSC bonded to CARDIFRC
after 0 TC
$\alpha = 0.6$

NSC bonded to CARDIFRC
after 120 TC
$\alpha = 0.2$

NSC bonded to CARDIFRC
after 120 TC
$\alpha = 0.6$

NSC bonded to CARDIFRC
after 180 TC
$\alpha = 0.2$

NSC bonded to CARDIFRC
after 180 TC
$\alpha = 0.6$

Control HSC
After 0 TC
$\alpha = 0.2$

Control HSC
After 120 TC
$\alpha = 0.6$

Control HSC
After 120 TC
$\alpha = 0.2$

Control HSC
After 120 TC
$\alpha = 0.6$

Control HSC
After 180 TC
α = 0.2

Control HSC
After 180 TC
α = 0.6

HSC bonded to CARDIFRC
After 0 TC
$\alpha = 0.2$

HSC bonded to CARDIFRC
After 0 TC
$\alpha = 0.6$

HSC bonded to CARDIFRC
After 120 TC
$\alpha = 0.2$

HSC bonded to CARDIFRC
After 120 TC
$\alpha = 0.6$

HSC bonded to CARDIFRC
After 180 TC
α = 0.2

HSC bonded to CARDIFRC
After 180 TC
α = 0.6

Appendix C

Computer programme

```
                    ┌──────────────┐
                    │    Start     │
                    └──────┬───────┘
                           │
                           ▼
         ┌──────────▶┌──────────────┐◀──────────┐
         │           │  c<a<0.9h    │           │
         │           └──────┬───────┘           │
         │                  │                   │
         │                  ▼                   │
    ┌────┼──────────▶┌──────────────┐◀──────────┼────┐
    │    │           │  0<w<1mm     │           │    │
    │    │           └──────┬───────┘           │    │
    │    │                  │                   │    │
    ▼    ▼                  │                   ▼    ▼
┌─────────────────┐         │         ┌─────────────────┐
│ Crack Tip Smooth│         │         │  Crack Opening  │
│ Closure Condition│◀───────┼────────▶│  Compatibility  │
│     (8.31)      │         │         │   Equation      │
│                 │         │         │     (8.46)      │
└────────┬────────┘         │         └────────┬────────┘
         │                  │                  │
         ▼                  │                  ▼
```

$$\{a_i, \ w_i, \ M_i\} \qquad \{a_k, \ w_k, \ M_k\} \qquad \{a_j, \ w_j, \ M_j\}$$

$$A, \ w, \ M_{kmax} = M_F$$
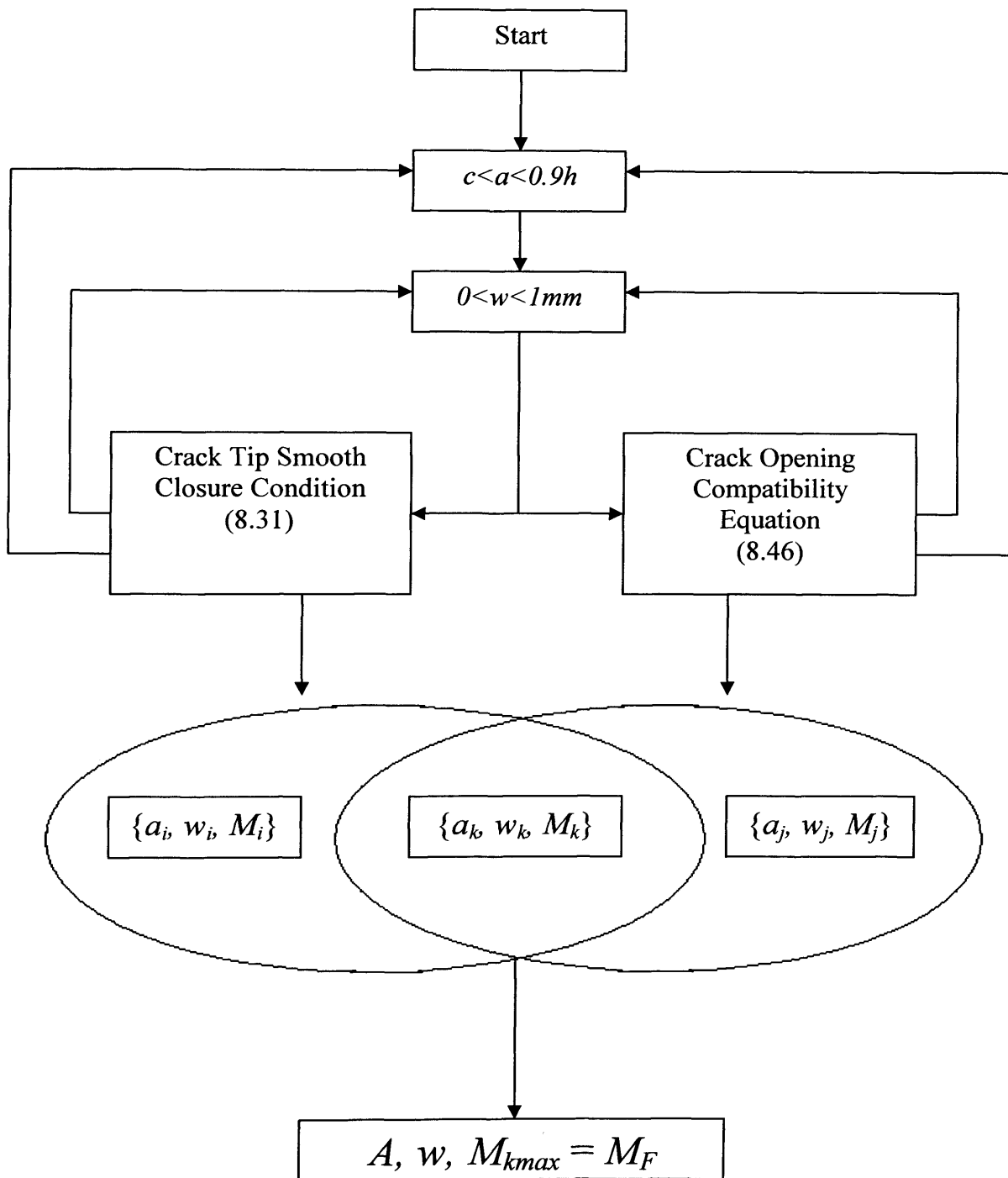
Flowchart of the programme for calculating the moment resistance of the beams using the fracture mechanics method (After Alaee and Karihaloo 2003b)

Solution of the stress intensity factor equation (8.30) for the beams retrofitted with one strip

```
CLS
COLOR 15, 1
pi = 3.141592

PRINT
PRINT "*********************************************************"
PRINT "     CALCULATION OF RESISTANT MOMENT OF A CONCRETE
"
PRINT "          BEAM STRENGTHENED BY ONE CARDIFRC STRIP
"
PRINT "               Using the concept of FRACTURE MECHANICS
"
PRINT "*********************************************************"
PRINT
PRINT

INPUT "Enter input file name:       ", IS
INPUT "Input the first output file name:       ", oS

OPEN IS FOR INPUT AS #1
OPEN oS FOR OUTPUT AS #2

LINE INPUT #1, NS
LINE INPUT #1, NS
INPUT #1, b, h, c, Ec

LINE INPUT #1, NS
LINE INPUT #1, NS
LINE INPUT #1, NS
LINE INPUT #1, NS
LINE INPUT #1, NS
INPUT #1, Ass, fy, Es

LINE INPUT #1, NS
LINE INPUT #1, NS
LINE INPUT #1, NS
LINE INPUT #1, NS
LINE INPUT #1, NS
INPUT #1, t, fctm, Ef, wc

Ec = Ec * 1000
Es = Es * 1000
Ef = Ef * 1000                ' GPa to MPa

'INPUT "a ="; a               ' a is the depth of crack
'INPUT "w ="; w               ' w is the opening of crack at the bottom of the beam
```

```
Print #2,
Print #2,"*****************************************************"
Print #2, "*   CALCULATION OF RESISTANT MOMENT OF CONCRETE      *"
Print #2, "*      BEAMS STRENGTHENED BY ONE CARDIFRC STRIP      *"
Print #2, "*          Using the concept of FRACTURE MECHANICS   *"
Print #2, "*****************************************************"
Print #2,
Print #2, "--------------------------------------------------------------------"
Print #2, "                        INPUT  DATA
"
Print #2, "--------------------------------------------------------------------"
Print #2, " Width of beam, b (mm): "; b
Print #2, " Height of beam h (mm): "; h
Print #2, " Distance between rebar and the bottom of beam, c (mm): "; c
Print #2, " Modulus of elasticity of concrete, Ec (MPa): "; Ec
Print #2, "--------------------------------------------------------------------"
Print #2, " Cross sectional area of rebar, As (mm^2): "; Ass
Print #2, " Yield stress of steel, fy (MPa): "; fy
Print #2, " Modulus of elasticity of steel, Es (MPa): "; Es
Print #2, "--------------------------------------------------------------------"
Print #2, " Thickness of tension HPFRC strip, t (mm): "; t
Print #2, " Tensile strength of HPFRC, fctm (MPa): "; fctm
Print #2, " Modulus of Elasticity of HPFRC, Ef (MPa): "; Ef
Print #2, " Maximum crack opening of HPFRC, wc (mm): "; wc
Print #2, ""
"*****************************************************"
Print #2, "*                                                   *"
Print #2, "*                      RESULTS                      *"
Print #2, "*                                                   *"
Print #2, "*****************************************************"
For a = c + t + 2 To 130 Step 2
Print #2, " ********************************"
Print #2, " * a = ";
Print #2, Format (a, "General Number")
Print #2, " ********************************"
"                                                                    "
_____

Print #2, , " w M - tot M - c M - s M - p"
Print #2, , "(mm) (kNm) (kNm) (kNm) (kNm) "
Print #2,
"                                                                    "
_____

ksi = a / h
For w = 0 To 1 Step 0.01
ym = 6 * ksi ^ 0.5 * (1.99 + 0.83 * ksi - 0.31 * ksi ^ 2 + 0.14 * ksi ^ 3) / ((1 - ksi) ^
1.5 * (1 + 3 * ksi))
'_____ STEEL BAR _____

Bta = c / h
ws = (1 - Bta / ksi) * w
```

AA = 4000 ' Effective area of concrete
ffs = 4.8 * 11876.5 * ws / (AA ^ 0.25) ' stress in steel
If ffs > fy Then
ffs = fy
End If
Fs = Ass * ffs
Fls = ((1.3 - 0.3 * (Bta / ksi) ^ 1.5) / (1 - (Bta / ksi) ^ 2) ^ 0.5 + 0.83 - 1.76 * Bta / ksi)
* (1 - (1 - Bta / ksi) * ksi)
Funcs = ((3.52 * (1 - Bta / ksi) / (1 - ksi) ^ 1.5 - (4.35 - 5.28 * Bta / ksi) / (1 - ksi) ^
0.5) + Fls) * 2 / (pi
* ksi) ^ 0.5

'_____RETROFITTING PLATE BONDED ON THE TENSION FACE_____

wte = (1 - t / (2 * h * ksi)) * w
If 0 < wte And wte < 6.5 Then
ppp = 0.003069107 * wte ^ 7 - 0.078952 * wte ^ 6 + 0.822382 * wte ^ 5 - 4.420119 *
wte ^ 4 +
12.797151 * wte ^ 3 - 18.105342 * wte ^ 2 + 5.732789 * wte + 12.894413
ElseIf wc <= wte Then
ppp = 0
End If
N = t / (2 * h)
FFp = ((1.3 - 0.3 * (N / ksi) ^ 1.5) / (1 - (N / ksi) ^ 2) ^ 0.5 + 0.83 - 1.76 * N / ksi) * (1
- (1 - N / ksi) * ksi)
Funcp = ((3.52 * (1 - N / ksi) / (1 - ksi) ^ 1.5 - (4.35 - 5.28 * N / ksi) / (1 - ksi) ^ 0.5)
+ FFp) * 2 / (pi * ksi) ^ 0.5
'_____CONCRETE IN TENSION_____

Int1 = 0
For ys = t / h To 0.999 * ksi Step ksi / 1000
wy = (1 - ys / ksi) * w
If wy < 0.019 Then 'cracked (1st part)
dppc = (-0.85 * 4.01 * wy / 0.0195 + 3.5)
ElseIf wy < 0.128 Then
dppc = (0.15 * 4.01 * (wy - 0.128) / (0.019 - 0.128)) ' cracked (2nd part)
Else 'cracked (without any stress
dppc = 0 'transformation)
End If
Flc = ((1.3 - 0.3 * (ys / ksi) ^ 1.5) / (1 - (ys / ksi) ^ 2) ^ 0.5 + 0.83 - 1.76 * ys / ksi) *
(1 - (1 - ys / ksi) * ksi)
dFuncc = ((3.52 * (1 - ys / ksi) / (1 - ksi) ^ 1.5 - (4.35 - 5.28 * ys / ksi) / (1 - ksi) ^ 0.5)
+ Fls) * 2 / (pi * ksi) ^ 0.5
Int1 = Int1 + dFuncc * dppc * ksi / 1000
Next ys

'_____

M = h ^ 1.5 * b * (h ^ 0.5 * Int1 + ppp * Funcp * (t / h ^ 0.5) + Fs * Funcs / (h ^ 0.5 *
b)) / ym

```
Mc = h ^ 2 * b * Int1 / ym
Ms = h * Fs * Funcs / ym
Mp = h * b * ppp * Funcp * t / ym

'Print #2, USING; " #.## #.## #.## #.## #.## "; w; M /
1000000; Mc / 1000000; Ms / 1000000; Mp / 1000000
Print #2, , Format(w, "0.00"), Format(M / 1000000, "0.000"), Format(Mc / 1000000,
"0.000"), Format
(Ms / 1000000, "0.000"), Format (Mp / 1000000, "0.000")
Next w
Next a
```

Solution of the crack opening compatibility equation (8.45) for the beams retrofitted with one strip

```
CLS
COLOR 15, 1
pi = 3.141592

Print
Print "*****************************************************"
Print "    CALCULATION OF RESISTANT MOMENT OF A CONCRETE    "
Print "        BEAM STRENGTHENED BY one CARDIFRC STRIP      "
Print "             Using the concept of FRACTURE MECHANICS "
Print "*****************************************************"
Print

INPUT "Enter input file name:                      ", iS
INPUT "Enter the first output file name:           ", oS

OPEN iS FOR INPUT AS #1
OPEN oS FOR OUTPUT AS #2

LINE INPUT #1, NS
LINE INPUT #1, NS
INPUT #1, b, h, c, Ec

LINE INPUT #1, nS
LINE INPUT #1, nS
LINE INPUT #1, nS
LINE INPUT #1, nS
LINE INPUT #1, nS
INPUT #1, Ass, fy, Es

LINE INPUT #1, nS
LINE INPUT #1, nS
LINE INPUT #1, nS
LINE INPUT #1, nS
LINE INPUT #1, nS
INPUT #1, t, fctm, Ef, wc

Ec = Ec * 1000
Es = Es * 1000
Ef = Ef * 1000

Print#2,
Print #2,
```

```
Print #2, "****************************************************** "
Print #2, " CALCULATION OF RESISTANT MOMENT OF A CONCRETE   "
Print #2, "        BEAM STRENGTHENED BY one CARDIFRC STRIP         "
Print #2, "            Using the concept of FRACTURE MECHANICS        "
Print #2, "******************************************************"
Print #2,
Print #2, "-----------------------------------------------------------"
Print #2, " INPUT DATA "
Print #2, "-----------------------------------------------------------"


Print #2, " Width of beam, b (mm): "; b
Print #2, " Height of beam h (mm): "; h
Print #2, " Distance between rebar and the bottom of beam, c (mm): "; c
Print #2, " Modulus of elasticity of concrete, Ec (MPa): "; Ec

Print #2, " --------------------------------------------------- "
Print #2, " Cross sectional area of rebar, As (mm^2): "; Ass
Print #2, " Yield stress of steel, fy (MPa): "; fy
Print #2, " Modulus of elasticity of steel, Es (MPa): "; Es

Print #2, " ---------------------------------------------------"
Print #2, " Thickness of tension HPFRC strip, t (mm): "; t
Print #2, " Tensile strength of CARDIFRC, fctm(MPa): "; fctm
Print #2, " Modulus of elasticity of HPFRC, Ef (MPa): "; Ef
Print #2, " Maximum crack opening of HPFRC, wc (mm): "; wc
Print #2,


Print #2, " ***************************************************"
Print #2, " * * "
Print #2, " * RESULTS * "
Print #2, " * * "
Print #2, "***************************************************"

Print #2, "_____        "
Print #2, "        a              w              M        "
Print #2, "       (mm)           (mm)          (kNm)       "
Print #2, "_____ "

'For n = 1 To 50
' a = 130
' For iii = 1 To 101
For a = c + t + 2 To 130 Step 2
' w = 0.08
' Mk = 9.55
' Mk = Mk * 1000000

'%%%%%%%%%%%%%%%%%%%%%%%%%%%%%%%%%%%%%%%%%%%%%%
```

```
'_____STEEL BAR_____
Bta = c / h
ksi = a / h
For w = 0 To 1 Step 0.01
ws = (1 - Bta / ksi) * w
aaa = 4000 'Effective area of concrete
ffs = 4.8 * 11876.5 * ws / (aaa ^ 0.25) 'stress in steel
If ffs > fy Then
ffs = fy
End If
Fs = Ass * ffs
'_____RETROFITING PLATE_____

wte = (1 - t / (2 * h * ksi)) * w
If 0 < wte And wte < 6.5 Then
ppp = 0.003069107 * wte ^ 7 - 0.078952 * wte ^ 6 + 0.822382 * wte ^ 5 - 4.420119 *
wte ^ 4 + 12.797151 * wte ^ 3 - 18.105342 * wte ^ 2 + 5.732789 * wte + 12.894413
ElseIf wc < wte Then
ppp = 0
End If

'_____

Intm = 0
Ints = 0
Intp = 0
Intc = 0
Intcc = 0
del = (ksi - Bta) / 1000
'Print Bta, del, ksi
For x = Bta + del To ksi Step del
Ym = 6 * x ^ 0.5 * (1.99 + 0.83 * x - 0.31 * x ^ 2 + 0.14 * x ^ 3) / ((1 - x) ^ 1.5 * (1 +
3 * x))
F1 = ((1.3 - 0.3 * (Bta / x) ^ 1.5) / (1 - (Bta / x) ^ 2) ^ 0.5 + 0.83 - 1.76 * Bta / x) * (1
- (1 - Bta / x) * x)
Yp = (2 / (pi * x) ^ 0.5) * (3.52 * (1 - Bta / x) / (1 - x) ^ 1.5 - (4.35 - 5.28 * Bta / x) /
(1 - x) ^ 0.5 + F1)
YmYp = Yp * Ym * del
Intm = Intm + YmYp
Yp2 = Yp ^ 2 * del
Ints = Ints + Yp2
q = t / (2 * h)
'Print Ym; F1; Yp; YmYp; Intm; Yp2; Ints; q; t; h
FFp = ((1.3 - 0.3 * (q / x) ^ 1.5) / (1 - (q / x) ^ 2) ^ 0.5 + 0.83 - 1.76 * q / x) * (1 - (1 -
q / x) * x)
F2 = (2 / (pi * ksi) ^ 0.5) * ((3.52 * (1 - q / x) / (1 - x) ^ 1.5 - (4.35 - 5.28 * q / x) / (1 -
x) ^ 0.5) + FFp)
F3 = F2 * Yp * del
Intp = Intp + F3
Next x
```

```
For ys = t / h To 0.999 * ksi Step ksi / 1000
Intcc = 0
wy = (1 - ys / ksi) * w
If wy < 0.019 Then 'cracked (1st part)
dppc = (-0.85 * 4.01 * wy / 0.0195 + 4.01)
ElseIf 0.019 < wy And wy < 0.128 Then
dppc = (0.15 * 4.01 * (wy - 0.128) / (0.195 - 0.128)) 'cracked (2nd part)
Else 'cracked (without any stress
dppc = 0 'transformation)
End If
BS = ys
If ys < Bta Then
BS = Bta
End If
del1 = (ksi - BS) / 100
For x = BS + del1 To ksi Step del1
Ym = 6 * x ^ 0.5 * (1.99 + 0.83 * x - 0.31 * x ^ 2 + 0.14 * x ^ 3) / ((1 - x) ^ 1.5 * (1 +
3 * x))
```

' _____Y (x, Bta) _____

```
F4 = ((1.3 - 0.3 * (Bta / x) ^ 1.5) / (1 - (Bta / x) ^ 2) ^ 0.5 + 0.83 - 1.76 * Bta / x) * (1
- (1 - Bta / x) * x)
F5 = (2 / (pi * x) ^ 0.5) * ((3.52 * (1 - Bta / x) / (1 - x) ^ 1.5 - (4.35 - 5.28 * Bta / x) /
(1 - x) ^ 0.5) + F4)
```

' _____Y (x, ys) _____

```
F6 = ((1.3 - 0.3 * (ys / x) ^ 1.5) / (1 - (ys / x) ^ 2) ^ 0.5 + 0.83 - 1.76 * ys / x) * (1 - (1
- ys / x) * x)
F7 = (2 / (pi * x) ^ 0.5) * ((3.52 * (1 - ys / x) / (1 - x) ^ 1.5 - (4.35 - 5.28 * ys / x) / (1 -
x) ^ 0.5) + F6)
F8 = F5 * F7 * del1
```

' _____

```
Intcc = Intcc + F8
Next x
F9 = 2 * h * dppc * Intcc * ksi / (1000 * E) 'ksi /1000 = dys
Intc = Intc + F9
Next ys
m = h * b * E * (ws + 2 * Fs * Ints / (b * E) + 2 * ppp * t * Intp / E + Intc) / (Intm * 2)
Ms = h * Fs * Ints / Intm
Mp = h * b * ppp * t * Intp / Intm
Mws = h * b * E * ws / (2 * Intm)
Mc = h * b * E * Intc / (2 * Intm)

'Print m / 1000000; Ms; Mp; Mws; Mc
'Print (m - Mk)
'If (Abs (m - Mk) < 100000) Then
```

```
'Print #2, USING; " ###.# #.## ##.## "; a; w; M / 1000000

Print #2, , Format(a, "0.00"), Format(w, "0.000"), Format(m / 1000000, "0.000")
'End If
Next w
Next a
Next iii
Next n
```

Solution of the stress intensity factor equation (8.30) for the beams retrofitted with three strips

```
CLS
COLOR 15, 1
pi = 3.141592

Print
Print "*********************************************************"
Print "  CALCULATION OF RESISTANT MOMENT OF A CONCRETE       "
Print "     BEAM STRENTHENED BY THREE CARDIFRC STRIPS         "
Print "             Using the concept of FRACTURE MECHNICS    "
Print "*********************************************************"

INPUT "Enter input file name:            ", IS
INPUT "Enter the first output file name:     ", oS

OPEN IS FOR INPUT AS #1
OPEN oS FOR OUTPUT AS #2

LINE INPUT #1, NS
LINE INPUT #1, NS
INPUT #1, b, h, c, Ec

LINE INPUT #1, NS
LINE INPUT #1, NS
LINE INPUT #1, NS
LINE INPUT #1, NS
LINE INPUT #1, NS
INPUT #1, Ass, fy, Es

LINE INPUT #1, NS
LINE INPUT #1, NS
LINE INPUT #1, NS
LINE INPUT #1, NS
LINE INPUT #1, NS
Input #1, t, fctm, Ef, wc

Ec = Ec * 1000
Es = Es * 1000
Ef = Ef * 1000                'GPa to MPa

'INPUT "a=" ; a               'a is the depth of crack
'INPUT "w=" ; w               'w is the opening of crack at the bottom of beam

Print #2,
Print #2,
Print #2,
```

```
Print #2, "**********************************************************"
Print #2, "    CALCULATION OF RESISTANT MOMENT OF A CONCRETE     "
Print #2, "       BEAM STRENTHENED BY THREE CARDIFRC STRIPS       "
Print #2, "            Using the concept of FRACTURE MECHNICS      "
Print #2, "**********************************************************"
Print #2, "
Print #2, " -----------------------------------------------------------"
Print #2, "                      INPUT DATA                          "
Print #2, " -----------------------------------------------------------"
Print #2, " Width of beam, b (mm):"; b
Print #2, " Height of beam, h (mm):"; h
Print #2, " Distance between rebar and the bottom of beam, c (mm):"; c
Print #2, " Modulus of elasticity of concrete, Ec (MPa):"; Ec
Print #2, " -----------------------------------------------------------"
Print #2, " Cross sectional area of rebars, Ass (mm^2):"; Ass
Print #2, " Yield stress of steel, fy (MPa):"; fy
Print #2, " Modulus of elasticity of steel, Es (MPa):"; Es
Print #2, " -----------------------------------------------------------"
Print #2, " Thickness of tension HPFRC strip, t (mm):"; t
Print #2, " Tensile strength of HPFRC, fctm (MPa):"; fctm
Print #2, " Modulus of elasticity of HPFRC, Ef (MPa):"; Ef
Print #2, " Maximum crack opening of HPFRC, wc (mm):"; wc


Print #2, "**********************************************************"
Print #2, " *                                                    * "
Print #2, " *                      RESULTS                       * "
Print #2, " *                                                    * "
Print #2, "**********************************************************"
For a = c + t + 2 To 130 Step 2
Print #2, ""
Print #2, ""
Print #2, ""
Print #2, " *******************"
Print #2, " * a = ";
Print #2, USING; "###.# *"; a
Print #2, " *******************"
Print #2, "
Print #2, "
Print #2, "_____"
Print #2, " w M-tot M-c M-s M-p M-sp "
Print #2, " (mm) (kNm) (kNm) (kNm) (kNm) (kNm) "
Print #2, "_____"

ksi = a / h
For w = 0 To 1 Step 0.01
```

Ym = 6 * ksi ^ 0.5 * (1.99 + 0.83 * ksi - 0.31 * ksi ^ 2 + 0.14 * ksi ^ 3) / ((1 - ksi) ^ 1.5 * (1 + 3 * ksi))
'_____ STEEL BAR _____ "

Bta = c / h
ws = (1 - Bta / ksi) * w
AA = 4000 'Effective area of concrete
ffs = 4.8 * 11876.5 * ws / (AA ^ 0.25) 'stress in steel
If ffs > fy Then
ffs = fy
End If
Fs = Ass * ffs
Fls = ((1.3 - 0.3 * (Bta / ksi) ^ 1.5) / (1 - (Bta / ksi) ^ 2) ^ 0.5 + 0.83 - 1.76 * Bta / ksi) * (1 - (1 - Bta / ksi) * ksi)
 Funcs = ((3.52 * (1 - Bta / ksi) / (1 - ksi) ^ 1.5 - (4.35 - 5.28 * Bta / ksi) / (1 - ksi) ^ 0.5) + Fls) * 2 / (pi * ksi) ^ 0.5

'_____ RETROFITTING PLATE BONDED ON THR TENSION FACE _____

wte = (1 - t / (2 * h * ksi)) * w
If 0 < wte And wte < 6.5 Then
ppp = 0.003069107 * wte ^ 7 - 0.078952 * wte ^ 6 + 0.822382 * wte ^ 5 - 4.420119 * wte ^ 4 + 12.797151 * wte ^ 3 - 18.105342 * wte ^ 2 + 5.732789 * wte * 12.894413
ElseIf wc < wte Then
ppp = 0
End If
N = t / (2 * h)
FFp = ((1.3 - 0.3 * (N / ksi) ^ 1.5) / (1 - (N / ksi) ^ 2) ^ 0.5 + 0.83 - 1.76 * N / ksi) * (1 - (1 - N / ksi) * ksi)
Funcp = ((3.52 * (1 - N / ksi) / (1 - ksi) ^ 1.5 - (4.35 - 5.28 * N / ksi) / (1 - ksi) ^ 0.5) + FFp) * 2 / (pi * ksi) ^ 0.5

'_____ CONCRETE IN TENSION _____

Int1 = 0
For ys = t / h To 0.999 * ksi Step ksi / 1000
wy = (1 - ys / ksi) * w
If wy < 0.019 Then 'cracked (1st part)
dppc = (-0.85 * 4.01 * wy / 0.0195 + 3.5)
ElseIf wy < 0.128 Then
dppc = (0.15 * 4.01 * (wy - 0.128) / (0.0195 - 0.128)) 'cracked (2nd part)
Else 'cracked (without any stress
dppc = 0 'transformation)
End If
Flc = ((1.3 - 0.3 * (ys / ksi) ^ 1.5) / (1 - (ys / ksi) ^ 2) ^ 0.5 + 0.83 - 1.76 * ys / ksi) * (1 - (1 - ys / ksi) * ksi)
dFuncc = ((3.52 * (1 - ys / ksi) / (1 - ksi) ^ 1.5 - (4.35 - 5.28 * ys / ksi) / (1 - ksi) ^ 0.5) + Flc) * 2 / (pi * ksi) ^ 0.5
Int1 = Int1 + dFuncc * dppc * ksi / 1000
Next ys

```
Int2 = 0
For ys = 0 To 0.999 * ksi Step ksi / 1000
If ys > (100 / h) Then 'limitation of the height of the side plate
GoTo 2
End If
wy = (1 - ys / ksi) * w
If 0 < wy And wy < 6.5 Then
dpsp = 0.003069107 * wy ^ 7 - 0.078952 * wy ^ 6 + 0.822382 * wy ^ 5 - 4.420119 *
wy ^ 4 + 12.797151 * wy ^ 3 - 18.105342 * wy ^ 2 + 5.732789 * wy + 12.894413
ElseIf wc < wy Then
dpsp = 0
End If
Flsp = ((1.3 - 0.3 * (ys / ksi) ^ 1.5) / (1 - (ys / ksi) ^ 2) ^ 0.5 + 0.83 - 1.76 * ys / ksi) *
(1 - (1 - ys / ksi) * ksi)
dFuncsp = ((3.52 * (1 - ys / ksi) / (1 - ksi) ^ 1.5 - (4.35 - 5.28 * ys / ksi) / (1 - ksi) ^
0.5) + Flsp) * 2 / (pi * ksi) ^ 0.5
Int2 = Int2 + dFuncsp * dpsp * ksi / 1000
Next ys
```

'_____

```
2 M = h ^ 1.5 * b * (h ^ 0.5 * Int1 + 2 * h ^ 0.5 * t * (Int2 / b) + ppp * Funcp * (t / h ^
0.5) + Fs * Funcs / (h ^ 0.5 * b)) / Ym
Mc = h ^ 2 * b * Int1 / Ym
Ms = h * Fs * Funcs / Ym
Mp = h * b * ppp * Funcp * t / Ym
Msp = 2 * h ^ 2 * t * Int2 / Ym

'Print #2, USING; " #.## ##.## ##.## ##.## ##.## ##.## "
'; w,; M; / 1000000; Mc / 1000000; Ms / 1000000; Mp / 1000000; Msp / 1000000
Print #2, , Format(w, "0.00"), Format(M / 1000000, "0.000"), Format(Mc / 1000000,
"0.000"), Format(Ms / 1000000, "0.000"), Format(Mp / 1000000, "0.000"),
Format(Msp / 1000000, "0.000")
Next w
Next a
End Sub
```

Solution of the crack opening compatibility equation (8.45) for the beams retrofitted with three strips


```
CLS
COLOR 15, 1
pi = 3.141592


Print
Print "****************************************************************"
Print "      CALCULATION OF RESISTANT MOMENT OF A CONCRETE BEAM      "
Print "            STRENGTHENED BY THREE CARDIFRC STRIPS             "
Print "            Using the concept of FRACTURE MECHANICS           "
Print "****************************************************************"
Print
Print

INPUT " Enter input file name:            ",is
INPUT " Enter the first  output file name:      ",os

Open is For Output As #1
Open os1 For Output As #2

LINE INPUT #1, NS
LINE INPUT #1, NS
INPUT #1, b, h, c, Ec

LINE INPUT #1, NS
LINE INPUT #1, NS
LINE INPUT #1, NS
LINE INPUT #1, NS
LINE INPUT #1, NS
INPUT #1, Ass, fy, Es

LINE INPUT #1, NS
LINE INPUT #1, NS
LINE INPUT #1, NS
LINE INPUT #1, NS
LINE INPUT #1, NS
Input #1, t, fctm, Ef, wc

Ec = Ec * 1000
Es = Es * 1000
Ef = Ef * 1000                'GPa to MP
Print #2,
Print #2,
Print #2,
```

```
Print #2, "   ****************************************************"
Print #2, "   *    CALCULATION OF RESISTANT MOMENT OF A CONCRETE   *   "
Print #2, "   *      BEAM STRENTHENED BY THREE CARDIFRC STRIPS      *   "
Print #2, "   *         Using the concept of FRACTURE MECHNICS      *   "
Print #2, "   **************************************************** "
Print #2,
Print #2,

Print #2, "      ---------------------------------------------------------------------------"
Print #2, "                              INPUT DATA                          "
Print #2, "      ---------------------------------------------------------------------------"

Print #2, "       Width of beam,                              b (mm):"; b
Print #2, "       Height of beam,                             h (mm):"; h
Print #2, "       Distance between rebar and the bottom of beam,   c (mm):"; c
Print #2, "       Modulus of elasticity of concrete,         Ec (MPa):"; E
Print #2, "      -------------------------------------------------------------------"
Print #2, "       Cross sectional area of rebars,        As (mm^2):"; Ass
Print #2, "       Yield stress of steel,                 fy (MPa):"; fy
Print #2, "       Modulus of elasticity of steel,        Es (MPa):"; Es
Print #2, "      -------------------------------------------------------------------"
Print #2, "       Thickness of tension HPFRC strip,      t (mm):"; t
Print #2, "       Tensile strength of HPFRC,             fctm (MPa):"; fctm
Print #2, "       Modulus of elasticity of HPFRC,        Ef (MPa):"; Ef
Print #2, "       Maximum crack opening of HPFRC,        wc (mm):"; wc
Print #2,
Print #2,
Print #2, "*********************************************************"
Print #2, "   *                                              *   "
Print #2, "   *                    RESULTS                   *   "
Print #2, "   *                                              *   "
Print #2, "*********************************************************"
Print #2, "        a              w              M          "
Print #2, "       (mm)           (mm)           (kNm)        "
Print #2, "_____"

'For j = 1 To 33
   'Line Input #3, nS
'Next j
'For n = 1 To 50

 ' For j = 1 To 4
   ' Line Input #3, nS
 ' Next j

 ' Line Input #3, mlS
 ' BS = MIDS(mlS, 37, 5)
 ' a = Val(BS)
```

```
' For j = 1 To 6
   ' Line Input #3, nS
' Next j

' For iii = 1 To 101
   'Line Input #3, l1S

  ' BS = MIDS(l1S, 5, 4)
  ' cS = MIDS(l1S, 18, 5)

  ' w = Val(BS)
  ' Mk = VAT(cS)
  ' Mk = Mk * 1000000
  '_____ STEEL BAR _____`

     For a = c + t + 2 To 130 Step 2
  Bta = c / h
ksi = a / h

     For w = 0 To 1 Step 0.01
Line Input #1, t1

b1 = Mid(t1, 29, 6)
  'Print #3, b1

Mk = Val(b1) * 1000000

ws = (1 - Bta / ksi) * w
   aaa = 4000                            'Effective area of concrete
   ffs = 4.8 * 11876.5 * ws / (aaa ^ 0.25)      'stress in steel

   If ffs > fy Then
   ffs = fy
   End If

   Fs = Ass * ffs
'_____ RETROFITTING PLATE _____

   wte = (1 - t / (2 * h * ksi)) * w

   If 0 < wte And wte < 6.5 Then

     ppp = 0.003069107 * wte ^ 7 - 0.078952 * wte ^ 6 + 0.822382 * wte ^ 5 -
4.420119 * wte ^ 4 + 12.797151 * wte ^ 3 - 18.105342 * wte ^ 2 + 5.732789 * wte +
12.894413
ElseIf wc < wte Then
ppp = 0
End If
```

```
'_____

Intm = 0
Ints = 0
Intp = 0
Intc = 0
Intcc = 0
Intspp = 0
Intsp = 0

del = (ksi - Bta) / 1000
For x = Bta + del To ksi Step del
Ym = 6 * x ^ 0.5 * (1.99 + 0.83 * x - 0.31 * x ^ 2 + 0.14 * x ^ 3) / ((1 - x) ^ 1.5 * (1 +
3 * x))
F1 = ((1.3 - 0.3 * (Bta / x) ^ 1.5) / (1 - (Bta / x) ^ 2) ^ 0.5 + 0.83 - 1.76 * Bta / x) * (1
- (1 - Bta / x) * x)
Yp = (2 / (pi * x) ^ 0.5) * (3.52 * (1 - Bta / x) / (1 - x) ^ 1.5 - (4.35 - 5.28 * Bta / x) /
(1 - x) ^ 0.5 + F1)
YmYp = Yp * Ym * del
Intm = Intm + YmYp
Yp2 = Yp ^ 2 * del
Ints = Ints + Yp2
q = t / (2 * h)
FFp = ((1.3 - 0.3 * (q / x) ^ 1.5) / (1 - (q / x) ^ 2) ^ 0.5 + 0.83 - 1.76 * q / x) * (1 - (1 -
q / x) * x)
F2 = (3.52 * (1 - q / x) / (1 - x) ^ 1.5 - (4.35 - 5.28 * q / x) / (1 - x) ^ 0.5) + FFp
F3 = F2 * 2 / (pi * ksi) ^ 0.5
F4 = F3 * Yp * del
Intp = Intp + F4
Next x
'_____CONCRETE IN TENSION_____

For ys = t / h To 0.999 * ksi Step ksi / 1000
Intcc = 0
wy = (1 - ys / ksi) * w
If wy < 0.019 Then 'cracked (1st part)
dppc = (-0.85 * 4.01 * wy / 0.0195 + 3.5)
ElseIf wy < 0.128 Then
dppc = (0.15 * 4.01 * (wy - 0.128) / (0.0195 - 0.128)) 'cracked (2nd part)
Else 'cracked (without any stress
dppc = 0 'transformation)
End If
BS = ys
If ys < Bta Then
BS = Bta
End If
del1 = (ksi - BS) / 100
For x = BS + del1 To ksi Step del1
```

Ym = 6 * x ^ 0.5 * (1.99 + 0.83 * x - 0.31 * x ^ 2 + 0.14 * x ^ 3) / ((1 - x) ^ 1.5 * (1 + 3 * x))
'_____Y (x, Bta) _____

F5 = ((1.3 - 0.3 * (Bta / x) ^ 1.5) / (1 - (Bta / x) ^ 2) ^ 0.5 + 0.83 - 1.76 * Bta / x) * (1 - (1 - Bta / x) * x)
F6 = (3.52 * (1 - Bta / x) / (1 - x) ^ 1.5 - (4.35 - 5.28 * Bta / x) / (1 - x) ^ 0.5 + F5)
E7 = F6 * 2 / (pi * x) ^ 0.5
'_____Y (x, ys) _____

F8 = ((1.3 - 0.3 * (ys / x) ^ 1.5) / (1 - (ys / x) ^ 2) ^ 0.5 + 0.83 - 1.76 * ys / x) * (1 - (1 - ys / x) * x)
F9 = (3.52 * (1 - ys / x) / (1 - x) ^ 1.5 - (4.35 - 5.28 * ys / x) / (1 - x) ^ 0.5 + F8)
F10 = F9 * 2 / (pi * x) ^ 0.5
F11 = F10 * F7 * del1
'_____

Intcc = Intcc + F11
Next x
 F12 = 2 * h * dppc * Intcc * ksi / (1000 * Ec) 'ksi /1000 = dy

Intc = Intc + F12
Next ys
'_____ Side Strip in Tension _____

For ys = 0 To 0.999 * ksi Step ksi / 1000
If ys > (100 / h) Then 'limitation of the height of the side strip
GoTo 2
End If
Intspp = 0
wy = (1 - ys / ksi) * w
If 0 < wy And wy < 6.5 Then
    dpsp = 0.003069107 * wy ^ 7 - 0.078952 * wy ^ 6 + 0.822382 * wy ^ 5 - 4.420119 * wy ^ 4 + 12.797151 * wy ^ 3 - 18.105342 * wy ^ 2 + 5.732789 * wy + 12.894413
ElseIf wc < wy Then
dpsp = 0
End If
BS = ys
If ys < Bta Then
BS = Bta
End If
del1 = (ksi - BS) / 100
For x = BS + del1 To ksi Step del1
Ym = 6 * x ^ 0.5 * (1.99 + 0.83 * x - 0.31 * x ^ 2 + 0.14 * x ^ 3) / ((1 - x) ^ 1.5 * (1 + 3 * x))
'_____ Y(x, Bta) _____

F5 = ((1.3 - 0.3 * (Bta / x) ^ 1.5) / (1 - (Bta / x) ^ 2) ^ 0.5 + 0.83 - 1.76 * Bta / x) * (1 - (1 - Bta / x) * x)
F6 = (3.52 * (1 - Bta / x) / (1 - x) ^ 1.5 - (4.35 - 5.28 * Bta / x) / (1 - x) ^ 0.5 + F5)

```
F7 = F6 * 2 / (pi * x) ^ 0.5

'_____ Y(x, ys) _____

F8 = ((1.3 - 0.3 * (ys / x) ^ 1.5) / (1 - (ys / x) ^ 2) ^ 0.5 + 0.83 - 1.76 * ys / x) * (1 - (1
- ys / x) * x)
F9 = (3.52 * (1 - ys / x) / (1 - x) ^ 1.5 - (4.35 - 5.28 * ys / x) / (1 - x) ^ 0.5 + F8)
F10 = F9 * 2 / (pi * x) ^ 0.5
F11 = F10 * F7 * del1
'_____


Intspp = Intspp + F11
Next x
'Print #2, "ys"; ys, dpsp, h, t, Intsp, ksi, b
 F12 = 4 * dpsp * h * t * Intspp * ksi / (1000 * Ec * b) 'ksi / 1000 = dys

Intsp = Intsp + F12
Next ys
'Print #2, b, ws, Ints, ppp, Intp, Intc, Intsp, Intm
2 m = h * b * Ec * (ws + 2 * Fs * Ints / (b * Ec) + 2 * ppp * t * Intp / Ec + Intc +
Intsp) / (Intm * 2)
'Print #3, m, m / 1000000
Ms = h * Fs * Ints / Intm
Mp = h * b * ppp * t * Intp / Intm
Mws = h * b * Ec * ws / (2 * Intm)
Mc = h * b * Ec * Intc / (2 * Intm)
Msp = h * b * Ec * Intsp / (2 * Intm)
Print #3, a, w, m, Mk, Abs(m - Mk)
 If (Abs(m - Mk) < 100000) Then
Print #2, a, w, (m + Mk) / 2000000
End If
 Next w
 Print #3, "-----------------"
 Print #2, "-----------------"

For j = 1 To 10
Line Input #1, t1
Next j
 Next a


End Sub
```